Generalisations of the Laplace–Runge–Lenz Vector in Classical Mechanics

Vivian Mervyn Gorringe

CHAPTER 3 AND 4

A thesis submitted to the Faculty of Science, University of the Witwatersrand, Johannesburg, in fulfilment of the requirements for the degree of Doctor of Philosophy.

Johannesburg, June 1995

CHAPTER 3

MOTION WITH CONSERVED L

3.1 The Conserved Laplace–Runge–Lenz Vector Analogue for the Equation of Motion $\ddot{\boldsymbol{r}} + f\boldsymbol{L} + g\hat{\boldsymbol{r}} = \boldsymbol{0}$

The contents of §§3.1–3.4 are described in Leach and Gorringe [78]. If we introduce the constraint that L is constant rather than its direction as was discussed in Chapter 2, we may write

$$\frac{1}{2}L^2 = \frac{1}{2}\boldsymbol{L}\cdot\boldsymbol{L} = \text{const.} \tag{3.1.1}$$

Upon differentiation of (3.1.1) we obtain

$$\dot{\boldsymbol{L}}\cdot\boldsymbol{L} = 0. \tag{3.1.2}$$

Equation (3.1.2) implies that $\dot{\boldsymbol{L}}$ and $\boldsymbol{L}$ are orthogonal. It follows that equations of motion arising from $\dot{\boldsymbol{L}}$ and combinations of other vectors orthogonal to $\boldsymbol{L}$ describe motion where L is conserved. One such orthogonal vector is $\boldsymbol{r}\times\boldsymbol{L}$ and hence the equation

$$\dot{\boldsymbol{L}} + f\boldsymbol{r}\times\boldsymbol{L} = \boldsymbol{0} \tag{3.1.3}$$

describes one possible class meeting the angular momentum requirement and should not be regarded as the most general. To generalise the results still further, we introduce a zero vector $g\boldsymbol{r}\times\hat{\boldsymbol{r}}$, allowing us to write (3.1.3) as

$$\boldsymbol{r}\times\ddot{\boldsymbol{r}} + f\boldsymbol{r}\times\boldsymbol{L} + g\boldsymbol{r}\times\hat{\boldsymbol{r}} = \boldsymbol{0}. \tag{3.1.4}$$

If we further assume that f and g are arbitrary functions, it follows that the equation

$$\ddot{\boldsymbol{r}} + f\boldsymbol{L} + g\hat{\boldsymbol{r}} = \boldsymbol{0} \tag{3.1.5}$$

describes motion subject to the constraint that L is constant. We now construct Laplace–Runge–Lenz analogues for (3.1.5) using the techniques described earlier by imposing restrictions upon the arbitrary functions f and g. It is of course also possible to introduce additional terms such as $e\dot{\boldsymbol{r}}\times\boldsymbol{L}$ into (3.1.3), although these types of problems which are connected with those described in §§2.10–2.17 are not investigated here.

The vector product of $\boldsymbol{r}$ with (3.1.5) gives

$$\dot{\boldsymbol{L}} = f\boldsymbol{L}\times\boldsymbol{r}. \tag{3.1.6}$$

The scalar product of (3.1.6) with $\boldsymbol{L}$ is zero since the magnitude of L was initially assumed constant.

Taking the vector product of (3.1.5) with $\boldsymbol{L}$ gives

$$\ddot{\boldsymbol{r}}\times\boldsymbol{L} + g\hat{\boldsymbol{r}}\times\boldsymbol{L} = \boldsymbol{0} \tag{3.1.7}$$

which can equivalently be written as

$$(\dot{\boldsymbol{r}}\times\boldsymbol{L})^{\cdot} - f\dot{\boldsymbol{r}}\times(\boldsymbol{L}\times\boldsymbol{r}) + \frac{g}{r}\,\boldsymbol{r}\times\boldsymbol{L} = \boldsymbol{0} \tag{3.1.8}$$

using (3.1.6). The vector triple product expansion of the middle term in (3.1.8) gives

$$f\dot{\boldsymbol{r}}\times(\boldsymbol{L}\times\boldsymbol{r}) = fr\dot{r}\boldsymbol{L}. \tag{3.1.9}$$

The term second from the right in (3.1.8) can be written using two alternate forms as

$$\frac{g}{r}\,\boldsymbol{r}\times\boldsymbol{L} = -\frac{g}{rf}\,\dot{\boldsymbol{L}} \tag{3.1.10}$$

and

$$\frac{g}{r}\,\boldsymbol{r}\times\boldsymbol{L} = -gr^2\dot{\hat{\mathbf{r}}}. \tag{3.1.11}$$

The two forms (3.1.10) and (3.1.11) suggest that we write

$$g = g_1 + g_2 \tag{3.1.12}$$

so that (3.1.8) becomes

$$(\dot{\boldsymbol{r}}\times\boldsymbol{L})^{\cdot} - fr\dot{r}\boldsymbol{L} - \frac{g_1}{rf}\,\dot{\boldsymbol{L}} - g_2r^2\dot{\hat{\boldsymbol{r}}} = \boldsymbol{0}. \tag{3.1.13}$$

Equation (3.1.13) is trivially integrable to a constant vector if we let $f = h'(r)/r$, $g_1 = h(r)h'(r)$ and $g_2 = k/r^2$. In this case we obtain

$$\boldsymbol{J} = \dot{\boldsymbol{r}}\times\boldsymbol{L} - h(r)\boldsymbol{L} - k\hat{\boldsymbol{r}} \tag{3.1.14}$$

which is a conserved Laplace–Runge–Lenz vector for the system described by the equation of motion

$$\ddot{\boldsymbol{r}} + \frac{h'(r)}{r}\,\boldsymbol{L} + \left(h(r)h'(r) + \frac{k}{r^2}\right)\hat{\boldsymbol{r}} = \boldsymbol{0}. \tag{3.1.15}$$

It should be noted that the structure of $\boldsymbol{J}$ given in (3.1.14) is opposite in sign to that often used in the literature. This is done to be consistent with the results of Chapters 1 and 2. It does not seem possible to construct a general Hamilton vector analogue for the equation of motion (3.1.15) although it is possible in special cases (see §3.5).

Taking the scalar product of $\dot{\boldsymbol{r}}$ with (3.1.15) gives an energy–like scalar integral

$$I = \frac{1}{2}\,\dot{\boldsymbol{r}}^2 + \frac{1}{2}\,h^2(r) - \frac{k}{r}. \tag{3.1.16}$$

It should be appreciated that J, L and I are not independent since

$$J^2 = 2L^2 I + k^2. \tag{3.1.17}$$

3.2 The Orbit Equation

Since there is no Hamilton–like vector in general, it does not appear possible to express the velocity hodograph in any recognisable or useful form nor does it seem possible to construct a velocity hodograph from the Laplace–Runge–Lenz vector analogue. It is possible, however, in special cases (see §3.6).

As in the two–dimensional case, the existence of the Laplace–Runge–Lenz–like vector $\boldsymbol{J}$ gives rise in a natural way to the orbit equation using $\boldsymbol{J}\cdot\boldsymbol{r}$. However, as the motion is truly three–dimensional we need one more scalar equation to specify the orbit completely. As in the case of planar motion we measure the polar angle θ from $\boldsymbol{J}$, but no longer confine θ to be in the plane of the orbit. The scalar product of (3.1.14) with $\boldsymbol{r}$ gives

$$\boldsymbol{J}\cdot\boldsymbol{r} = (\dot{\boldsymbol{r}}\times\boldsymbol{L})\cdot\boldsymbol{r} - kr \tag{3.2.1}$$

and upon rearranging

$$r = \frac{L^2}{k + J\cos\theta} \tag{3.2.2}$$

which is one of the required equations. The other equation is obtained by taking the scalar product of $\boldsymbol{J}$ with $r^{-2}\hat{\boldsymbol{\phi}}$, where ϕ is the azimuthal angle, giving

$$\dot{r}\dot{\phi}\sin\theta + h\dot{\theta} = 0 \tag{3.2.3}$$

so that

$$\dot{\phi} = -\frac{h\dot{\theta}}{\dot{r}\sin\theta}. \tag{3.2.4}$$

Differentiation of (3.2.2) with respect to time gives

$$\dot{r} = \frac{Jr^2\sin\theta\dot{\theta}}{L^2} \tag{3.2.5}$$

and hence (3.2.4) becomes

$$\dot{\phi} = -\frac{hL^2}{Jr^2\sin^2\theta}. \tag{3.2.6}$$

The conserved quantity L^2 can be written in terms of spherical polar coordinates as

$$L^2 = r^4(\dot{\theta}^2 + \sin^2\theta\dot{\phi}^2) \tag{3.2.7}$$

which combined with (3.2.6) gives

$$\dot{\theta}^2 = \frac{L^2(J^2\sin^2\theta - h^2L^2)}{J^2r^4\sin^2\theta}. \tag{3.2.8}$$

Thus we find that

$$\begin{aligned}\phi &= \int_{\theta_0}^{\theta} \frac{\dot{\phi}}{\dot{\theta}}\,\mathrm{d}\theta \\ &= -\int_{\theta_0}^{\theta} \frac{hL}{\sin\theta}\,(J^2\sin^2\theta - h^2L^2)^{-\frac{1}{2}}\,\mathrm{d}\theta.\end{aligned} \tag{3.2.9}$$

Using the orbit equation (3.2.2), $h(r)$ can be expressed in terms of θ and (3.2.2) and (3.2.9) together, fully describe the orbit. In general the integration in (3.2.9) would not be possible in closed form, but may be done for certain forms of $h(r)$.

3.3 The Motion in Time

Equation (3.2.8) can in theory be solved to give t as a function of θ using the orbit equation (3.2.2) to replace functions of r. Assuming that this is possible we may write

$$t = f_1(\theta), \tag{3.3.1}$$

where

$$f_1(\theta) = \int_{\theta_0}^{\theta} \frac{JL^3\sin\theta\,\mathrm{d}\theta}{(k + J\cos\theta)^2\left(J^2\sin^2\theta - h^2(r(\theta))L^2\right)^{\frac{1}{2}}}. \tag{3.3.2}$$

Provided (3.3.1) can be inverted to obtain θ as a function of t, the orbit equation (3.2.2) can be written as

$$r(t) = \frac{L^2}{k + J\cos(\theta(t))}. \tag{3.3.3}$$

$\phi(t)$ can in principle be obtained by solving (3.2.9), replacing occurrences of θ with the inverse of (3.3.1). In practice, however, it is very unlikely that (3.2.8) can be solved and even less likely that the necessary inversion would be possible.

The areal velocity or area swept out by the radius vector is given by

$$\mathrm{d}\boldsymbol{A} = \frac{1}{2}\boldsymbol{r} \times \dot{\boldsymbol{r}}\,\mathrm{d}t, \tag{3.3.4}$$

and after dividing (3.3.4) throughout by $\mathrm{d}t$ and equating the magnitudes of the resulting expression gives

$$\frac{\mathrm{d}A}{\mathrm{d}t} = \frac{1}{2}|\boldsymbol{r} \times \dot{\boldsymbol{r}}| = \frac{1}{2}L. \tag{3.3.5}$$

Since L is conserved for this class of problems, the areal velocity is constant or, in other words, equal areas are swept out in equal times, *i.e.*

$$A = \frac{1}{2}Lt. \tag{3.3.6}$$

If the motion occurs on a recognisable surface, by expressing the area in terms of well–known geometric quantities, an expression relating the period and the geometry of the orbit can in theory be obtained. A less geometric approach would be to evaluate (3.3.1) over a suitable fraction of the period.

3.4 Examples

1.) The three–dimensional orbits vary considerably depending on the choice of the parameters. For $h(r) = \lambda r$, we have the three–dimensional isotropic harmonic oscillator plus the forces $\lambda \boldsymbol{L}/r$ and $k\hat{\boldsymbol{r}}/r^2$. The addition of the angular momentum term in the force changes the character of the conserved quantities from a tensorial nature to a vectorial expression (see §1.7). The integration does not appear possible in closed form and so

$$\phi = -\int_{\theta_0}^{\theta} \left[\sin^2\theta\left(a^2\sin^2\theta(k + J\cos\theta)^2 - 1\right)\right]^{-\frac{1}{2}} \mathrm{d}\theta, \tag{3.4.1}$$

where $a^2 = J^2\lambda^{-2}L^{-6}$, can only be evaluated numerically. The orbits close only for certain choices of the parameter k. The figures below show the orbits, velocity hodographs and angular momentum curves for increasing values of k for which the orbits are closed. Figures 3.4.1 and 3.4.2 show the circular orbit and velocity hodographs respectively as a result of $\dot{r}$ and $\dot{\theta}$ remaining zero and $\dot{\phi} = -2^{\frac{1}{2}}/4$ throughout the motion. Figure 3.4.3 shows the variation of the angular momentum. Figures 3.4.4 and 3.4.5 show the orbit and the velocity hodograph respectively for an example with four–fold rotational symmetry about $\boldsymbol{J}$. Figure 3.4.6 shows the variation of the angular momentum. Figures 3.4.7 and 3.4.8 show the orbit and the velocity hodograph respectively for an example with twenty–one–fold rotational symmetry about $\boldsymbol{J}$. Figure 3.4.9 shows the variation of the angular momentum. Figures 3.4.10 and 3.4.11 show the orbit and the velocity hodograph respectively for an example with fourteen–fold rotational symmetry about $\boldsymbol{J}$. Figure 3.4.12 shows the variation of the angular momentum.

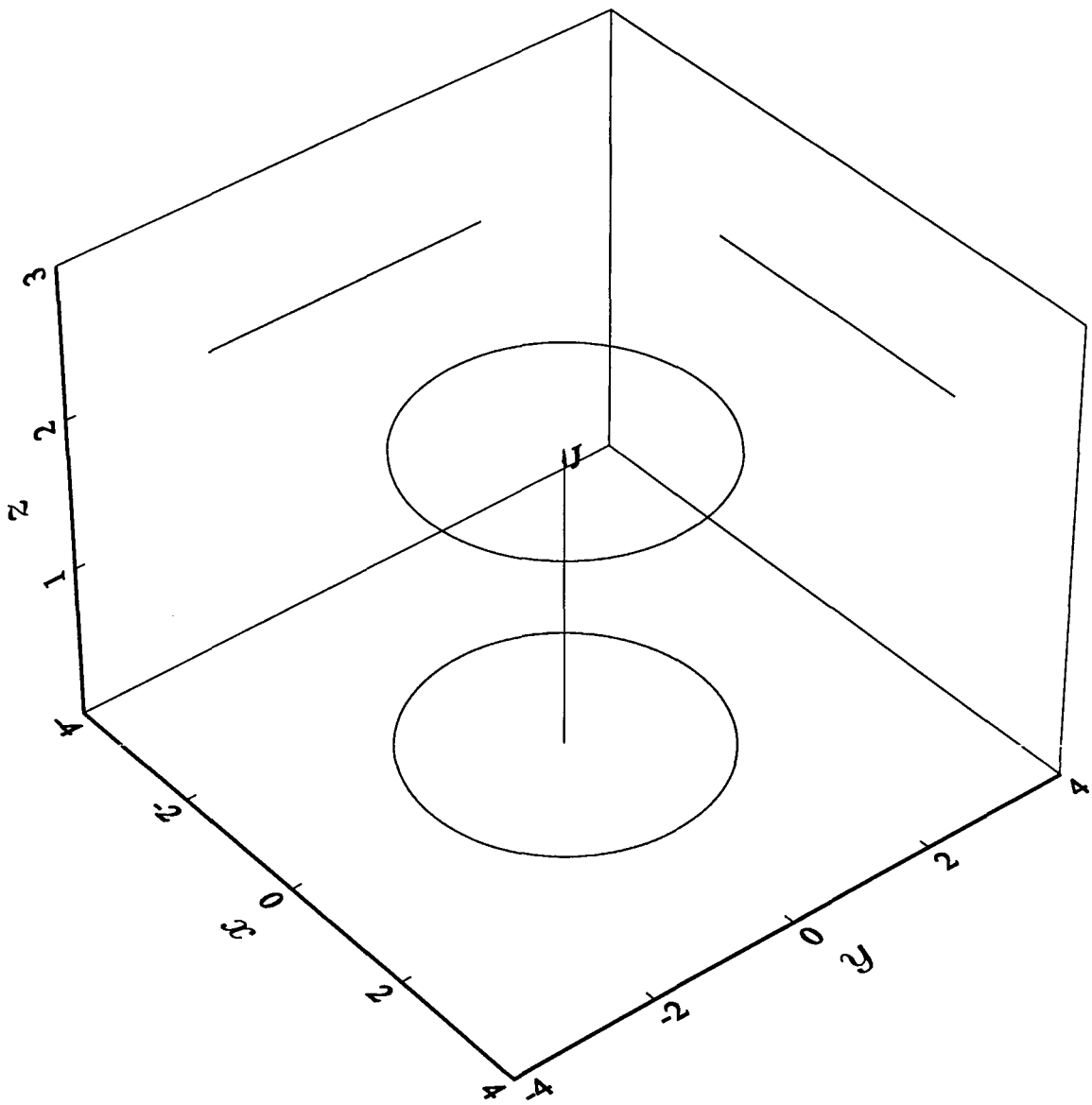

Figure 3.4.1. The circular orbit for $k = 0$, $\lambda = 1/4$, $\theta_0 = \pi/4$, $\phi_0 = 0$, $J = 2$ and $L = 2$. $\dot{r}$ and $\dot{\theta}$ are zero and $\dot{\phi} = -2^{\frac{1}{2}}/4$ throughout the motion which results in the z component of the orbit being constant and correspondingly the orbit being parallel to the azimuthal plane. Note that the height of the orbit above the azimuthal plane is given by L^2/J. The locus of radial vectors describes a right circular cone with the apex at the origin and the axis extending along the direction of $\boldsymbol{J}$. The projections of the orbit onto planes parallel to the xy, xz and yz planes are also shown.

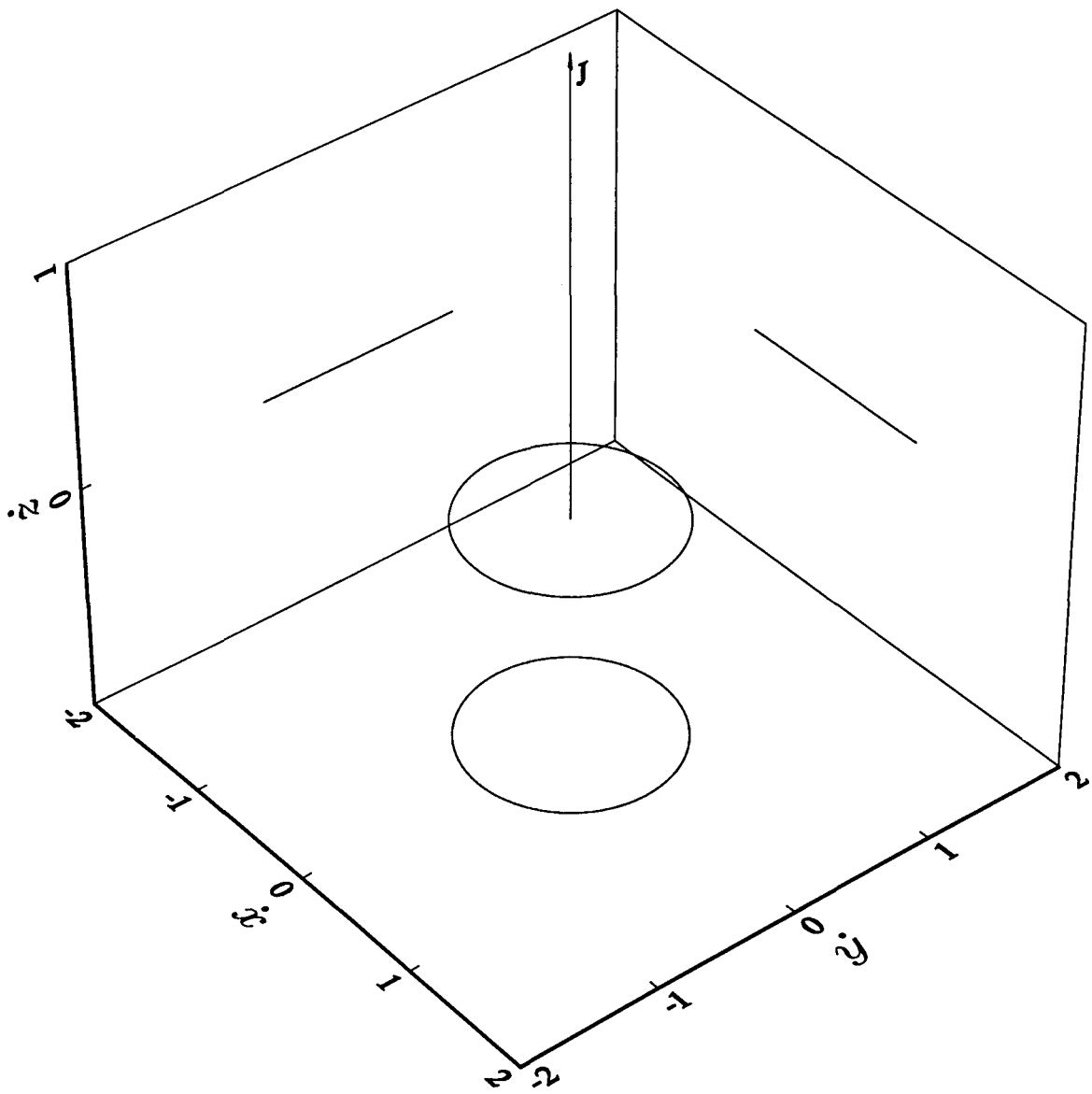

Figure 3.4.2. The circular velocity hodograph associated with Figure 3.4.1. Since $\dot{\boldsymbol{r}} = r \sin\theta \dot{\phi} \hat{\boldsymbol{\phi}}$, the velocity hodograph has no $\dot{z}$ component and lies in the $\dot{x}\dot{y}-$plane. The projections of the velocity hodograph onto planes parallel to the $\dot{x}\dot{y}$, $\dot{x}\dot{z}$ and $\dot{y}\dot{z}$ planes are also shown.

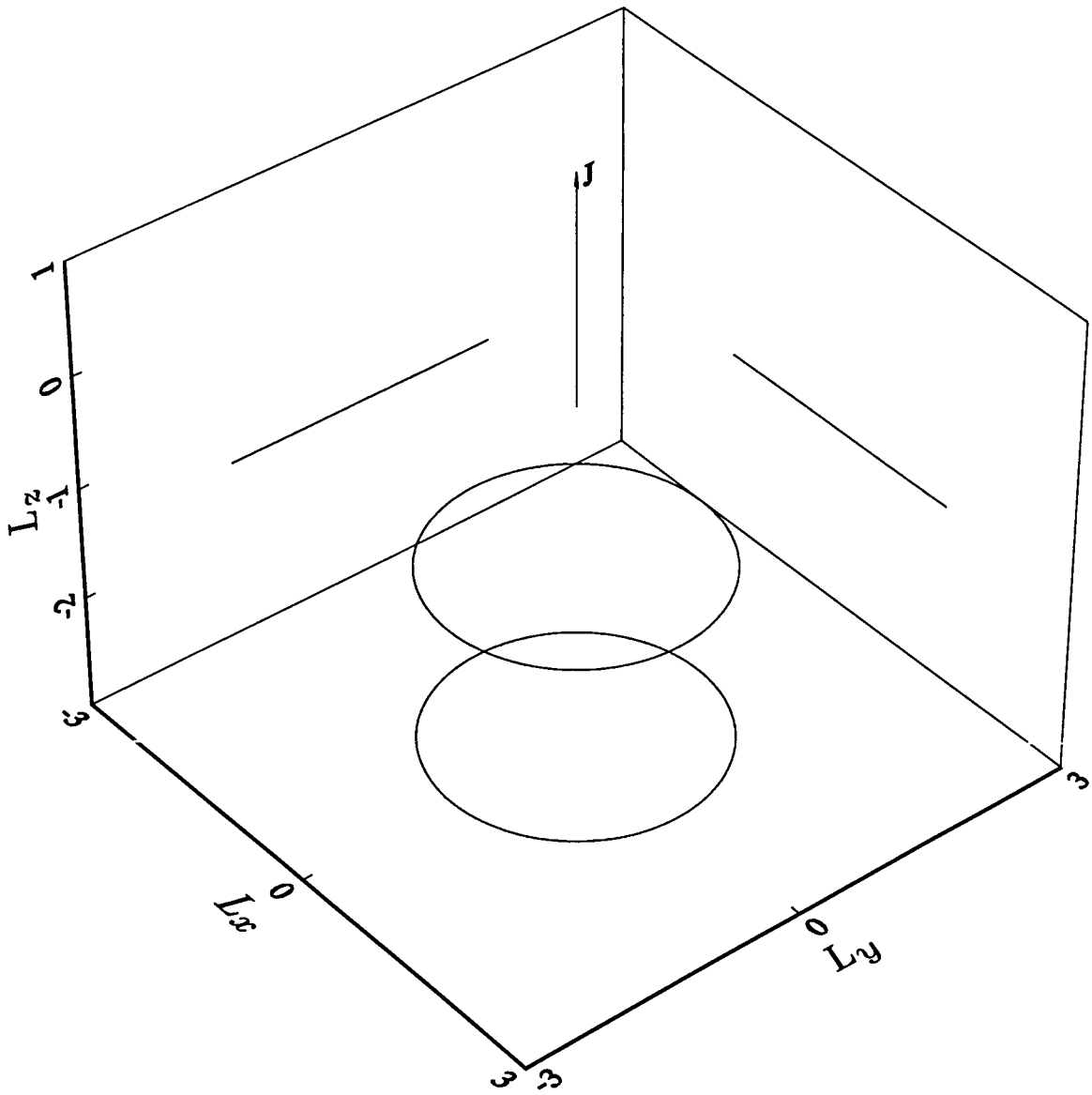

Figure 3.4.3. The circular angular momentum curve associated with Figures 3.4.1 and 3.4.2. In this example the angular momentum is constant in magnitude but not in direction. The angular momentum curve is a distance of $2\frac{1}{2}$ below the origin since $\boldsymbol{L}$ is orthogonal to $\boldsymbol{r}$ and $L = 2$. The locus of angular momentum vectors describes a right circular cone with the apex at the origin and the axis extending in the opposite direction to that of $\boldsymbol{J}$. The projections of the angular momentum curve onto planes parallel to the L_xL_y, L_xL_z and L_yL_z planes are also shown.

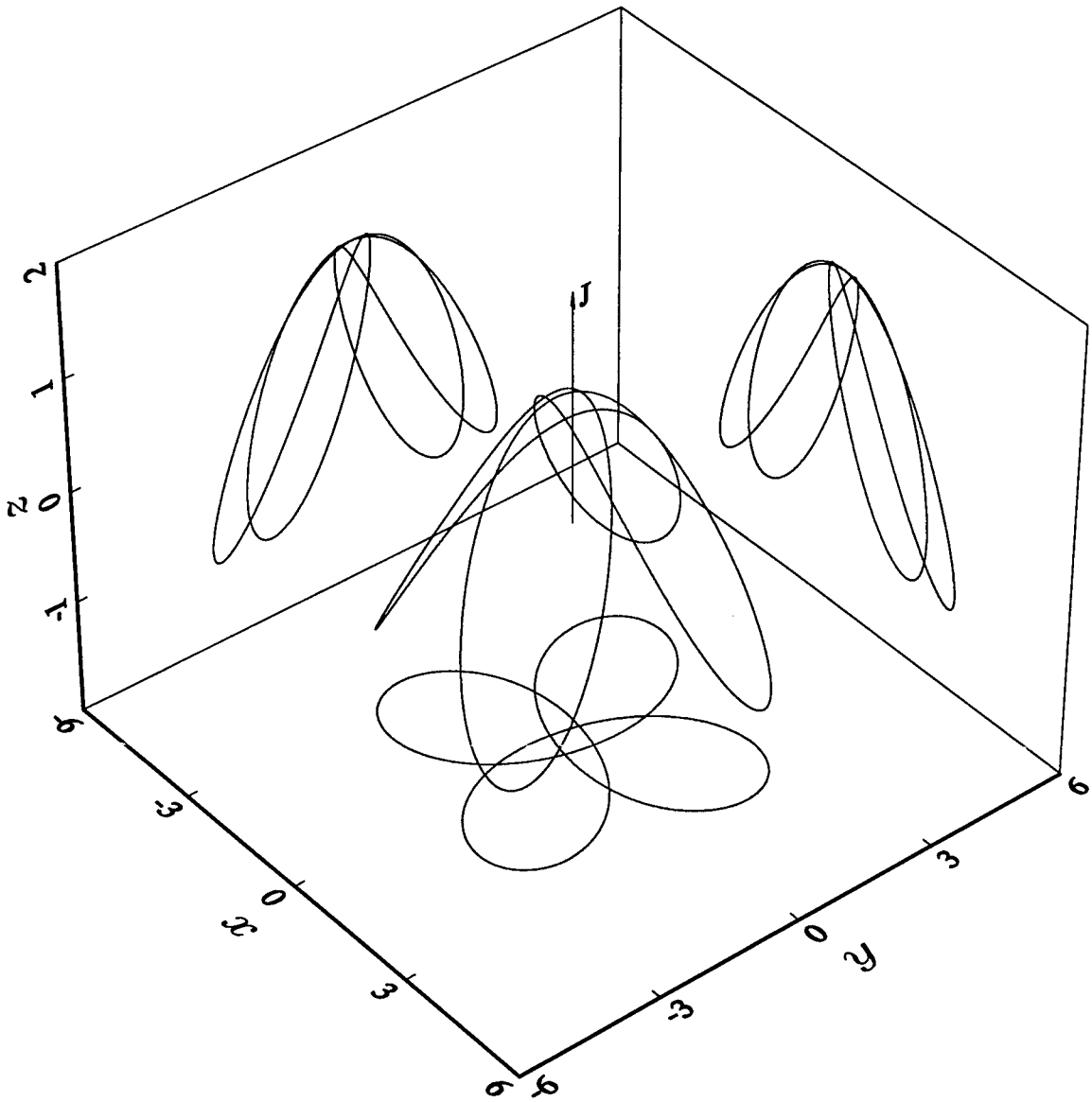

Figure 3.4.4. The orbit for $k = 1.745$, $\lambda = 1/4$, $\theta_0 = \pi/4$, $\phi_0 = 0$, $J = 2$ and $L = 2$. The value of k has been chosen to close the orbit. The orbit has four–fold rotational symmetry about $\boldsymbol{J}$. The projections of the orbit onto planes parallel to the xy, xz and yz planes are also shown. The xy projection is reminiscent of a four–leafed clover.

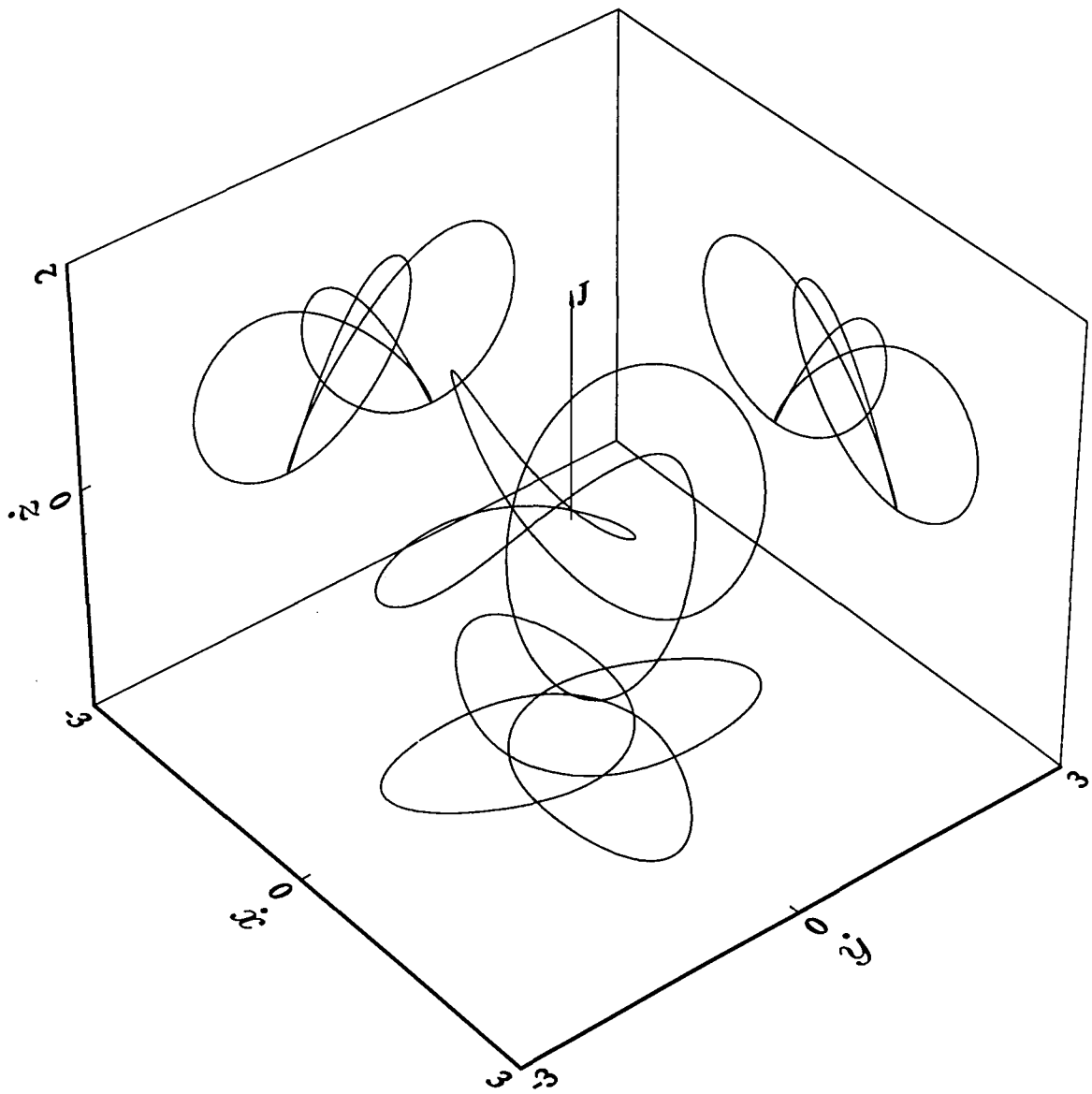

Figure 3.4.5. The velocity hodograph associated with Figure 3.4.4. The velocity hodograph has four–fold rotational symmetry about $\boldsymbol{J}$. The projections of the velocity hodograph onto planes parallel to the $\dot{x}\dot{y}$, $\dot{x}\dot{z}$ and $\dot{y}\dot{z}$ planes are also shown.

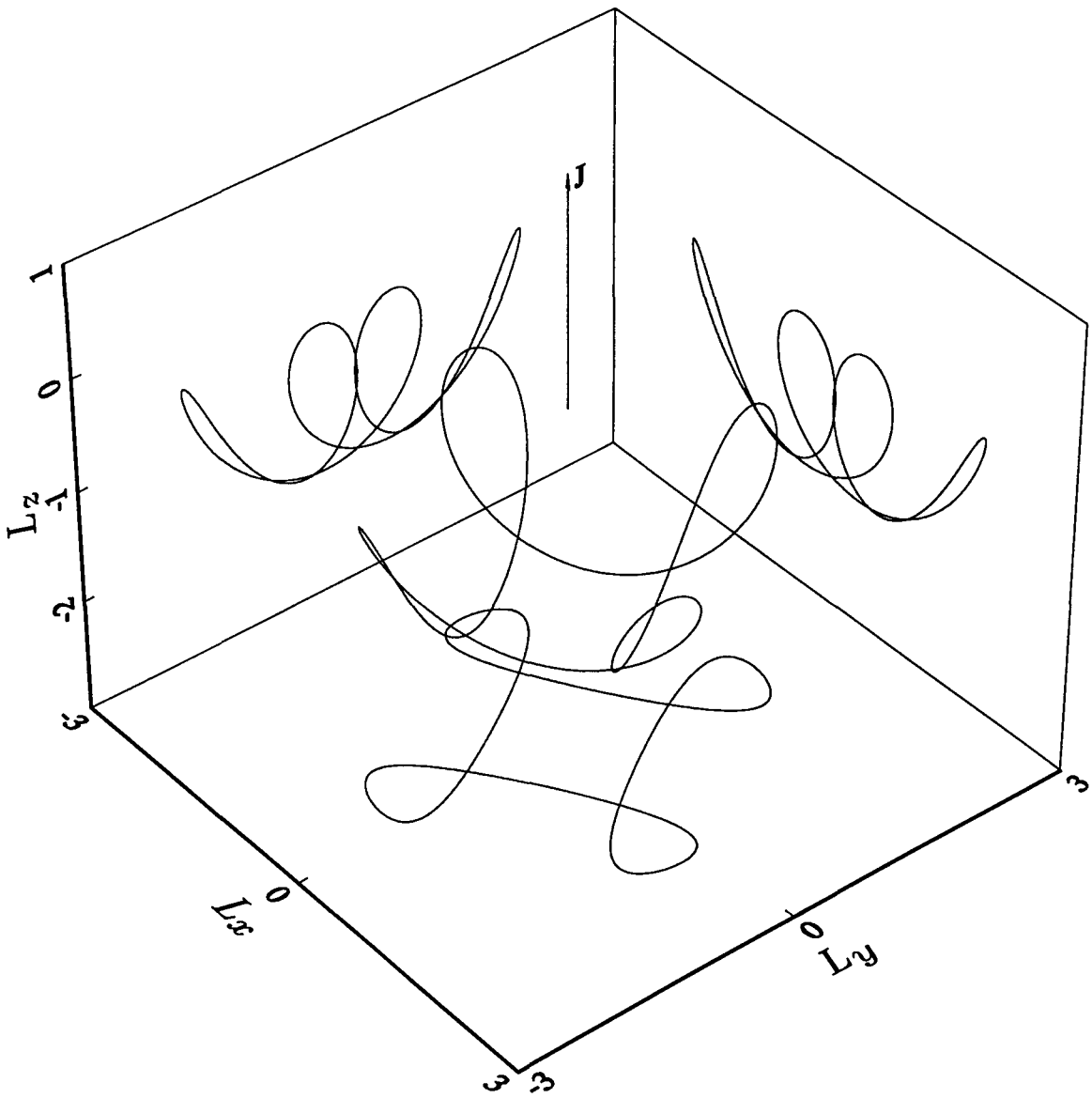

Figure 3.4.6. The angular momentum curve associated with Figures 3.4.4 and 3.4.5. The angular momentum curve has four–fold rotational symmetry about $\boldsymbol{J}$. In this example the angular momentum is constant in magnitude but not in direction. The heads of the angular momentum vectors move on the surface of a zone of a sphere of radius L. The projections of the angular momentum curve onto planes parallel to the L_xL_y, L_xL_z and L_yL_z planes are also shown.

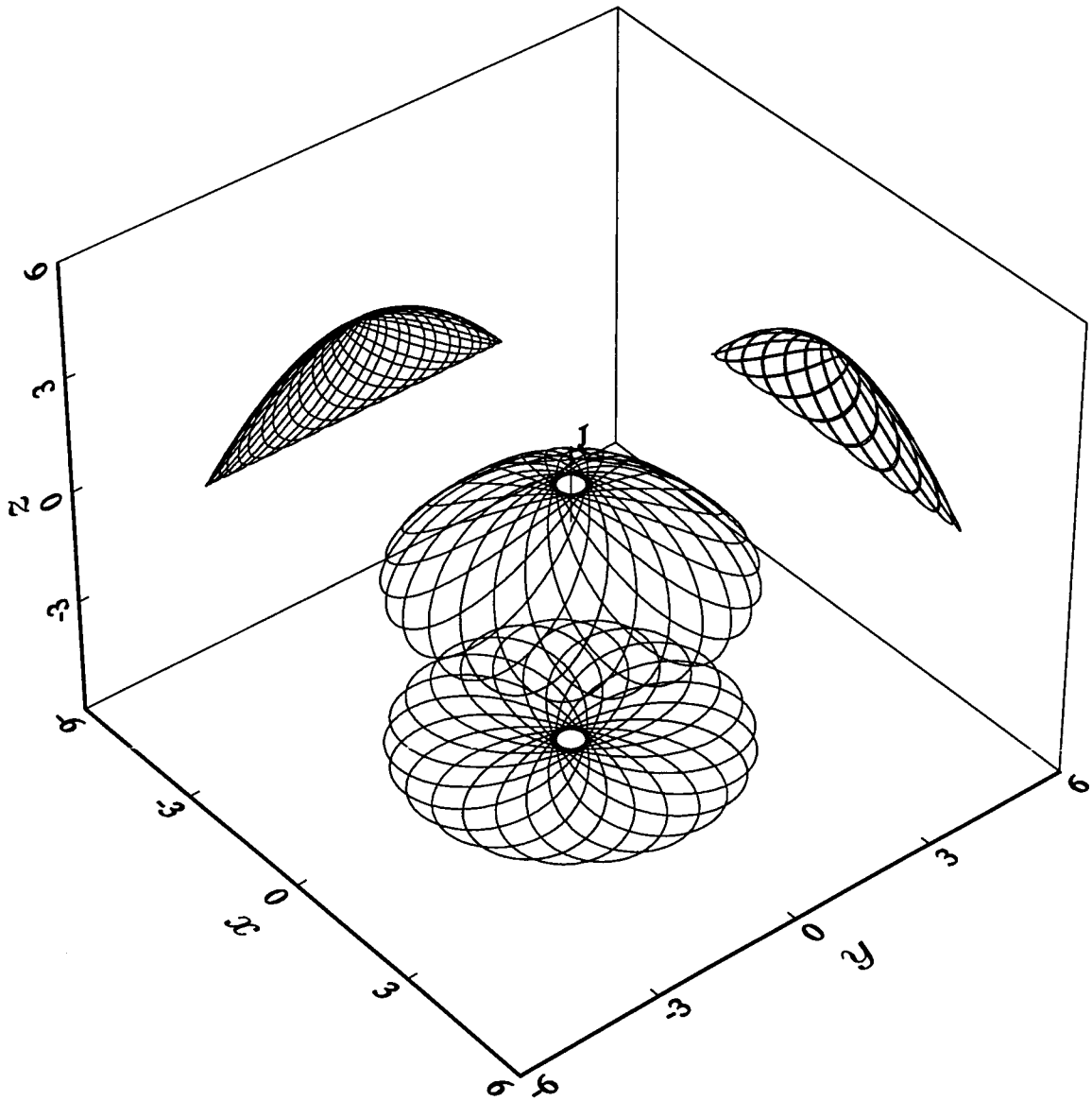

Figure 3.4.7. The orbit for $k = 1.947$, $\lambda = 1/4$, $\theta_0 = \pi/4$, $\phi_0 = 0$, $J = 2$ and $L = 2$. The value of k has been chosen to close the orbit. The motion takes place on a dome. The orbit has twenty–one–fold rotational symmetry about $\boldsymbol{J}$. The projections of the orbit onto planes parallel to the xy, xz and yz planes are also shown. The xy projection is bounded by two concentric circles.

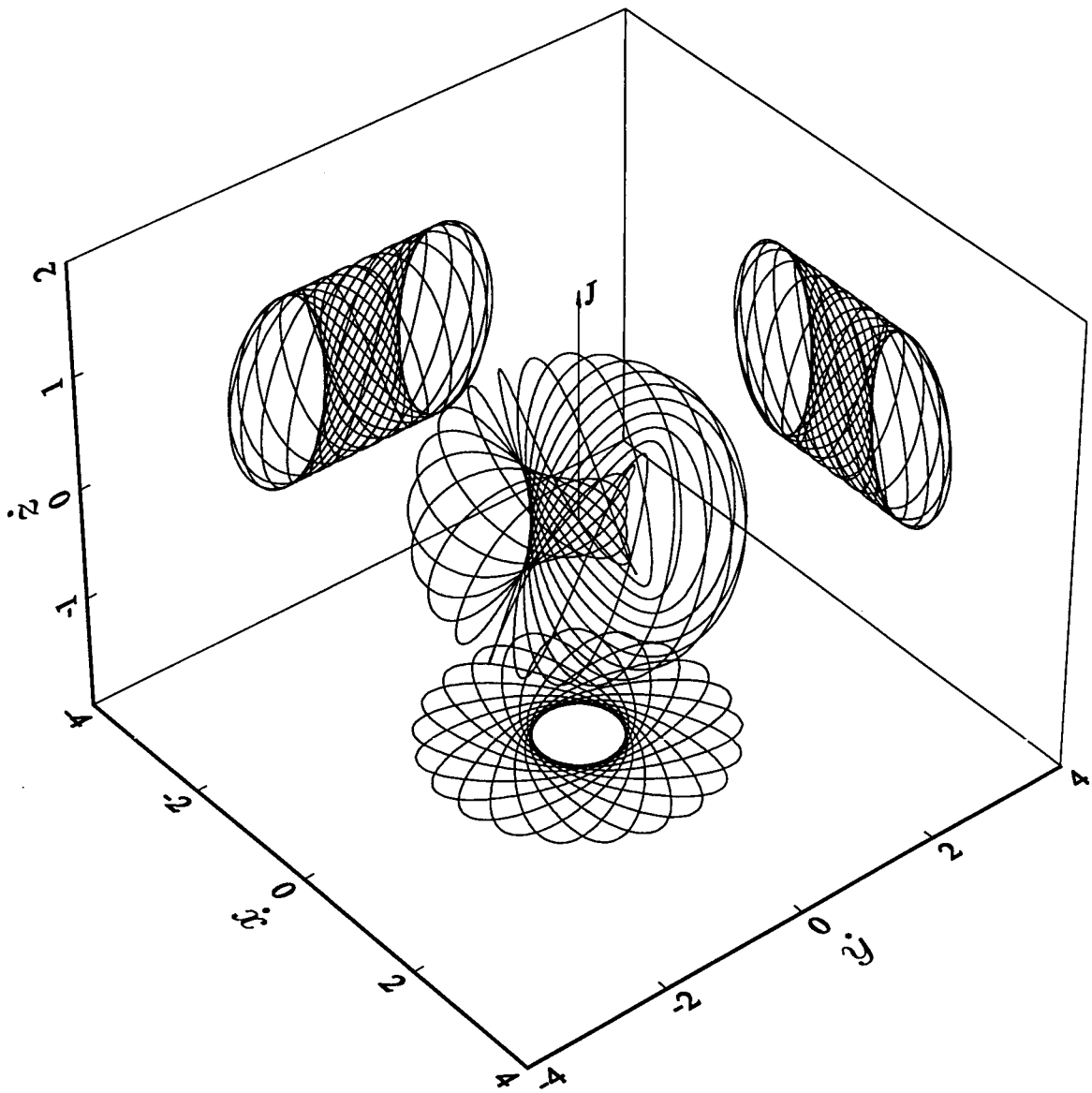

Figure 3.4.8. The velocity hodograph associated with Figure 3.4.7 which is reminiscent of a ball of string with a hollow centre. The velocity hodograph has twenty–one–fold rotational symmetry about $\boldsymbol{J}$. The projections of the velocity hodograph onto planes parallel to the $\dot{x}\dot{y}$, $\dot{x}\dot{z}$ and $\dot{y}\dot{z}$ planes are also shown. The $\dot{x}\dot{y}$ projection is bounded by two concentric circles.

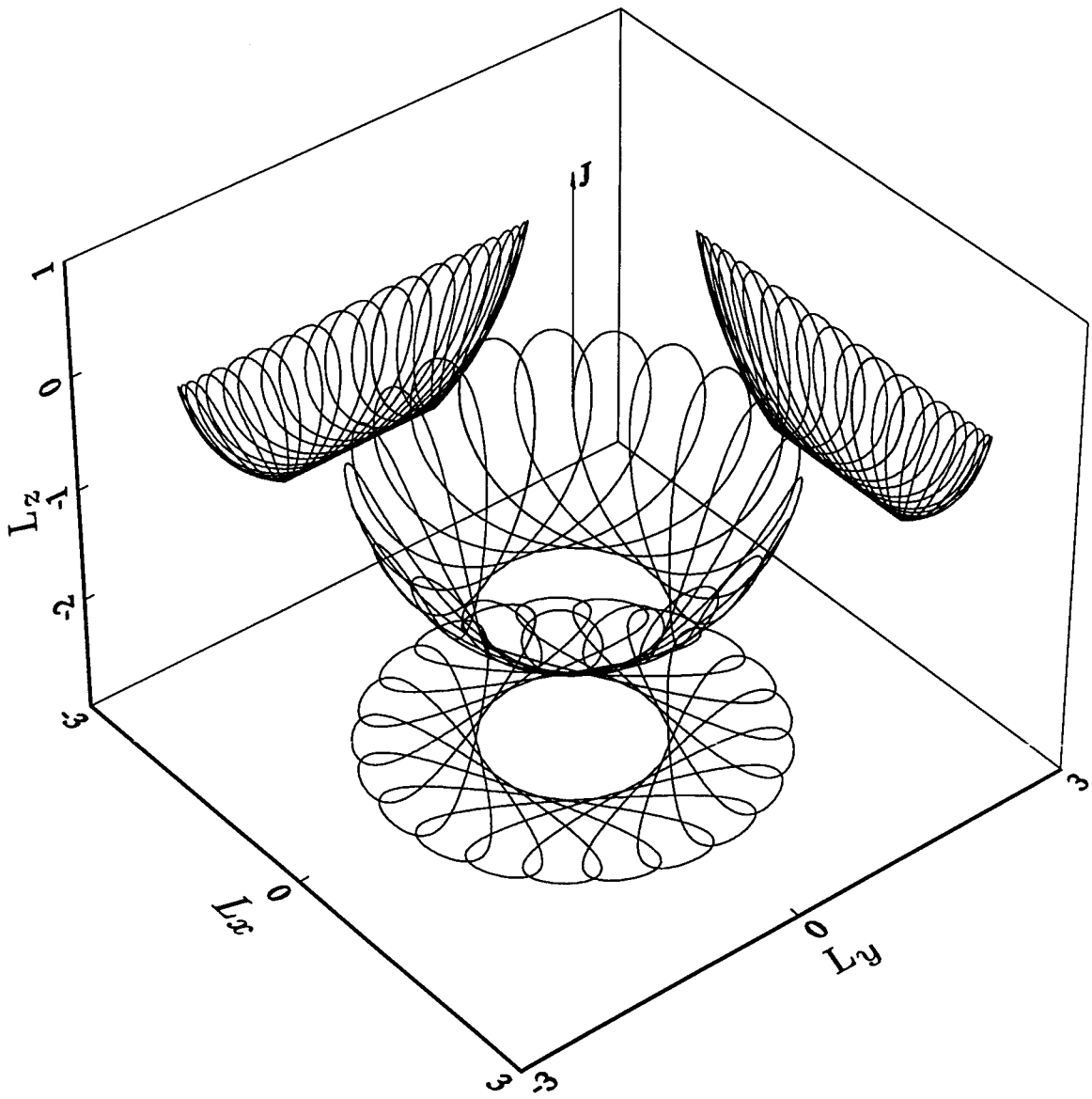

Figure 3.4.9. The angular momentum curve associated with Figures 3.4.7 and 3.4.8. The angular momentum curve has twenty–one–fold rotational symmetry about $\boldsymbol{J}$. In this example the angular momentum is constant in magnitude but not in direction. The heads of the angular momentum vectors move on the surface of a zone of a sphere of radius L. The projections of the angular momentum curve onto planes parallel to the L_xL_y, L_xL_z and L_yL_z planes are also shown. The L_xL_y projection is bounded by two concentric circles.

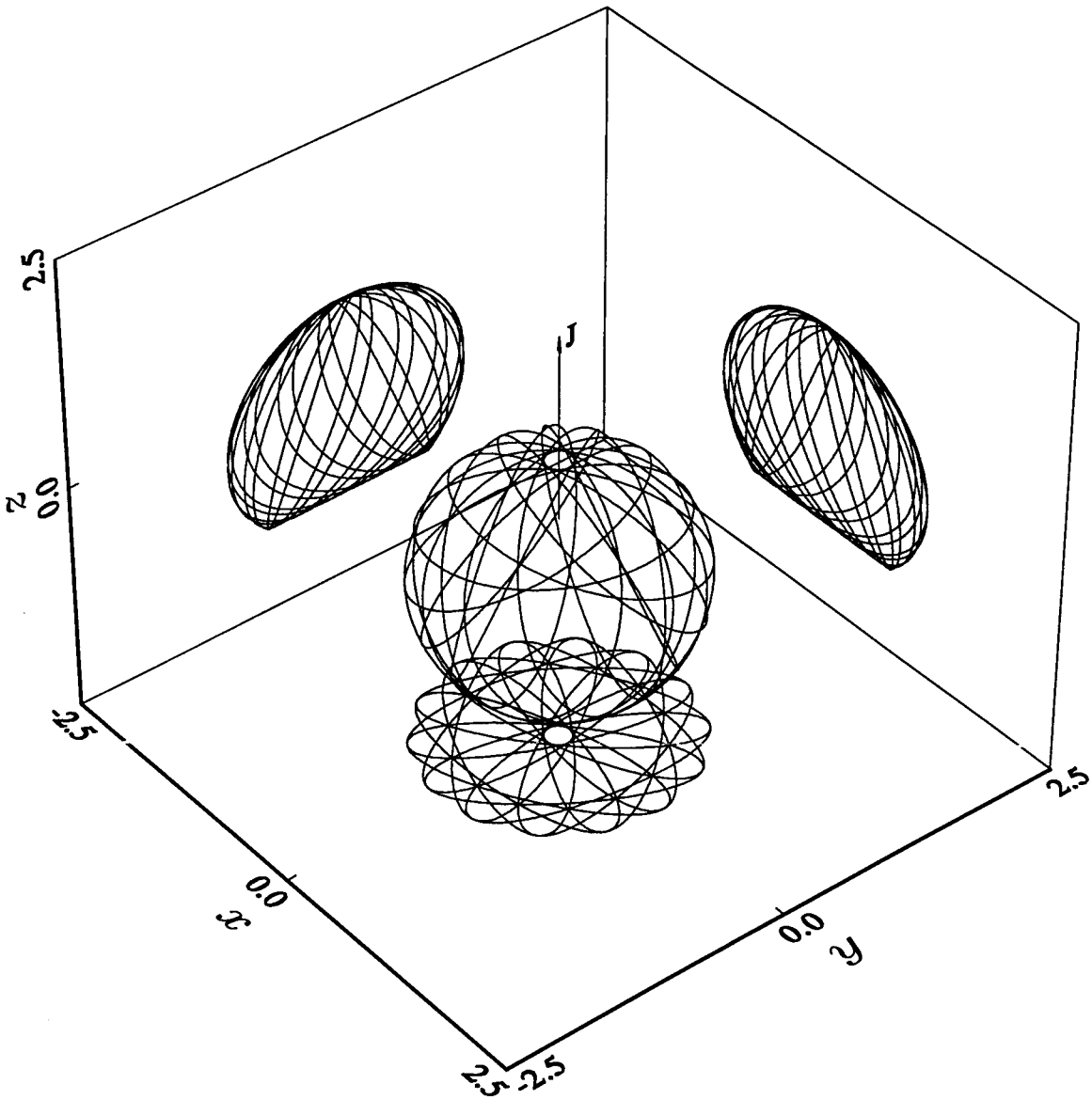

Figure 3.4.10. The orbit for $k = 4.097$, $\lambda = 1/4$, $\theta_0 = \pi/4$, $\phi_0 = 0$, $J = 2$ and $L = 2$. The value of k has been chosen to close the orbit. The motion takes place on a surface. The orbit has fourteen–fold rotational symmetry about $\boldsymbol{J}$. The projections of the orbit onto planes parallel to the xy, xz and yz planes are also shown. The xy projection is bounded by two concentric circles.

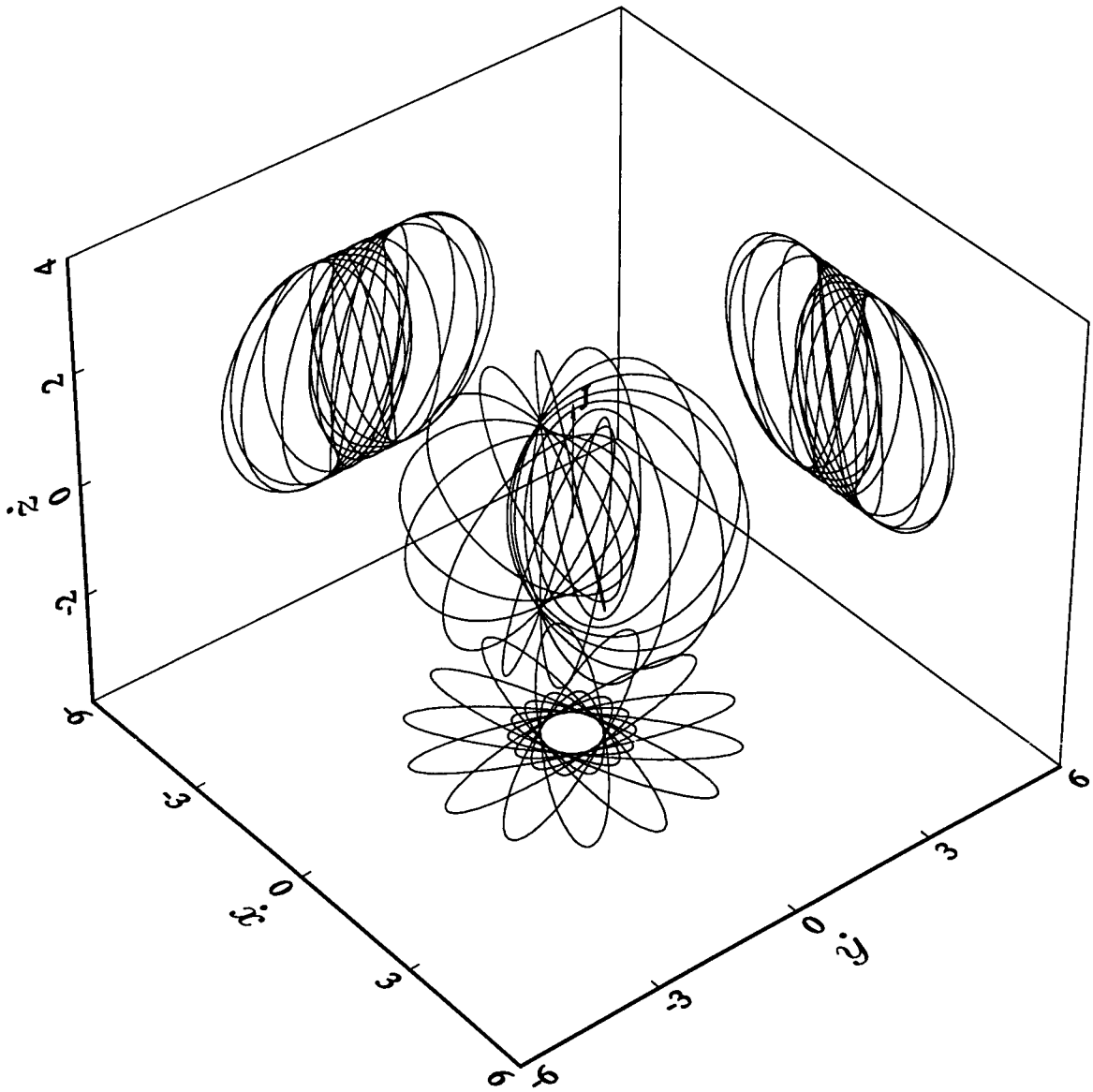

Figure 3.4.11. The velocity hodograph associated with Figure 3.4.10 which is reminiscent of a ball of string with a hollow centre. The velocity hodograph has fourteen–fold rotational symmetry about $\boldsymbol{J}$. The projections of the velocity hodograph onto planes parallel to the $\dot{x}\dot{y}$, $\dot{x}\dot{z}$ and $\dot{y}\dot{z}$ planes are also shown. The $\dot{x}\dot{y}$ projection is bounded by two concentric circles.

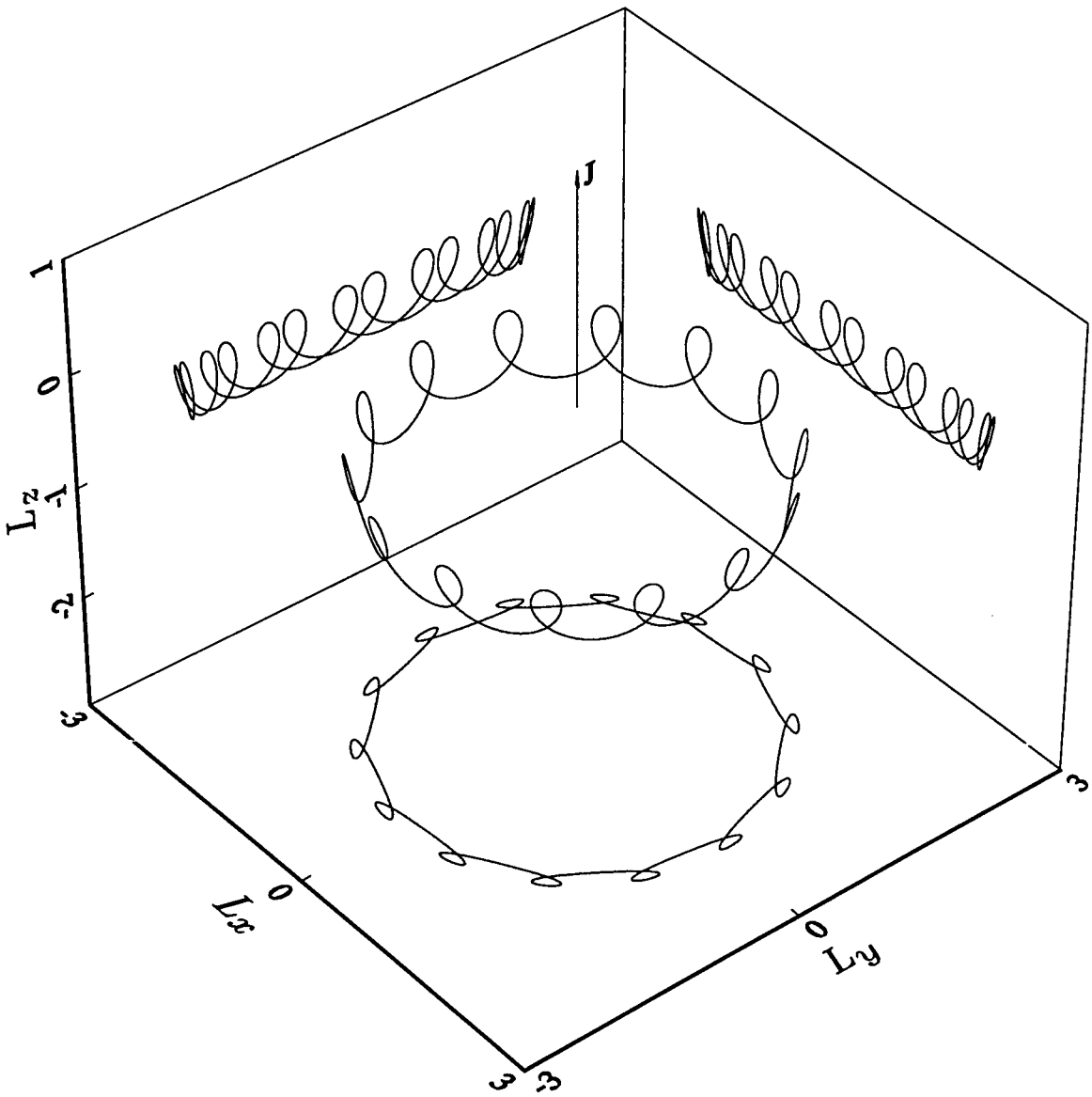

Figure 3.4.12. The angular momentum curve associated with Figures 3.4.10 and 3.4.11. The angular momentum curve has fourteen–fold rotational symmetry about $\boldsymbol{J}$. In this example the angular momentum is constant in magnitude but not in direction. The heads of the angular momentum vectors move on the surface of a zone of a sphere of radius L. The projections of the angular momentum curve onto planes parallel to the L_xL_y, L_xL_z and L_yL_z planes are also shown. The L_xL_y projection is bounded by two concentric circles.

2.) The equation of motion

$$\ddot{\boldsymbol{r}} = \frac{\lambda \dot{\boldsymbol{r}} \times \boldsymbol{r} + F(r)\boldsymbol{r}}{r^3} \tag{3.4.2}$$

has been studied in some detail by Thompson [126]. He established conditions on $F(r)$ in order that (3.4.2) possess an autonomous second independent first integral quadratic in the momenta besides the energy. He concluded the following:

1) $\lambda = 0$ and $F(r) = k_1$ a constant which is of course the Kepler–Coulomb problem or, when $k_1 = 0$, the free particle,

2) $\lambda = 0$ and $F(r) = k_1 r^3$ which is the three–dimensional isotropic harmonic oscillator or

3) $\lambda = 1$ and $F(r) = k_1 - 1/r$.

For case 3) he found the conserved vector

$$\boldsymbol{J} = \boldsymbol{L} \times \dot{\boldsymbol{r}} + \frac{\boldsymbol{L}}{r} - k_1 \hat{\boldsymbol{r}} \tag{3.4.3}$$

which is an analogue of the Laplace–Runge–Lenz vector for the standard Kepler problem. Case 3) of equation (3.4.2) is of course a special case of (3.1.15) with $h = -1/r$ and $k = -k_1$. It would appear, however, that the expression Thompson uses for $F(r)$ is in fact incorrect and should be $F(r) = k_1 + 1/r$. The error would appear to stem from the incorrect solution of (4.12) in his paper [126]. As a result the sign of the angular momentum term of (3.4.3) is also in error. Case 3) of the equation (3.4.2) is a specific example of the more general equation

$$\ddot{\boldsymbol{r}} + \frac{\lambda \boldsymbol{L}}{r^3} + \left(\frac{k}{r^2} - \frac{\lambda^2}{r^3} \right) \hat{\boldsymbol{r}} = \boldsymbol{0} \tag{3.4.4}$$

which has attracted a great deal of interest in connection with monopoles. It will be treated in great detail later in this chapter (see §3.5). It should further be appreciated that for $\lambda = 1$ and $F(r) = 0$, (3.4.2) reduces to the equation of motion describing an electric charge interacting with a magnetic monopole fixed at the origin, after a suitable rescaling, for which it has been shown that analogues of the mechanical angular momentum first integrals exist as well as some additional first integrals which are quadratic in the momentum, but explicitly time dependent (see Moreira [101]). The monopole system, however, has no other (time–independent) quadratic integrals apart from the conserved energy (see §3.12). It should further be stressed that the vector approach developed above does appear to offer more general results with far less mathematical complexity than the approaches adopted by other writers.

It is possible to find closed–form solutions for ϕ for the equation of motion (3.4.4) which describes motion of an electric charge interacting with a magnetic monopole fixed at the origin with the additional centripetal forces $k\hat{\boldsymbol{r}}/r^2$ and $-\lambda^2\hat{\boldsymbol{r}}/r^3$ using the results developed earlier in the chapter. For $h(r) = -\lambda/r$ and $k = 0$, using (3.2.2) we see that

$$r\cos\theta = \frac{L^2}{J}. \tag{3.4.5}$$

This means that $\boldsymbol{r}$ has a constant projection onto $\boldsymbol{J}$ of length L^2/J. The integration in (3.2.9) is easily performed using standard methods giving

$$\phi = \operatorname{arcsec}\left(\left(1+\frac{L^2}{\lambda^2}\right)^{\frac{1}{2}}\sin\theta\right)\Bigg|_{\theta_0}^{\theta}. \tag{3.4.6}$$

Since the modulus of the argument of the arcsec must be greater than or equal to one and given that θ is in the first quadrant,

$$\arcsin\frac{1}{(1+L^2/\lambda^2)^{\frac{1}{2}}} \leq \theta \leq \frac{\pi}{2}. \tag{3.4.7}$$

The geometry of this orbit and those described below are intimately connected with those of the Kepler problem and will be discussed at great length below.

For $h(r) = -\lambda/r$ and $k \neq 0$ we have a truly three–dimensional motion for which there exists a Laplace–Runge–Lenz analogue. The orbit may or may not be closed depending on whether $k > J$ or $k \leq J$. Making the substitution $\eta = \cos\theta$, using partial fractions and G&R [43, 2.266.3], (3.2.9) can be integrated. There are three distinct cases

$J \neq k$ or $-k$,

$$\begin{aligned}\phi &= \frac{1}{2}\arctan\left[\frac{\frac{J^2L^2}{\lambda^2} - Jk - k^2 - J\left(\frac{JL^2}{\lambda^2} + J + k\right)\cos\theta}{(J+k)\left(\frac{J^2L^2}{\lambda^2}\sin^2\theta - (k+J\cos\theta)^2\right)^{\frac{1}{2}}}\right]\Bigg|_{\theta_0}^{\theta} \\ &+ \frac{1}{2}\arctan\left[\frac{\frac{J^2L^2}{\lambda^2} + Jk - k^2 + J\left(\frac{JL^2}{\lambda^2} + J - k\right)\cos\theta}{(J-k)\left(\frac{J^2L^2}{\lambda^2}\sin^2\theta - (k+J\cos\theta)^2\right)^{\frac{1}{2}}}\right]\Bigg|_{\theta_0}^{\theta},\end{aligned} \tag{3.4.8}$$

$J = k$,

$$\phi = \frac{1}{2}\arctan\left[\frac{\frac{L^2}{\lambda^2} - 2 - \left(\frac{L^2}{\lambda^2} + 2\right)\cos\theta}{2\left(\frac{L^2}{\lambda^2}\sin^2\theta - (1+\cos\theta)^2\right)^{\frac{1}{2}}}\right]\Bigg|_{\theta_0}^{\theta}, \tag{3.4.9}$$

$J = -k$,

$$\phi = -\frac{1}{2}\arctan\left[\frac{\frac{L^2}{\lambda^2} - 2 + \left(\frac{L^2}{\lambda^2} + 2\right)\cos\theta}{2\left(\frac{L^2}{\lambda^2}\sin^2\theta - (1-\cos\theta)^2\right)^{\frac{1}{2}}}\right]\Bigg|_{\theta_0}^{\theta}. \tag{3.4.10}$$

In §3.5 the geometry and orbits of the monopole–Kepler problem will be considered in more detail as well as their connection with the standard Kepler problem.

The illustrative examples above have concentrated on the monopole because of its physical interest, although any differentiable function $h(r)$ could have been used. It should be appreciated that Laplace–Runge–Lenz vector analogues do exist for truly three–dimensional problems where only the magnitude of the angular momentum is conserved. The orbit equation was obtained using the Laplace–Runge–Lenz vector in two separate vector combinations.

3.5 The Conserved Hamilton and Laplace–Runge–Lenz Vector Analogues and the Lie Algebras of the First Integrals of the Classical MICZ Problem

The motion of a spinless test particle in the field of a Dirac monopole plus Coulomb potential with an additional centrifugal potential has been called the MIC problem by Mladenov and Tsanov [97] and the MICZ problem by Cordani [23] after the studies of this problem by McIntosh and Cisneros [94] and also by Zwanziger [134]. The MICZ system is related to the problem of the asymptotic scattering of two self–dual monopoles via a canonical transformation [23] which gives the reduced Hamiltonian of a particle in an Euclidean Taub–NUT space. This in turn is related to the scattering of slowly moving Bogomol'nyi–Prasad–Sommerfield (BPS) monopoles [1, 2, 89].

Classically the MICZ system is described by the equation of motion

$$\ddot{\boldsymbol{r}} + \frac{\lambda}{r^3}\boldsymbol{L} + \left(\frac{\mu}{r^2} - \frac{\lambda^2}{r^3}\right)\hat{\boldsymbol{r}} = \boldsymbol{0}, \tag{3.5.1}$$

where the mass is taken as unity, λ is the strength of the monopole and μ is the strength of the Coulomb field. The system (3.5.1) possesses the Hamiltonian

$$H = \frac{1}{2}\left(\boldsymbol{p}\cdot\boldsymbol{p} + \frac{\lambda^2}{r^2}\right) - \frac{\mu}{r}, \tag{3.5.2}$$

where $\boldsymbol{p} = \dot{\boldsymbol{r}}$ is not the canonical momentum since, although $[x_i, x_j]_{PB} = 0$ and $[x_i, p_j]_{PB} = \delta_{ij}$ $(x_i x_i = r^2)$, the Poisson Bracket of components of the mechanical momentum, $\boldsymbol{p}$, is

$$[p_i, p_j]_{PB} = \lambda \epsilon_{ijk} \frac{x_k}{r^3}, \tag{3.5.3}$$

where δ_{ij} and ϵ_{ijk} are the Kronecker delta and Kronecker epsilon respectively. The MICZ system possesses two conserved vectors which can be easily derived. Taking the vector product of $\boldsymbol{r}$ with (3.5.1) and integrating gives

$$\boldsymbol{P} = \boldsymbol{L} - \lambda \hat{\boldsymbol{r}} \tag{3.5.4}$$

which is known as Poincaré's vector [107]. Taking the scalar product of (3.5.4) with itself determines the magnitude of $\boldsymbol{P}$ as

$$P^2 = L^2 + \lambda^2. \tag{3.5.5}$$

Taking the vector product of (3.5.1) with $\boldsymbol{L}$ and integrating gives the second conserved vector

$$\boldsymbol{J} = \dot{\boldsymbol{r}} \times \boldsymbol{L} + \frac{\lambda}{r}\boldsymbol{L} - \mu \hat{\boldsymbol{r}}. \tag{3.5.6}$$

A Hamilton vector analogue can be constructed from the Laplace–Runge–Lenz vector analogue by taking the vector product of $\boldsymbol{J}$ with $\boldsymbol{P}$,

$$\begin{aligned} \boldsymbol{K} &= \boldsymbol{J} \times \boldsymbol{P} \\ &= (\dot{\boldsymbol{r}} \times \boldsymbol{P}) \times \boldsymbol{P} - \frac{\mu}{r}\boldsymbol{r} \times \boldsymbol{P}. \end{aligned} \tag{3.5.7}$$

Since there can be only five independent autonomous first integrals for a three–dimensional system, there must be at least two relationships between the integrals. They are

$$J^2 = 2L^2 H + \mu^2 \tag{3.5.8}$$

and

$$\boldsymbol{J} \cdot \boldsymbol{P} = \lambda \mu. \tag{3.5.9}$$

The existence of two conserved vectors is well known for a variety of two–dimensional problems (see Chapters 1 and 2). However, in the three–dimensional context the presence of both vectors gives rise to a rather special geometry which we investigate below.

If the velocity $\dot{\boldsymbol{r}}$ is replaced by the momentum $\boldsymbol{p}$ in $\boldsymbol{P}$ and $\boldsymbol{J}$, the Poisson Bracket relations are given by [96]

$$[P_i, P_j]_{PB} = \epsilon_{ijk} P_k, \quad [P_i, J_j]_{PB} = \epsilon_{ijk} J_k, \quad [J_i, J_j]_{PB} = -2H \epsilon_{ijk} P_k. \tag{3.5.10}$$

The Lie algebra of the first integrals under the operation of taking the Poisson Bracket is then $so(4), e(3)$ or $so(3,1)$ depending on whether H is negative, zero or positive. This is the same result as found for the standard Kepler Coulomb problem. It should also be noted that the Lie algebra of the Lie symmetries of (3.5.1) is $A_1 \oplus so(3)$ whereas in the Kepler–Coulomb problem case it is $A_2 \oplus so(3)$, where A_1 and A_2 are the abelian subalgebras of dimension one and two respectively [79]. (See §§4.1 and 4.5 respectively).

The motion of a particle described by (3.5.1) is known to be a conic section. There do not, however, appear to have been any detailed studies of the geometry of the orbit. McIntosh and Cisneros [94] state that they did not find any simple algebraic expressions for the parameters of the orbit in terms of the constants of the motion. In what follows we will look at the geometry of the orbit in some detail to understand the MICZ problem more fully. One important feature which emerges is that the line of $\boldsymbol{J}$ intersects with the geometric centre of the orbit. A linear combination of $\boldsymbol{P}$ and $\boldsymbol{J}$ naturally gives rise to two vectors one of which is parallel to the normal to the orbital and hodographic planes and the other which is parallel to the orbital and hodographic planes. The latter vector also behaves like a Laplace–Runge–Lenz vector in that it provides the orbit equation in a natural way using a suitable scalar product. Although many of the geometric relationships between features on the orbit and the conserved quantities are fairly involved, there is a lot of insight to be gained from this approach.

Since the orbit is a conic section, the different cases are treated separately. We begin by looking at the hyperbolic case $\mu = 0$ followed by the parabolic case $\mu = J$ and then the more general elliptic and hyperbolic cases $\mu > J$ and $\mu < J$ respectively.

Throughout the subsequent discussion, θ and ϕ correspond to the usual polar and azimuthal angles of spherical polar coordinates, respectively. The equation of motion (3.5.1) can be written as a standard Kepler problem by projecting the orbit into the $\phi-$plane, where now we use the line of the Poincaré vector to give the direction of the polar axis. This is easily achieved by taking the vector product of the equation of motion (3.5.1) with $\boldsymbol{P}$. The effect of this operation is to project certain vector quantities into the $\phi-$plane, followed by a $\pi/2$ rotation about the projection axis and a scaling by P. Since $\boldsymbol{r} \times \boldsymbol{P} = \boldsymbol{r} \times \boldsymbol{L}$ and $\boldsymbol{r}$ and $\boldsymbol{L}$ are orthogonal, the vector product of (3.5.1) with $\boldsymbol{P}$ can be written as

$$(\boldsymbol{r} \times \boldsymbol{P})^{\cdot\cdot} + \left(\frac{\mu L^3}{|\boldsymbol{r} \times \boldsymbol{P}|^3} \right) (\boldsymbol{r} \times \boldsymbol{P}) = \boldsymbol{0}. \tag{3.5.11}$$

Equation (3.5.11) is the equation of motion for the Kepler problem in the new variable $\boldsymbol{r} \times \boldsymbol{P}$. It should also be appreciated that in the new coordinates one focus of the orbit is centred at the origin. For the general equation of motion (3.5.1) the orbit plane is lifted onto the cone. However, the origin remains on the $\phi-$plane, out of the plane of the conic section. It will also become clear how the vector first integrals for the MICZ problems can be projected into the $\phi-$plane where they become important features of the planar Kepler problem. In the case of the elliptic orbit, the analogues of Kepler's three laws of motion are demonstrated on the cone and shown to have remarkable similarities with the planar problem.

3.6 Geometric Preliminaries and the Connection with the Kepler Problem

Before discussing the detailed geometry, there are certain geometric features of the problem which apply in general. We let $\pi - \alpha$ and β be the angles between $\boldsymbol{P}$ and $\boldsymbol{r}$ and $\boldsymbol{P}$ and $\boldsymbol{J}$ respectively.

Taking the scalar product between $\boldsymbol{P}$ (3.5.4) and $\boldsymbol{r}$ gives

$$\cos\alpha = \lambda/P. \tag{3.6.1}$$

The scalar product between $\boldsymbol{P}$ (3.5.4) and $\boldsymbol{J}$ (3.5.6) gives

$$\cos\beta = \frac{\lambda\mu}{PJ}. \tag{3.6.2}$$

If we let the angle between $\boldsymbol{J}$ and $\boldsymbol{r}$ be $\pi - \psi$, the scalar product between $\boldsymbol{J}$ (3.5.6) and $\boldsymbol{r}$, after rearranging, gives the orbit equation

$$r = \frac{L^2}{\mu - J\cos\psi}. \tag{3.6.3}$$

Equation (3.6.3) describes a surface of revolution with the line of $\boldsymbol{J}$ being the axis of symmetry and one focus of the surface centred at the origin. Since any cross–section of the the surface of revolution in a plane parallel to $\boldsymbol{J}$ is a plane conic section, the ratio J/μ determines the shape of the surface. The constancy of the angle between $\boldsymbol{P}$ and $\boldsymbol{r}$ means that the particle moves on the surface of a cone with vertex at the origin. The curve of intersection of the cone and the surface of revolution (which is termed a conicoid) is the orbit of the particle and also a plane conic section. By virtue of (3.5.4), $\boldsymbol{P}$, $\boldsymbol{L}$ and $\boldsymbol{r}$ are always coplanar. However, the scalar triple product

$$[\boldsymbol{P}, \boldsymbol{J}, \boldsymbol{r}] = L^2 r\dot{r}, \tag{3.6.4}$$

implies that $\boldsymbol{P}, \boldsymbol{J}$ and $\boldsymbol{r}$ are only co–planar when $\dot{r}$ is zero, *i.e.* at the extremities of the motion. It is convenient to introduce the conserved vector

$$\boldsymbol{N} = \boldsymbol{P} - \frac{\lambda}{\mu}\boldsymbol{J}. \tag{3.6.5}$$

Taking the scalar product of $\boldsymbol{N}$ with $\boldsymbol{r}$ gives

$$\boldsymbol{N} \cdot \boldsymbol{r} = \left(\boldsymbol{P} - \frac{\lambda}{\mu}\boldsymbol{J}\right) \cdot \boldsymbol{r} = -\frac{\lambda}{\mu}L^2, \tag{3.6.6}$$

which confirms that the orbit lies on a plane. However, the origin does not lie on the plane since the scalar product produces a non–zero constant. It should also be obvious that the vector $\boldsymbol{N}$ is parallel to the normal to the orbital plane. This vector is also orthogonal to the velocity hodograph since

$$\boldsymbol{N} \cdot \dot{\boldsymbol{r}} = \left(\boldsymbol{P} - \frac{\lambda}{\mu}\boldsymbol{J}\right) \cdot \dot{\boldsymbol{r}} = 0. \tag{3.6.7}$$

Clearly the origin lies on the same plane as the velocity hodograph and $\boldsymbol{N}$ is also normal to the hodographic plane. This also means that the hodographic and orbital planes are parallel to each other, as will be obvious from the diagrams later in the chapter. It is also possible to construct a vector $\boldsymbol{S}$ which is a linear combination of $\boldsymbol{P}$ and $\boldsymbol{J}$ which is parallel to the orbital plane. Using the requirement that $\boldsymbol{S} \cdot \boldsymbol{N} = 0$, one suitable vector is found to be

$$\boldsymbol{S} = \left(\boldsymbol{P} + \frac{\mu}{2\lambda H}\boldsymbol{J}\right). \tag{3.6.8}$$

The angle, ξ, between $\boldsymbol{P}$ and $\boldsymbol{N}$ is found by taking the scalar product between these two vectors which gives

$$\cos\xi = \sin\gamma = \frac{\mu L}{P(2H\lambda^2 + \mu^2)^{\frac{1}{2}}}, \tag{3.6.9}$$

where $\gamma = \pi/2 - \xi$ is the angle between the orbital plane and the vector $\boldsymbol{P}$ which can be used to find the cartesian equation of the plane. Similarly, the angle between $\boldsymbol{J}$ and $\boldsymbol{N}$ is found by taking the scalar product between these two vectors which gives

$$\cos\eta = \frac{-2HL\lambda}{(2HL^2 + \mu^2)^{\frac{1}{2}}(2H\lambda^2 + \mu^2)^{\frac{1}{2}}}. \tag{3.6.10}$$

Using (3.6.6) the projection of $\boldsymbol{r}$ onto $\boldsymbol{N}$ which defines the orbital plane is given by

$$\boldsymbol{r} \cdot \hat{\boldsymbol{N}} = r\cos\zeta = \frac{\lambda L}{(2H\lambda^2 + \mu^2)^{\frac{1}{2}}}, \tag{3.6.11}$$

where ζ is the angle between $\boldsymbol{r}$ and $\boldsymbol{N}$. If we fix $\boldsymbol{P}$ to lie along the $-\boldsymbol{k}$ direction and rotate the orbit about $\boldsymbol{P}$ so that the major axis of the orbit lies in the $xz-$plane, the unit normal is given by $\hat{\boldsymbol{N}} = (\cos\gamma, 0, \sin\gamma)$ and correspondingly the equation of the orbital plane described by (3.6.11) can be expressed in terms of cartesian components as

$$x\cos\gamma + z\sin\gamma = \frac{\lambda P}{\mu}\sin\gamma, \tag{3.6.12}$$

where γ is the angle between $\boldsymbol{P}$ and the plane of the orbit. The cartesian representation for the trajectory in spherical polar coordinates is given by

$$\begin{aligned} x &= r\sin\alpha\cos\phi \\ y &= r\sin\alpha\sin\phi \\ z &= r\cos\alpha. \end{aligned} \tag{3.6.13}$$

Substituting the above expressions for x, y and z into (3.6.12) gives

$$r = \frac{\lambda P\sin\gamma/\mu}{\cos\alpha\sin\gamma + \sin\alpha\cos\gamma\cos\phi} \tag{3.6.14}$$

which can be equated with the orbit equation (3.6.3) to give

$$\psi = \arccos\left(\frac{\lambda^2\mu - L^2(2HP^2+\mu^2)^{\frac{1}{2}}\cos\phi}{P^2J}\right). \tag{3.6.15}$$

The general features of the motion are as follows: the particle moves on a plane section of a cone with axis of symmetry along the line of $\boldsymbol{P}$ and semi–vertex angle determined by λ/P. The ratio J/μ determines whether the orbit is an ellipse, parabola or hyperbola. As $\boldsymbol{r}$ moves over the cone, $\boldsymbol{L}$, which is coplanar with $\boldsymbol{r}$ and $\boldsymbol{P}$, describes a circle on its own cone which has semi–vertex angle $\pi/2-\alpha$ with $\boldsymbol{P}$ its axis of symmetry. The vector $\boldsymbol{N}$ is parallel to the normal to the orbital and hodographic planes whilst the vector $\boldsymbol{S}$ is parallel to the orbital and hodographic planes.

Since the projected orbit in the $\phi-$plane is a focus–centred conic section, it is instructive to consider this orbit in conjunction with the orbit on a cone to provide a better understanding of the underlying geometry. In the planar problem the conserved Laplace–Runge–Lenz vector is given by $\boldsymbol{J}_\perp = \boldsymbol{J}\times\boldsymbol{P}$, where $\boldsymbol{J}$ is of course the Laplace–Runge–Lenz vector for the complete system (3.5.1). We use $\boldsymbol{J}_\perp$ to denote the Laplace–Runge–Lenz vector in the $\phi-$plane and obtain the form

$$\boldsymbol{J}_\perp = (\dot{\boldsymbol{r}}\times\boldsymbol{P})\times\boldsymbol{P} - \mu L\widehat{\boldsymbol{r}\times\boldsymbol{P}}. \tag{3.6.16}$$

Taking the scalar product of (3.6.16) with $(\boldsymbol{r}\times\boldsymbol{P})$ gives

$$\boldsymbol{J}_\perp\cdot(\boldsymbol{r}\times\boldsymbol{P}) = J_\perp Lr\cos\phi = P^2L^2 - \mu L^2 r, \tag{3.6.17}$$

and so

$$|\boldsymbol{r} \times \boldsymbol{P}| = Lr = \frac{P^2 L}{\mu + J_\perp / L \cos\phi}, \tag{3.6.18}$$

where the azimuthal angle ϕ is measured from the line joining the focus (which is also the origin and the point where $\boldsymbol{P}$ cuts the $\phi-$plane) and the point of closest approach to the focus of the curve in the plane. Equation (3.6.18) describes the usual planar focus–centred conic section depending on the size of the eccentricity $e = J_\perp/(L\mu)$, *i.e.* elliptical for $e < 1$, parabolic for $e = 1$, hyperbolic for $e > 1$ and a straight line for $e = \infty$. This equation will be investigated in conjunction with the orbit on the cone later in the chapter. Taking the scalar product of $\boldsymbol{J}_\perp$ with itself gives

$$\begin{aligned} {J_\perp}^2 &= (\boldsymbol{J} \times \boldsymbol{P}) \cdot (\boldsymbol{J} \times \boldsymbol{P}) \\ &= L^2(2HP^2 + \mu^2). \end{aligned} \tag{3.6.19}$$

It can also be shown that

$$\boldsymbol{J}_\perp \cdot \boldsymbol{P} = 0 \tag{3.6.20}$$

as it should be since the motion in the projected system is planar.

The angular momentum for the planar Kepler problem (3.5.11) is given by

$$\boldsymbol{L}_K = (\boldsymbol{r} \times \boldsymbol{P}) \times (\dot{\boldsymbol{r}} \times \boldsymbol{P}) = L^2 \boldsymbol{P} \tag{3.6.21}$$

and the energy integral

$$E_K = \frac{1}{2}(\dot{\boldsymbol{r}} \times \boldsymbol{P}) \cdot (\dot{\boldsymbol{r}} \times \boldsymbol{P}) - \frac{\mu L^3}{|\boldsymbol{r} \times \boldsymbol{P}|} = L^2 H. \tag{3.6.22}$$

In addition to these integrals (3.5.11), which is the equation of motion for the Kepler problem in the variable $\boldsymbol{r} \times \boldsymbol{P}$, has the usual Hamilton's and Laplace–Runge–Lenz conserved vectors which are found as follows. Using the substitution $\boldsymbol{u} = \boldsymbol{r} \times \boldsymbol{P}$, equation (3.6.21) can alternatively be expressed as

$$\boldsymbol{L}_K = \boldsymbol{u} \times \dot{\boldsymbol{u}} = u^2 \dot{\phi} \hat{\boldsymbol{L}_K} = u^2 \dot{\phi} \hat{\boldsymbol{P}}. \tag{3.6.23}$$

The equation of motion (3.5.11) can be expressed in terms of $\boldsymbol{u}$ as

$$\ddot{\boldsymbol{u}} + \frac{\mu L^3}{u^2} \hat{\boldsymbol{u}} = \boldsymbol{0}, \tag{3.6.24}$$

which on multiplying the $\hat{\boldsymbol{u}}$ term both top and bottom by $\dot{\phi}$ can be integrated to give

$$\boldsymbol{K}_K = \dot{\boldsymbol{u}} - \frac{\mu L^3}{L_K} \hat{\boldsymbol{\phi}} = \dot{\boldsymbol{u}} - \frac{\mu L}{P} \hat{\boldsymbol{\phi}}. \tag{3.6.25}$$

Now, $\hat{\boldsymbol{P}}$, $\hat{\boldsymbol{u}}$ and $\hat{\boldsymbol{\phi}}$ are orthogonal with

$$\hat{\boldsymbol{\phi}} = \hat{\boldsymbol{P}} \times \hat{\boldsymbol{u}}, \tag{3.6.26}$$

so (3.6.25) becomes

$$\begin{aligned} \boldsymbol{K}_K &= (\boldsymbol{r} \times \boldsymbol{P})^{\cdot} - \frac{\mu L}{P} \hat{\boldsymbol{P}} \times (\boldsymbol{r} \widehat{\times} \boldsymbol{P}) \\ &= (\boldsymbol{r} \times \boldsymbol{P})^{\cdot} - \frac{\mu}{P^2 r} \boldsymbol{P} \times (\boldsymbol{r} \times \boldsymbol{P}), \end{aligned} \tag{3.6.27}$$

and similarly $\boldsymbol{J}_K$ is found from $\boldsymbol{K}_K \times \boldsymbol{L}_K$ which gives

$$\begin{aligned} \boldsymbol{J}_K &= L^2 (\boldsymbol{r} \times \boldsymbol{P})^{\cdot} \times \boldsymbol{P} - \mu L^3 \boldsymbol{r} \widehat{\times} \boldsymbol{P} \\ &= L^2 (\boldsymbol{r} \times \boldsymbol{P})^{\cdot} \times \boldsymbol{P} - \frac{\mu L^2}{r} \boldsymbol{r} \times \boldsymbol{P}. \end{aligned} \tag{3.6.28}$$

It is now apparent that (3.6.27) and (3.6.28) can be obtained directly from the standard Kepler conserved vectors (1.5.7) and (1.5.8) using the variable substitutions $\mu \to \mu L^3$, $\boldsymbol{r} \to \boldsymbol{r} \times \boldsymbol{P}$, $\dot{\boldsymbol{r}} \to \dot{\boldsymbol{r}} \times \boldsymbol{P}$, $\boldsymbol{L} \to \boldsymbol{L}_K$. It is also possible to show that

$$\begin{aligned} \boldsymbol{K}_\perp &= \boldsymbol{P} \times (\boldsymbol{J} \times \boldsymbol{P}) = P^2 \, \boldsymbol{K}_K = P^2 \boldsymbol{J} - \lambda \mu \boldsymbol{P}, \\ \boldsymbol{J}_\perp &= \boldsymbol{J} \times \boldsymbol{P} = \frac{1}{L^2} \, \boldsymbol{J}_K, \end{aligned} \tag{3.6.29}$$

which indicate that the conserved vectors for the MICZ problem are consistent with those of the equivalent two–dimensional Kepler problem.

As can be expected, the presence of a Hamilton vector for the planar problem indicates the existence of a planar velocity hodograph for the projection of the velocities in the ϕ–plane. Using the techniques of §1.2 and assuming that $\boldsymbol{K}_K$ is in the direction of the cartesian unit vector $\boldsymbol{i}$ and $\boldsymbol{P}$ along the direction $\boldsymbol{k}$, it is possible to show using $\boldsymbol{K}_K$ in (3.6.27) that (ignoring any rotations)

$$\dot{x}^2 + \left(\dot{y} - \frac{K_K}{P} \right)^2 = \frac{\mu^2 L^2}{P^4}, \tag{3.6.30}$$

which is a circle of radius $\mu L / P^2$ with centre at K_K / P along the $\dot{y}$–axis.

The presence of two orthogonal vectors in the xy–plane would seem to suggest the existence of additional vectors lying out of the plane which would project onto the lines of $\boldsymbol{J}_K$ and $\boldsymbol{K}_K$ in the xy–plane, respectively. Two such vectors are given by

$$\boldsymbol{U} = \pm \boldsymbol{J} \times \boldsymbol{P} - \frac{\lambda J}{L} \boldsymbol{P}, \tag{3.6.31}$$

where the top vector passes through the point marked E on the cone (see Figures 3.8.1, 3.9.1 and 3.10.1) and the bottom vector passes through the corresponding point on the opposite side of the cone. Two other such vectors are given by

$$\boldsymbol{T} = \pm\boldsymbol{P} \times (\boldsymbol{J} \times \boldsymbol{P}) - \frac{\lambda K_\perp}{LP}\boldsymbol{P}, \tag{3.6.32}$$

which lie on the surface of the cone collinear with the two vectors directed from the origin to the points of closest and furthest approach (infinity in the case of the parabola and the hyperbola, see Figures 3.8.1, 3.9.1 and 3.10.1), respectively. Note that $\boldsymbol{P} \times \boldsymbol{U} = \pm\boldsymbol{K}_\perp$ and $\boldsymbol{P} \times \boldsymbol{T} = \mp P^2\boldsymbol{J}_\perp$. Different linear combinations of the vectors shown above can also be made. However, they are not nearly as important as those described above because they do not appear to provide any useful additional geometric information on the MICZ problem. In some three–dimensional problems such as the one described here, linear combinations of conserved vectors can be used to simplify the construction of the orbit equation as will be demonstrated in §§3.7–3.10.

We will now consider the different types of orbits possible depending on the choice of μ.

3.7 The Geometry of the MICZ Problem with $\mu = 0$

When $\mu = 0$, (3.6.2) gives $\beta = \pi/2$, *i.e.* $\boldsymbol{J}$ is normal to $\boldsymbol{P}$. From (3.6.3), $r\cos\psi = L^2/J$, (the sign is positive since in this case the angle between $\boldsymbol{J}$ and $\boldsymbol{r}$ is acute), *i.e.* the projection of $\boldsymbol{r}$ onto $\boldsymbol{J}$ is L^2/J along the line of $\boldsymbol{J}$ and the motion is in a plane normal to $\boldsymbol{J}$ or parallel to $\boldsymbol{P}$. The orbit is correspondingly an hyperbola and the motion is unbounded. The salient features of the geometry are depicted in Figure 3.7.1 which shows the orientation of the larger orbital and smaller angular momentum cones which meet at the origin. A typical hyperbolic orbit is shown together with the construction of the Poincaré vector $\boldsymbol{P}$ from $\boldsymbol{L}$ and $\hat{\boldsymbol{r}}$ and the orientation of the vector $\boldsymbol{J}$. Note that $\boldsymbol{L}$ and $\boldsymbol{r}$ are orthogonal throughout the motion and that $\boldsymbol{P}$, $\boldsymbol{L}$ and $\boldsymbol{r}$ are coplanar at any instant in time. The vectors $\boldsymbol{P}$, $\boldsymbol{J}$ and $\boldsymbol{r}$ are only coplanar at the turning points of the motion. It is easy to show that

$$AB = \lambda L/J \qquad OB = PL/J. \tag{3.7.1}$$

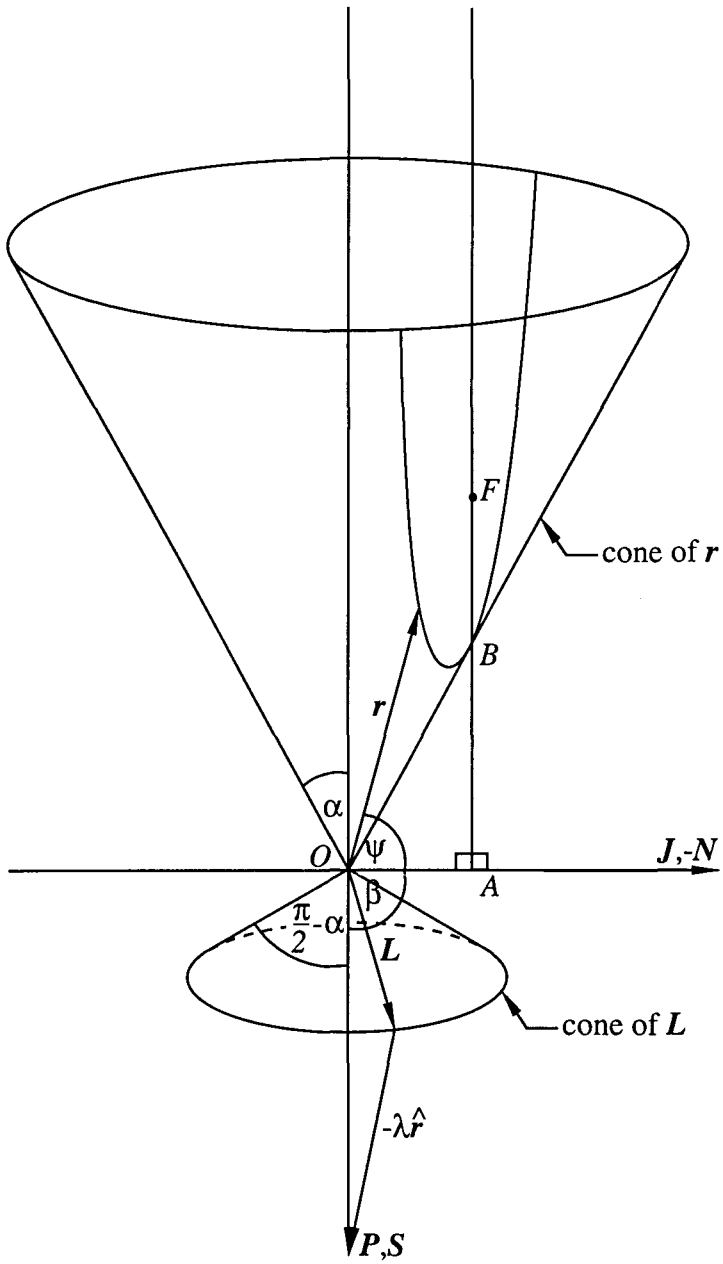

Figure 3.7.1. The typical geometry of the MICZ orbit when $\mu = 0$. The larger orbital and smaller angular momentum cones are shown together with a typical hyperbolic orbit and the orientation of $\boldsymbol{P}$, $\boldsymbol{J}$, $-\boldsymbol{N}$ and $\boldsymbol{S}$. The origin O is at the point of contact between the two cones, F is the focus of the hyperbola and A marks the geometric centre of the hyperbola. The line segment AF lies along the axis of symmetry of the hyperbola. α and $\pi/2 - \alpha$ are the the semi–vertex angles of the orbital and angular momentum cones respectively, ψ is the angle between $\boldsymbol{J}$ and $\boldsymbol{r}$ and β is between $\boldsymbol{P}$ and $\boldsymbol{J}$.

Figure 3.7.2 shows the plane of the typical hyperbolic orbit together with the asymptotes which coincide with the images or outline of the cone when projected onto the orbital plane. The focus can be found by considering the plane of the orbit (see Figure 3.7.2). The equation of the hyperbola is

$$\frac{v^2}{a^2} - \frac{u^2}{b^2} = 1, \tag{3.7.2}$$

and the asymptotes are given by

$$\frac{v}{a} \pm \frac{u}{b} = 0. \tag{3.7.3}$$

The modulus of the gradient of the asymptotes is given by $\cot\alpha$ so that

$$\frac{a}{b} = \frac{\lambda}{L}. \tag{3.7.4}$$

At B, the point of closest approach, $v = \lambda L/J$ so that

$$a = \frac{\lambda L}{J} \qquad b = \frac{L^2}{J} \tag{3.7.5}$$

and the eccentricity, given by $e^2 = 1 + b^2/a^2$, is

$$e = P/\lambda. \tag{3.7.6}$$

The distance $AF = ae = PL/J = OB$. In other words the distance of the focus from the line of $\boldsymbol{J}$ equals the distance of closest approach of the orbit to the origin. Finally we observe that the line of $\boldsymbol{J}$ passes through the geometric centre of the double hyperbola.

It is a simple procedure to obtain the cartesian equation for the orbit. The equation of the plane of the hyperbola on the cone is given by (3.6.12) putting $\gamma = 0$ which gives

$$x = \frac{L^2}{J}. \tag{3.7.7}$$

Using the first equation of (3.6.13) gives

$$r = \frac{L^2}{J}\mathrm{cosec}\alpha \sec\phi, \tag{3.7.8}$$

which can be substituted into the remaining equations of (3.6.13) to give

$$\begin{aligned} x &= \frac{L^2}{J} \\ y &= \frac{L^2}{J}\tan\phi \\ z &= \frac{L^2}{J}\cot\alpha\sec\phi. \end{aligned} \tag{3.7.9}$$

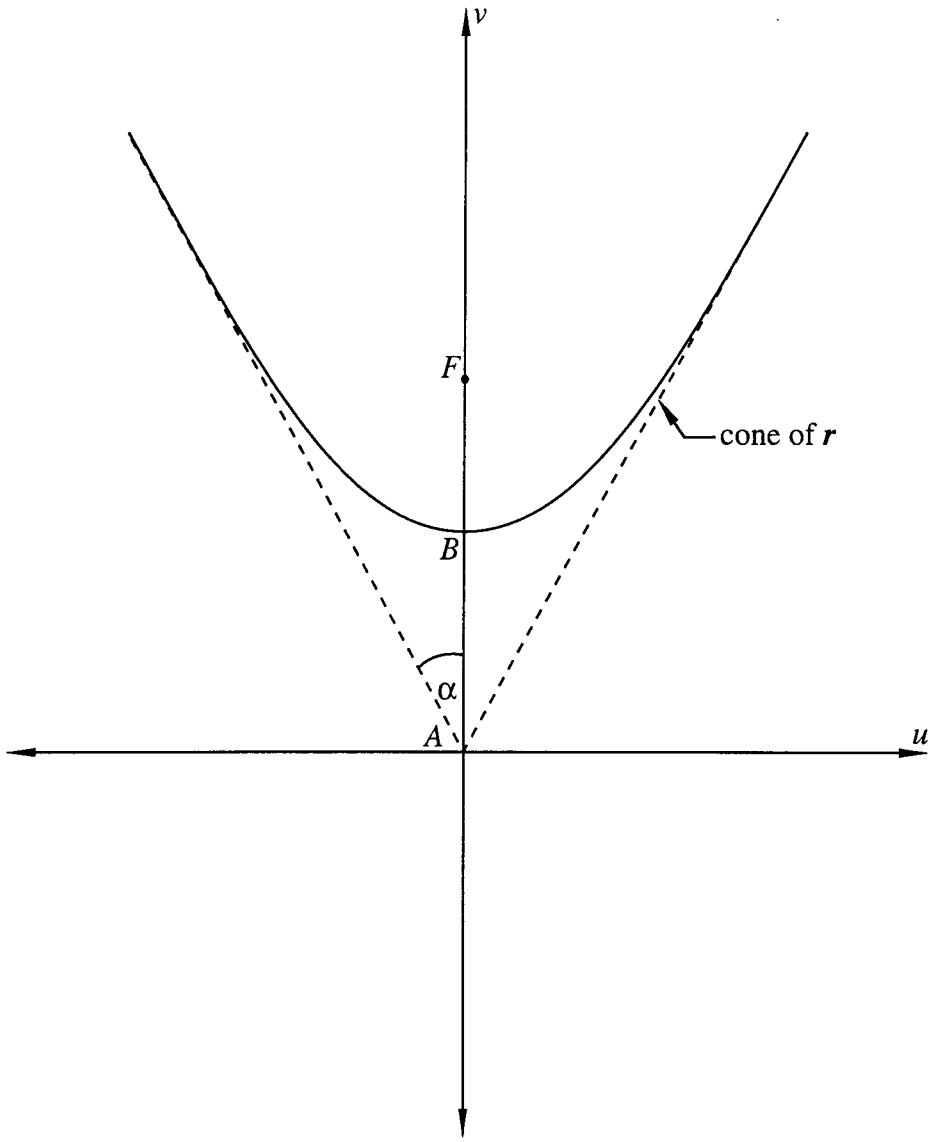

Figure 3.7.2. The plane of the typical hyperbolic orbit when $\mu = 0$. The dashed lines indicate the asymptotes which are also the images of the cone, F marks the focus of the hyperbola, B the vertex and A the geometric centre.

Replacing $\cot\alpha$ in (3.7.9) using (3.6.1), the y and z components of (3.7.9) can be manipulated into the form

$$\left(\frac{z}{\frac{\lambda L}{J}}\right)^2 - \left(\frac{y}{\frac{L^2}{J}}\right)^2 = 1, \tag{3.7.10}$$

which is the standard cartesian representation for a hyperbola (P2.17) symmetrically placed about the $y = 0$ axis, with vertices at $(L^2/J, 0, \pm\lambda L/J)$, foci at $(L^2/J, 0, \pm PL/J)$, eccentricity of P/λ and centred at $(L^2/J, 0, 0)$. The height of the top vertex a distance $\lambda L/J$ above the $xy-$plane agrees (as it should) with the length AB (3.7.1) and the height of the focus above the centre which is a distance PL/J agrees with the result found earlier for $AF = OB$ as does (3.7.10) with (3.7.2) and (3.7.5). The transverse axis is the same length as the distance between the two vertices $2a$, *i.e.* $2\lambda L/J$, and the conjugate axis is twice that of b, *i.e.* $2L^2/J$, which is consistent with (3.7.5).

If we consider the equation of the orbit in the $\phi-$plane, using (3.6.18) we find that

$$|\boldsymbol{r} \times \boldsymbol{P}| = Lr = \frac{P^2L^2}{J_\perp \cos\phi}, \tag{3.7.11}$$

i.e. the projection of the orbit into the plane describes a straight line symmetrically placed about the $\phi = 0$ axis. In the case $\phi = 0$, the projection of the orbit in the $\phi-$plane has the length

$$\frac{P^2L^2}{J_\perp} = \frac{PL^2}{J} \tag{3.7.12}$$

which is consistent with the earlier result for the length of the projection of $\boldsymbol{r}$ on $\boldsymbol{J}$, *i.e.* OA, up to the scaling factor of P.

The equation of motion (3.5.11) for $\mu = 0$ is

$$(\boldsymbol{r} \times \boldsymbol{P})^{\cdot\cdot} = \boldsymbol{0}, \tag{3.7.13}$$

which has the solution

$$\boldsymbol{r} \times \boldsymbol{P} = \boldsymbol{A}t + \boldsymbol{B}, \tag{3.7.14}$$

i.e. the motion in the plane is linear with respect to time. Remembering that the $x-$component of the solution is constant in this case with the value L^2/J, $\boldsymbol{A}$ and $\boldsymbol{B}$ can be calculated from (3.7.9), integrating the angular momentum equation $\dot{\phi} = -L/(r^2 \sin\alpha)$ and using (3.7.8) to replace r. This gives

$$\boldsymbol{A} = \begin{pmatrix} -J \\ 0 \end{pmatrix}, \quad \boldsymbol{B} = \begin{pmatrix} 0 \\ -PL^2/J \end{pmatrix}. \tag{3.7.15}$$

Alternatively, an elegant vector combination can be used to calculate the plane polar equation of the orbit in the orbital plane. In order to extract the orbit equation using a scalar product a new vector must be constructed from $\boldsymbol{r}$ which lies in the orbital plane and is thus parallel to $\boldsymbol{P}$. One suitable vector is

$$\begin{aligned} \boldsymbol{R} &= \boldsymbol{r} - |\boldsymbol{r} \cdot \hat{\boldsymbol{J}}|\, \hat{\boldsymbol{J}} \\ &= \boldsymbol{r} - \frac{L^2}{J}\hat{\boldsymbol{J}}, \end{aligned} \tag{3.7.16}$$

where the $\hat{\boldsymbol{J}}$ component is the projection of $\boldsymbol{r}$ on $\hat{\boldsymbol{J}}$. The vector $\boldsymbol{R}$ moves in the orbital plane, parallel to the $z-$axis and is displaced from the origin by $L^2\hat{\boldsymbol{J}}/J$. Measuring the angle ϑ which lies in the orbital plane from $\boldsymbol{P}$ gives the equation for the orbit in the orbital plane as

$$\boldsymbol{P} \cdot \boldsymbol{R} = PR\cos\vartheta = -\lambda r. \tag{3.7.17}$$

Rearranging the expression (3.7.16) to obtain $\boldsymbol{r}$ as the subject of the equation and squaring both sides of the expression produce a quadratic equation in r which can be solved to give

$$r = \left(R^2 + \frac{L^4}{J^2}\right)^{\frac{1}{2}}. \tag{3.7.18}$$

Note that for $R = \lambda L/J$ (the minimum allowed value), $r = PL/J$ which is consistent with the result for OB (3.7.1). Now substituting (3.7.18) in (3.7.17) we finally obtain

$$R^2 = \frac{2\frac{L^4}{J^2}}{\left(\left(\frac{P^2}{\lambda^2} - 2\right) + \frac{P^2}{\lambda^2}\cos 2\vartheta\right)}, \tag{3.7.19}$$

which is the plane polar expression for a geometric–centred hyperbola (P2.16) symmetrically placed about the $\vartheta = 0$ axis, eccentricity of P/λ which is consistent with (3.7.6), vertices at $(0, \pm\lambda L/J)$ and foci at $(0, \pm PL/J)$ which are consistent with (3.7.10) and (3.7.5). The distance from the centre to a vertex $\lambda L/J$ agrees with the length AB and the distance from the centre to a focus PL/J agrees with the length AF. The length of the transverse and conjugate axes are given by $2\lambda L/J$ and $2L^2/J$ respectively, which are twice the lengths of a and b in (3.7.5) as expected. Since the plane polar equation describes a geometric–centred hyperbola on the orbital plane, if follows that A marks the centre of the hyperbola in the plane.

The velocity hodograph can be obtained by individually differentiating the cartesian components x, y and z (3.7.9), realising that the x component of the orbit is constant with the value L^2/J and using the expression $\dot{\phi} = -L/(r^2 \sin\alpha)$ since the orbit and velocity hodograph are being viewed from above with $\boldsymbol{P}$ pointing in the $-\boldsymbol{k}$ direction, *i.e.* the sense of the rotation of the orbit is clockwise. Note that, when the cone is

rotated about the $x-$axis so that $\boldsymbol{P}$ lies along $\boldsymbol{k}$ and the vectors $\boldsymbol{K}_K$ and $\boldsymbol{J}_K$ lie along the cartesian unit vectors $\boldsymbol{j}$ and $\boldsymbol{i}$ respectively and hence mimic the behaviour of $\boldsymbol{L}$, $\boldsymbol{K}$ and $\boldsymbol{J}$ respectively of the standard Kepler problem, the sense of the rotation is counter–clockwise when viewed from $\boldsymbol{k}$ as for the Kepler problem. Using the substitutions described above gives the set of equations

$$\begin{aligned} \dot{x} &= 0 \\ \dot{y} &= -\frac{J}{P} \\ \dot{z} &= -\frac{\lambda J}{LP}\sin\phi, \end{aligned} \tag{3.7.20}$$

which describes a straight line of length $2\lambda J/LP$ symmetrically placed about the $xy-$plane, extending along the $\boldsymbol{k}$ direction and centred at $(0, -J/P, 0)$. Note that the velocity hodograph is bounded. Since the sense of the rotation of the orbit is clockwise, $\dot{z}$ starts off being negative and becomes positive as ϕ passes through zero. The projection of the velocity hodograph into the $\phi-$plane is the point $(0, -J/P)$. This result is consistent with equation (3.6.30) for a velocity hodograph with zero radius, which gives using (3.6.29)

$$\frac{K_K}{P} = \frac{J}{P}, \tag{3.7.21}$$

remembering that $\boldsymbol{P}$ was chosen to lie along the $-\boldsymbol{k}$ direction in the figures which accounts for the discrepancy with the sign of the centre of (3.6.30).

It does not seem possible to calculate the plane polar equation of the velocity hodograph on the plane using simple vector operations as was done for the orbit.

The initial conditions were chosen so that the projection of the orbit on the cone into the $\phi-$plane is identical to the corresponding free particle orbit and also that the projection of the velocity hodograph into the $\phi-$plane is coincident with that of the free particle. This was achieved by solving a system of nonlinear equations which were obtained by equating certain quantities on the cone on projection into the $\phi-$plane with the equivalent quantities for the free particle. In the subsequent discussion, the starred quantities will be used to denote the constants for the free particle. For convenience we choose $L^* = 1$, $\mu^* = 0$ and $J^* = 2.25$. With reference to Figure 3.7.3, the length of the projection of $\boldsymbol{r}$ onto $\boldsymbol{J}$ must be equal in length to the radius vector of the free particle at $\phi = 0$, which gives

$$\frac{L^2}{J} = \frac{L^{*2}}{J^*}. \tag{3.7.22}$$

The centre of the projected velocity hodograph was equated with that of the free particle to force both the orbits and the velocity hodographs to coincide so that a comparison between the two problems can be made. Comparing equations (1.5.9) and (3.6.30) gives

$$\frac{K_K}{P} = \frac{J}{P} = K^* = \frac{J^*}{L^*}, \tag{3.7.23}$$

which combined with (3.7.22) can be solved to give

$$P = \frac{L^2}{L^*}. \tag{3.7.24}$$

It follows from the definition of P, equation (3.5.5), that

$$\lambda = \frac{L}{L^*}\left(L^2 - L^{*2}\right)^{\frac{1}{2}}. \tag{3.7.25}$$

The semi–vertex angle of the cone α is obtained from (3.6.1), (3.7.24) and (3.7.25) which combine to give

$$\alpha = \arccos\left(\frac{(L^2 - L^{*2})^{\frac{1}{2}}}{L}\right) = \arcsin\left(\frac{L^*}{L}\right), \tag{3.7.26}$$

i.e. the angle α only depends on the projection of the MICZ angular momentum, $\boldsymbol{L}$, onto the Kepler angular momentum, $\boldsymbol{L}^*$, which is directed along the line of $\boldsymbol{P}$. Equations (3.7.23) and (3.7.24) can be used to find an expression for J, *i.e.*

$$J = \frac{L^2}{L^{*2}}J^*. \tag{3.7.27}$$

The angle β was shown above to be $\pi/2$ radians. For convenience, L was chosen to be 1.85 and using the values for the starred quantities given above, P, λ, α and J were calculated using (3.7.24)–(3.7.27).

Figure 3.7.3 shows the hyperbolic orbit in the case where $\mu = 0$. The diagram shows the two right circular orbital and angular momentum cones which extend in opposite directions along the line of $\boldsymbol{P}$ with origin and point of contact at the apices of the two cones. A selection of displacement and corresponding angular momentum vectors have been drawn from the origin to their respective positions on the orbital and angular momentum cones. The orbit is hyperbolic and lies on a plane which does not include the origin. In order to illustrate the behaviour more clearly, projections of the orbit onto planes parallel to the xy, xz and yz planes are shown, together with projections of the angular momentum curve and the projected images of the cones onto the respective planes. The constant magnitude of the angular momentum is reflected by the angular momentum vectors moving on the surface

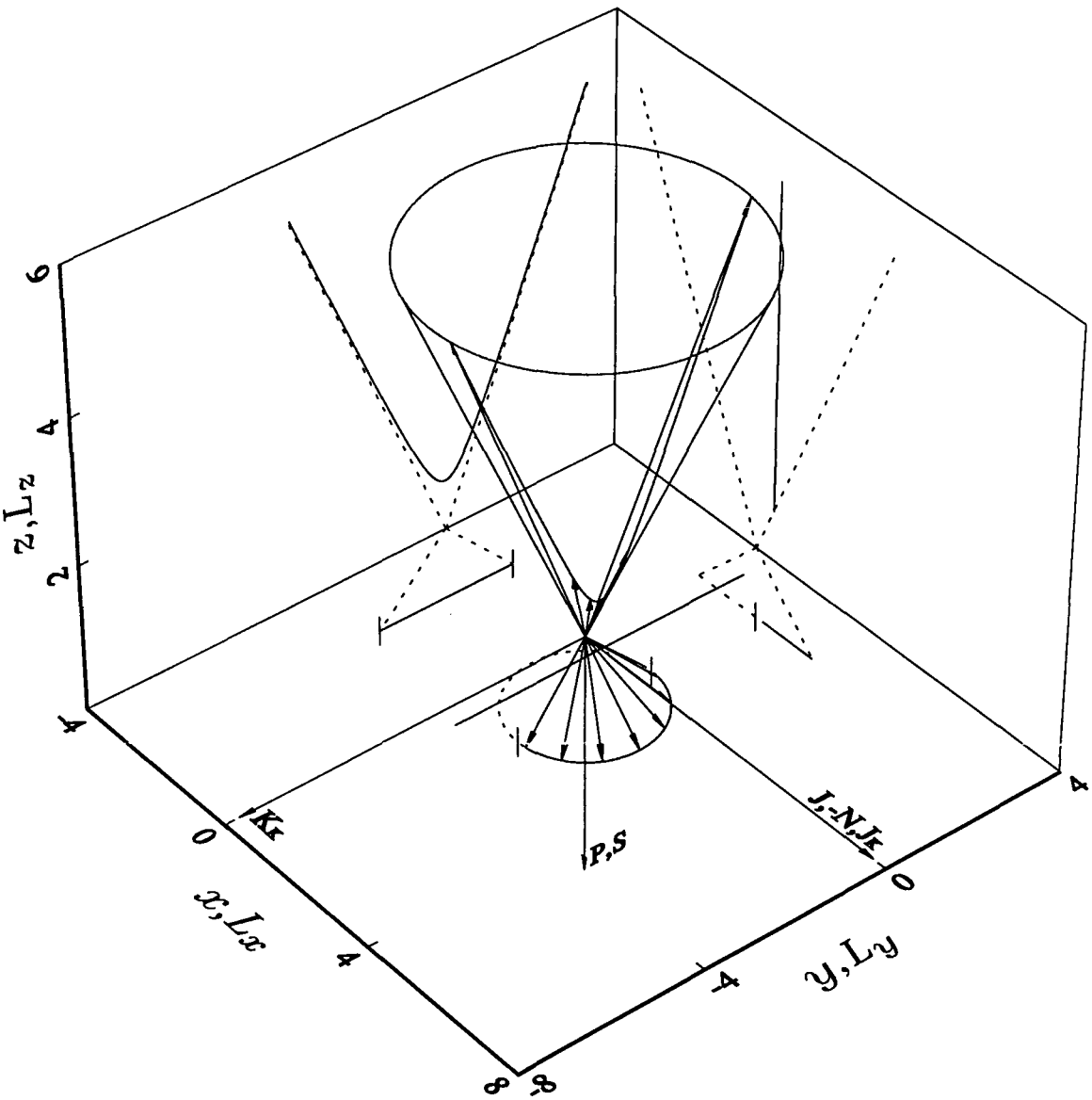

Figure 3.7.3. The hyperbolic MICZ orbit and angular momentum curve for $\mu = 0$ with a selection of displacement and angular momentum vectors drawn from the origin. The radial and angular momentum vectors move on the surfaces of two right circular cones extending in opposite directions along the line of $\boldsymbol{P}$ with origin and point of contact at the apices of the two cones. The projections of the orbit and angular momentum curve onto planes parallel to the xy, xz, yz, L_xL_y, L_xL_z and L_yL_z planes are also shown. The constants have the values $J = 7.7006$, $P = 3.4225$, $\lambda = 2.8794$, $\alpha = 0.5711$, $\beta = \pi/2$ and $L = 1.85$. The origin lies out of the orbital plane.

of a cone which is truncated perpendicular to the axis of symmetry to a height of L^2/P below the origin. The components of the angular momentum are given by $L = (\lambda L \cos\phi/P, \lambda L \sin\phi/P, -L^2/P)$ using (3.7.9) and (3.7.20). The two short line segments drawn perpendicular to the angular momentum curve indicate the limits of extent of the angular momentum as t ranges from negative through positive infinity.

The xy projection of the orbit is a straight–line symmetrically placed about the $y = 0$ axis, as described by the first two equations of (3.7.9), which extends parallel to the $y-$axis from right to left across the page and centred at $(L^2/J, 0)$. The perpendicular distance from the projected curve to the origin has the length L^2/J which is also the length of the projection of $\boldsymbol{r}$ onto $\boldsymbol{J}$, *i.e.* OA. The projected orbit is consistent with the planar orbit for the free particle with $L^* = 1$, $\mu^* = 0$ and $J^* = 2.25$. As t ranges from negative through positive infinity, the azimuthal angle ϕ ranges between $\pi/2$ and $-\pi/2$ and so the projection ranges from $(L^2/J, +\infty)$ when $\phi = \pi/2$ to $(L^2/J, L^2/J)$ when $\phi = \pi/4$ to $(L^2/J, 0)$ when $\phi = 0$ to $(L^2/J, -L^2/J)$ when $\phi = -\pi/4$ to $(L^2/J, -\infty)$ when $\phi = -\pi/2$. The projection of the angular momentum curve onto its corresponding plane describes part of a semi–circle with radius $\lambda L/P$ symmetrically placed about the L_x-axis extending to the right of the L_y-axis, *i.e.* ${L_x}^2 + {L_y}^2 = (\lambda L/P)^2, L_y \geq 0$. As t ranges from negative through positive infinity, the projection ranges from $(0, \lambda L/P)$ when $\phi = \pi/2$ to $\left(\lambda L/(2^{\frac{1}{2}}P), \lambda L/(2^{\frac{1}{2}}P)\right)$ when $\phi = \pi/4$ to $(\lambda L/P, 0)$ when $\phi = 0$ to $\left(\lambda L/(2^{\frac{1}{2}}P), -\lambda L/(2^{\frac{1}{2}}P)\right)$ when $\phi = -\pi/4$ to $(0, -\lambda L/P)$ when $\phi = -\pi/2$, *i.e.* the semi–circle is completed. The dotted line completes the angular momentum cone. However, it should be remembered that the projection of the angular momentum vectors never crosses over the L_y-axis.

The xz projection shows the images of the orbital and angular momentum cones with dotted lines, together with the projections of the orbit and angular momentum curves. Note that the xz projection of the orbit is a line with origin $(L^2/J, \lambda L/J)$ (see the first and third equations of (3.7.9)) parallel to the $z-$axis and hence parallel to the axis of the orbital cone which confirms the well–known result that a cone intersected by a plane which is parallel but not coincident with the axis of the cone describes an hyperbola on the plane. The vertical height of the base of the straight line above the xy plane has the length $\lambda L/J$ which is consistent with the length AB (3.7.1) and also half the length of the transverse axis of the hyperbola, *i.e.* a in (3.7.5). The orbit lies on a plane section through the orbital cone. As t ranges from negative through positive infinity, the projection ranges from $(L^2/J, +\infty)$ when $\phi = \pi/2$ to $\left(L^2/J, 2^{\frac{1}{2}}\lambda L/J\right)$ when $\phi = \pi/4$ to $(L^2/J, \lambda L/J)$ when $\phi = 0$ to $\left(L^2/J, 2^{\frac{1}{2}}\lambda L/J\right)$ when $\phi = -\pi/4$ to $(L^2/J, +\infty)$ when $\phi = -\pi/2$. The L_xL_z projection of the angular

momentum curve extends a short distance along the base of the triangle describing the L_xL_z projection of the image of the angular momentum cone, perpendicular to the L_z-axis. As t ranges from negative through positive infinity, the projection ranges from $(0,-L^2/P)$ when $\phi=\pi/2$ to $\left(\lambda L/(2\frac{1}{2}P),-L^2/P\right)$ to $(\lambda L/P,-L^2/P)$ when $\phi=0$ to $\left(\lambda L/(2\frac{1}{2}P),-L^2/P\right)$ when $\phi=-\pi/4$ to $(0,-L^2/P)$ when $\phi=-\pi/2$, *i.e.* half the length of the base of the angular momentum triangle. In other words the angular momentum vectors will have swept over half the surface area of the angular momentum cone. The short line segment drawn perpendicular to the xz projection of the angular momentum curve indicates the limit of extent of the projection of the angular momentum as t ranges from negative through positive infinity.

The yz projection shows the images of the orbital and angular momentum cones with dotted lines, together with the projections of the orbit and angular momentum curves. Note that the yz projection of the orbit is hyperbolic, symmetrically placed about the $y=0$ axis and flanked by the asymptotes which are in this case also the images of the orbital cone. The equation of the hyperbolic projection is given by (3.7.10) with asymptotes $z=\pm\cot\alpha\ y$. The yz projection of the orbit does not distort the hyperbola since the projection plane is parallel to the orbital plane (see the second and third equations of (3.7.9)). The vertices are at $(0,\pm\lambda L/J)$, foci at $(0,\pm PL/J)$, eccentricity of P/λ and centred at $(0,0)$. The height of the top vertex is a distance $\lambda L/J$ above the xy plane which is consistent with the length AB (3.7.1) and also half the length of the transverse axis of the hyperbola, *i.e.* a in (3.7.5). The height of the focus which is a distance PL/J above the origin agrees with the result for $AF=OB$ found earlier using purely geometric considerations. The conjugate axis has the length $2L^2/J$, *i.e.* $2b$ in (3.7.5). As t ranges from negative through positive infinity, the projection ranges from $(+\infty,+\infty)$ when $\phi=\pi/2$ to $\left(L^2/J,2\frac{1}{2}\lambda L/J\right)$ when $\phi=\pi/4$ to $(0,\lambda L/J)$ when $\phi=0$ to $\left(-L^2/J,2\frac{1}{2}\lambda L/J\right)$ when $\phi=-\pi/4$ to $(-\infty,+\infty)$ when $\phi=-\pi/2$. The L_yL_z projection of the angular momentum curve lies along the base of the triangle describing the L_yL_z projection of the image of the angular momentum cone, perpendicular to the L_z-axis. As t ranges from negative through positive infinity, the line segment extends along the full length of the base of the angular momentum triangle from the point $(\lambda L/P,-L^2/P)$ when $\phi=\pi/2$ to $\left(\lambda L/(2\frac{1}{2}P),-L^2/P\right)$ when $\phi=\pi/4$ to $(0,-L^2/P)$ when $\phi=0$ to $\left(-\lambda L/(2\frac{1}{2}P),-L^2/P\right)$ when $\phi=-\pi/4$ to $(-\lambda L/P,-L^2/P)$ when $\phi=-\pi/2$. In other words the angular momentum vectors will have swept over half the surface area of the angular momentum cone. The two short line segments drawn perpendicular to the yz projection of the angular momentum curve indicate the limits of extent of

the projection of the angular momentum as t ranges from negative through positive infinity.

The conserved vector $\boldsymbol{K}_K$ which has been rotated clockwise through $\pi/2$ radians to lie along the cartesian unit vector $-\boldsymbol{j}$ is given by (3.6.29) and has length $L(2H)^{\frac{1}{2}}$ as shown in Figure 3.7.3. The vector $\boldsymbol{J}_K$, which is perpendicular to $\boldsymbol{K}_K$, is also rotated clockwise through $\pi/2$ radians to lie along the cartesian unit vector $\boldsymbol{i}$. $\boldsymbol{J}_K$ has the length PL^2K_K and is conveniently drawn to the same length as $\boldsymbol{K}_K$ in Figure 3.7.3. The Poincaré vector, $\boldsymbol{P}$, which is orthogonal to $\boldsymbol{J}$, lies along the cartesian unit vector $-\boldsymbol{k}$. Note that, when the cone is rotated about the $x-$axis so that $\boldsymbol{P}$ lies along $\boldsymbol{k}$, the vectors $\boldsymbol{K}_K$ and $\boldsymbol{J}_K$ lie along the cartesian unit vectors $\boldsymbol{j}$ and $\boldsymbol{i}$ respectively and hence mimic the behaviour of $\boldsymbol{L}$, $\boldsymbol{K}$ and $\boldsymbol{J}$ respectively of the standard Kepler problem. The components of the conserved vectors are found by taking the scalar products of the relevant vectors with $\hat{\boldsymbol{K}}_K$, $\hat{\boldsymbol{J}}_K$ and $-\hat{\boldsymbol{P}}$, remembering that the projected quantities have been rotated clockwise through $\pi/2$ radians to preserve the alignment with the orbit on the cone. The Laplace–Runge–Lenz analogue $\boldsymbol{J}$ is given by (3.5.6) with $\mu = 0$ and is coincident with $\boldsymbol{K}_K$ with components $\boldsymbol{J} = \left(L(2H)^{\frac{1}{2}}, 0, 0\right)$. Note that the $x-$component of $\boldsymbol{J}$ is equal in magnitude to $\boldsymbol{K}_K$ from (3.6.29) since the vector product with $\hat{\boldsymbol{P}}$ has the effect of projecting $\boldsymbol{J}$ into the plane followed by a counter–clockwise rotation through $\pi/2$ radians. The angle between $\boldsymbol{J}$ and $\boldsymbol{r}$ is acute in this case, which accounts for the discrepancy in the sign of the $\cos\psi$ term of (3.6.3). The Poincaré vector is given by (3.5.4) and has components $\left(0, 0, -(L^2 + \lambda^2)^{\frac{1}{2}}\right)$. The normal vector $\boldsymbol{N}$ (3.6.5) is perpendicular to the plane of the orbit and coincident with $-\boldsymbol{J}$ since $\mu = 0$. The vector $\boldsymbol{S}$ (3.6.8) is parallel to the plane of the orbit and coincident with $\boldsymbol{P}$ since $\mu = 0$.

Figure 3.7.4 shows the straight–line velocity hodograph in the case where $\mu = 0$. A selection of velocity vectors corresponding to the displacement vectors shown in Figure 3.7.3 has been drawn from the origin to their respective positions on the velocity hodograph. In order to illustrate the $\dot{\boldsymbol{r}}$ behaviour more clearly, projections of the velocity hodograph onto planes parallel to the $\dot{x}\dot{y}$, $\dot{x}\dot{z}$ and $\dot{y}\dot{z}$ planes are also shown, together with the projected images of the orbital cone onto the respective planes. The two short line segments drawn perpendicular to the velocity hodograph indicate the limits of extent of the velocity hodograph as t ranges from negative through positive infinity.

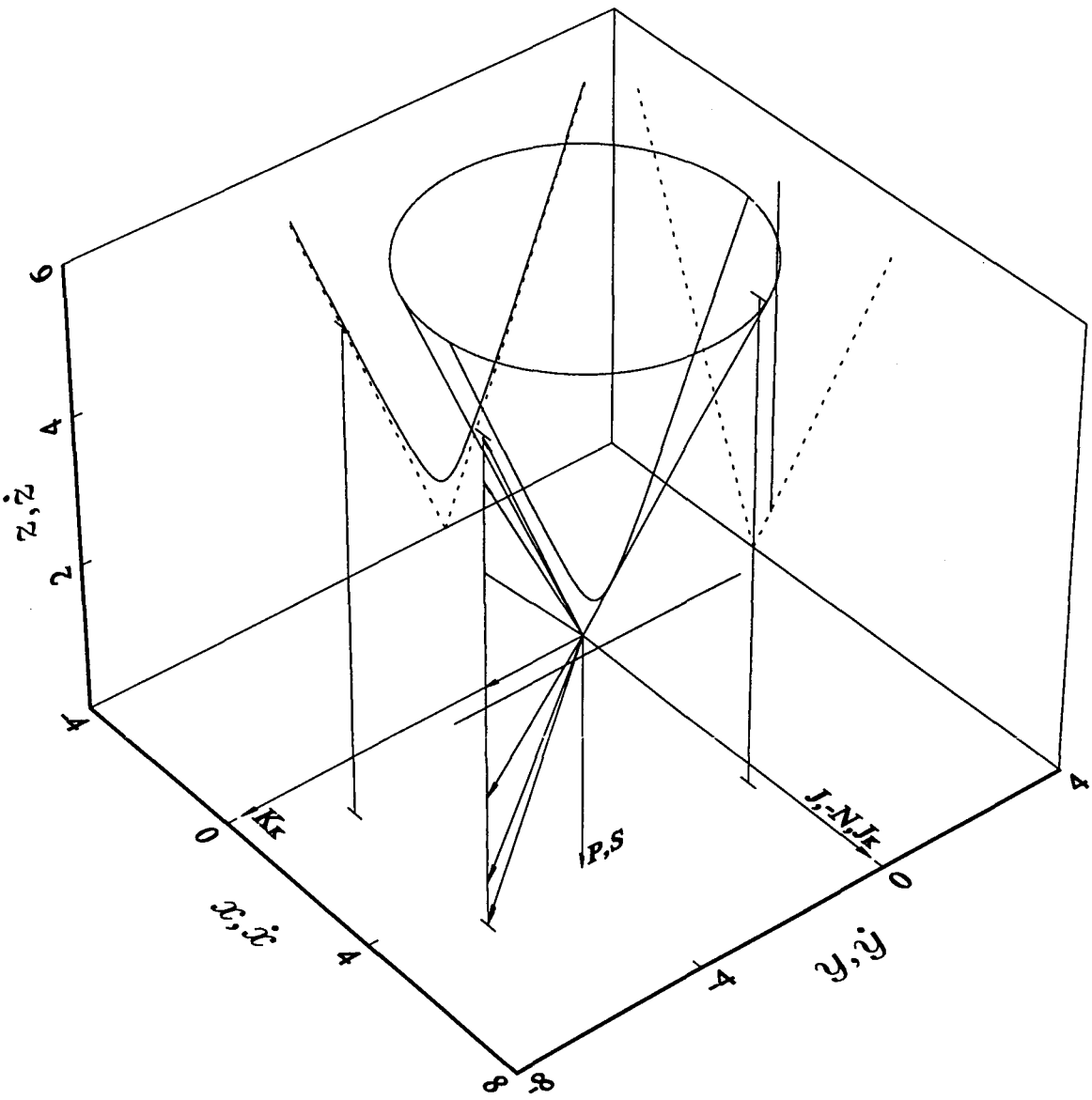

Figure 3.7.4. The straight–line MICZ velocity hodograph and hyperbolic orbit for $\mu = 0$ with a selection of velocity vectors drawn from the origin. The velocity vectors move on a plane which is parallel to the orbital plane and, as t ranges from negative through positive infinity, the velocity vectors sweep out a plane isoceles triangle lying in the $\dot{y}\dot{z}-$plane with base of length $2\lambda J/LP$ and height J/P. The projections of the velocity hodograph and orbit onto planes parallel to the $\dot{x}\dot{y}$, $\dot{x}\dot{z}$, $\dot{y}\dot{z}$, xy, xz and yz planes are also shown. The constants are chosen as for Figure 3.7.3. The origin lies in the hodographic plane touching one vertex of the triangle.

The $\dot{x}\dot{y}$ projection of the velocity hodograph is the point $(0, -J/P)$ as described by the first two equations of (3.7.20) and is consistent with the planar velocity hodograph for the free particle with $L^* = 1$, $\mu^* = 0$ and $J^* = 2.25$ and also (3.6.30) setting $\mu = 0$ and reversing the sign inside the $\dot{y}$ term since the velocity hodograph is being viewed with $\boldsymbol{P}$ directed along the $-\boldsymbol{k}$ direction.

The $\dot{x}\dot{z}$ projection shows the images of the orbital cone with dotted lines, together with the respective projections of the orbit and velocity hodograph. Note that the $\dot{x}\dot{z}$ projection of the velocity hodograph plane is a line parallel to the $\dot{z}-$axis symmetrically placed about the $\dot{z} = 0$ axis, which passes through the origin and which is bisected by the $\dot{x}-$axis (see the first and second equations of (3.7.20)). The projection of the velocity hodograph is seen to be parallel to the projection of the orbit as was shown in (3.6.6) and (3.6.7). As t ranges from negative through positive infinity, the projection ranges from the point $(0, -\lambda J/LP)$ when $\phi = \pi/2$ to $\left(0, -\lambda J/(2^{\frac{1}{2}}LP)\right)$ when $\phi = \pi/4$ to $(0, 0)$ when $\phi = 0$ to $\left(0, \lambda J/(2^{\frac{1}{2}}LP)\right)$ when $\phi = -\pi/4$ to $(0, \lambda J/LP)$ when $\phi = -\pi/2$, *i.e.* the length of the projection of the velocity hodograph tends to $2\lambda J/LP$. The two short line segments drawn perpendicular to the $\dot{x}\dot{z}$ projection of the velocity hodograph indicate the limits of extent of the projection of the velocity hodograph as t ranges from negative through positive infinity.

The $\dot{y}\dot{z}$ projection shows the images of the orbital cone with dotted lines, together with the respective projections of the orbit and velocity hodograph. Note that the $\dot{y}\dot{z}$ projection of the velocity hodograph is a line parallel to the $\dot{z}-$axis symmetrically placed about the $\dot{z} = 0$ axis with centre $(-J/P, 0)$ and which is bisected by the $\dot{y}-$axis (see the second and third equations of (3.7.20)). As t ranges from negative through positive infinity, the projection ranges from the point $(-J/P, -\lambda J/LP)$ when $\phi = \pi/2$ to $\left(-J/P, -\lambda J/(2^{\frac{1}{2}}LP)\right)$ when $\phi = \pi/4$ to $(-J/P, 0)$ when $\phi = 0$ to $\left(-J/P, \lambda J/(2^{\frac{1}{2}}LP)\right)$ when $\phi = -\pi/4$ to $(-J/P, \lambda J/LP)$ when $\phi = -\pi/2$, *i.e.* the length of the projection of the velocity hodograph tends to $2\lambda J/LP$. The two short line segments drawn perpendicular to the $\dot{y}\dot{z}$ projection of the velocity hodograph indicate the limits of extent of the projection of the velocity hodograph as t ranges from negative through positive infinity.

The conserved vectors $\boldsymbol{K}_K$, $\boldsymbol{J}_K$, $\boldsymbol{J}$ and $\boldsymbol{P}$ are drawn as in Figure 3.7.3.

3.8 The Geometry of the MICZ Problem with $\mu = J$

From (3.6.3) a parabolic orbit exists when $\mu = J$. The salient features of the geometry are depicted in Figure 3.8.1 which shows the orientation of the larger orbital and smaller angular momentum cones which meet at the origin. A typical parabolic orbit is shown together with the construction of the Poincaré vector $\boldsymbol{P}$ from $\boldsymbol{L}$ and $\hat{\boldsymbol{r}}$ and the orientation of the vector $\boldsymbol{J}$. Note that $\boldsymbol{L}$ and $\boldsymbol{r}$ are orthogonal throughout the motion and that $\boldsymbol{P}$, $\boldsymbol{L}$ and $\boldsymbol{r}$ are coplanar at any instant in time. The vectors $\boldsymbol{P}$, $\boldsymbol{J}$ and $\boldsymbol{r}$ are only coplanar at the turning points of the motion. In this case $\beta = \alpha$ which means that the line of $\boldsymbol{J}$ lies on the surface of the cone. This situation is shown in Figure 3.8.1 which is drawn with $\alpha < \pi/4$, *i.e.* $L < \lambda$ (this does not affect the subsequent discussion). When θ is 2α, the particle is at B. Using the orbit equation (3.6.3)

$$OB = P^2/2J = BC = AB = \frac{1}{2}\,AC \tag{3.8.1}$$

and from the triangle AOC

$$OC = AC\cos\alpha = P\lambda/J. \tag{3.8.2}$$

Figure 3.8.2 shows the plane of the typical parabolic orbit. To determine the position of the focus of the parabola we use the equation $u^2 = 4av$ (see Figure 3.8.2) as well as the knowledge of the ordinate at the point E on the parabola since

$$CE = OC\tan\alpha = PL/J. \tag{3.8.3}$$

Substituting $(PL/J,\ P^2/2J)$ into the equation of the parabola gives

$$a = L^2/2J \tag{3.8.4}$$

so that the focus, F, which is a above B is always between B and the intersection of the line of $\boldsymbol{P}$ with the plane of the parabola.

It is also worth noting that the line of $\boldsymbol{J}$ could be said to be pointing to the geometric 'centre' of the parabola which is at infinity.

It is possible to rotate the orbital parabola on the cone into the plane. The equation of the plane of the parabola on the cone is given by (3.6.12) with $\gamma = \alpha$ which gives

$$x\cos\alpha + z\sin\alpha = OC\sin\alpha, \tag{3.8.5}$$

replacing $\lambda P/\mu$ by OC. Substituting the general expressions for x, y and z in spherical polar coordinates from (3.6.13) into (3.8.5) and rearranging gives

$$r = \frac{OC}{\cos\alpha(1+\cos\phi)}. \tag{3.8.6}$$

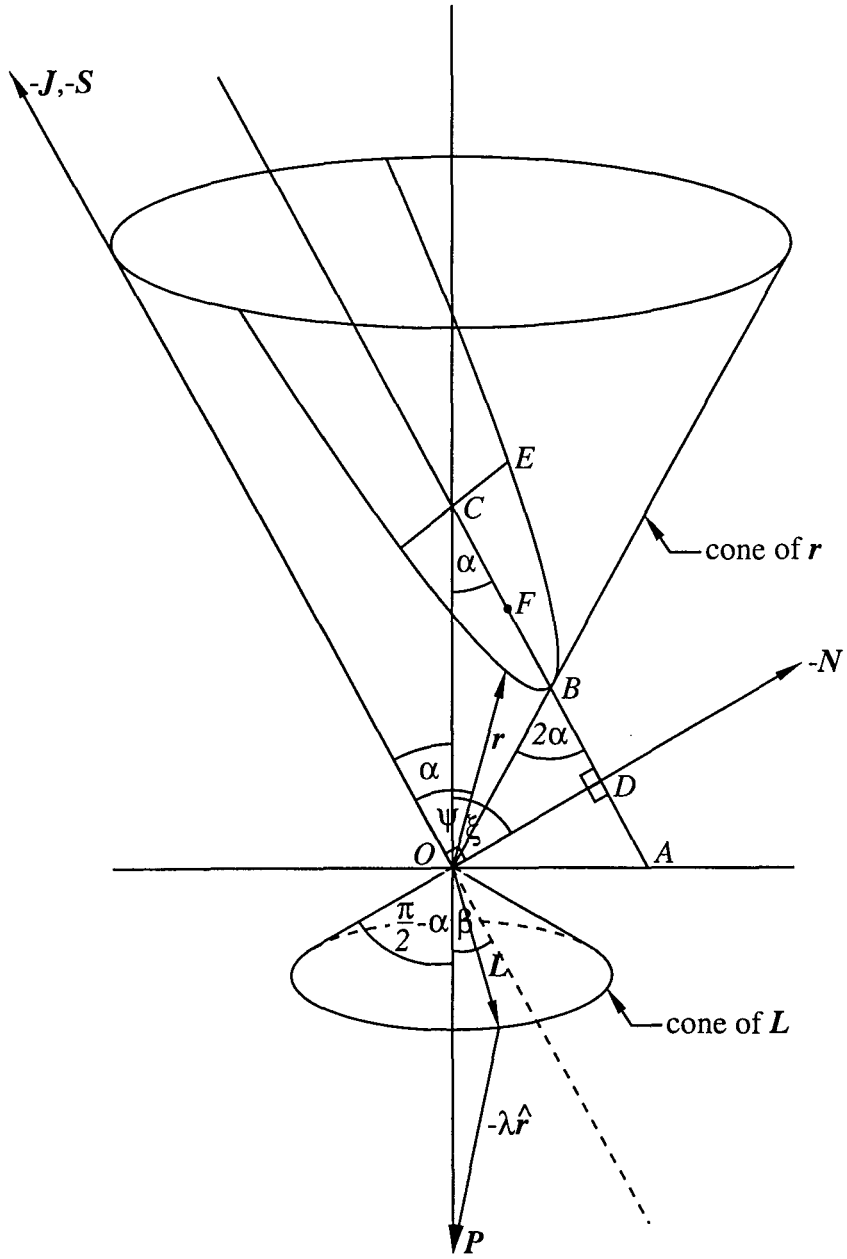

Figure 3.8.1. The typical geometry of the MICZ orbit when $\mu = J$. The larger orbital and smaller angular momentum cones are shown together with a typical parabolic orbit and the orientation of $\boldsymbol{P}$, $-\boldsymbol{J}$, $-\boldsymbol{N}$ and $-\boldsymbol{S}$. The origin O is at the point of contact between the two cones, F is the focus of the parabola and B marks the vertex of the parabola. The line segment AC lies along the axis of symmetry of the parabola. α and $\pi/2 - \alpha$ are the the semi-vertex angles of the orbital and angular momentum cones respectively, ψ is the angle between $-\boldsymbol{J}$ and $\boldsymbol{r}$, β is between $\boldsymbol{P}$ and $\boldsymbol{J}$ and ξ is between $\boldsymbol{P}$ and $\boldsymbol{N}$.

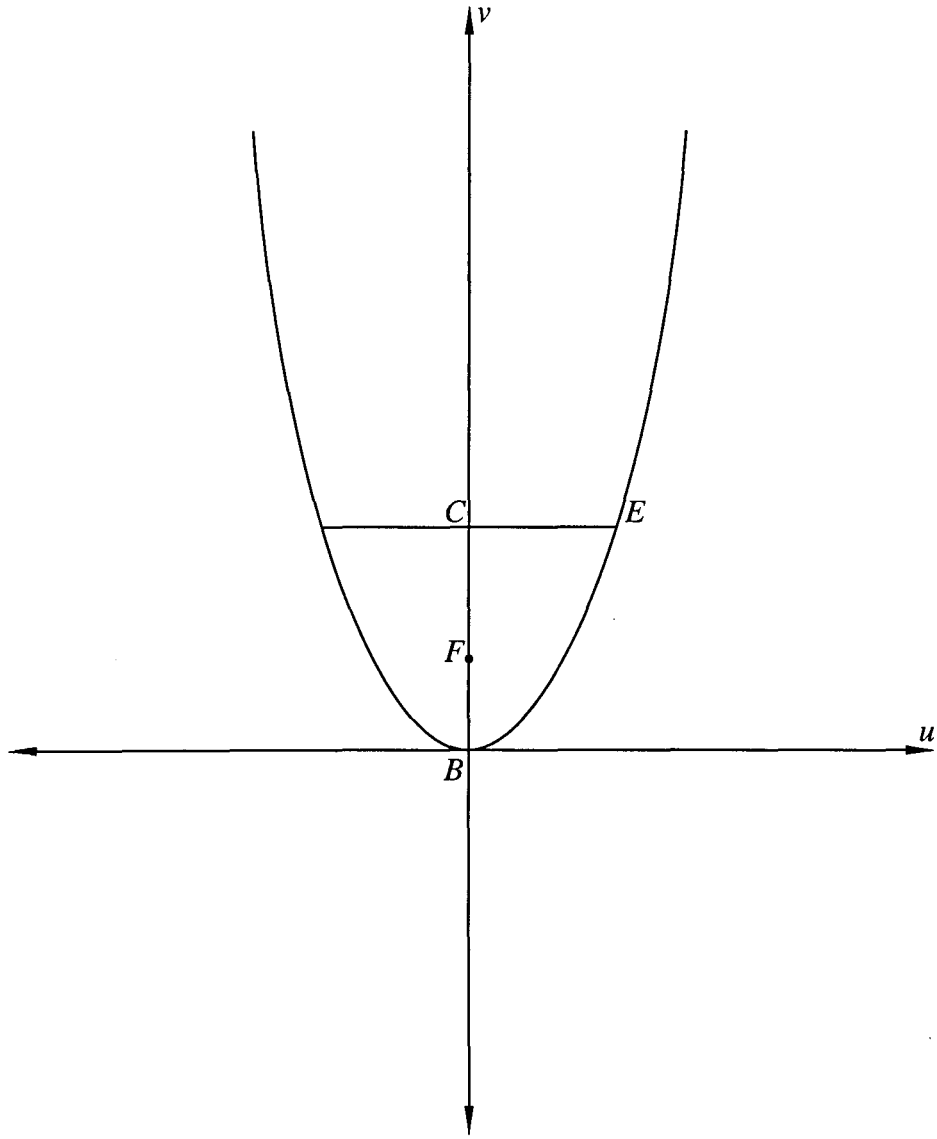

Figure 3.8.2. The plane of the typical parabolic orbit when $\mu = J$. The point F marks the focus of the parabola and B the vertex. The point C is the intersection of the line of $\boldsymbol{P}$ and the plane of the parabola.

Substituting for r (3.8.6) in (3.6.13) we obtain

$$\begin{aligned} x &= \frac{OC \sin\alpha \cos\phi}{\cos\alpha(1+\cos\phi)} \\ y &= \frac{OC \sin\alpha \sin\phi}{\cos\alpha(1+\cos\phi)} \\ z &= \frac{OC}{(1+\cos\phi)}. \end{aligned} \tag{3.8.7}$$

Since the orbit lies on a plane, it is convenient to rotate the plane counter–clockwise through $(\pi/2-\alpha)$ radians about the $y-$axis to manipulate the parametric equations into a recognisable form. In order to relocate the origin at OC, the z component has the length OC subtracted from it before performing the rotation. The rotation matrix is given by

$$\boldsymbol{Q} = \begin{pmatrix} \sin\alpha & 0 & -\cos\alpha \\ 0 & 1 & 0 \\ \cos\alpha & 0 & \sin\alpha \end{pmatrix}. \tag{3.8.8}$$

Premultiplying the row vector formed from (3.8.7) by (3.8.8) with $z \rightarrow z - OC$ gives the parametric equations of the orbit rotated into the plane

$$\begin{aligned} X &= \frac{OC\cos\phi}{\cos\alpha(1+\cos\phi)} = \frac{a\cos\phi}{b(1+\cos\phi)} \\ Y &= \frac{OC\sin\alpha\sin\phi}{\cos\alpha(1+\cos\phi)} = \frac{c\sin\phi}{b(1+\cos\phi)} \\ Z &= 0, \end{aligned} \tag{3.8.9}$$

where $a = OC$, $b = \cos\alpha$ and $c = OC\sin\alpha$. The first two equations of (3.8.9) can be manipulated into the form

$$\left(\frac{X^2}{a^2} + \frac{Y^2}{c^2}\right) b^2\big(1+\cos\phi\big)^2 = 1 \tag{3.8.10}$$

and using the first equation of (3.8.9) it is easily shown that

$$\cos\phi = \frac{bX}{a-bX}. \tag{3.8.11}$$

Replacing $\cos\phi$ with (3.8.11) and substituting for a, b and c from above, equation (3.8.10) can be rearranged to give

$$\frac{1}{(a-bX)^2}\left(b^2X^2 + \frac{a^2b^2}{c^2}Y^2\right) = 1. \tag{3.8.12}$$

Replacing trigonometric expressions containing α using (3.6.1), (3.8.12) can be manipulated into the form

$$Y^2 = -4\left(\frac{L^2}{2J}\right)\left(X - \frac{P^2}{2J}\right) \tag{3.8.13}$$

which is the standard cartesian representation for a parabola (P2.19) symmetrically placed about the $Y = 0$ axis, vertex at $(P^2/2J, 0)$ and focus at $(\lambda^2/2J, 0)$. The distance from the origin to the vertex $P^2/2J$ agrees with the length BC in (3.8.1) while the distance from the origin to the focus $\lambda^2/2J$ agrees with the length CF in Figure 3.8.1. The distance between the vertex and the focus $L^2/2J$ agrees with the length BF and also (3.8.4). The $Y-$intercepts of (3.8.13) which have lengths PL/J when measured from the origin are consistent with the length of CE (3.8.3).

If we consider the equation of the orbit in the $\phi-$plane, using (3.6.18) we find that

$$|\boldsymbol{r} \times \boldsymbol{P}| = \frac{P^2 L}{J(1 + \cos\phi)}, \tag{3.8.14}$$

i.e. the projection of the orbit into the plane decribes a parabola symmetrically placed about the $\phi = 0$ axis with the focus at the intersection of $\boldsymbol{P}$ and the $\phi-$plane. The projection of OB onto the $\phi-$plane has the length $PL/2J$, *i.e.* $OB\sin\alpha = BC\sin\alpha$ which agrees up to a scaling factor of P with equation (3.8.14) with $\phi = 0$. The projection of CE (3.8.3) onto the $\phi-$plane which remains unchanged in length since it is parallel to the $\phi-$plane is also consistent with equation (3.8.14) with $\phi = \pi/2$ up to a scaling factor of P.

Alternatively, an elegant vector combination can be used to calculate the plane polar equation of the orbit in the orbital plane. Following the procedure adopted in the $\mu = 0$ case, we construct a vector $\boldsymbol{R}$ which lies in the orbital plane and is thus parallel to $\boldsymbol{J}$. One suitable vector is

$$\begin{aligned} \boldsymbol{R} &= \boldsymbol{r} + |\boldsymbol{r}\cdot\hat{\boldsymbol{N}}|\,\hat{\boldsymbol{N}} + \cot 2\alpha|\boldsymbol{r}\cdot\hat{\boldsymbol{N}}|\,\hat{\boldsymbol{J}} \\ &= \boldsymbol{r} + \frac{\lambda L}{J}\hat{\boldsymbol{N}} + \left(\frac{P^2 - 2L^2}{2J}\right)\hat{\boldsymbol{J}}, \end{aligned} \tag{3.8.15}$$

where $\hat{\boldsymbol{N}}$ is the unit vector of $\boldsymbol{N}$ which is given in (3.6.5) and is normal to the plane of the parabola. Note that all the required scalar quantities are easily constructed using scalar products on combinations of the conserved vectors. The vector $\boldsymbol{R}$ moves in the orbital plane, parallel to $\boldsymbol{J}$ and is displaced from the origin by $\lambda L\hat{\boldsymbol{N}}/J + \left(P^2 - 2L^2\right)\hat{\boldsymbol{J}}/2J$. Measuring the angle ϑ which lies in the orbital plane from $\boldsymbol{J}$ gives the equation for the orbit in the orbital plane as

$$\boldsymbol{J}\cdot\boldsymbol{R} = JR\cos\vartheta = \frac{P^2}{2} - \mu r. \tag{3.8.16}$$

Rearranging the expression (3.8.15) to obtain $\boldsymbol{r}$ as the subject of the equation and squaring both sides of the expression produce a quadratic equation in r which can be solved to give

$$r = \frac{\lambda^2}{J} - \frac{P^2}{2J} + \left(R^2 + \frac{L^4}{J^2}\right)^{\frac{1}{2}}. \tag{3.8.17}$$

Note that for $R = 0$ (the minimum allowed value), $r = P^2/2J$ which is consistent with the result for OB (3.8.1). Now substituting (3.8.17) into (3.8.16) we finally obtain

$$R = -8\frac{L^2 \cos\vartheta}{2J\left(1 - \cos 2\vartheta\right)}, \tag{3.8.18}$$

which is the plane polar expression for a parabola with vertex at the origin (P2.18), symmetrically placed about the $\vartheta = 0$ axis with focus at $\left(-L^2/(2J), 0\right)$ which is consistent with (3.8.4). The distance from the origin or vertex to a focus $L^2/(2J)$ agrees with the length BF. Since the plane polar equation describes a vertex centred parabola on the orbital plane, it follows that B marks the vertex of the parabola in the plane.

The velocity hodograph can be obtained by differentiating the cartesian components x, y and z (3.8.7) and substituting $\dot{\phi} = -L/(r^2 \sin\alpha)$ to give

$$\begin{aligned}
\dot{x} &= \frac{L}{OC}\cos\alpha \sin\phi \\
\dot{y} &= -\frac{L}{OC}\cos\alpha\cos\phi - \frac{L}{OC}\cos\alpha \\
\dot{z} &= -\frac{L}{OC}\cos\alpha\cot\alpha\sin\phi.
\end{aligned} \tag{3.8.19}$$

Since the velocity hodograph lies on a plane, it is convenient to rotate the plane counter–clockwise through $(\pi/2 - \alpha)$ radians about the $\dot{y}$–axis to manipulate the parametric equations into a recognisable form. Premultiplying the row vector formed from (3.8.19) by $\boldsymbol{Q}$ (3.8.8) gives the parametric equations of the velocity hodograph rotated into the plane

$$\begin{aligned}
\dot{X} &= \frac{L}{OC}\cot\alpha\sin\phi \\
\dot{Y} &= -\frac{L}{OC}\cos\alpha\cos\phi - \frac{L}{OC}\cos\alpha \\
\dot{Z} &= 0,
\end{aligned} \tag{3.8.20}$$

which can be manipulated into the standard cartesian representation for an ellipse (P2.17) using (3.8.2) and (3.6.1)

$$\left(\frac{\dot{X}}{\frac{\mu}{P}}\right)^2 + \left(\frac{\dot{Y} + \frac{\mu L}{P^2}}{\frac{\mu L}{P^2}}\right)^2 = 1, \tag{3.8.21}$$

symmetrically placed about the $\dot{X} = 0$ axis, with semi–major and semi–minor axes of lengths $a = \mu/P$ and $b = \mu L/P^2$ respectively, eccentricity of $\lambda/P = \cos\alpha$ and centred at $(0, -\mu L/P^2)$. This result is as expected from the projection of the velocity hodograph into the plane. The corresponding Kepler problem has a circular velocity hodograph in the plane with radius $\mu L/P^2$ and centre $(0, -\mu L/P^2)$ from (3.6.30) and (3.6.29) when $\boldsymbol{P}$ is directed along the $-\boldsymbol{k}$ direction and viewed from above. Consequently, it is to be expected that the semi–major axis length of the ellipse described above has the same length as the radius of the Kepler velocity hodograph when projected into the plane, *i.e.* $a\sin\alpha = \mu L/P^2$. However, the semi–minor axis length which has the same length as the radius of the velocity hodograph does not change in length on projection into the ϕ–plane since it is parallel to the ϕ–plane. The centre of the ellipse rotated into the ϕ–plane also marks the centre of the circle at $(0, -\mu L/P^2)$ because the $\dot{y}$–axis about which the rotation takes place passes through the centre of the ellipse on the hodographic plane. As with the Kepler velocity hodograph, the MICZ velocity hodograph only closes as t ranges from negative through positive infinity. The origin similarly lies on the circumference of the hodographic ellipse.

It does not seem possible to calculate the plane polar equation of the velocity hodograph on the plane using simple vector operations as was done for the orbit.

The initial conditions were chosen so that the projection of the orbit on the cone into the ϕ–plane is identical to the corresponding Kepler orbit and also that the projection of the velocity hodograph into the ϕ–plane is coincident with that of the Kepler problem as shown in Figure 1.5.3 of Chapter 1. This was done in much the same way as that described for the $\mu = 0$ case by equating certain quantities on the cone on projection into the ϕ–plane with the equivalent quantities for the Kepler problem. In the subsequent discussion, the starred quantities will be used to denote the constants used in Chapter 1 for the Kepler problem. The constants have the values, as before, $\mu^* = 1.25$, $\theta_0^* = 0$, $K^* = J^* = 1.25$ and $L^* = 1$. The radius of the projected velocity hodograph was equated with that of the Kepler problem to force both the orbits and the velocity hodographs to coincide so that a comparison

between the two problems can be made. Comparing equations (1.5.9) and (3.6.30) and taking square roots on both sides of the resulting equation gives

$$\frac{\mu L}{P^2} = \frac{\mu^*}{L*}. \tag{3.8.22}$$

The perpendicular distance from the intersection between the line of $\boldsymbol{P}$ and the axis of symmetry of the orbit to a point on the orbit remains unchanged in length on projection into the $\phi-$plane. This distance is equal in length to the semi-latus rectum of the plane conic section in the $\phi-$plane which gives

$$\frac{PL}{\mu} = \frac{L^{*2}}{\mu^*}. \tag{3.8.23}$$

Eliminating μ^* from (3.8.22) and (3.8.23) gives

$$P = \frac{L^2}{L^*}, \tag{3.8.24}$$

and it follows using the definition of P, equation (3.5.5), that

$$\lambda = \frac{L}{L^*}\left(L^2 - L^{*2}\right)^{\frac{1}{2}} \tag{3.8.25}$$

and

$$\mu = \mu^* \left(\frac{L}{L^*}\right)^3. \tag{3.8.26}$$

Using (3.8.24) and (3.8.25), equation (3.6.1) can be rewritten as

$$\alpha = \arccos\left(\frac{(L^2 - L^{*2})^{\frac{1}{2}}}{L}\right) = \arcsin\left(\frac{L^*}{L}\right), \tag{3.8.27}$$

i.e. the angle α only depends on the projection of the MICZ angular momentum, $\boldsymbol{L}$, onto the Kepler angular momentum, $\boldsymbol{L}^*$, which is directed along the line of $\boldsymbol{P}$. Equating the location of the projected centre of the velocity hodograph into the plane with the centre of the velocity hodograph of the Kepler problem gives, using (1.5.9) and (3.6.30)

$$\frac{K_K}{P} = \frac{1}{P}\left(J^2 - \frac{\lambda^2\mu^2}{P^2}\right)^{\frac{1}{2}} = \frac{J^*}{L^*}, \tag{3.8.28}$$

which can be solved for J using (3.8.24)–(3.8.26) to give

$$J = \frac{L^2}{L^{*3}}\left(L^2\mu^{*2} + L^{*2}(J^{*2} - \mu^{*2})\right)^{\frac{1}{2}}, \tag{3.8.29}$$

which in the parabolic case $J^* = \mu^*$ reduces to (3.8.26). Using (3.6.2), (3.8.24)–(3.8.26) and (3.8.29), the angle β can be found to be

$$\beta = \arccos\left(\frac{\mu^*(L^2 - L^{*2})^{\frac{1}{2}}}{\left(L^2\mu^{*2} + L^{*2}(J^{*2} - \mu^{*2})\right)^{\frac{1}{2}}}\right), \tag{3.8.30}$$

which in the parabolic case $J^* = \mu^*$ reduces to (3.8.27). For convenience, L was chosen to be 1.85 and using the values for the starred quantities given above, P, λ, μ, α, J and β were calculated using (3.8.24)–(3.8.27), (3.8.29) and (3.8.30).

Figure 3.8.3 shows the parabolic orbit in the case where $\mu = J$. The diagram shows the two right circular orbital and angular momentum cones which extend in opposite directions along the line of $\boldsymbol{P}$ with origin and point of contact at the apices of the two cones. A selection of displacement and corresponding angular momentum vectors has been drawn from the origin to their respective positions on the orbital and angular momentum cones. The orbit is parabolic and lies on a plane which does not include the origin. In order to illustrate the bahaviour more clearly, projections of the orbit onto planes parallel to the xy, xz and yz planes are shown, together with projections of the angular momentum curve and the projected images of the cones onto the respective planes. The constant magnitude of the angular momentum is reflected by the angular momentum vectors moving on the surface of a cone which is truncated perpendicular to the axis of symmetry to a height of L^2/P below the origin. The components of the angular momentum are given by $L = (\lambda L \cos\phi/P, \lambda L \sin\phi/P, -L^2/P)$ using (3.8.7) and (3.8.19).

The xy projection of the orbit is also parabolic as described by the first two equations of (3.8.7) which can be manipulated into the form

$$y^2 = -4\frac{PL}{2J}\left(x - \frac{PL}{2J}\right), \tag{3.8.31}$$

which is the cartesian representation of (3.8.14) scaled by P, symmetrically placed about the $y = 0$ axis, vertex at $(PL/2J, 0)$ and focus at the origin. The distance from the origin to the vertex $PL/2J$ agrees with the length of the projection of OB into the $xy-$plane, *i.e.* $OB \sin\alpha = BC \sin\alpha$. Since this distance is equal to a in (3.8.31), this confirms that the origin is at a focus. The $y-$intercepts of (3.8.31) which have lengths PL/J when measured from the origin are consistent with the length of the projection of CE (3.8.3) into the $xy-$plane which is unchanged in length since it lies parallel to the $xy-$plane. It is worth noting that the focus of the parabola on the cone does not project onto the focus of the parabola projected into the $xy-$plane in general. The projected orbit is consistent with the planar parabolic Kepler orbit with $L^* = 1$ and $\mu = J^* = 1.25$. As t ranges from negative through positive infinity, the azimuthal angle ϕ ranges between π and $-\pi$ and so the projection ranges from $(-\infty, +\infty)$ when $\phi = \pi$ to $(0, PL/J)$ when $\phi = \pi/2$ to $(PL/2J, 0)$ when $\phi = 0$ to $(0, -PL/J)$ when $\phi = -\pi/2$ to $(-\infty, -\infty)$ when $\phi = -\pi$. The projection of the angular momentum curve onto its corresponding plane describes part of a circle with

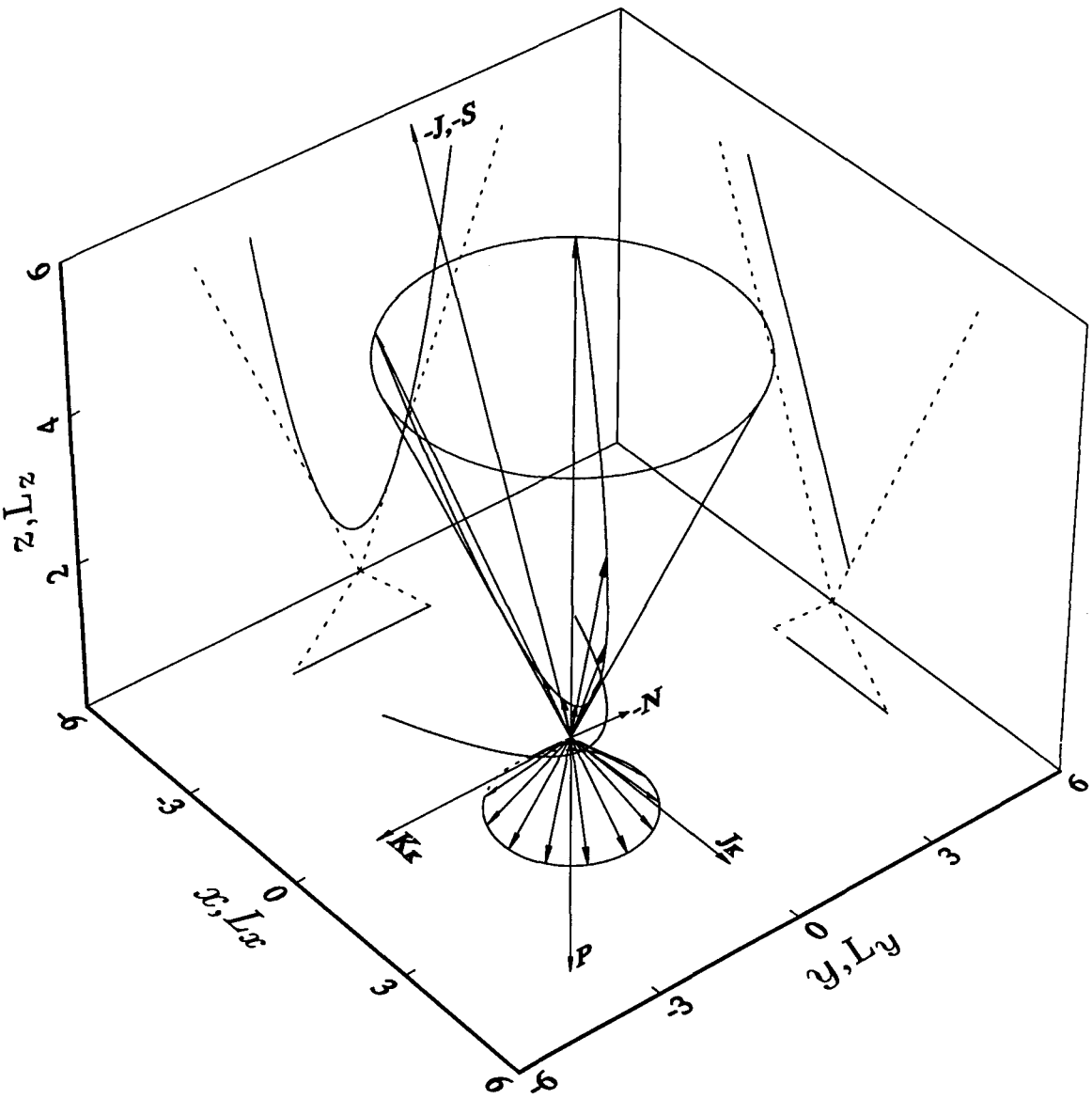

Figure 3.8.3. The parabolic MICZ orbit and angular momentum curve for $\mu = J$ with a selection of displacement and angular momentum vectors drawn from the origin. The radial and angular momentum vectors move on the surfaces of two right circular cones extending in opposite directions along the line of $\boldsymbol{P}$ with origin and point of contact at the apices of the two cones. The projections of the orbit and angular momentum curve onto planes parallel to the xy, xz, yz, L_xL_y, L_xL_z and L_yL_z planes are also shown. The constants have the values $\mu = 7.9145$, $J = 7.9145$, $P = 3.4225$, $\lambda = 2.8794$, $\alpha = 0.5711$, $\beta = 0.5711$ and $L = 1.85$. The origin lies out of the orbital plane.

radius $\lambda L/P$ symmetrically placed about the L_x-axis, *i.e.* ${L_x}^2+{L_y}^2=(\lambda L/P)^2$. As t ranges from negative through positive infinity, the projection ranges from $(-\lambda L/P,0)$ when $\phi=\pi$ to $(0,\lambda L/P)$ when $\phi=\pi/2$ to $(\lambda L/P,0)$ when $\phi=0$ to $(0,-\lambda L/P)$ when $\phi=-\pi/2$ to $(-\lambda L/P,0)$ when $\phi=-\pi$, *i.e.* the circle is completed. The dotted line completes the angular momentum cone. However, it should be remembered that the projection of the angular momentum vectors only closes as t ranges from negative through positive infinity.

The xz projection shows the images of the orbital and angular momentum cones with dotted lines, together with the projections of the orbit and angular momentum curves. Note that the xz projection of the orbit is obtained by manipulating the first and third equations of (3.8.7) into the form

$$z=-\cot\alpha x+\frac{\lambda P}{J},\quad -\infty\leq x\leq\frac{PL}{2J}, \tag{3.8.32}$$

which is the equation of a straight line with slope $-\cot\alpha$ and $z-$intercept $\lambda P/J$ in agreement with (3.6.12). The slope of the line is the same as that of the cone and confirms the well-known result that a cone intersected by a plane which is parallel to a face of the cone describes a parabola on the plane. The $z-$intercept is given by the length of OC which is consistent with Figure 3.8.1. The orbit lies on a plane section through the orbital cone. As t ranges from negative through positive infinity, the projection ranges from $(-\infty,+\infty)$ when $\phi=\pi$ to $(0,\lambda P/J)$ when $\phi=\pi/2$ to $(PL/2J,\lambda P/2J)$ when $\phi=0$ to $(0,\lambda P/J)$ when $\phi=-\pi/2$ to $(-\infty,+\infty)$ when $\phi=-\pi$. The L_xL_z projection of the angular momentum curve extends along the base of the triangle describing the L_xL_z projection of the image of the angular momentum cone, perpendicular to the L_z-axis. As t ranges from negative through positive infinity, the projection ranges from $(-\lambda L/P,-L^2/P)$ when $\phi=\pi$ to $(0,-L^2/P)$ when $\phi=\pi/2$ to $(\lambda L/P,-L^2/P)$ when $\phi=0$ to $(0,-L^2/P)$ when $\phi=-\pi/2$ to $(-\lambda L/P,-L^2/P)$ when $\phi=-\pi$, *i.e.* the full length of the base of the angular momentum triangle. In other words the angular momentum vectors will have swept over the entire surface area of the angular momentum cone.

The yz projection shows the images of the orbital and angular momentum cones with dotted lines, together with the projections of the orbit and angular momentum curves. Note that the yz projection of the orbit is obtained by manipulating the second and third equations of (3.8.7) into the form

$$y^2=4\frac{PL^2}{2\lambda J}\left(z-\frac{\lambda P}{2J}\right), \tag{3.8.33}$$

which is the equation of a parabola symmetrically placed about the $y = 0$ axis, vertex at $(0, \lambda P/2J)$ and focus at $\left(0, P^3/(2\lambda J)\right)$. The distance from the origin to the vertex $\lambda P/(2J)$ agrees with the length of the projection of OB into the $yz-$plane, *i.e.* $OB\cos\alpha = BC\cos\alpha$. The $y-$components of (3.8.33) when $z = OC = \lambda P/J$ which have the length PL/J when measured from the origin are consistent with the length of the projection of CE (3.8.3) into the $yz-$plane which is unchanged in length since it lies parallel to the $yz-$plane. It is worth noting that the focus of the parabola on the cone does not project onto the focus of the parabola projected into the $yz-$plane in general. As t ranges from negative through positive infinity, the projection ranges from $(+\infty, +\infty)$ when $\phi = \pi$ to $(PL/J, \lambda P/J)$ when $\phi = \pi/2$ to $(0, \lambda P/2J)$ when $\phi = 0$ to $(-PL/J, \lambda P/J)$ when $\phi = -\pi/2$ to $(-\infty, +\infty)$ when $\phi = -\pi$. The L_yL_z projection of the angular momentum curve lies along the base of the triangle describing the L_yL_z projection of the image of the angular momentum cone, perpendicular to the L_z-axis. As t ranges from negative through positive infinity, the line segment extends along the full length of the base of the angular momentum triangle from the point $(0, -L^2/P)$ when $\phi = \pi$ to $(\lambda L/P, -L^2/P)$ when $\phi = \pi/2$ to $(0, -L^2/P)$ when $\phi = 0$ to $(-\lambda L/P, -L^2/P)$ when $\phi = -\pi/2$ to $(0, -L^2/P)$ when $\phi = -\pi$. In other words the angular momentum vectors will have swept over the entire surface area of the angular momentum cone.

The conserved vector $\boldsymbol{K}_K$ which has been rotated clockwise through $\pi/2$ radians to lie along the cartesian unit vector $-\boldsymbol{j}$ is given by (3.6.29) and has length JL/P as shown in Figure 3.8.3. The vector $\boldsymbol{J}_K$, which is perpendicular to $\boldsymbol{K}_K$, is also rotated clockwise through $\pi/2$ radians to lie along the cartesian unit vector $\boldsymbol{i}$. $\boldsymbol{J}_K$ has the length PL^2K_K and is conveniently drawn to the same length as $\boldsymbol{K}_K$ in Figure 3.8.3. The Poincaré vector, $\boldsymbol{P}$, no longer orthogonal to $\boldsymbol{J}$, lies along the cartesian unit vector $-\boldsymbol{k}$. Note that, when the cone is rotated about the $x-$axis so that $\boldsymbol{P}$ lies along $\boldsymbol{k}$, the vectors $\boldsymbol{K}_K$ and $\boldsymbol{J}_K$ lie along the cartesian unit vectors $\boldsymbol{j}$ and $\boldsymbol{i}$ respectively and hence mimic the behaviour of $\boldsymbol{L}$, $\boldsymbol{K}$ and $\boldsymbol{J}$ respectively of the standard Kepler problem. The components of the conserved vectors are found by taking the scalar products of the relevant vectors with $\hat{\boldsymbol{K}}_K$, $\hat{\boldsymbol{J}}_K$ and $-\hat{\boldsymbol{P}}$, remembering that the projected quantities have been rotated clockwise through $\pi/2$ radians to preserve the alignment with the orbit on the cone. The Laplace–Runge–Lenz analogue $\boldsymbol{J}$ is given by (3.5.6) with $\mu = J$ and has components $\boldsymbol{J} = (JL/P, 0, -\lambda J/P)$. Note that the $x-$component of $\boldsymbol{J}$ is equal in magnitude to $\boldsymbol{K}_K$ from (3.6.29) since the vector product with $\hat{\boldsymbol{P}}$ has the effect of projecting $\boldsymbol{J}$ into the plane followed by a counter–clockwise rotation through $\pi/2$ radians. The Poincaré vector is given by (3.5.4) and has components $\left(0, 0, -(L^2 + \lambda^2)^{\frac{1}{2}}\right)$. The normal vector $\boldsymbol{N}$ (3.6.5)

is perpendicular to the plane of the orbit and using (3.6.29) and (3.8.24) the components are found to be $(-L^* \cot\alpha, 0, -L^*)$. The vector $\boldsymbol{S}$ (3.6.8) is parallel to the plane of the orbit and coincident with $\boldsymbol{J}$ from (3.6.8).

Figure 3.8.4 shows the elliptical velocity hodograph in the case where $\mu = J$. A selection of velocity vectors corresponding to the displacement vectors shown in Figure 3.8.3 has been drawn from the origin to their respective positions on the velocity hodograph. In order to illustrate the $\dot{\boldsymbol{r}}$ behavior more clearly, projections of the velocity hodograph onto planes parallel to the $\dot{x}\dot{y}$, $\dot{x}\dot{z}$ and $\dot{y}\dot{z}$ planes are also shown, together with the projected images of the orbital cone onto the respective planes.

The $\dot{x}\dot{y}$ projection of the velocity hodograph is obtained by manipulating the first two equations of (3.8.19) into the form

$$\dot{x}^2 + \left(\dot{y} + \frac{\mu L}{P^2}\right)^2 = \left(\frac{\mu L}{P^2}\right)^2, \tag{3.8.34}$$

which is the equation of a circle in cartesian coordinates symmetrically placed about the $\dot{x} = 0$ axis, radius $\mu L/P^2$ with origin $(0, -\mu L/P^2)$ and is consistent with the planar velocity hodograph for the parabolic Kepler orbit with $L^* = 1$ and $\mu = J^* = 1.25$ and (3.6.30) reversing the sign inside the $\dot{y}$ term since the velocity hodograph is being viewed with $\boldsymbol{P}$ directed along the $-\boldsymbol{k}$ direction. The semi-major axis length of (3.8.21) projected into the $\dot{x}\dot{y}-$plane reduces to the length of the radius, *i.e.* $a \sin\alpha = \mu L/P^2$, as it should. The semi-minor axis length of (3.8.21) is unchanged in length on projection into the $\dot{x}\dot{y}-$plane because it is parallel to that plane and the location of the origin agrees with that of (3.8.21) because it lies along the $\dot{y}-$axis. As t ranges from negative through positive infinity, the projection ranges from the point $(0,0)$ when $\phi = \pi$ to $(\mu L/P^2, -\mu L/P^2)$ when $\phi = \pi/2$ to $(0, -2\mu L/P^2)$ when $\phi = 0$ to $(-\mu L/P^2, -\mu L/P^2)$ when $\phi = -\pi/2$ to $(0,0)$ when $\phi = -\pi$, *i.e.* the circle is completed. The dotted line completes the projection of the velocity hodograph. However, it should be remembered that the projection of the velocity vectors only closes as t ranges from negative through positive infinity.

The $\dot{x}\dot{z}$ projection shows the images of the orbital cone with dotted lines, together with the respective projections of the orbit and velocity hodograph. Note that the $\dot{x}\dot{z}$ projection of the velocity hodograph is obtained by manipulating the first and third equations of (3.8.19) into the form

$$\dot{z} = -\cot\alpha \dot{x}, \quad |\dot{x}| \leq \frac{\mu L}{P^2}, \tag{3.8.35}$$

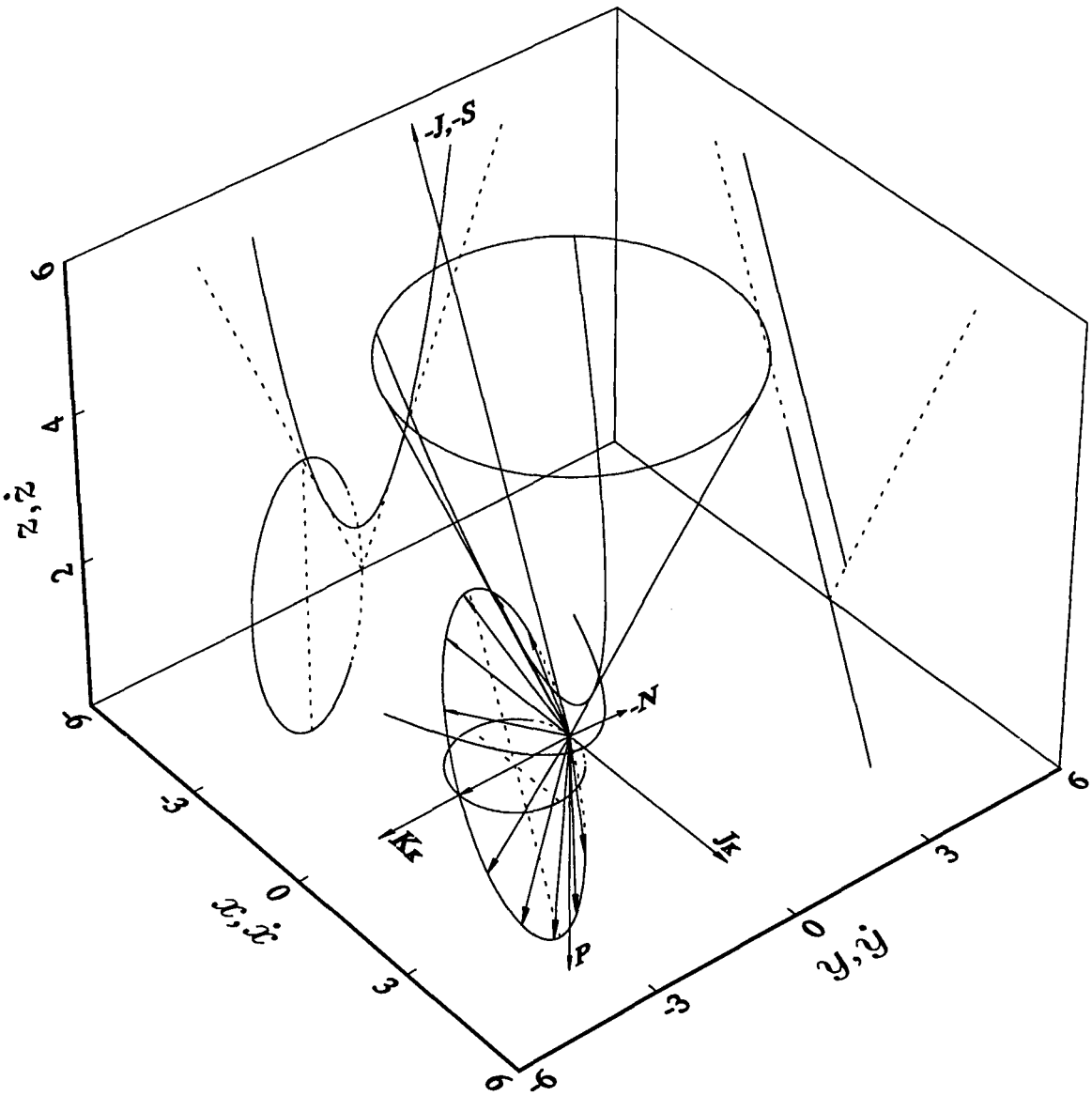

Figure 3.8.4. The elliptical MICZ velocity hodograph and parabolic orbit for $\mu = J$ with a selection of velocity vectors drawn from the origin. The velocity vectors move on a plane which is parallel to the orbital plane and, as t ranges from negative through positive infinity, the heads of the velocity vectors trace out a complete ellipse. The projections of the velocity hodograph and orbit onto planes parallel to the $\dot{x}\dot{y}$, $\dot{x}\dot{z}$, $\dot{y}\dot{z}$, xy, xz and yz planes are also shown. The constants are chosen as for Figure 3.8.3. The origin lies on the hodographic plane and touches the circumference of the hodographic ellipse.

which is the equation of a straight line with slope $-\cot\alpha$ which passes through the origin and which is bisected by the $\dot{x}-$axis. The projection of the velocity hodograph is seen to be parallel to the projection of the orbit as was shown in (3.6.6) and (3.6.7). As t ranges from negative through positive infinity, the projection ranges from the point $(0,0)$ when $\phi=\pi$ to $(\mu L/P^2,-\mu\lambda/P^2)$ when $\phi=\pi/2$ to $(0,0)$ when $\phi=0$ to $(-\mu L/P^2,\mu\lambda/P^2)$ when $\phi=-\pi/2$ to $(0,0)$ when $\phi=-\pi$, *i.e.* the length of the projection of the velocity hodograph tends to $2\mu/P$.

The $\dot{y}\dot{z}$ projection shows the images of the orbital cone with dotted lines, together with the respective projections of the orbit and velocity hodograph. Note that the $\dot{y}\dot{z}$ projection of the velocity hodograph is obtained by manipulating the second and third equations of (3.8.19) into the form

$$\left(\frac{\dot{y}+\frac{\mu L}{P^2}}{\frac{\mu L}{P^2}}\right)^2+\left(\frac{\dot{z}}{\frac{\mu\lambda}{P^2}}\right)^2=1, \tag{3.8.36}$$

which is the equation for an ellipse symmetrically placed about the $\dot{z}=0$ axis, with semi-major axis length $\mu\lambda/P^2$ which is just the projection of the semi-major axis of (3.8.21) onto the $\dot{y}\dot{z}-$plane, *i.e.* $a\cos\alpha$, semi-minor axis length $\mu L/P^2$ which is consistent with that of (3.8.21) since it is parallel to the $\dot{y}\dot{z}-$plane, eccentricity of $(1-L^2/\lambda^2)^{\frac{1}{2}}$ and centred at $(-\mu L/P^2,0)$ which also agrees with the centre of (3.8.21) which lies along the $\dot{y}-$axis. It is worth noting that the focus of the ellipse on the cone does not project onto the focus of the ellipse projected into the $\dot{y}\dot{z}-$plane in general. As t ranges from negative through positive infinity, the projection ranges from the point $(0,0)$ when $\phi=\pi$ to $(-\mu L/P^2,-\mu\lambda/P^2)$ when $\phi=\pi/2$ to $(-2\mu L/P^2,0)$ when $\phi=0$ to $(-\mu L/P^2,\mu\lambda/P^2)$ when $\phi=-\pi/2$ to $(0,0)$ when $\phi=-\pi$, *i.e.* the ellipse is completed. The dotted line completes the projection of the velocity hodograph. However, it should be remembered that the projection of the velocity vectors only closes as t ranges from negative through positive infinity.

The conserved vectors $\boldsymbol{K}_K$, $\boldsymbol{J}_K$, $\boldsymbol{J}$, $\boldsymbol{P}$, $\boldsymbol{N}$ and $\boldsymbol{S}$ are drawn as in Figure 3.8.3.

3.9 The Geometry of the MICZ Problem with $\mu > J$

From (3.6.3) an elliptic orbit exists when $\mu > J$. The salient features of the geometry are depicted in Figure 3.9.1 which shows the orientation of the larger orbital and smaller angular momentum cones which meet at the origin. A typical elliptical orbit is shown together with the construction of the Poincaré vector $\boldsymbol{P}$ from $\boldsymbol{L}$ and $\hat{\boldsymbol{r}}$ and the orientation of the vector $\boldsymbol{J}$. Note that $\boldsymbol{L}$ and $\boldsymbol{r}$ are orthogonal throughout the motion and that $\boldsymbol{P}$, $\boldsymbol{L}$ and $\boldsymbol{r}$ are coplanar at any instant in time. The vectors $\boldsymbol{P}$, $\boldsymbol{J}$ and $\boldsymbol{r}$ are only coplanar at the turning points of the motion. It follows from (3.6.1) and (3.6.2) that $\mu/J = \cos\beta/\cos\alpha$ and so $\beta < \alpha$. The particle is at A and D when $\psi = \alpha + \beta$ and $\alpha - \beta$ respectively. Making use of the orbit equation (3.6.3)

$$OA = \frac{L^2/J}{\mu/J - \cos(\alpha+\beta)} \qquad OD = \frac{L^2/J}{\mu/J - \cos(\alpha-\beta)}. \tag{3.9.1}$$

Using $\mu/J = \cos\beta/\cos\alpha$,

$$\frac{\mu}{J} - \cos(\alpha \pm \beta) = \tan\alpha \sin(\alpha \pm \beta) \tag{3.9.2}$$

so that (3.9.1) becomes

$$OA = \frac{\lambda L/J}{\sin(\alpha+\beta)} \qquad OD = \frac{\lambda L/J}{\sin(\alpha-\beta)}. \tag{3.9.3}$$

We let the angle ACO be ρ. Applying the sine rule to the triangles ACO and DCO

$$\frac{AC}{\sin(\alpha+\beta)} = \frac{OA}{\sin\rho}, \quad \frac{CD}{\sin(\alpha-\beta)} = \frac{OD}{\sin(\pi-\rho)} = \frac{OD}{\sin\rho} \tag{3.9.4}$$

so that

$$\frac{AC}{CD} = \frac{\sin(\alpha+\beta)}{\sin(\alpha-\beta)} \frac{OA}{OD} = 1 \tag{3.9.5}$$

from (3.9.3). Hence the line of $\boldsymbol{J}$ passes through the geometric centre of the ellipse.

To calculate the position of the focus and the eccentricity of the ellipse we must establish the length of the semi-major axis, BC, and BE. To find the length of the semi-major axis we use the cosine rule on triangle ADO to give

$$\begin{aligned} AD^2 &= OA^2 + OD^2 - 2OA.OD\cos 2\alpha \\ &= \left(\frac{\lambda L}{J}\right)^2 \left[\frac{1}{\sin^2(\alpha+\beta)} + \frac{1}{\sin^2(\alpha-\beta)} - \frac{2\cos 2\alpha}{\sin(\alpha+\beta)\sin(\alpha-\beta)}\right]. \end{aligned} \tag{3.9.6}$$

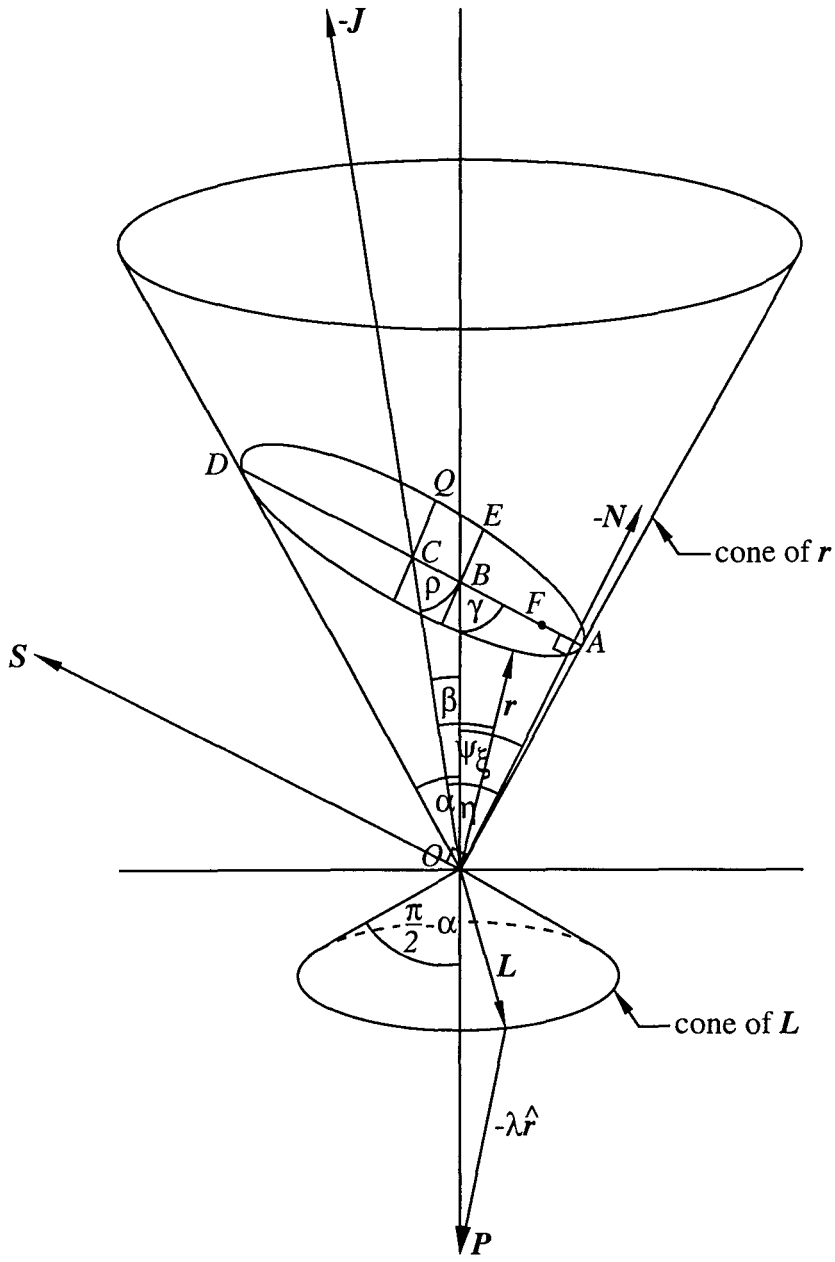

Figure 3.9.1. The typical geometry of the MICZ orbit when $\mu > J$. The larger orbital and smaller angular momentum cones are shown together with a typical elliptical orbit and the orientation of $\boldsymbol{P}$, $-\boldsymbol{J}$, $-\boldsymbol{N}$ and $\boldsymbol{S}$. The origin O is at the point of contact between the two cones, F is the focus of the ellipse and C marks the geometric centre of the ellipse. The line segment AD lies along the axis of symmetry of the ellipse. α and $\pi/2 - \alpha$ are the the semi–vertex angles of the orbital and angular momentum cones respectively, ψ is the angle between $-\boldsymbol{J}$ and $\boldsymbol{r}$, β is between $\boldsymbol{P}$ and $\boldsymbol{J}$, ξ is between $\boldsymbol{P}$ and $\boldsymbol{N}$ and η is between $\boldsymbol{J}$ and $\boldsymbol{N}$.

After tedious, but routine, manipulation of (3.9.6) we observe that the semi-major axis $a = \frac{1}{2}\ AD$ has length

$$a = \frac{(2H\lambda^2 + \mu^2)^{\frac{1}{2}}}{-2H}. \tag{3.9.7}$$

It should of course be remembered that for an elliptic orbit H is negative. To find BC and BE we need expressions for OB and OC. Applying the cosine rule to the triangles ACO and DCO

$$\begin{aligned} AC^2 &= OA^2 + OC^2 - 2OA.OC\cos(\alpha+\beta) \\ CD^2 &= OC^2 + OD^2 - 2OC.OD\cos(\alpha-\beta) \end{aligned}$$

and so

$$\begin{aligned} OC &= \frac{OD^2 - OA^2}{2[OD\cos(\alpha-\beta) - OA\cos(\alpha+\beta)]} \\ &= \frac{J}{-2H}. \end{aligned} \tag{3.9.8}$$

Remembering that the angle ACO was called ρ we apply the sine rule to the triangles ABO and BDO to obtain

$$\frac{OB}{\sin(\rho+\alpha+\beta)} = \frac{OA}{\sin(\rho+\beta)} \tag{3.9.9}$$

$$\frac{OB}{\sin(\rho-\alpha+\beta)} = \frac{OD}{\sin(\rho+\beta)}. \tag{3.9.10}$$

Dividing (3.9.9) by (3.9.10) gives

$$\frac{\sin(\rho-\alpha+\beta)}{\sin(\rho+\alpha+\beta)} = \frac{OA}{OD} = \frac{\sin(\alpha-\beta)}{\sin(\alpha+\beta)} \tag{3.9.11}$$

which leads to

$$\tan\rho = \frac{\cos 2\beta - \cos 2\alpha}{\sin 2\beta}. \tag{3.9.12}$$

Combining (3.9.12) with (3.9.9) after some routine manipulation we find

$$OB = \frac{\lambda P}{\mu}. \tag{3.9.13}$$

Now applying the cosine rule to the triangle BCO, the length BC is found to be

$$BC = \frac{1}{-2H\mu}\left[\left(2HP^2 + \mu^2\right)\left(2H\lambda^2 + \mu^2\right)\right]^{\frac{1}{2}}. \tag{3.9.14}$$

In the triangle BEO

$$BE = OB\tan\alpha = \frac{PL}{\mu}. \tag{3.9.15}$$

The standard expression for the eccentricity is given by

$$\begin{aligned} e^2 &= 1 - \frac{BE^2}{a^2 - BC^2} \\ &= \frac{2HP^2 + \mu^2}{2H\lambda^2 + \mu^2} = \frac{c^2(1+m^2)}{m^2(1+c^2)}, \end{aligned} \tag{3.9.16}$$

where c is the slope of the plane of the ellipse ($\cot\gamma$) and m is the slope of the cone ($\cot\alpha$).

The focus is located at F, ae to the left of C, and

$$CF = \frac{(2HP^2 + \mu^2)^{\frac{1}{2}}}{-2H}. \tag{3.9.17}$$

By comparing (3.9.17) with (3.9.14) and recalling that H is negative we see that $CF > CB$ and so the focus is between A and B.

It is possible to rotate the orbital ellipse on the cone into the plane as was previously done in the parabolic case. Substituting for r (3.6.14) in (3.6.13) we obtain

$$\begin{aligned} x &= \frac{OB\sin\gamma\sin\alpha\cos\phi}{\cos\alpha\sin\gamma + \sin\alpha\cos\gamma\cos\phi} \\ y &= \frac{OB\sin\gamma\sin\alpha\sin\phi}{\cos\alpha\sin\gamma + \sin\alpha\cos\gamma\cos\phi} \\ z &= \frac{OB\sin\gamma\cos\alpha}{\cos\alpha\sin\gamma + \sin\alpha\cos\gamma\cos\phi}, \end{aligned} \tag{3.9.18}$$

replacing $\lambda P/\mu$ by OB. Since the orbit lies on a plane, it is convenient to rotate the plane counter–clockwise through $(\pi/2 - \gamma)$ radians about the $y-$axis to manipulate the parametric equations into a recognisable form. In order to relocate the origin at OB, the z component has the length OB subtracted from it before performing the rotation. Premultiplying the row vector formed from (3.9.18) by (3.8.8) with α replaced by γ and $z \to z - OB$ gives the parametric equations of the orbit rotated into the plane

$$\begin{aligned} X &= \frac{OB\sin\alpha\cos\phi}{\cos\alpha\sin\gamma + \sin\alpha\cos\gamma\cos\phi} = \frac{a\cos\phi}{b + c\cos\phi} \\ Y &= \frac{OB\sin\gamma\sin\alpha\sin\phi}{\cos\alpha\sin\gamma + \sin\alpha\cos\gamma\cos\phi} = \frac{d\sin\phi}{b + c\cos\phi} \\ Z &= 0, \end{aligned} \tag{3.9.19}$$

where $a = OB\sin\alpha$, $b = \cos\alpha\sin\gamma$, $c = \sin\alpha\cos\gamma$ and $d = OB\sin\alpha\sin\gamma$. The first two equations of (3.9.19) can be manipulated into the form

$$\left(\frac{X^2}{a^2} + \frac{Y^2}{d^2}\right)\left(b + c\cos\phi\right)^2 = 1 \tag{3.9.20}$$

and using the first equation of (3.9.19) it is easily shown that

$$\cos\phi = \frac{bX}{a - cX}. \tag{3.9.21}$$

Replacing $\cos\phi$ with (3.9.21) and substituting for a, b, c and d from above, equation (3.9.20) can be rearranged to give

$$\frac{1}{(a - cX)^2}\left(b^2X^2 + \frac{a^2b^2}{d^2}Y^2\right) = 1. \tag{3.9.22}$$

Replacing trigonometric expressions containing α and γ using (3.6.1) and (3.6.9), (3.9.22) can be manipulated into the form

$$\left(\frac{X + \frac{1}{-2H\mu}(2HP^2 + \mu^2)^{\frac{1}{2}}(2H\lambda^2 + \mu^2)^{\frac{1}{2}}}{\frac{(2H\lambda^2+\mu^2)^{\frac{1}{2}}}{-2H}}\right)^2 + \left(\frac{Y}{\frac{L}{(-2H)^{\frac{1}{2}}}}\right)^2 = 1 \tag{3.9.23}$$

which is the standard cartesian representation for an ellipse (P2.17) symmetrically placed about the $Y = 0$ axis, with semi–major and semi–minor axes of lengths $a = (2H\lambda^2 + \mu^2)^{\frac{1}{2}}/(-2H)$ and $b = L/(-2H)^{\frac{1}{2}}$ respectively, eccentricity of $(2HP^2 + \mu^2)^{\frac{1}{2}}/(2H\lambda^2 + \mu^2)^{\frac{1}{2}}$ which can be expressed in terms of $c = \cot\gamma$ and $m = \cot\alpha$ as $c^2(1 + m^2)/(m^2(1 + c^2))$ (*cf.* (3.9.16) and (3.9.25)) and centred at $\left(-(2HP^2+\mu^2)^{\frac{1}{2}}(2H\lambda^2+\mu^2)^{\frac{1}{2}}/(-2H\mu), 0\right)$. The semi–major axis length is consistent with (3.9.7) and the location of the centre of the ellipse is consistent with the result for the length BC (3.9.14). Similarly the eccentricity is in agreement with (3.9.16) and similarly b agrees with (3.9.28). The $Y-$intercepts of (3.9.23) which have lengths PL/μ when measured from B are consistent with the length of BE (3.9.15).

If we consider the equation of the orbit in the $\phi-$plane, using (3.6.18) we find that

$$|\boldsymbol{r} \times \boldsymbol{P}| = \frac{P^2L}{\mu + J_\perp/L\cos\phi}, \quad \mu > J, \tag{3.9.24}$$

i.e. the projection of the orbit into the plane describes a focus–centred ellipse symmetrically placed about the $\phi = 0$ axis with the focus at the intersection of $\boldsymbol{P}$ and the ϕ–plane. It is well–known that the intersection of a plane and a right circular cone describes a conic section on the cone. The projection of the conic section into the ϕ–plane, perpendicular to $\boldsymbol{P}$, also describes a conic section which has its focus at the apex of the cone. The eccentricity is easily seen from (3.9.24) to be

$$e^* = \frac{J_\perp}{L\mu} = \frac{1}{\mu}(2HP^2 + \mu^2)^{\frac{1}{2}} = \frac{c}{m}, \tag{3.9.25}$$

where c is the slope of the plane of the ellipse and m is the slope of the cone. Since $H < 0$, $(2H\lambda^2 + \mu^2)^{-1} > \mu^{-2}$ and so it is clear that $e^* < e$. Note also that the eccentricities of both the ellipse on the cone and in the plane are determined only by the respective slopes of the plane of the ellipse on the cone and of the cone itself.

Note that (3.9.16) is equivalent to (3.9.25) when $\lambda = 0$. It should also be appreciated that, although $\boldsymbol{P}$ does not pass through the focus of the ellipse on the cone, it does mark the focus of the ellipse in the plane. The projection of the intersection point of the line of $\boldsymbol{J}$ and the plane of the ellipse on the cone marks the geometric centre of the ellipse on the ϕ–plane. Note also that $\boldsymbol{P}$ behaves like $\boldsymbol{L}$ in the standard Kepler problem and $\boldsymbol{J}$ like the usual Laplace–Runge–Lenz vector.

The semi–major axis length a of the ellipse on the cone is reduced in length by the factor $\sin\gamma$ when projected into the plane due to its inclination with respect to $\boldsymbol{P}$ and so the projection

$$2a\sin\gamma = AD\sin\gamma = \frac{\mu L}{-HP} \tag{3.9.26}$$

is consistent with the result for the semi–major axis length of the projected ellipse from (3.9.24)

$$2a^* = \frac{P^2 L}{\mu - J_\perp/L} + \frac{P^2 L}{\mu + J_\perp/L} = \frac{\mu L}{-H}. \tag{3.9.27}$$

The semi–minor axis length, however, remains unchanged on projection onto the ϕ–plane, since it is parallel to the ϕ–plane. This is easy to verify by calculating the semi–minor axis length b on the ellipse on the cone using

$$b = a(1 - e^2)^{\frac{1}{2}} = \frac{L}{(-2H)^{\frac{1}{2}}}. \tag{3.9.28}$$

Similarly the ellipse in the ϕ–plane has a semi–minor axis length of

$$b^* = a^*(1 - e^{*2})^{\frac{1}{2}} = \frac{PL}{(-2H)^{\frac{1}{2}}}, \tag{3.9.29}$$

which is the same length as (3.9.28) up to a scaling factor of P. The relationship between the eccentricities, using (3.9.28), (3.9.29) and the results that $b^* = Pb$, $a^* = Pa\sin\gamma$, is given by

$$e^2 = 1 - \sin^2\gamma\left(1 - e^{*2}\right). \tag{3.9.30}$$

The projection of $AB = a - BC$ onto the ϕ–plane has the length $\left(\mu L - L(2HP^2 + \mu^2)^{\frac{1}{2}}\right)/(-2HP)$ which agrees up to a scaling factor of P with equation (3.9.24) with $\phi = 0$. The projection of BE (3.9.15) onto the ϕ–plane is unchanged in length since it is parallel to the ϕ–plane and is also consistent with (3.9.24) with $\phi = \pi/2$ up to a scaling factor of P. The projection of $BD = a + BC$ onto the ϕ–plane has the length $\left(\mu L + L(2HP^2 + \mu^2)^{\frac{1}{2}}\right)/(-2HP)$ which agrees up to a scaling factor of P with equation (3.9.24) with $\phi = \pi$.

Alternatively, an elegant vector combination can be used to calculate the plane polar equation of the orbit in the orbital plane. Following the procedure adopted in the $\mu = J$ case, we construct a vector $\boldsymbol{R}$ which lies in the orbital plane and is thus parallel to $\boldsymbol{S}$. One suitable vector is

$$\begin{aligned} \boldsymbol{R} &= \boldsymbol{r} - \frac{|\boldsymbol{r}\cdot\hat{\boldsymbol{N}}|}{|\boldsymbol{J}\cdot\hat{\boldsymbol{N}}|}\boldsymbol{J} \\ &= \boldsymbol{r} - \frac{J}{2H}\hat{\boldsymbol{J}}. \end{aligned} \tag{3.9.31}$$

Note that all the required scalar quantities are easily constructed using scalar products on combinations of the conserved vectors. The vector $\boldsymbol{R}$ moves in the orbital plane normal to $\boldsymbol{N}$ and is displaced from the origin by $\boldsymbol{J}/2H$. Measuring the angle ϑ which lies in the orbital plane from $\boldsymbol{S}$ gives rise to the equation for the orbit in the orbital plane. Although the origin of $\boldsymbol{S}$ is located at the apex of the cone whilst $\boldsymbol{R}$ has its origin at the intersection of $\boldsymbol{J}$ and the plane of the orbit, the scalar product of $\boldsymbol{S}$ and $\boldsymbol{R}$ still gives rise to the orbit equation. This is because the scalar product between $\boldsymbol{R}$ and a combination of $\boldsymbol{S}$ and an offset $d\boldsymbol{S}$ added or subtracted to $\boldsymbol{S}$ in order to produce a vector which is parallel to $\boldsymbol{S}$ but originating from the same point as $\boldsymbol{R}$, i.e $(1 \pm d)\boldsymbol{S}\cdot\boldsymbol{R} = (1 \pm d)SR\cos\vartheta$ can be scaled throughout by $1 \pm d$. Taking the scalar product of $\boldsymbol{S}$ and $\boldsymbol{R}$ gives

$$\boldsymbol{S}\cdot\boldsymbol{R} = SR\cos\vartheta = \frac{1}{4\lambda H^2}(2H\lambda^2 + \mu^2)(-2Hr - \mu). \tag{3.9.32}$$

Rearranging the expression (3.9.31) to obtain $\boldsymbol{r}$ as the subject of the equation and squaring both sides of the expression produce a quadratic equation in r which can be solved to give

$$r = \frac{\mu}{-2H} + \left(R^2 + \frac{L^2}{2H}\right)^{\frac{1}{2}}. \tag{3.9.33}$$

Note that, when $R = b = L/(-2H)^{\frac{1}{2}}$ (the minimum allowed value), $r = \mu/(-2H)$ which is consistent with the result for OQ (3.9.49). Now substituting (3.9.33) in (3.9.32) we finally obtain

$$R^2 = \frac{\frac{L^2}{-H}}{\left(\left(2 - \frac{2HP^2+\mu^2}{2H\lambda^2+\mu^2}\right) - \frac{2HP^2+\mu^2}{2H\lambda^2+\mu^2}\cos 2\vartheta\right)}, \tag{3.9.34}$$

which is the plane polar expression for a geometric–centred ellipse (P2.16) symmetrically placed about the $\vartheta = 0$ axis, with eccentricity of $(2HP^2 + \mu^2)^{\frac{1}{2}}/(2H\lambda^2 + \mu^2)^{\frac{1}{2}}$, with semi–minor axis length $L/(-2H)^{\frac{1}{2}}$ and semi–major axis length $(2H\lambda^2 + \mu^2)^{\frac{1}{2}}/(-2H)$ which are consistent with (3.9.16), (3.9.28) and (3.9.7) respectively. The distance from the origin to a focus $(2HP^2 + \mu^2)^{\frac{1}{2}}/(-2H)$ agrees with the length CF (3.9.17) and also the distance ae which confirms that the origin is in the centre of the ellipse. Since the plane polar equation describes a geometric–centred ellipse on the orbital plane, it follows that C marks the centre of the ellipse in the plane and correspondingly $AC = CD$ which is the same result as obtained using geometric considerations (*cf.* (3.9.5)).

The velocity hodograph can be obtained by differentiating the cartesian components x, y and z (3.9.18) and substituting $\dot{\phi} = -L/(r^2 \sin\alpha)$ to give

$$\begin{aligned}
\dot{x} &= \frac{L}{OB}\cos\alpha\sin\phi \\
\dot{y} &= -\frac{L}{OB}\cos\alpha\cos\phi - \frac{L}{OB}\cot\gamma\sin\alpha \\
\dot{z} &= -\frac{L}{OB}\cos\alpha\cot\gamma\sin\phi.
\end{aligned} \tag{3.9.35}$$

Since the velocity hodograph lies on a plane, it is convenient to rotate the plane counter–clockwise through $(\pi/2 - \gamma)$ radians about the $\dot{y}$ axis to manipulate the parametric equations into a recognisable form. The rotation matrix is given by (3.8.8) with α replaced by γ. Premultiplying the row vector formed from (3.9.35) by $\boldsymbol{Q}$ (3.8.8) gives the parametric equations of the velocity hodograph rotated into the plane

$$\begin{aligned}
\dot{X} &= \frac{L}{OB}\frac{\cos\alpha}{\sin\gamma}\sin\phi \\
\dot{Y} &= -\frac{L}{OB}\cos\alpha\cos\phi - \frac{L}{OB}\cot\gamma\sin\alpha \\
\dot{Z} &= 0,
\end{aligned} \tag{3.9.36}$$

which can be manipulated into the standard cartesian representation for an ellipse (P2.17) using (3.9.13) and (3.6.1)

$$\left(\frac{\dot{X}}{\frac{(2H\lambda^2+\mu^2)^{\frac{1}{2}}}{P}}\right)^2+\left(\frac{\dot{Y}+\frac{L}{P^2}(2HP^2+\mu^2)^{\frac{1}{2}}}{\frac{\mu L}{P^2}}\right)^2=1, \tag{3.9.37}$$

symmetrically placed about the $\dot{X}=0$ axis, with semi–major and semi–minor axes of lengths $a=(2H\lambda^2+\mu^2)^{\frac{1}{2}}/P$ and $b=\mu L/P^2$ respectively, eccentricity of $\lambda\left(2HP^2+\mu^2\right)^{\frac{1}{2}}/\left(P(2H\lambda^2+\mu^2)^{\frac{1}{2}}\right)$ and centred at $\left(0,-L(2HP^2+\mu^2)^{\frac{1}{2}}/P^2\right)$. This result is as expected from the projection of the velocity hodograph into the plane. The corresponding Kepler problem has a circular velocity hodograph in the plane with radius $\mu L/P^2$ and centre $\left(0,-L(2HP^2+\mu^2)^{\frac{1}{2}}/P^2\right)$ from (3.6.30) and (3.6.29) when $\boldsymbol{P}$ is directed along the $-\boldsymbol{k}$ direction and viewed from above. Consequently, it is to be expected that the semi–major axis length of the ellipse described above has the same length as the radius of the Kepler velocity hodograph when projected into the plane, *i.e.* $a\sin\gamma=\mu L/P^2$. However, the semi–minor axis length which has the same length as the radius of the velocity hodograph does not change in length on projection into the $\phi-$plane since it is parallel to the $\phi-$plane. The centre of the ellipse rotated into the $\phi-$plane also marks the centre of the circle at $\left(0,-L(2HP^2+\mu^2)^{\frac{1}{2}}/P^2\right)$ because the $\dot{y}-$axis about which the rotation takes place passes through the centre of the ellipse on the hodographic plane. As with the Kepler velocity hodograph, the MICZ velocity hodograph is closed. The origin similarly lies within the circumference of the hodographic ellipse.

It does not seem possible to calculate the plane polar equation of the velocity hodograph on the plane using simple vector operations as was done for the orbit.

We are now in a position to describe the analogues for Kepler's three laws of motion on the cone (see Bates [6] for a different approach using differential geometry) :–

(i) For negative energy the orbit is elliptical. However, the origin is not coplanar with the ellipse.

(ii) Equal areas are swept out on the cone in equal times. The proof of this is quite simple. The element of area on the cone is given by (denoting the quantities on the cone with the subscript MK and those in the plane with $\perp MK$)

$$\mathrm{d}\mathbf{A_{MK}}=\frac{1}{2}\boldsymbol{r}\times\dot{\boldsymbol{r}}\,\mathrm{d}t, \tag{3.9.38}$$

and so

$$\frac{\mathrm{d}A_{MK}}{\mathrm{d}t} = \frac{1}{2}L \tag{3.9.39}$$

and, since L is constant, $\dfrac{\mathrm{d}A_{MK}}{\mathrm{d}t}$ is constant. Note that for the ellipse on the $\phi-$plane

$$\frac{\mathrm{d}A_{\perp MK}}{\mathrm{d}t} = \frac{1}{2}\left|(\boldsymbol{r}\times\boldsymbol{P})\times(\dot{\boldsymbol{r}}\times\boldsymbol{P})\right| = \frac{1}{2}L^2P. \tag{3.9.40}$$

Note that the constant of proportionality has changed. Upon dividing (3.9.40) by P^2, since we are dealing with an area, it is clear that the rate of increase in area on the cone is larger than on the projected ellipse by the factor $P/L = 1/\sin\alpha > 1$.

The surface area extending from the base of the orbital cone to the line of the orbit is found by integrating (3.9.39) over the period of the motion which gives

$$A_{MK} = \frac{1}{2}\int_0^{2\pi} r^2 \sin\alpha\dot{\phi}\,\mathrm{d}t. \tag{3.9.41}$$

Substituting for r^2 from (3.6.14) we can express the integrand in terms of ϕ and obtain

$$A_{MK} = \frac{OB^2\tan^2\gamma}{2\sin\alpha}\int_0^{2\pi}\frac{\mathrm{d}\phi}{(\cot\alpha\tan\gamma+\cos\phi)^2}. \tag{3.9.42}$$

Using G&R[43, 2.554.3 with n=2], the expression for the area becomes

$$A_{MK} = \frac{OB^2\cot\alpha\tan^3\gamma}{2\sin\alpha(\cot^2\alpha\tan^2\gamma-1)}\int_0^{2\pi}\frac{\mathrm{d}\phi}{\cot\alpha\tan\gamma+\cos\phi}. \tag{3.9.43}$$

From G&R[43, 3.661.4] we see that

$$\int_0^{2\pi}\frac{\mathrm{d}x}{a+b\cos x} = \frac{2\pi}{(a^2-b^2)^{\frac{1}{2}}}P_0\left(\frac{a}{(a^2-b^2)^{\frac{1}{2}}}\right),\ a>|b|, \tag{3.9.44}$$

where P_0 is the zeroth Legendre polynomial and hence (3.9.43) can be reduced to

$$A_{MK} = \frac{OB^2\cot\alpha\tan^3\gamma}{2\sin\alpha(\cot^2\alpha\tan^2\gamma-1)}\times\frac{2\pi}{(\cot^2\alpha\tan^2\gamma-1)^{\frac{1}{2}}}. \tag{3.9.45}$$

Using (3.9.13) to replace OB, and (3.6.1) and (3.6.9) to replace trigonometric functions of α and γ, equation (3.9.45) can be simplified to give

$$A_{MK} = \frac{\pi\mu L}{(-2H)^{3/2}}. \tag{3.9.46}$$

The area of the ellipse projected in the plane is given by

$$A_{\perp MK} = \frac{\pi a^*b^*}{P^2} = \frac{\pi\mu L^2}{P(-2H)^{3/2}}. \tag{3.9.47}$$

We must now try to express the geometric quantities appearing in the expressions for the surface area in terms of the dynamical parameters. With reference to Figure 3.9.1, if we place a right–handed cartesian coordinate system with origin at O with the triangle OBC lying in the $xz-$plane, the coordinate at the point Q is given by $(-BC\sin\gamma, CQ, BC\cos\gamma + OB)$. The length of OQ is then easily found from

$$OQ^2 = CQ^2 + BC^2 + OB^2 + 2OB.BC\cos\gamma \tag{3.9.48}$$

and after routine maniplation is found to be

$$OQ = \frac{\mu}{-2H}. \tag{3.9.49}$$

The quantity we term R, or 'generalised' semi–major axis, can be expressed as

$$R = \frac{1}{2}\big(OA + OD\big) = \left(\frac{\mu}{-2H}\right). \tag{3.9.50}$$

The expression for the surface area on the cone (3.9.46) can now be written as

$$A_{MK} = \frac{\pi\mu L}{(-2H)^{3/2}} = \frac{1}{2}\pi\big(OA + OD\big)\ CQ = \pi\ OQ.CQ, \tag{3.9.51}$$

and so we observe that the surface area of the section of cone between the origin and the line of the orbit is given by the product of the semi–minor axis length of the ellipse on the cone and the average of the minimum and maximum distances on the orbit from the origin. This is like a 'generalised' semi–major axis, except that the distance is now out of the plane of the ellipse. Indeed the projection of $(OA + OD)$ is exactly twice the length of the semi–major axis of the projected ellipse. The area can also be described by the last term of (3.9.51), which is understandable when one considers the projection of OQ in the $\phi-$plane. The projected length OQ is the distance between the closest point on the ellipse from the geometric centre and the focus. For the planar ellipse this distance is well–known to have the same length as that of the semi–major axis. It is then not surprising that the area can also be expressed in this way.

As expected the ratio of $A_{MK}/A_{\perp MK}$ is again P/L which is the same ratio as we obtained for the areal velocities. Alternatively we can consider an infinitesimal area on the cone stretching from the origin to two closely spaced points on the orbit. If we project this area into the plane, it is clear that the projection is just $\Delta A_{\perp MK} = \Delta A_{MK}\sin\alpha$ which, extended over the complete area in both cases, is the result we obtained previously.

(iii) Equation (3.9.39) can be integrated over one revolution to give an alternate expression for the area,

$$A_{MK} = \frac{1}{2}LT. \tag{3.9.52}$$

Equating (3.9.46) with (3.9.52) gives the analogue of Kepler's third law, *i.e.*,

$$T = \frac{2\pi\mu}{(-2H)^{\frac{3}{2}}} = \frac{2\pi(a^*/L)^{\frac{3}{2}}}{\mu^{\frac{1}{2}}} = \frac{2\pi R^{\frac{3}{2}}}{\mu^{\frac{1}{2}}}, \tag{3.9.53}$$

where $R = (OA + OD)/2$ and a^* is the semi–major axis length of the ellipse projected onto the plane. Thus it is obvious that on the cone, the 'generalised' semi–major axis is half of the maximum and minimum lengths of $\boldsymbol{r}$, just as the semi–major axis is in the ellipse when the focus is in the plane. It is also possible to express (3.9.53) in terms of the semi–minor axis of the ellipse on the cone which has the same length as the semi–minor axis of the projected ellipse after scaling by P. This expression is equivalent for both ellipses, (ignoring the scaling by P)

$$T = 2\pi\mu b^3/L^3. \tag{3.9.54}$$

Bates [6] was only able to express Kepler's third law in terms of the expression involving the energy (the first equation of (3.9.53)) since he did not study the geometry of the orbit.

The values of the constants used to draw Figures 3.9.2 and 3.9.3 were calculated in the same way as was done for the case $\mu = J$, except that $J^* = 0.95$ as was chosen in Chapter 1 for the elliptic Kepler orbits. L was again chosen to be 1.85 and P, λ, μ, α, J and β were calculated using (3.8.24)–(3.8.27), (3.8.29) and (3.8.30).

Figure 3.9.2 shows the elliptic orbit in the case where $\mu > J$. The diagram shows the two right circular orbital and angular momentum cones which extend in opposite directions along the line of $\boldsymbol{P}$ with origin and point of contact at the apices of the two cones. A selection of displacement and corresponding angular momentum vectors has been drawn from the origin to their respective positions on the orbital and angular momentum cones. The orbit is elliptical and lies on a plane which does not include the origin. In order to illustrate the behaviour more clearly, projections of the orbit onto planes parallel to the xy, xz and yz planes are shown, together with projections of the angular momentum curve and the projected images of the cones onto the respective planes. The constant magnitude of the angular momentum is reflected by the angular momentum vectors moving on the surface of a cone which is truncated perpendicular to the axis of symmetry to a height of L^2/P below the origin. The components of the

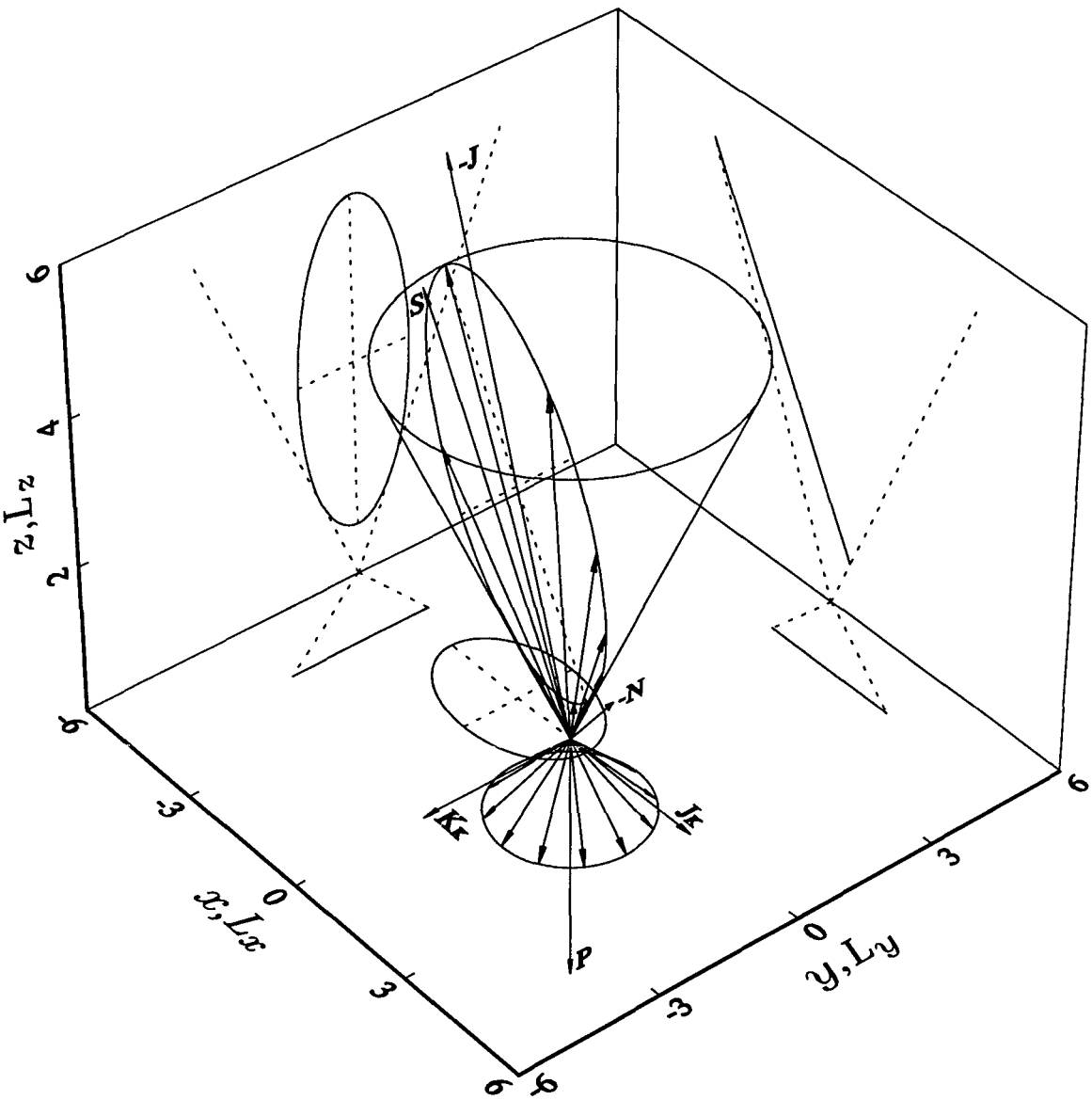

Figure 3.9.2. The elliptical MICZ orbit and angular momentum curve for $\mu > J$ with a selection of displacement and angular momentum vectors drawn from the origin. The radial and angular momentum vectors move on the surfaces of two right circular cones extending in opposite directions along the line of $\boldsymbol{P}$ with origin and point of contact at the apices of the two cones. The projections of the orbit and angular momentum curve onto planes parallel to the xy, xz, yz, L_xL_y, L_xL_z and L_yL_z planes are also shown. The constants have the values $\mu = 7.9145$, $J = 7.4101$, $P = 3.4225$, $\lambda = 2.8794$, $\alpha = 0.5711$, $\beta = 0.4542$ and $L = 1.85$. The origin lies out of the orbital plane.

angular momentum are given by $L = (\lambda L \cos\phi/P, \lambda L \sin\phi/P, -L^2/P)$ using (3.9.18) and (3.9.35).

The xy projection of the orbit is also elliptical as described by the first two equations of (3.9.18) which can be manipulated into the form

$$\left(\frac{x + \frac{L}{-2HP}(2HP^2 + \mu^2)^{\frac{1}{2}}}{\frac{\mu L}{-2HP}}\right)^2 + \left(\frac{y}{\frac{L}{(-2H)^{\frac{1}{2}}}}\right)^2 = 1 \qquad (3.9.55)$$

which is the cartesian representation of (3.9.24) scaled by P, symmetrically placed about the $y = 0$ axis, with semi-major axis length $\mu L/(-2HP)$ (3.9.26) which is the projection of the semi-major axis length a of (3.9.23) onto the $xy-$plane, *i.e.* $a \sin\gamma$, semi-minor axis length $L/(-2H)^{\frac{1}{2}}$ (3.9.28) which is the same length as the semi-minor axis of (3.9.23) since it is parallel to the $xy-$plane, eccentricity of $(2HP^2 + \mu^2)^{\frac{1}{2}}/\mu$ which can be expressed in terms of $c = \cot\gamma$ and $m = \cot\alpha$ as c/m (*cf.* (3.9.16) and (3.9.25)) and centred at $\left(-L(2HP^2 + \mu^2)^{\frac{1}{2}}/(-2HP), 0\right)$ which is the length $-BC \sin\gamma$ and also the distance $-ae$ which confirms that the origin is at a focus. The $y-$intercepts of (3.9.55) which have lengths PL/μ when measured from the origin are consistent with the length of the projection of BE (3.9.15) into the $xy-$plane which is unchanged in length since it lies parallel to the $xy-$plane. It is worth noting that the focus of the ellipse on the cone does not project onto the focus of the ellipse projected into the $xy-$plane in general. The projected orbit is consistent with the planar elliptical Kepler orbit with $L^* = 1$, $\mu^* = 1.25$ and $J^* = 0.95$. As t ranges over one period and choosing the azimuthal angle ϕ to range between π and $-\pi$, the projection ranges from $\left(-PL/(\mu - q), 0\right)$ when $\phi = \pi$ and $q = (2HP^2 + \mu^2)^{\frac{1}{2}}$, to $(0, PL/\mu)$ when $\phi = \pi/2$ to $\left(PL/(\mu + q), 0\right)$ when $\phi = 0$ to $(0, -PL/\mu)$ when $\phi = -\pi/2$ to $\left(-PL/(\mu - q), 0\right)$ when $\phi = -\pi$. The projection of the angular momentum curve onto its corresponding plane describes a circle with radius $\lambda L/P$ symmetrically placed about the L_x-axis, *i.e.* ${L_x}^2 + {L_y}^2 = (\lambda L/P)^2$. As t ranges over one period, the projection ranges from $(-\lambda L/P, 0)$ when $\phi = \pi$ to $(0, \lambda L/P)$ when $\phi = \pi/2$ to $(\lambda L/P, 0)$ when $\phi = 0$ to $(0, -\lambda L/P)$ when $\phi = -\pi/2$ to $(-\lambda L/P, 0)$ when $\phi = -\pi$, *i.e.* the circle is completed. The projection of the angular momentum vectors describes a circle after one revolution of the orbit.

The xz projection shows the images of the orbital and angular momentum cones with dotted lines, together with the projections of the orbit and angular momentum curves. Note that the xz projection of the orbit is obtained by manipulating the first and third equations of (3.9.18) into the form

$$z = -\cot\gamma x + \frac{\lambda P}{\mu}, \quad -\frac{PL}{\mu - q} \leq x \leq \frac{PL}{\mu + q}, \tag{3.9.56}$$

which is the equation of a straight line with slope $-\cot\gamma$ and $z-$intercept $\lambda P/\mu$ in agreement with (3.6.12). The straight-line projection confirms the well-known result that a cone intersected by a plane which is at an angle, γ, to the symmetry axis which is larger than the angle between the sides of the cone and the symmetry axis, but less than $\pi/2$ radians describes an ellipse on the plane. The $z-$intercept is given by the length of OB which is consistent with Figure 3.9.1. The orbit lies on a plane section through the orbital cone. As t ranges over one period, the projection ranges from $\big(-PL/(\mu - q), \lambda P/(\mu - q)\big)$ when $\phi = \pi$, to $(0, \lambda P/\mu)$ when $\phi = \pi/2$ to $\big(PL/(\mu + q), \lambda P/(\mu + q)\big)$ when $\phi = 0$ to $(0, \lambda P/\mu)$ when $\phi = -\pi/2$ to $\big(-PL/(\mu - q), \lambda P/(\mu - q)\big)$ when $\phi = -\pi$. The L_xL_z projection of the angular momentum curve extends along the base of the triangle describing the L_xL_z projection of the image of the angular momentum cone, perpendicular to the L_z-axis. As t ranges over one period, the projection ranges from $(-\lambda L/P, -L^2/P)$ when $\phi = \pi$ to $(0, -L^2/P)$ when $\phi = \pi/2$ to $(\lambda L/P, -L^2/P)$ when $\phi = 0$ to $(0, -L^2/P)$ when $\phi = -\pi/2$ to $(-\lambda L/P, -L^2/P)$ when $\phi = -\pi$, *i.e.* the full length of the base of the angular momentum triangle. In other words the angular momentum vectors will have swept over the entire surface area of the angular momentum cone.

The yz projection shows the images of the orbital and angular momentum cones with dotted lines, together with the projections of the orbit and angular momentum curves. Note that the yz projection of the orbit is obtained by manipulating the second and third equations of (3.9.18) into the form

$$\left(\frac{z - \frac{\lambda\mu}{-2HP}}{\frac{\lambda(2HP^2+\mu^2)^{\frac{1}{2}}}{-2HP}}\right)^2 + \left(\frac{y}{\frac{L}{(-2H)^{\frac{1}{2}}}}\right)^2 = 1 \tag{3.9.57}$$

which is the equation of an ellipse symmetrically placed about the $y = 0$ axis, with semi-major axis length $\lambda(2HP^2 + \mu^2)^{\frac{1}{2}}/(-2HP)$ which is equivalent to the projection of a (3.9.7) onto the $yz-$plane, *i.e.* $a\cos\gamma$, semi-minor axis length $L/(-2H)^{\frac{1}{2}}$ unchanged in length from (3.9.28) since it is parallel to the $yz-$plane, eccentricity of $\big(2HP^4 + \lambda^2\mu^2\big)^{\frac{1}{2}}/\big(\lambda(2HP^2 + \mu^2)^{\frac{1}{2}}\big)$ which can be expressed in terms of $c = \cot\gamma$ and $m = \cot\alpha$ as $\big(c^2(1 + m^2) - m^2\big)^{\frac{1}{2}}/(mc)$ (*cf.* (3.9.16) and (3.9.25)) and centred

at $\left(0, \lambda\mu/(-2HP)\right)$ where the $z-$component is just the projection of OC onto the $yz-$plane, *i.e.* $OC\cos\beta$. The $y-$components of (3.9.57) when $z = OB = \lambda P/\mu$ which have the length PL/μ when measured from B are consistent with the length of the projection of BE (3.9.15) into the yz plane which is unchanged in length since it lies parallel to the $yz-$plane. It is worth noting that the focus of the ellipse on the cone does not project onto the focus of the ellipse projected into the $yz-$plane in general. The relationship between the eccentricity e of the elliptical projection in the $yz-$plane and that of the elliptical projection in the $xy-$plane, e^*, is found to be $e^2 = a^{*2}/a^2(e^{*2} - 1) + 1$ where the superscript $*$ refers to the equivalent quantities in (3.9.55). Note that the semi–minor axis lengths of both projections are not involved in the relationship between the two eccentricities. The relationship between the eccentricity e of the elliptical projection in the $yz-$plane and that of the ellipse on the cone, $e^\dagger$, has the same structure as that shown above, with e^* replaced by $e^\dagger$. As t ranges over one period the projection ranges from $\left(0, \lambda P/(\mu - q)\right)$ when $\phi = \pi$ to $(PL/\mu, \lambda P/\mu)$ when $\phi = \pi/2$ to $\left(0, \lambda P/(\mu + q)\right)$ when $\phi = 0$ to $(-PL/\mu, \lambda P/\mu)$ when $\phi = -\pi/2$ to $\left(0, \lambda P/(\mu - q)\right)$ when $\phi = -\pi$. The L_yL_z projection of the angular momentum curve lies along the base of the triangle describing the L_yL_z projection of the image of the angular momentum cone, perpendicular to the L_z-axis. As t ranges over one period the line segment extends along the full length of the base of the angular momentum triangle from the point $(0, -L^2/P)$ when $\phi = \pi$ to $(\lambda L/P, -L^2/P)$ when $\phi = \pi/2$ to $(0, -L^2/P)$ when $\phi = 0$ to $(-\lambda L/P, -L^2/P)$ when $\phi = -\pi/2$ to $(0, -L^2/P)$ when $\phi = -\pi$. In other words the angular momentum vectors will have swept over the entire surface area of the angular momentum cone.

The conserved vector $\boldsymbol{K}_K$ which has been rotated clockwise through $\pi/2$ radians to lie along the cartesian unit vector $-\boldsymbol{j}$ is given by (3.6.29) and has length $L(2HP^2 + \mu^2)^{\frac{1}{2}}/P$ as shown in Figure 3.9.2. The vector $\boldsymbol{J}_K$, which is perpendicular to $\boldsymbol{K}_K$, is also rotated clockwise through $\pi/2$ radians to lie along the cartesian unit vector $\boldsymbol{i}$. $\boldsymbol{J}_K$ has the length PL^2K_K and is conveniently drawn to the same length as $\boldsymbol{K}_K$ in Figure 3.9.2. The Poincaré vector, $\boldsymbol{P}$, no longer orthogonal to $\boldsymbol{J}$, lies along the cartesian unit vector $-\boldsymbol{k}$. Note that, when the cone is rotated about the $x-$axis so that $\boldsymbol{P}$ lies along $\boldsymbol{k}$, the vectors $\boldsymbol{K}_K$ and $\boldsymbol{J}_K$ lie along the cartesian unit vectors $\boldsymbol{j}$ and $\boldsymbol{i}$ respectively and hence mimic the behaviour of $\boldsymbol{L}$, $\boldsymbol{K}$ and $\boldsymbol{J}$ respectively of the standard Kepler problem. The components of the conserved vectors are found by taking the scalar products of the relevant vectors with $\hat{\boldsymbol{K}}_K$, $\hat{\boldsymbol{J}}_K$ and $-\hat{\boldsymbol{P}}$, remembering that the projected quantities have been rotated clockwise through $\pi/2$ radians to preserve the alignment with the orbit on the cone. The Laplace–Runge–Lenz analogue $\boldsymbol{J}$ is given by (3.5.6) with $\mu > J$ and has components

$\boldsymbol{J} = \left(L(2HP^2+\mu^2)^{\frac{1}{2}}/P, 0, -\lambda\mu/P\right)$. Note that the $x-$component of $\boldsymbol{J}$ is equal in magnitude to $\boldsymbol{K}_K$ from (3.6.29) since the vector product with $\hat{\boldsymbol{P}}$ has the effect of projecting $\boldsymbol{J}$ into the plane followed by a counter–clockwise rotation through $\pi/2$ radians. The Poincaré vector is given by (3.5.4) and has components $\left(0, 0, -(L^2+\lambda^2)^{\frac{1}{2}}\right)$. The normal vector $\boldsymbol{N}$ (3.6.5) is perpendicular to the plane of the orbit and using (3.6.29) and (3.8.24) the components are found to be $(-L^* \cot\gamma, 0, -L^*)$. The vector $\boldsymbol{S}$ (3.6.8) is parallel to the plane of the orbit and using (3.6.29) the components are found to be $\left(\mu L(2HP^2+\mu^2)^{\frac{1}{2}}/(2\lambda HP), 0, -(2HP^2+\mu^2)/(2HP)\right)$.

Figure 3.9.3 shows the elliptical velocity hodograph in the case where $\mu > J$. A selection of velocity vectors corresponding to the displacement vectors shown in Figure 3.9.2 has been drawn from the origin to their respective positions on the velocity hodograph. In order to illustrate the $\dot{\boldsymbol{r}}$ behaviour more clearly, projections of the velocity hodograph onto planes parallel to the $\dot{x}\dot{y}$, $\dot{x}\dot{z}$ and $\dot{y}\dot{z}$ planes are also shown, together with the projected images of the orbital cone onto the respective planes.

The $\dot{x}\dot{y}$ projection of the velocity hodograph is obtained by manipulating the first two equations of (3.9.35) into the form

$$\dot{x}^2 + \left(\dot{y} + \frac{L}{P^2}(2HP^2+\mu^2)^{\frac{1}{2}}\right)^2 = \left(\frac{\mu L}{P^2}\right)^2, \tag{3.9.58}$$

which is the equation of a circle in cartesian coordinates symmetrically placed about the $\dot{x} = 0$ axis, radius $\mu L/P^2$ with origin $\left(0, -L(2HP^2+\mu^2)^{\frac{1}{2}}/P^2\right)$ and is consistent with the planar velocity hodograph for the elliptical Kepler orbit with $L^* = 1$, $\mu = 1.25$ and $J^* = 0.95$ and (3.6.30) reversing the sign inside the $\dot{y}$ term since the velocity hodograph is being viewed with $\boldsymbol{P}$ directed along the $-\boldsymbol{k}$ direction. The semi–major axis length of (3.9.37) projected into the $\dot{x}\dot{y}-$plane reduces to the length of the radius, *i.e.* $a\sin\gamma = \mu L/P^2$, as it should. The semi–minor axis length of (3.9.37) is unchanged in length on projection into the $\dot{x}\dot{y}-$plane because it is parallel to that plane and the location of the origin agrees with that of (3.9.37) because it lies along the $\dot{y}-$axis. As t ranges over one period, the projection ranges from the point $\left(0, L(\mu-q)/P^2\right)$ when $\phi = \pi$ to $(L\mu/P^2, -Lq/P^2)$ when $\phi = \pi/2$ to $\left(0, -L(\mu+q)/P^2\right)$ when $\phi = 0$ to $(-L\mu/P^2, -Lq/P^2)$ when $\phi = -\pi/2$ to $\left(0, L(\mu-q)/P^2\right)$ when $\phi = -\pi$, *i.e.* the circle is completed. The projection of the velocity vectors describes a circle after one revolution of the orbit.

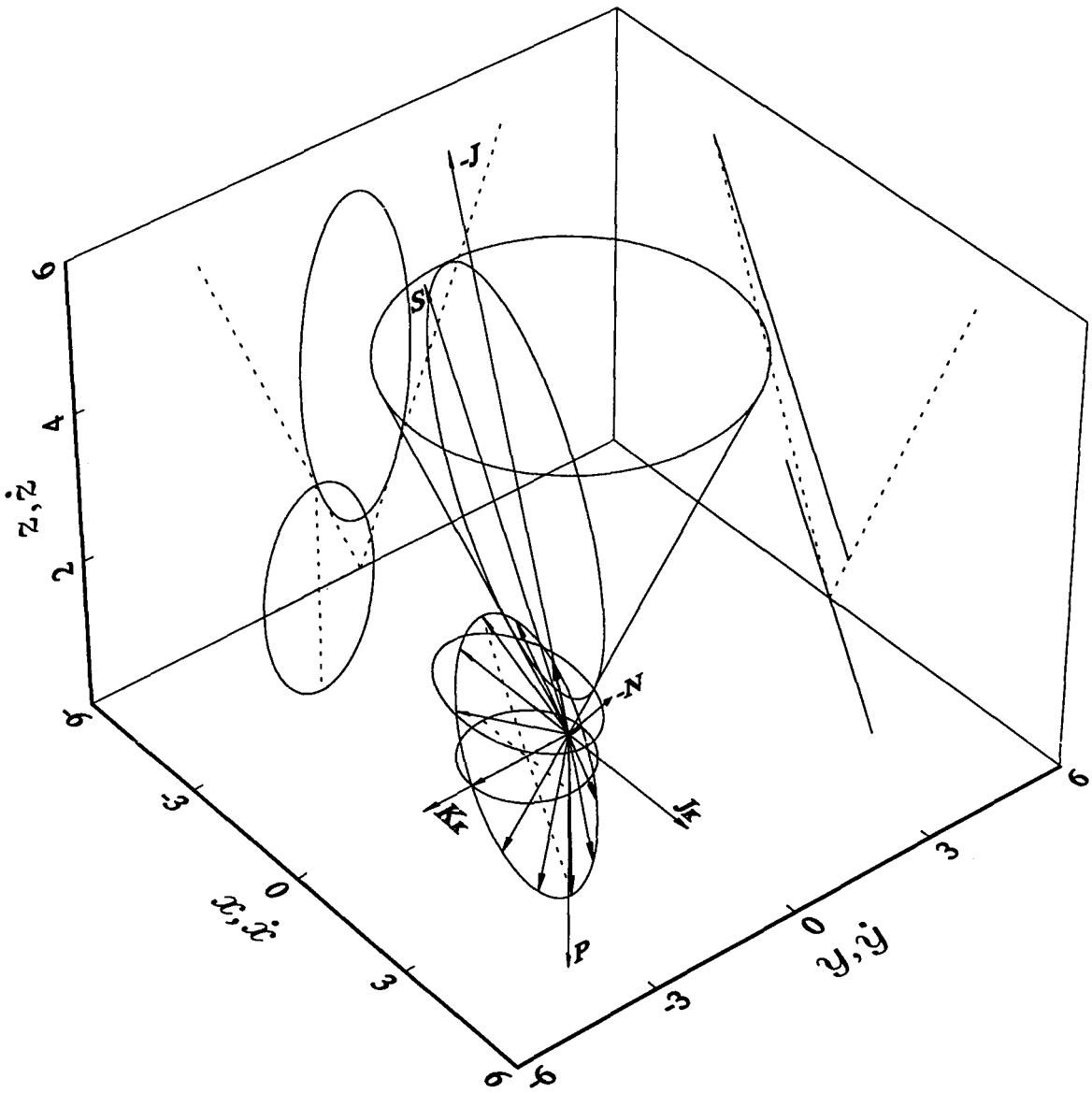

Figure 3.9.3. The elliptical MICZ velocity hodograph and elliptical orbit for $\mu > J$ with a selection of velocity vectors drawn from the origin. The velocity vectors move on a plane which is parallel to the orbital plane and, as t ranges over one period, the heads of the velocity vectors trace out a complete ellipse. The projections of the velocity hodograph and orbit onto planes parallel to the $\dot{x}\dot{y}$, $\dot{x}\dot{z}$, $\dot{y}\dot{z}$, xy, xz and yz planes are also shown. The constants are chosen as for Figure 3.9.2. The origin lies on the hodographic plane inside the circumference of the hodographic ellipse.

The $\dot{x}\dot{z}$ projection shows the images of the orbital cone with dotted lines, together with the respective projections of the orbit and velocity hodograph. Note that the $\dot{x}\dot{z}$ projection of the velocity hodograph is obtained by manipulating the first and third equations of (3.9.35) into the form

$$\dot{z} = -\cot\gamma\dot{x}, \quad |\dot{x}| \leq \frac{\mu L}{P^2}, \tag{3.9.59}$$

which is the equation of a straight line with slope $-\cot\gamma$ which passes through the origin and which is bisected by the $\dot{x}-$axis. The projection of the velocity hodograph is seen to be parallel to the projection of the orbit as was shown in (3.6.6) and (3.6.7). As t ranges over one period, the projection ranges from the point $(0,0)$ when $\phi = \pi$ to $(\mu L/P^2, -\lambda q/P^2)$ when $\phi = \pi/2$ to $(0,0)$ when $\phi = 0$ to $(-\mu L/P^2, \lambda q/P^2)$ when $\phi = -\pi/2$ to $(0,0)$ when $\phi = -\pi$, *i.e.* the length of the projection of the velocity hodograph tends to $2(2H\lambda^2 + \mu^2)^{\frac{1}{2}}/P$.

The $\dot{y}\dot{z}$ projection shows the images of the orbital cone with dotted lines, together with the respective projections of the orbit and velocity hodograph. Note that the $\dot{y}\dot{z}$ projection of the velocity hodograph is obtained by manipulating the second and third equations of (3.9.35) into the form

$$\left(\frac{\dot{y} + \frac{L}{P^2}(2HP^2 + \mu^2)^{\frac{1}{2}}}{\frac{\mu L}{P^2}}\right)^2 + \left(\frac{\dot{z}}{\frac{\lambda}{P^2}(2HP^2 + \mu^2)^{\frac{1}{2}}}\right)^2 = 1, \tag{3.9.60}$$

which is the equation for an ellipse symmetrically placed about the $\dot{z} = 0$ axis, with semi-major axis length $\lambda(2HP^2 + \mu^2)^{\frac{1}{2}}/P^2$ which is just the projection of the semi-major axis of (3.9.37) onto the $\dot{y}\dot{z}-$plane, *i.e.* $a\cos\gamma$, semi-minor axis length $\mu L/P^2$ which is consistent with that of (3.9.37) since it is parallel to the $\dot{y}\dot{z}-$plane, eccentricity of $\left(1-\mu^2L^2/(\lambda^2(2HP^2+\mu^2))\right)^{\frac{1}{2}}$ and centred at $\left(-L(2HP^2+\mu^2)^{\frac{1}{2}}/P^2, 0\right)$ which also agrees with the centre of (3.9.37) which lies along the $\dot{y}-$axis. It is worth noting that the focus of the ellipse on the cone does not project onto the focus of the ellipse projected into the $\dot{y}\dot{z}-$plane in general. As t ranges over one period, the projection ranges from the point $\left(L(\mu-q)/P^2, 0\right)$ when $\phi = \pi$ to $(-Lq/P^2, -\lambda q/P^2)$ when $\phi = \pi/2$ to $\left(-L(\mu+q)/P^2, 0\right)$ when $\phi = 0$ to $(-Lq/P^2, \lambda q/P^2)$ when $\phi = -\pi/2$ to $\left(L(\mu-q)/P^2, 0\right)$ when $\phi = -\pi$, *i.e.* the ellipse is completed. The projection of the velocity vectors describes an ellipse after one revolution of the orbit.

The conserved vectors $\boldsymbol{K}_K$, $\boldsymbol{J}_K$, $\boldsymbol{J}$, $\boldsymbol{P}$, $\boldsymbol{N}$ and $\boldsymbol{S}$ are drawn as in Figure 3.9.2.

Figure 3.9.4 geometrically demonstrates the construction of $\boldsymbol{L}$ corresponding with Figures 3.9.2 and 3.9.3. The parallelograms which represent the magnitude of $\boldsymbol{L} = \boldsymbol{r} \times \dot{\boldsymbol{r}}$ have equal areas as a consequence of L being conserved. In this case the parallelograms are no longer confined to the same plane as was the case with the Kepler problem (see Figure 1.5.5). The orbital cone is shown together with the orbit, velocity hodograph and the xz and yz projections of the orbit, velocity hodograph and images of the cone. The dotted line linking opposite vertices divides the parallelogram in two which gives a geometric representation of the constant magnitude of the areal velocity.

Figure 3.9.5 shows both the projected displacements and corresponding projected velocities in the xy and $\dot{x}\dot{y}$ planes at regular time intervals for the MICZ problem. The projections of the displacements and the corresponding velocities both in this diagram and in the following three figures are coincident with those of the standard Kepler problem as shown in Figures 1.5.2, 1.5.5 and 1.5.6 when the cone is rotated about the $x-$axis so that $\boldsymbol{P}$ lies along $\boldsymbol{k}$ and the vectors $\boldsymbol{K}_K$ and $\boldsymbol{J}_K$ lie along the cartesian unit vectors $\boldsymbol{j}$ and $\boldsymbol{i}$ respectively and hence mimic the behaviour of $\boldsymbol{L}$, $\boldsymbol{K}$ and $\boldsymbol{J}$ respectively of the standard Kepler problem, on account of the choice of constants as described earlier in §3.8. The shaded regions confirm Kepler's second law in the plane that equal areas are swept out in equal times. This result also extends to the cone where equal areas are swept out on the surface of the cone in equal times. However, the area swept out on the cone is larger than that swept out in the plane by the factor P/L. It should be obvious that the initial phase difference between the projected displacement and projected velocity vectors in the xy and $\dot{x}\dot{y}$ planes is $\pi/2$ radians as the projected displacement lies along the $+x-$axis at $t = 0$ while the projected velocity is purely along the $+\dot{y}-$axis. The phase difference in general between the projected displacement and projected velocity vectors is not constant as with the Kepler problem since $(\boldsymbol{r} \times \boldsymbol{P}) \cdot (\dot{\boldsymbol{r}} \times \boldsymbol{P}) = L^2 r\dot{r}$ which is nonzero except when $\dot{r} = 0$, *i.e.* at the extremities of the motion. This is also evident by comparing the angle between the corresponding projected displacement and projected velocity vectors for a range of time intervals using the solid round time markers on the projected orbit and the corresponding solid square time markers on the projected velocity hodograph and counting the number of round markers from the rightmost vertex of the ellipse in a counter–clockwise direction to the projected displacement of interest and then counting off the same number of square markers on the projected velocity hodograph starting from the square marker at the top of the projected velocity hodograph (since at t=0 the projected velocity is purely along the $+\dot{y}-$axis) in a counter–clockwise direction to obtain the corresponding projected velocity or *vice versa*. Note, how-

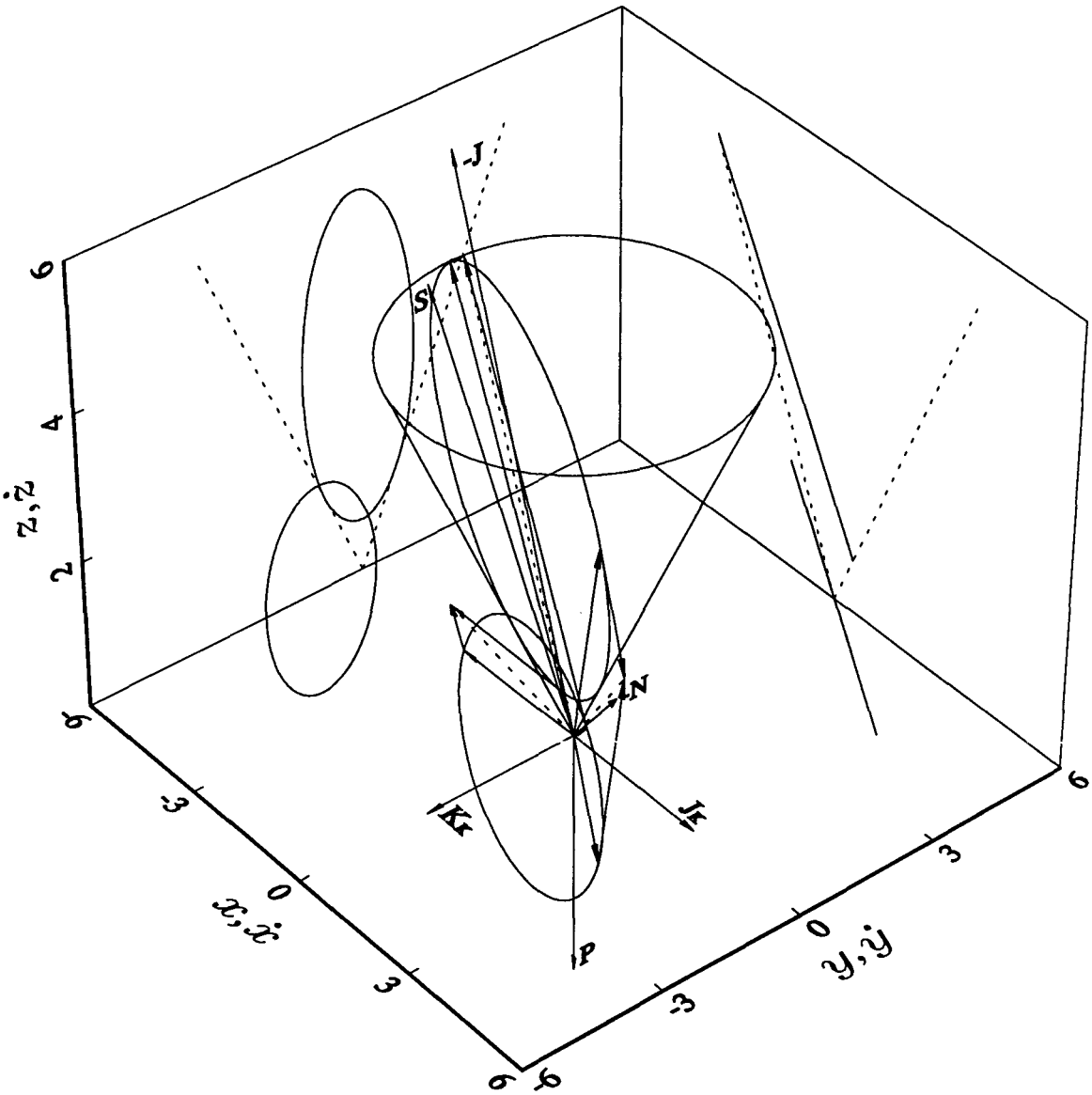

Figure 3.9.4. The elliptical MICZ orbit with its corresponding velocity hodograph associated with Figures 3.9.2 and 3.9.3 demonstrating the construction of $\boldsymbol{L}$. The area of the parallelograms which are now no longer confined to a plane is equal to the constant magnitude of $\boldsymbol{L}$. The orbital cone is shown together with the orbit, velocity hodograph and the projection of the orbit, velocity hodograph and images of the cone onto planes parallel to the xy, xz, yz, $\dot{x}\dot{y}$, $\dot{x}\dot{z}$ and $\dot{y}\dot{z}$ planes. The dotted lines linking opposite vertices divide the parallelograms in two and give a geometric representation of the constant areal velocity. The constants are chosen as for Figure 3.9.2.

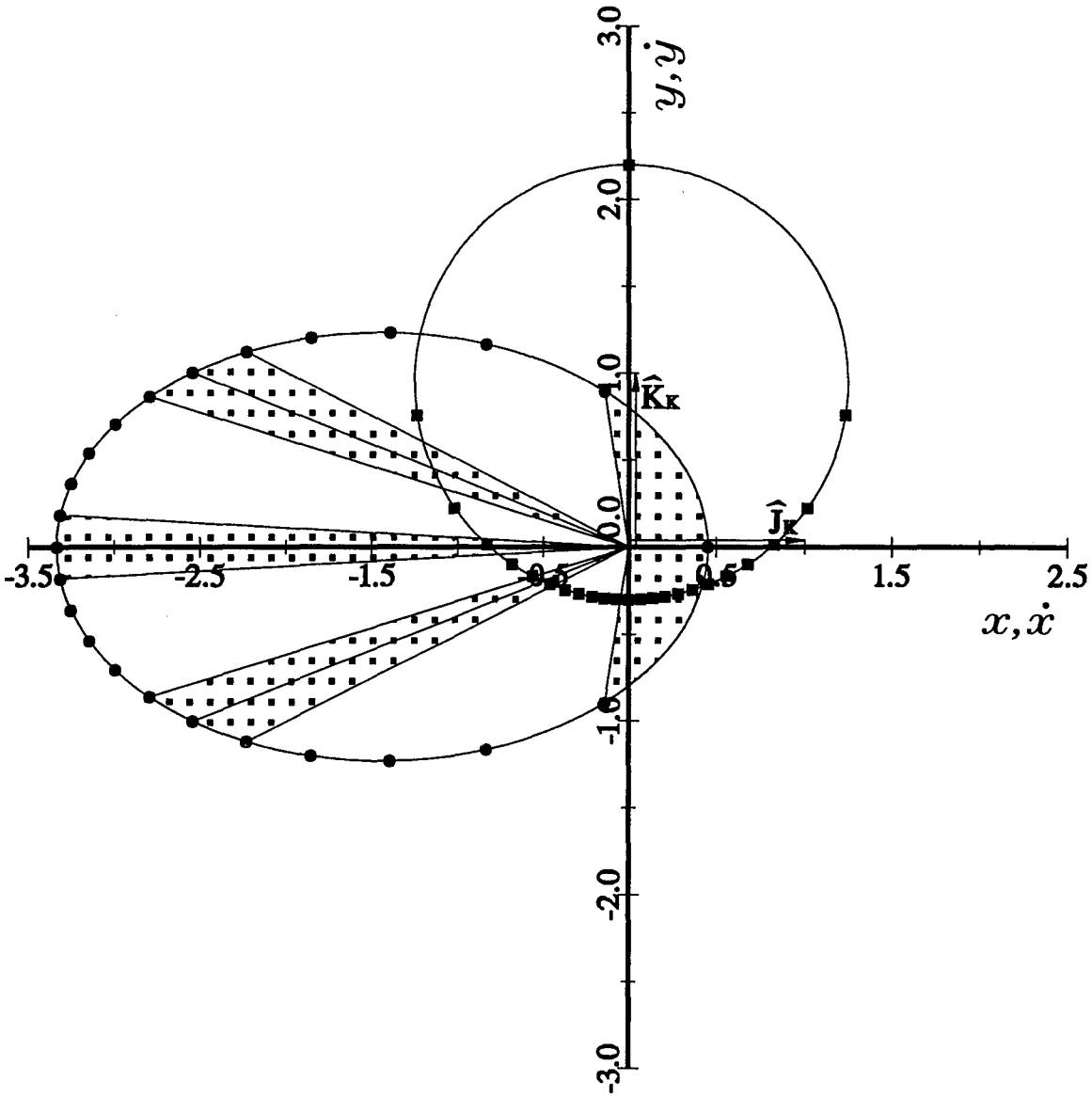

Figure 3.9.5. The projection of the MICZ orbit and corresponding velocity hodograph into the xy and $\dot{x}\dot{y}$ planes. The circles (-•-•-•-) show the projected displacements of the particle at the time intervals $iT/24$, $i = 0, \ldots, 24$ and the squares (-■-■-■-) give the corresponding projected velocities. The phase difference between the projected velocity and displacement vectors is not constant although it is a constant $\pi/2$ radians between the projected displacement vector and the vector directed from the centre of the projected velocity hodograph to the head of the corresponding projected velocity vector. The constants are chosen as for Figure 3.9.2.

ever, that the phase difference between the projection of the radial vector into the $xy-$plane, $\boldsymbol{r} \times \boldsymbol{P}$, and the vector directed from the head of the Hamilton vector $\boldsymbol{K}_K$ (the geometric centre of the elliptical velocity hodograph scaled by P) to the head of the projection of the velocity vector into the $\dot{x}\dot{y}-$plane, $\dot{\boldsymbol{r}} \times \boldsymbol{P}$, *i.e.* $(\dot{\boldsymbol{r}} \times \boldsymbol{P}) - \boldsymbol{K}_K$, is a constant $\pi/2$ radians since $(\boldsymbol{r} \times \boldsymbol{P}) \cdot \left((\dot{\boldsymbol{r}} \times \boldsymbol{P}) - \boldsymbol{K}_K\right) = 0$ which is as expected from the behaviour of the Kepler problem (see §1.5). It should also be noted that the displacement on the cone directed from the point B to the head of the vector $\boldsymbol{r}$, *i.e.* $\boldsymbol{r} + OB\hat{\boldsymbol{P}}$, does not move in phase with the corresponding velocity vector on the hodographic plane directed from the head of the scaled Hamilton vector $\boldsymbol{K}_K/P$ (the geometric centre of the elliptical velocity hodograph) to the head of the vector $\dot{\boldsymbol{r}}$, *i.e.* $\dot{\boldsymbol{r}} + K_K \widehat{\boldsymbol{J} \times \boldsymbol{P}}/P$, since $(\boldsymbol{r} + OB\hat{\boldsymbol{P}}) \cdot (\dot{\boldsymbol{r}} + K_K \widehat{\boldsymbol{J} \times \boldsymbol{P}}/P) = \lambda^2 r\dot{r}/P^2 - \lambda^2 \dot{r}/\mu$ which is nonzero except when $\dot{r} = 0$, *i.e.* at the extremities of the motion. This behaviour is also evident on superimposing the combined hodographic plots shown in Figure 3.9.7 with the combined displacement plots shown in Figure 3.9.6 and translating the combined hodographic plots so that the common geometric centre of both velocity hodographs is coincident with the origin of the displacement plots. Since the corresponding displacements on the orbital cone and velocities on the hodographic plane described above have been rotated into the plane about the $y, \dot{y}-$axis, they lie in the same horizontal line as those in the xy, $\dot{x}\dot{y}$ projections and as a result it can be seen that by horizontally stretching the corresponding displacement and velocity vectors of the projected problem until the respective points on the unprojected problem the angle between the corresponding displacement and velocity vectors is no longer constant at $\pi/2$ radians which qualitatively confirms the result shown above. Alternatively, if in addition to the translation and superposition described above, the velocity hodograph plots are rotated clockwise through $\pi/2$ radians about their common geometric centre, it is apparent that the corresponding projected displacements, projected velocities and the origin are collinear which demonstrates the constant $\pi/2$ phase difference, but this is not the case for the corresponding quantities on the cone which have been rotated into the plane. In summary, the phase difference between $\boldsymbol{r}$ and $\dot{\boldsymbol{r}}$ is not constant in the MICZ problem which is also the case between $\boldsymbol{r} \times \boldsymbol{P}$ and $\dot{\boldsymbol{r}} \times \boldsymbol{P}$ for the projected quantities of the MICZ problem, but the phase difference between $\boldsymbol{r} \times \boldsymbol{P}$ and $\boldsymbol{r} \times \boldsymbol{P} - \boldsymbol{K}_K$ is constant at $\pi/2$ radians or, in other words, the projection of the radial vector directed from the origin which is also a focus of the ellipse in the plane moves in phase with an offset projected velocity vector directed from the head of the scaled Hamilton vector (the geometric centre of the elliptical velocity hodograph scaled by P).

Figure 3.9.6 shows both the orbit on the cone which has been translated and then rotated into the $xy-$plane about B as given by (3.9.23) together with the xy projection of the orbit as given by (3.9.55) for purposes of comparison, when the cone is rotated about the $x-$axis so that $\boldsymbol{P}$ lies along $\boldsymbol{k}$ and the vectors $\boldsymbol{K}_K$ and $\boldsymbol{J}_K$ lie along the cartesian unit vectors $\boldsymbol{j}$ and $\boldsymbol{i}$ respectively and hence mimic the behaviour of $\boldsymbol{L}$, $\boldsymbol{K}$ and $\boldsymbol{J}$ respectively of the standard Kepler problem. The circles and squares show the respective displacements of the particle at equal time intervals and would normally be vertically aligned with each other when viewed from above provided the orbital ellipse is in its usual position on the cone. Note that the circles are aligned with the corresponding squares along parallel horizontal lines since the rotation of the orbit is performed about the $y-$axis. Note that the centre of the ellipse projected into the $xy-$plane is a distance $L(2HP^2+\mu^2)^{\frac{1}{2}}/(-2HP)$ or ae along the $x-$axis from the origin which means that the origin marks the focus of the ellipse projected into the $xy-$plane. However, the origin or equivalently the point B does not have the same geometrical significance in the case of the ellipse on the cone since the centre of that ellipse is a distance $(2HP^2+\mu^2)^{\frac{1}{2}}(2H\lambda^2+\mu^2)^{\frac{1}{2}}/(-2H\mu)$ or BC along the $x-$axis from the origin. The semi–major axis of the ellipse on the cone has length $(2H\lambda^2+\mu^2)^{\frac{1}{2}}/(-2H)$ which is scaled by the factor $\sin\gamma$ when projected into the $xy-$plane whilst the semi–minor axes of both ellipses have the same length $L/(-2H)^{\frac{1}{2}}$ since the semi–minor axis of the ellipse on the cone is parallel to the $xy-$plane.

Figure 3.9.7 shows both the velocity hodograph on the hodographic plane which has been rotated into the $\dot{x}\dot{y}-$plane about O as given by (3.9.37) together with the $\dot{x}\dot{y}$ projection of the velocity hodograph as given by (3.9.58) for purposes of comparison, when the cone is rotated about the $x-$axis so that $\boldsymbol{P}$ lies along $\boldsymbol{k}$ and the vectors $\boldsymbol{K}_K$ and $\boldsymbol{J}_K$ lie along the cartesian unit vectors $\boldsymbol{j}$ and $\boldsymbol{i}$ respectively and hence mimic the behaviour of $\boldsymbol{L}$, $\boldsymbol{K}$ and $\boldsymbol{J}$ respectively of the standard Kepler problem. The circles and squares show the respective velocities of the particle at equal time intervals and would normally be vertically aligned with each other when viewed from above provided the hodographic ellipse is in its usual position on the hodographic plane. Note that the circles are aligned with the corresponding squares along parallel horizontal lines since the rotation of the velocity hodograph is performed about the $\dot{y}-$axis. Note that the centre of the hodographic ellipse is a distance $L(2HP^2+\mu^2)^{\frac{1}{2}}/P^2$ or K_K/P along the $\dot{y}-$axis from the origin which is also the case for the circle and so the centres coincide as can be seen by comparing (3.9.37) with (3.9.58). The semi–major axis of the ellipse on the hodographic plane has length $(2H\lambda^2+\mu^2)^{\frac{1}{2}}/P$ which is scaled by the factor $\sin\gamma$ when projected into the $\dot{x}\dot{y}-$plane whilst the semi–minor axis of the

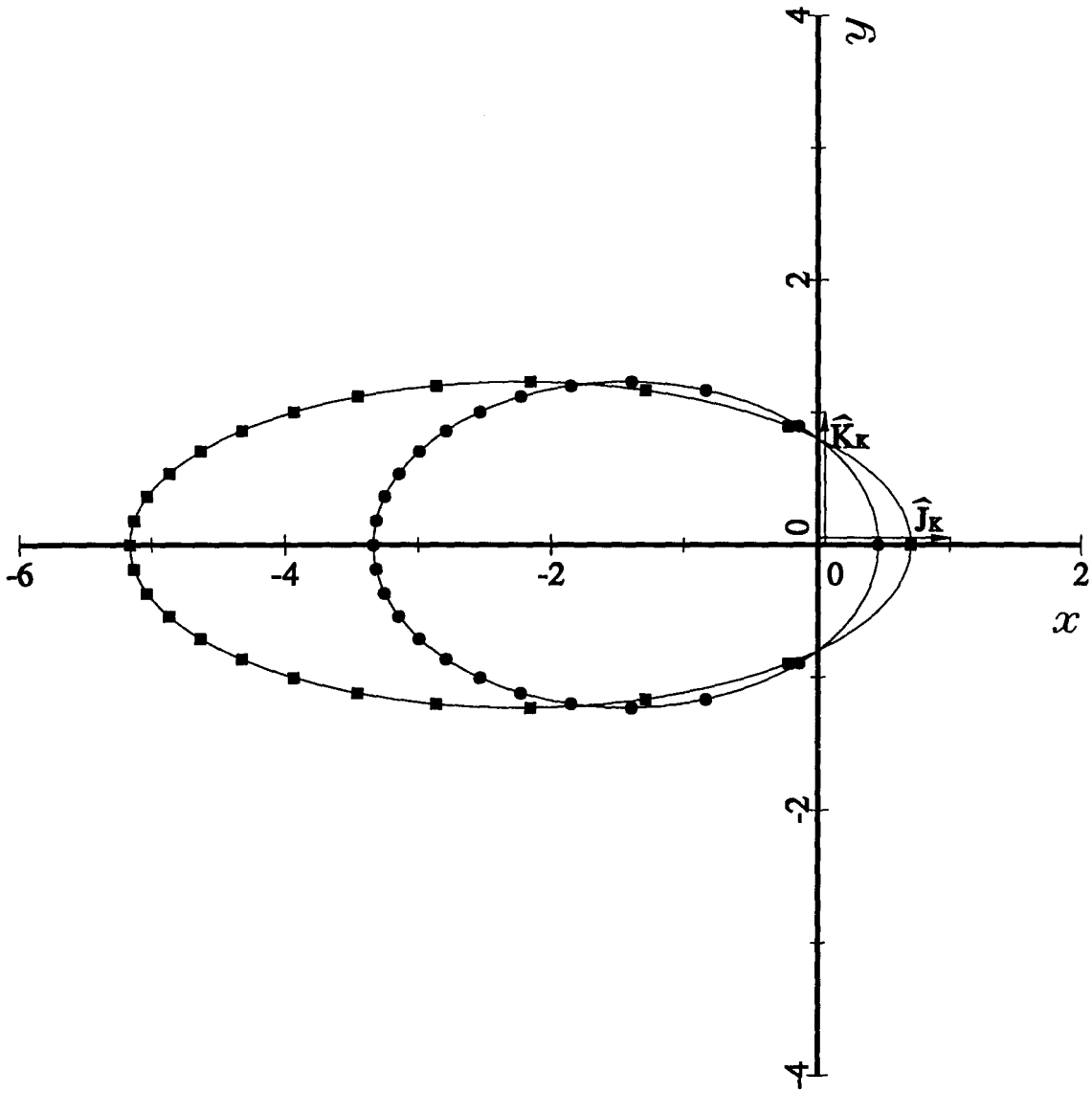

Figure 3.9.6. The elliptical orbit on the cone corresponding with Figure 3.9.2 which has been translated and then rotated into the $xy-$plane together with the xy projection of the orbit. The circles (-●-●-●-) show the projected displacements of the particle at the time intervals $iT/24$, $i = 0, \ldots, 24$ and the squares (-■-■-■-) give the corresponding positions on the orbit on the cone when translated and rotated into the same plane. Note that the circles are aligned with the corresponding squares along parallel horizontal lines since the rotation of the orbit is performed along the $y-$axis. The constants are chosen as for Figure 3.9.2.

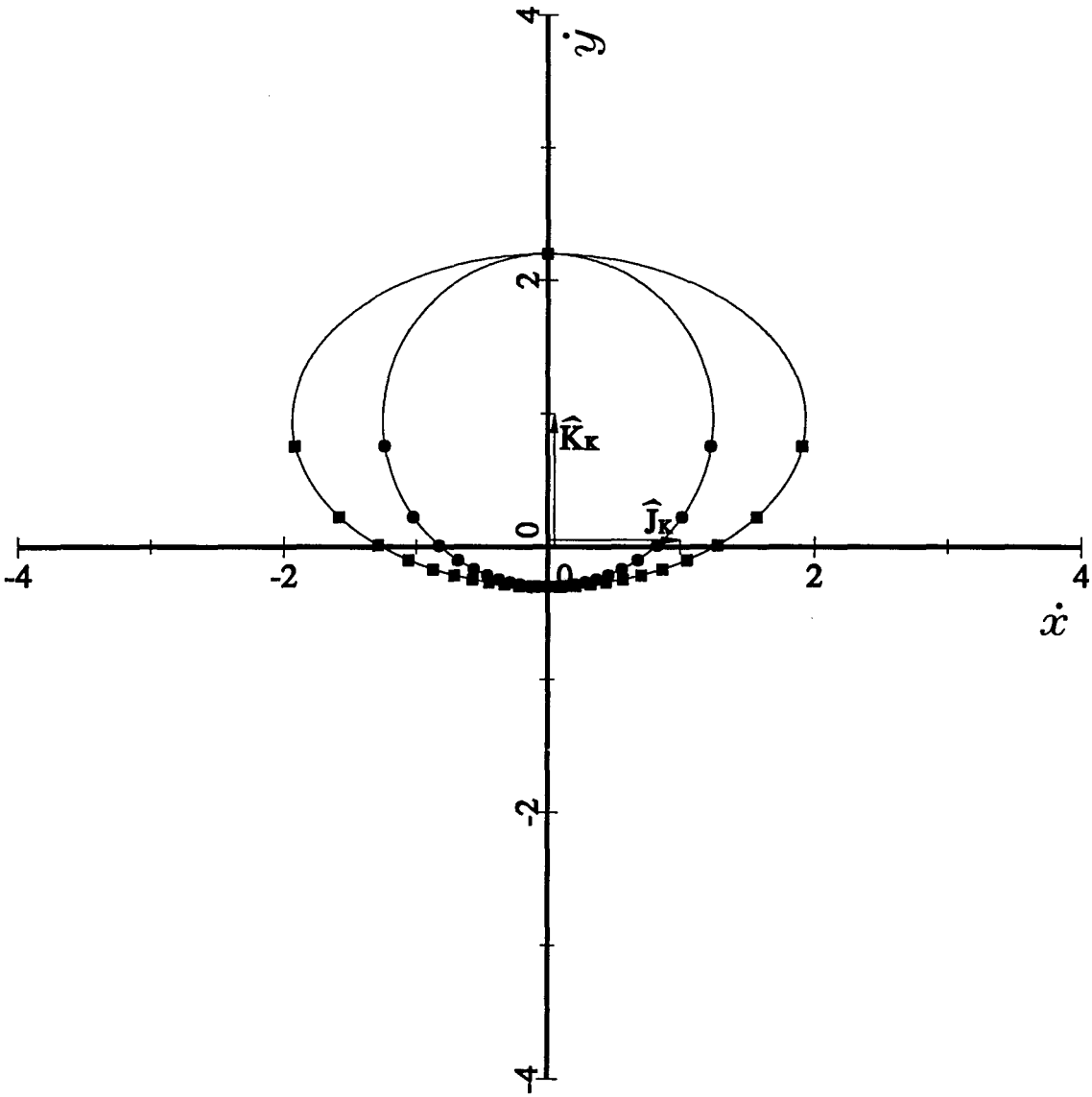

Figure 3.9.7. The elliptical velocity hodograph corresponding with Figure 3.9.3 which has been rotated into the $\dot{x}\dot{y}-$plane together with the $\dot{x}\dot{y}$ projection of the velocity hodograph. The circles (–•–•–•–) show the projected velocities of the particle at the time intervals $iT/24$, $i = 0, \ldots, 24$ and the squares (–■–■–■–) give the corresponding velocities on the hodograph on the hodographic plane when rotated into the same plane. Note that the circles are aligned with the corresponding squares along parallel horizontal lines since the rotation of the velocity hodograph is performed along the $\dot{y}-$axis. The constants are chosen as for Figure 3.9.2.

ellipse has the same length as the radius of the circle $\mu L/P^2$ since the semi–minor axis of the hodographic ellipse is parallel to the $\dot{x}\dot{y}-$plane.

The relationship between the periodic time of the orbit and the length of the generalised semi–major axis is identical to that shown in Figure 1.5.22 for a family of ellipses which have been rotated off the cone and into the plane and have the same dimensions as those shown in Figure 1.5.21. It must be appreciated, however, that R, the generalised semi–major axis, is a factor $1/\sin\alpha$ times larger than the semi–major axis length of the same ellipse projected into the $xy-$plane and that μ is a factor of $(1/\sin\alpha)^3$ (using (3.8.24) and (3.8.26)) times larger than μ^* for the equivalent problem in the plane and as a result the ratio $T = 2\pi R^{\frac{3}{2}}/\mu^{\frac{1}{2}} = 2\pi a^{*\frac{3}{2}}/\mu^{*\frac{1}{2}}$ is form invariant for the choice of initial conditions described in §3.8.

3.10 The Geometry of the MICZ Problem with $\mu < J$

The treatment for the hyperbolic orbit is very similar to that used in the elliptical case, provided we ensure that the orbit is on the top branch of the hyperbola. For motion along the bottom branch the directions of $\boldsymbol{P}$ and $\boldsymbol{J}$ would need to be reversed. From (3.6.3) a hyperbolic orbit exists when $\mu < J$. The salient features of the geometry are depicted in Figure 3.10.1 which shows the orientation of the larger orbital and smaller angular momentum cones which meet at the origin. A typical hyperbolic orbit is shown together with the construction of the Poincaré vector $\boldsymbol{P}$ from $\boldsymbol{L}$ and $\hat{\boldsymbol{r}}$ and the orientation of the vector $\boldsymbol{J}$. Note that $\boldsymbol{L}$ and $\boldsymbol{r}$ are orthogonal throughout the motion and that $\boldsymbol{P}$, $\boldsymbol{L}$ and $\boldsymbol{r}$ are coplanar at any instant in time. The vectors $\boldsymbol{P}$, $\boldsymbol{J}$ and $\boldsymbol{r}$ are only coplanar at the turning points of the motion. The particle is at A when $\psi = \beta + \alpha$ and would be at D if β and α were changed to $\pi - \beta$ and $\pi - \alpha$ respectively giving an effective angle $\psi_e = \beta - \alpha$.

The expressions for OA and OD are as given in (3.9.3). Applying the sine rule to the triangles ACO and DCO, we again find that $AC = DC$ and so the line of $\boldsymbol{J}$ passes through the geometric centre of the double hyperbola. Application of the cosine rule to the triangle ADO leads to

$$a = AC = \frac{(2H\lambda^2 + \mu^2)^{\frac{1}{2}}}{2H}, \tag{3.10.1}$$

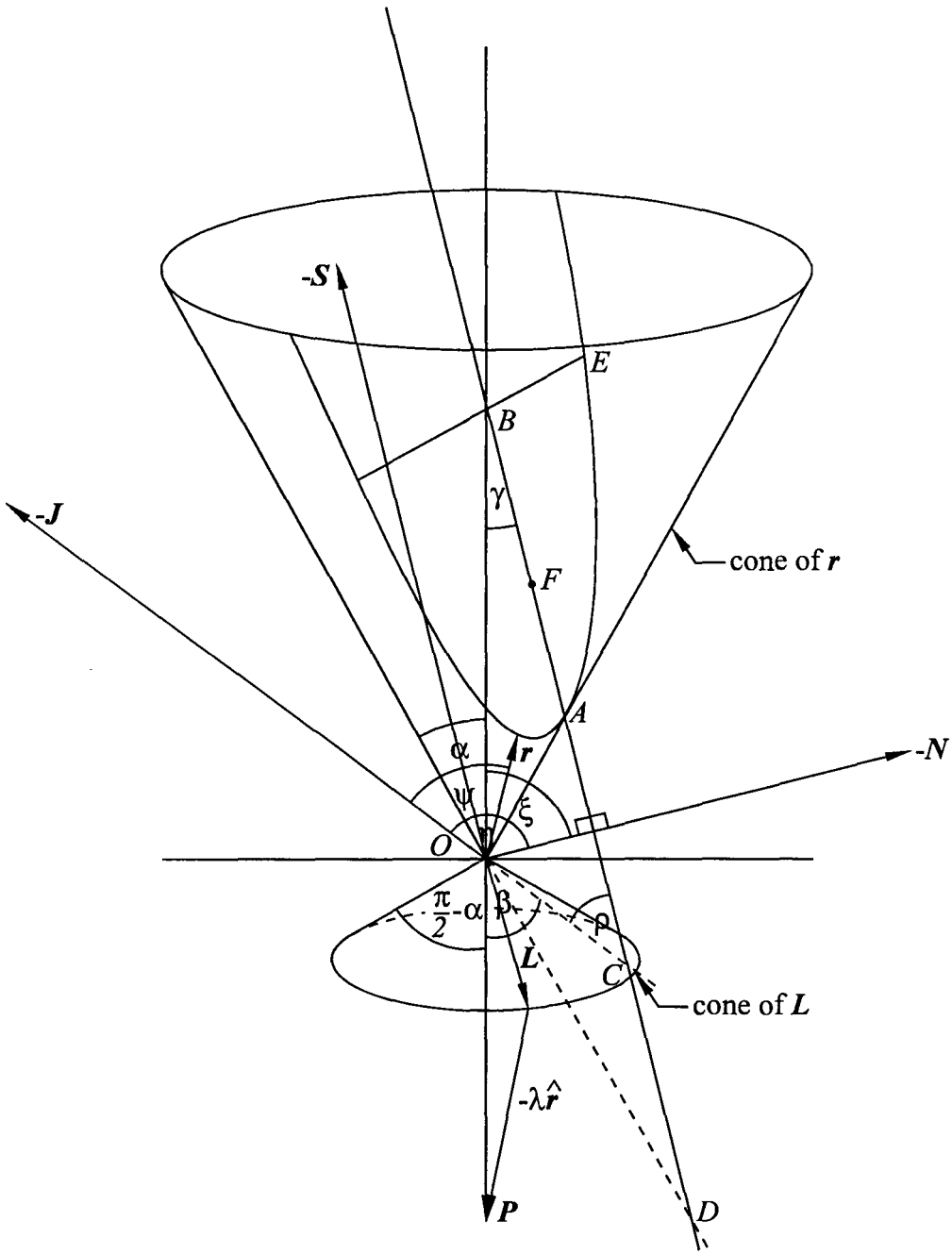

Figure 3.10.1. The typical geometry of the MICZ orbit when $\mu < J$. The larger orbital and smaller angular momentum cones are shown together with a typical hyperbolic orbit and the orientation of $\boldsymbol{P}$, $-\boldsymbol{J}$, $-\boldsymbol{N}$ and $-\boldsymbol{S}$. The origin O is at the point of contact between the two cones, F is the focus of the hyperbola and C marks the geometric centre of the hyperbola. The line segment DB lies along the axis of symmetry of the hyperbola. α and $\pi/2 - \alpha$ are the the semi-vertex angles of the orbital and angular momentum cones respectively, ψ is the angle between $-\boldsymbol{J}$ and $\boldsymbol{r}$, β is between $\boldsymbol{P}$ and $\boldsymbol{J}$, ξ is between $\boldsymbol{P}$ and $\boldsymbol{N}$ and η is between $\boldsymbol{J}$ and $\boldsymbol{N}$.

where the energy is of course positive for hyperbolic motion. In fact it eventuates that the quantities AC, CD, AD, OA, OB, OC, OD, BC, BE, CF and e amongst others are the same for the hyperbola as they are for the ellipse with the exception that explicit occurrences of $-H$ are replaced by H. This even extends to the location of the focus which is still between A and B even though the formulae for BC and CF are the same as their elliptical counterparts. The reason for this is that C is now to the right of B rather than to the left as it was in the elliptical case.

It is possible to rotate the orbital hyperbola on the cone into the plane as was done previously with the elliptical case. For the hyperbolic case we obtain

$$\left(\frac{X-\frac{1}{2H\mu}(2HP^2+\mu^2)^{\frac{1}{2}}(2H\lambda^2+\mu^2)^{\frac{1}{2}}}{\frac{(2H\lambda^2+\mu^2)^{\frac{1}{2}}}{2H}}\right)^2-\left(\frac{Y}{\frac{L}{(2H)^{\frac{1}{2}}}}\right)^2=1 \qquad (3.10.2)$$

which is the standard cartesian representation for a hyperbola (P2.17) symmetrically placed about the $Y=0$ axis, with vertices at $\left((2HP^2+\mu^2)^{\frac{1}{2}}(2H\lambda^2+\mu^2)^{\frac{1}{2}}/(2H\mu)\pm(2H\lambda^2+\mu^2)^{\frac{1}{2}}/2H,0\right)$, foci at $\left((2HP^2+\mu^2)^{\frac{1}{2}}(2H\lambda^2+\mu^2)^{\frac{1}{2}}/(2H\mu)\pm(2HP^2+\mu^2)^{\frac{1}{2}}/2H,0\right)$, eccentricity of $(2HP^2+\mu^2)^{\frac{1}{2}}/(2H\lambda^2+\mu^2)^{\frac{1}{2}}$ which can be expressed in terms of $c=\cot\gamma$ and $m=\cot\alpha$ as $c^2(1+m^2)/(m^2(1+c^2))$ (*cf.* (3.9.16) and (3.9.25)) and centred at $\left((2HP^2+\mu^2)^{\frac{1}{2}}(2H\lambda^2+\mu^2)^{\frac{1}{2}}/(2H\mu),0\right)$. The distance from the centre to a vertex $(2H\lambda^2+\mu^2)^{\frac{1}{2}}/2H$ agrees with the length AC (3.9.7) (with the sign of H reversed) and the distance from the centre to a focus $(2HP^2+\mu^2)^{\frac{1}{2}}/2H$ agrees with the length CF (3.9.17) (with the sign of H reversed). The transverse axis AD (3.9.7) (reversing the sign of H) is the same length as the distance between the vertices $2a$ and the length of the conjugate axis is twice that of b (3.9.28) (with the sign of H reversed). The location of the centre of the hyperbola is consistent with the result for the length BC (3.9.14) (with the sign of H reversed) and the eccentricity is in agreement with (3.9.16). The $Y-$intercepts of (3.10.2) which have lengths PL/μ when measured from the origin are consistent with the length of BE (3.9.15).

If we consider the equation of the orbit in the $\phi-$plane, using (3.6.18) we find that the projected orbit is, mutatis mutandis, the same as for the elliptical case (3.9.24). The projected orbit is also hyperbolic symmetrically placed about the $\phi=0$ axis and the focus is, as for the elliptical case, at the point where $\boldsymbol{P}$ crosses the $\phi-$plane. The eccentricity is also given by (3.9.25). The transverse axis is the same length as the distance between the two vertices $(2a^*/P)$ in (3.9.27) (with the sign of H reversed) and also agrees in length with the projection of the transverse axis of (3.10.2) onto the $\phi-$plane, *i.e.* $2a\sin\gamma$. The length of the conjugate axis is twice that of b^*/P in (3.9.29) (with the sign of H reversed) which is the same length as the conjugate axis

of (3.10.2) since it is parallel to the $\phi-$plane. The projection of AB onto the $\phi-$plane has the length $\left(L(2HP^2+\mu^2)^{\frac{1}{2}}-L\mu\right)/2HP$ which agrees up to a scaling factor of P with equation (3.9.24) with $\phi=0$. The projection of BE (3.9.15) onto the $\phi-$plane is unchanged in length since it is parallel to the $\phi-$plane and is also consistent with (3.9.24) with $\phi=\pi/2$ up to a scaling factor of P.

Alternatively, an elegant vector combination can be used to calculate the plane polar equation of the orbit in the orbital plane. The procedure closely follows that described in the elliptical $\mu > J$ case. The vector $\boldsymbol{R}$ is also given by (3.9.31) without any change of sign. Taking the scalar product of $\boldsymbol{S}$ and $\boldsymbol{R}$ also gives (3.9.32) where r is given by (3.9.33). The plane polar expression for the orbit is given by

$$R^2=\frac{\frac{L^2}{H}}{\left(\left(\frac{2HP^2+\mu^2}{2H\lambda^2+\mu^2}-2\right)+\frac{2HP^2+\mu^2}{2H\lambda^2+\mu^2}\cos 2\vartheta\right)}, \tag{3.10.3}$$

which is the plane polar expression for a geometric–centred hyperbola (P2.16) symmetrically placed about the $\vartheta=0$ axis, eccentricity of $(2HP^2+\mu^2)^{\frac{1}{2}}/(2H\lambda^2+\mu^2)^{\frac{1}{2}}$, vertices at $\left(\pm(2H\lambda^2+\mu^2)^{\frac{1}{2}}/2H,0\right)$ and foci at $\left(\pm(2HP^2+\mu^2)^{\frac{1}{2}}/2H,0\right)$. The eccentricity is consistent with (3.9.16) and the distance from the origin to a vertex $(2H\lambda^2+\mu^2)^{\frac{1}{2}}/2H$ agrees with the length AC (3.9.7) (with the sign of H reversed). Similarly the distance from the origin to a focus $(2HP^2+\mu^2)^{\frac{1}{2}}/2H$ agrees with the length CF (3.9.17) (with the sign of H reversed) and also the distance ae which confirms that the origin is at the centre of the hyperbola. The length of the transverse and conjugate axes are $(2H\lambda^2+\mu^2)^{\frac{1}{2}}/H$ and $2^{\frac{1}{2}}L/H^{\frac{1}{2}}$ which are twice (3.9.7) and (3.9.28) respectively (with the sign of H reversed) as expected. Since the plane polar equation describes a geometric–centred hyperbola on the orbital plane, it follows that C marks the geometric centre of the hyperbola in the plane and correspondingly $AC=CD$ which is the same result obtained using geometric considerations (*cf.* (3.9.5)).

The velocity hodograph can be obtained by rotating the plane of the hyperbola on the cone about the $\dot{y}-$axis in the same way as was done for the elliptical case. For the hyperbolic case we obtain the standard cartesian representation for an ellipse (P2.17)

$$\left(\frac{\dot{X}}{\frac{(2H\lambda^2+\mu^2)^{\frac{1}{2}}}{P}}\right)^2+\left(\frac{\dot{Y}+\frac{L}{P^2}(2HP^2+\mu^2)^{\frac{1}{2}}}{\frac{\mu L}{P^2}}\right)^2=1, \tag{3.10.4}$$

symmetrically placed about the $\dot{X} = 0$ axis, with semi–major and semi–minor axes of lengths $a = (2H\lambda^2 + \mu^2)^{\frac{1}{2}}/P$ and $b = \mu L/P^2$ respectively, eccentricity of $\lambda\big(2HP^2+\mu^2\big)^{\frac{1}{2}}/\big(P(2H\lambda^2+\mu^2)^{\frac{1}{2}}\big)$ and centred at $\big(0, -L(2HP^2+\mu^2)^{\frac{1}{2}}/P^2\big)$. This result is as expected from the projection of the velocity hodograph into the plane. The corresponding Kepler problem has a circular velocity hodograph in the plane with radius $\mu L/P^2$ and centre $\big(0, -L(2HP^2+\mu^2)^{\frac{1}{2}}/P^2\big)$ from (3.6.30) and (3.6.29) when $\boldsymbol{P}$ is directed along the $-\boldsymbol{k}$ direction and viewed from above. Consequently, it is to be expected that the semi–major axis length of the ellipse described above has the same length as the radius of the Kepler velocity hodograph when projected into the plane, *i.e.* $a\sin\gamma = \mu L/P^2$. However, the semi–minor axis length which has the same length as the radius of the velocity hodograph does not change in length on projection into the ϕ–plane since it is parallel to the ϕ–plane. The centre of the ellipse rotated into the ϕ–plane also marks the centre of the circle at $\big(0, -L(2HP^2+\mu^2)^{\frac{1}{2}}/P^2\big)$ because the $\dot{y}$–axis about which the rotation takes place passes through the centre of the ellipse on the hodographic plane. As with the Kepler velocity hodograph, the MICZ velocity hodograph does not close, but is bounded by the image of the asymptotes of the planar Kepler velocity hodograph (translated to the origin) when projected up onto the hodographic plane. The origin similarly lies outside the circumference of the completed hodographic ellipse.

It does not seem possible to calculate the plane polar equation of the velocity hodograph on the plane using simple vector operations as was done for the orbit.

The parametric equations for the asymptotes of the hyperbola on the cone can be found by rotating the parametric equations for the asymptotes of the hyperbola (3.10.2) which we denote $(X, Y, 0)^T$ back onto the cone. Denoting the rotated parametric equations by $(x, y, z)^T$, the equation describing the inverse transformation is

$$\begin{pmatrix} x \\ y \\ z \end{pmatrix} = \boldsymbol{Q}^{-1}\begin{pmatrix} X \\ Y \\ Z \end{pmatrix} + \begin{pmatrix} 0 \\ 0 \\ OB \end{pmatrix}, \tag{3.10.5}$$

where $\alpha = \gamma$ in the matrix $\boldsymbol{Q}$ (3.8.8). The parametric equations can now be written as

$$\begin{pmatrix} x \\ y \\ z \end{pmatrix} = \begin{pmatrix} t \\ \pm\left(\frac{(2H)^{\frac{1}{2}}P}{\mu}t - \frac{L}{(2H)^{\frac{1}{2}}\mu}(2HP^2+\mu^2)^{\frac{1}{2}}\right) \\ -\frac{\lambda}{\mu L}(2HP^2+\mu^2)^{\frac{1}{2}}t + \frac{\lambda P}{\mu} \end{pmatrix}, \tag{3.10.6}$$

where the x and y components given above in (3.10.6) are also the parametric equations for the projection of the asymptotes of the hyperbola on the cone into the $xy-$plane. The x and y components of the limits of extent of the elliptical velocity hodograph on the cone can be obtained by finding the intersection of the cartesian equation for the circular projection of the velocity hodograph in the $xy-$plane given by (3.6.30) and (3.6.29)

$$\dot{x}^2 + \left(\dot{y} + \frac{L}{P^2}(2HP^2 + \mu^2)^{\frac{1}{2}}\right)^2 = \left(\frac{\mu L}{P^2}\right)^2, \tag{3.10.7}$$

and the cartesian equations for the projection of the asymptotes (translated to the origin) which are (using (3.10.6))

$$\dot{y} = \pm\frac{(2H)^{\frac{1}{2}}P}{\mu}\dot{x}. \tag{3.10.8}$$

Substituting for $\dot{y}$ (3.10.8) in (3.10.7) gives

$$\dot{x}_e = \pm\frac{L(2H)^{\frac{1}{2}}\mu}{P(2HP^2 + \mu^2)^{\frac{1}{2}}} \tag{3.10.9}$$

$$\dot{y}_e = -\frac{2HL}{(2HP^2 + \mu^2)^{\frac{1}{2}}} \tag{3.10.10}$$

which are consistent with the expressions obtained in Chapter 1 (see (1.5.12)). The $\dot{z}$ component is obtained from (3.9.35) and can be written as

$$\dot{z}_e = -\cot\gamma\dot{x} = \mp\frac{(2H)^{\frac{1}{2}}\lambda}{P}. \tag{3.10.11}$$

Alternatively the limits of extent can be found from the intersection of the parametric equations for the asymptotes on the cone (3.10.6) (translated to the origin) with the parametric equations for the hodographic ellipse (3.9.35).

The values of the constants used to draw Figures 3.10.2 and 3.10.3 were calculated in the same way as was done for the case $\mu = J$, except that $J^* = 2.25$ as was chosen in Chapter 1 for the hyperbolic Kepler orbits. L was again chosen to be 1.85 and P, λ, μ, α, J and β were calculated using (3.8.24)–(3.8.27), (3.8.29) and (3.8.30).

Figure 3.10.2 shows the hyperbolic orbit in the case where $\mu < J$. The diagram shows the two right circular orbital and angular momentum cones which extend in opposite directions along the line of $\boldsymbol{P}$ with origin and point of contact at the apices of the two cones. A selection of displacement and corresponding angular momentum vectors has been drawn from the origin to their respective positions on

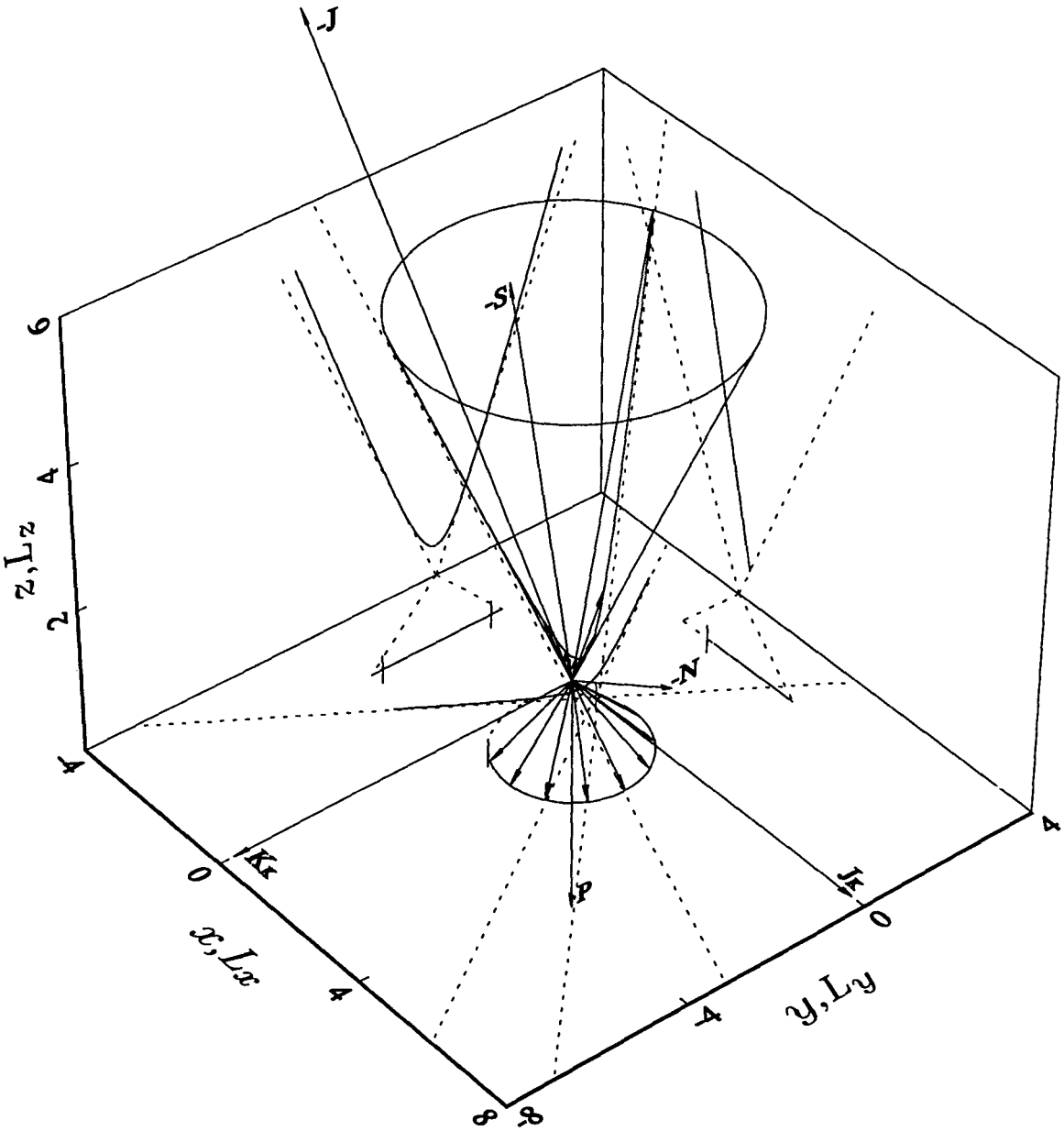

Figure 3.10.2. The hyperbolic MICZ orbit and angular momentum curve for $\mu < J$ with a selection of displacement and angular momentum vectors drawn from the origin. The radial and angular momentum vectors move on the surfaces of two right circular cones extending in opposite directions along the line of $\boldsymbol{P}$ with origin and point of contact at the apices of the two cones. The projections of the orbit and angular momentum curve onto planes parallel to the xy, xz, yz, L_xL_y, L_xL_z and L_yL_z planes are also shown. The constants have the values $\mu = 7.9145$, $J = 10.1802$, $P = 3.4225$, $\lambda = 2.8794$, $\alpha = 0.5711$, $\beta = 0.8578$ and $L = 1.85$. The origin lies out of the orbital plane.

the orbital and angular momentum cones. The orbit is hyperbolic and lies on a plane which does not include the origin. In order to illustrate the behaviour more clearly, projections of the orbit onto planes parallel to the xy, xz and yz planes are shown, together with projections of the angular momentum curve and the projected images of the cones onto the respective planes. The constant magnitude of the angular momentum is reflected by the angular momentum vectors moving on the surface of a cone which is truncated perpendicular to the axis of symmetry to a height of L^2/P below the origin. The components of the angular momentum are given by $L = (\lambda L \cos\phi/P, \lambda L \sin\phi/P, -L^2/P)$ using (3.9.18) and (3.9.35). The two short line segments drawn perpendicular to the angular momentum curve indicate the limits of extent of the angular momentum as t ranges from negative through positive infinity.

The xy projection of the orbit is also hyperbolic as described by the first two equations of (3.9.18) which can be manipulated into the form

$$\left(\frac{x - \frac{L}{2HP}(2HP^2 + \mu^2)^{\frac{1}{2}}}{\frac{\mu L}{2HP}}\right)^2 - \left(\frac{y}{\frac{L}{(2H)^{\frac{1}{2}}}}\right)^2 = 1 \qquad (3.10.12)$$

which is the cartesian representation of (3.9.24) scaled by P, symmetrically placed about the $y = 0$ axis, with vertices at $\big(L(2HP^2 + \mu^2)^{\frac{1}{2}}/(2HP) \pm \mu L/(2HP), 0\big)$, foci at $\big(L(2HP^2 + \mu^2)^{\frac{1}{2}}/(2HP) \pm L(2HP^2 + \mu^2)^{\frac{1}{2}}/(2HP), 0\big)$, *i.e.* one focus is at the origin as expected, eccentricity of $(2HP^2 + \mu^2)^{\frac{1}{2}}/\mu$ which can be expressed in terms of $c = \cot\gamma$ and $m = \cot\alpha$ as c/m (*cf.* (3.9.16) and (3.9.25)) and centred at $\big(L(2HP^2 + \mu^2)^{\frac{1}{2}}/(2HP), 0\big)$. The distance from the centre to a vertex $\mu L/(2HP)$ agrees with the length of the projection of AC onto the $xy-$plane, *i.e.* $AC\sin\gamma$. Similarly the distance from the centre to a focus $L(2HP^2 + \mu^2)^{\frac{1}{2}}/(2HP)$ agrees with the length of the projection of BC onto the $xy-$plane, *i.e.* $BC\sin\gamma$. The transverse axis is the same length as the distance between the two vertices $2a$ and also agrees in length with the projection of the transverse axis of (3.10.2) onto the $xy-$plane, *i.e.* $2a\sin\gamma$. The conjugate axis has the length $2b$, *i.e.* $2^{\frac{1}{2}}L/H^{\frac{1}{2}}$, which is the same length as the conjugate axis of (3.10.2) since it is parallel to the $xy-$plane. The location of the centre of the hyperbola is consistent with the result for the length of the projection of BC (3.9.14) (with the sign of H reversed) into the $xy-$plane, *i.e.* $BC\sin\gamma$, and also the distance ae which confirms that the origin is at a focus. The asymptotes are given by $y = \pm\big((2H)^{\frac{1}{2}}Px/\mu - L(2HP^2 + \mu^2)^{\frac{1}{2}}/((2H)^{\frac{1}{2}}\mu)\big)$, *i.e.* a combination of the first two equations of (3.10.6). The $y-$intercepts of (3.10.12) which have lengths PL/μ when measured from the origin are consistent with the length of the projection of BE (3.9.15) into the $xy-$plane which is unchanged in length since it lies parallel to the $xy-$plane. It is worth noting that the focus of the hyperbola on the cone

does not project onto the focus of the hyperbola projected into the $xy-$plane in general. The projected orbit is consistent with the planar hyperbolic Kepler orbit with $L^* = 1$ and $\mu^* = 1.25$, $J^* = 2.25$. As t ranges from negative through positive infinity, the azimuthal angle ϕ ranges between $\pi - \arccos(1/e^*)$ and $-\pi + \arccos(1/e^*)$, where $e^* = (2HP^2 + \mu^2)^{\frac{1}{2}}/\mu$ and the projection ranges from $(-\infty, +\infty)$ when $\phi = \pi - \arccos(1/e^*)$ to $(0, PL/\mu)$ when $\phi = \pi/2$ to $\big(PL/(\mu+q), 0\big)$ when $\phi = 0$ where $q = (2HP^2 + \mu^2)^{\frac{1}{2}}$ to $(0, -PL/\mu)$ when $\phi = -\pi/2$ to $(-\infty, -\infty)$ when $\phi = -\pi + \arccos(1/e^*)$. The projection of the angular momentum curve onto its corresponding plane describes a circle with radius $\lambda L/P$ symmetrically placed about the L_x-axis, *i.e.* ${L_x}^2 + {L_y}^2 = (\lambda L/P)^2$, $L_x \geq -\lambda L\mu/(Pq)$. As t ranges from negative through positive infinity, the projection ranges from $\big(-\lambda L\mu/(Pq), (2H)^{\frac{1}{2}}\lambda L/q\big)$ when $\phi = \pi - \arccos(1/e^*)$ to $(0, \lambda L/P)$ when $\phi = \pi/2$ to $(\lambda L/P, 0)$ when $\phi = 0$ to $(0, -\lambda L/P)$ when $\phi = -\pi/2$ to $\big(-\lambda L\mu/(Pq), -(2H)^{\frac{1}{2}}\lambda L/q\big)$ when $\phi = -\pi + \arccos(1/e^*)$, *i.e.* the circle is not completed even as t ranges from negative through positive infinity. The dotted line completes the angular momentum cone. However, it should be remembered that the projection of the angular momentum vectors never closes as t ranges from negative through positive infinity.

The xz projection shows the images of the orbital and angular momentum cones with dotted lines, together with the projections of the orbit and angular momentum curves. Note that the xz projection of the orbit is obtained by manipulating the first and third equations of (3.9.18) into the form

$$z = -\cot\gamma x + \frac{\lambda P}{\mu}, \quad -\infty \leq x \leq \frac{PL}{\mu + q}, \tag{3.10.13}$$

which is the equation of a straight line with slope $-\cot\gamma$ and $z-$intercept $\lambda P/\mu$ in agreement with (3.6.12). The straight-line projection confirms the well-known result that a cone intersected by a plane which is at an angle, γ, to the symmetry axis which is smaller than the angle between the sides of the cone and the symmetry axis but larger than zero describes an hyperbola on the plane. The $z-$intercept is given by the length of OB which is consistent with Figure 3.10.1. The orbit lies on a plane section through the orbital cone. As t ranges from negative through positive infinity, the projection ranges from $(-\infty, +\infty)$ when $\phi = \pi - \arccos(1/e^*)$ to $(0, \lambda P/\mu)$ when $\phi = \pi/2$ to $\big(PL/(\mu+q), \lambda P/(\mu+q)\big)$ when $\phi = 0$ to $(0, \lambda P/\mu)$ when $\phi = -\pi/2$ to $(-\infty, +\infty)$ when $\phi = -\pi + \arccos(1/e^*)$. The L_xL_z projection of the angular momentum curve extends along the base of the triangle describing the L_xL_z projection of the image of the angular momentum cone, perpendicular to the L_z-axis. As t ranges from negative through positive infinity, the projection ranges from $\big(-\lambda L\mu/(Pq), -L^2/P\big)$ when $\phi = \pi - \arccos(1/e^*)$ to $(0, -L^2/P)$ when $\phi = \pi/2$ to $(\lambda L/P, -L^2/P)$ when $\phi = 0$ to

$(0, -L^2/P)$ when $\phi = -\pi/2$ to $\left(-\lambda L\mu/(Pq), -L^2/P\right)$ when $\phi = -\pi + \arccos(1/e^*)$, *i.e.* only a section along the length of the base of the angular momentum triangle. In other words the angular momentum vectors will never sweep over the entire surface area of the angular momentum cone even as the time ranges from negative through positive infinity. The short line segment drawn perpendicular to the xz projection of the angular momentum curve indicates the limit of extent of the projection of the angular momentum as t ranges from negative through positive infinity.

The yz projection shows the images of the orbital and angular momentum cones with dotted lines, together with the projections of the orbit and angular momentum curves. Note that the yz projection of the orbit is obtained by manipulating the second and third equations of (3.9.18) into the form

$$\left(\frac{z + \frac{\lambda\mu}{2HP}}{\frac{\lambda(2HP^2+\mu^2)^{\frac{1}{2}}}{2HP}}\right)^2 - \left(\frac{y}{\frac{L}{(2H)^{\frac{1}{2}}}}\right)^2 = 1 \qquad (3.10.14)$$

which is the equation of an hyperbola symmetrically placed about the $y = 0$ axis, with vertices at $\left(0, -\lambda\mu/2HP \pm \lambda(2HP^2 + \mu^2)^{\frac{1}{2}}/2HP\right)$, foci at $\left(0, -\lambda\mu/2HP \pm (2HP^4 + \lambda^2\mu^2)^{\frac{1}{2}}/2HP\right)$, eccentricity of $\left(2HP^4 + \lambda^2\mu^2\right)^{\frac{1}{2}}/\left(\lambda(2HP^2 + \mu^2)^{\frac{1}{2}}\right)$ which can be expressed in terms of $c = \cot\gamma$ and $m = \cot\alpha$ as $\left(c^2(1 + m^2) - m^2\right)^{\frac{1}{2}}/(mc)$ (*cf.* (3.9.16) and (3.9.25)) and centred at $\left(0, -\lambda\mu/(2HP)\right)$. The distance from the centre to a vertex $\lambda(2HP^2 + \mu^2)^{\frac{1}{2}}/2HP$ agrees with the length of the projection of AC onto the $yz-$plane, *i.e.* $AC\cos\gamma$. The transverse axis is the same length as the distance between the two vertices $2a$ and also agrees in length with the projection of the transverse axis of (3.10.2) onto the $yz-$plane, *i.e.* $2a\cos\gamma$. The conjugate axis has the length $2b$, *i.e.* $2^{\frac{1}{2}}L/H^{\frac{1}{2}}$, which is the same length as the conjugate axis of (3.10.2) since it is parallel to the $yz-$plane. The location of the centre of the hyperbola is consistent with the result for the projection of OC (3.9.8) (with the sign of H reversed) onto the $yz-$plane, *i.e.* $OC\cos\beta$. The $y-$components of (3.10.14) when $z = OB = \lambda P/\mu$ which have the length PL/μ when measured from B are consistent with the length of the projection of BE (3.9.15) into the $yz-$plane which is unchanged in length since it lies parallel to the $yz-$plane. The asymptotes are given by $z = \left(\pm\lambda(2HP^2+\mu^2)^{\frac{1}{2}}y/(LP(2H)^{\frac{1}{2}}) - \lambda\mu/(2HP)\right)$ which are clearly not the images of the cone, *i.e.* $z = \pm\cot\alpha y$. It is worth noting that the focus of the hyperbola on the cone does not project onto the focus of the hyperbola projected into the $yz-$plane in general. The relationship between the eccentricity e of the hyperbolic projection in the $yz-$plane and that of the hyperbolic projection in the $xy-$plane, e^*, is found to be $e^2 = a^{*2}/a^2(e^{*2} - 1) + 1$ where the superscript $*$ refers to the

equivalent quantities in (3.10.12). Note that the semi–conjugate axis lengths of both projections are not involved in the relationship between the two eccentricities. The relationship between the eccentricity e of the hyperbolic projection in the $yz-$plane and that of the hyperbola on the cone, $e^{\dagger}$, has the same structure as that shown above, with e^{*} replaced by $e^{\dagger}$. As t ranges from negative through positive infinity, the projection ranges from (∞,∞) when $\phi = \pi - \arccos(1/e^{*})$ to $(PL/\mu, \lambda P/\mu)$ when $\phi = \pi/2$ to $\big(0, \lambda P/(\mu+q)\big)$ when $\phi = 0$ to $(-PL/\mu, \lambda P/\mu)$ when $\phi = -\pi/2$ to $(-\infty,\infty)$ when $\phi = -\pi + \arccos(1/e^{*})$. The L_yL_z projection of the angular momentum curve lies along the base of the triangle describing the L_yL_z projection of the image of the angular momentum cone, perpendicular to the L_z-axis. As t ranges from negative through positive infinity, the line segment extends along the full length of the base of the angular momentum triangle from the point $\big((2H)^{\frac{1}{2}}\lambda L/q, -L^2/P\big)$ when $\phi = \pi - \arccos(1/e^{*})$ to $(\lambda L/P, -L^2/P)$ when $\phi = \pi/2$ to $(0, -L^2/P)$ when $\phi = 0$ to $(-\lambda L/P, -L^2/P)$ when $\phi = -\pi/2$ to $\big(-(2H)^{\frac{1}{2}}\lambda L/q, -L^2/P\big)$ when $\phi = -\pi + \arccos(1/e^{*})$. In other words the angular momentum vectors will have swept over more than half of the surface area of the angular momentum cone. The two short line segments drawn perpendicular to the yz projection of the angular momentum curve indicate the limits of extent of the projection of the angular momentum as t ranges from negative through positive infinity.

The conserved vector $\boldsymbol{K}_K$ which has been rotated clockwise through $\pi/2$ radians to lie along the cartesian unit vector $-\boldsymbol{j}$ is given by (3.6.29) and has length $L(2HP^2+\mu^2)^{\frac{1}{2}}/P$ as shown in Figure 3.10.2. The vector $\boldsymbol{J}_K$, which is perpendicular to $\boldsymbol{K}_K$, is also rotated clockwise through $\pi/2$ radians to lie along the cartesian unit vector $\boldsymbol{i}$. $\boldsymbol{J}_K$ has the length PL^2K_K and is conveniently drawn to the same length as $\boldsymbol{K}_K$ in Figure 3.10.2. The Poincaré vector, $\boldsymbol{P}$, no longer orthogonal to $\boldsymbol{J}$, lies along the cartesian unit vector $-\boldsymbol{k}$. Note that, when the cone is rotated about the $x-$axis so that $\boldsymbol{P}$ lies along $\boldsymbol{k}$, the vectors $\boldsymbol{K}_K$ and $\boldsymbol{J}_K$ lie along the cartesian unit vectors $\boldsymbol{j}$ and $\boldsymbol{i}$ respectively and hence mimic the behaviour of $\boldsymbol{L}$, $\boldsymbol{K}$ and $\boldsymbol{J}$ respectively of the standard Kepler problem. The components of the conserved vectors are found by taking the scalar products of the relevant vectors with $\hat{\boldsymbol{K}}_K$, $\hat{\boldsymbol{J}}_K$ and $-\hat{\boldsymbol{P}}$, remembering that the projected quantities have been rotated clockwise through $\pi/2$ radians to preserve the alignment with the orbit on the cone. The Laplace–Runge–Lenz analogue $\boldsymbol{J}$ is given by (3.5.6) with $\mu < J$ and has components $\boldsymbol{J} = \big(L(2HP^2+\mu^2)^{\frac{1}{2}}/P, 0, -\lambda\mu/P\big)$. Note that the $x-$component of $\boldsymbol{J}$ is equal in magnitude to $\boldsymbol{K}_K$ from (3.6.29) since the vector product with $\hat{\boldsymbol{P}}$ has the effect of projecting $\boldsymbol{J}$ into the plane followed by a counter–clockwise rotation through $\pi/2$ radians. The Poincaré vector is given by (3.5.4) and has components $\big(0, 0, -(L^2+\lambda^2)^{\frac{1}{2}}\big)$. The

normal vector $\boldsymbol{N}$ (3.6.5) is perpendicular to the plane of the orbit and using (3.6.29) and (3.8.24) the components are found to be $(-L^* \cot\gamma, 0, -L^*)$. The vector $\boldsymbol{S}$ (3.6.8) is parallel to the plane of the orbit and using (3.6.29) the components are found to be $\left(\mu L(2HP^2+\mu^2)^{\frac{1}{2}}/(2\lambda HP), 0, -(2HP^2+\mu^2)/(2HP)\right)$.

Figure 3.10.3 shows the elliptical velocity hodograph in the case where $\mu < J$. A selection of velocity vectors corresponding to the displacement vectors shown in Figure 3.10.2 has been drawn from the origin to their respective positions on the velocity hodograph. In order to illustrate the $\dot{\boldsymbol{r}}$ behaviour more clearly, projections of the velocity hodograph onto planes parallel to the $\dot{x}\dot{y}$, $\dot{x}\dot{z}$ and $\dot{y}\dot{z}$ planes are also shown, together with the projected images of the orbital cone onto the respective planes. The two short line segments intersecting the velocity hodograph indicate the limits of extent of the velocity hodograph as t ranges from negative through positive infinity.

The $\dot{x}\dot{y}$ projection of the velocity hodograph is obtained by manipulating the first two equations of (3.9.35) into the form

$$\dot{x}^2 + \left(\dot{y} + \frac{L}{P^2}(2HP^2+\mu^2)^{\frac{1}{2}}\right)^2 = \left(\frac{\mu L}{P^2}\right)^2, \quad \dot{y} \leq -\frac{2HL}{(2HP^2+\mu^2)^{\frac{1}{2}}}, \tag{3.10.15}$$

which is the equation of a section of a circle in cartesian coordinates symmetrically placed about the $\dot{x} = 0$ axis, radius $\mu L/P^2$ with origin $\left(0, -L(2HP^2+\mu^2)^{\frac{1}{2}}/P^2\right)$ and is consistent with the planar velocity hodograph for the hyperbolic Kepler orbit with $L^* = 1$, $\mu = 1.25$ and $J^* = 2.25$ and (3.6.30) reversing the sign inside the $\dot{y}$ term since the velocity hodograph is being viewed with $\boldsymbol{P}$ directed along the $-\boldsymbol{k}$ direction. The semi-major axis length of (3.9.37) projected into the $\dot{x}\dot{y}-$plane reduces to the length of the radius, *i.e.* $a\sin\gamma = \mu L/P^2$, as it should. The semi-minor axis length of (3.9.37) is unchanged in length on projection into the $\dot{x}\dot{y}-$plane because it is parallel to that plane and the location of the origin agrees with that of (3.9.37) because it lies along the $\dot{y}-$axis. As t ranges from negative through positive infinity, the projection ranges from the point $\left((2H)^{\frac{1}{2}}L\mu/(Pq), -2LH/q\right)$ when $\phi = \pi - \arccos(1/e^*)$ to $(L\mu/P^2, -Lq/P^2)$ when $\phi = \pi/2$ to $\left(0, -L(\mu+q)/P^2\right)$ when $\phi = 0$ to $(-L\mu/P^2, -Lq/P^2)$ when $\phi = -\pi/2$ to $\left(-(2H)^{\frac{1}{2}}L\mu/(Pq), -2LH/q\right)$ when $\phi = -\pi + \arccos(1/e^*)$, *i.e.* the circle is not completed even as t ranges from negative through positive infinity. The dotted line completes the velocity hodograph. However, it should be remembered that the projection of the velocity vectors never closes as t ranges from negative through positive infinity. The two short line segments intersecting the $\dot{x}\dot{y}$ projection of the velocity hodograph indicate the limits of extent

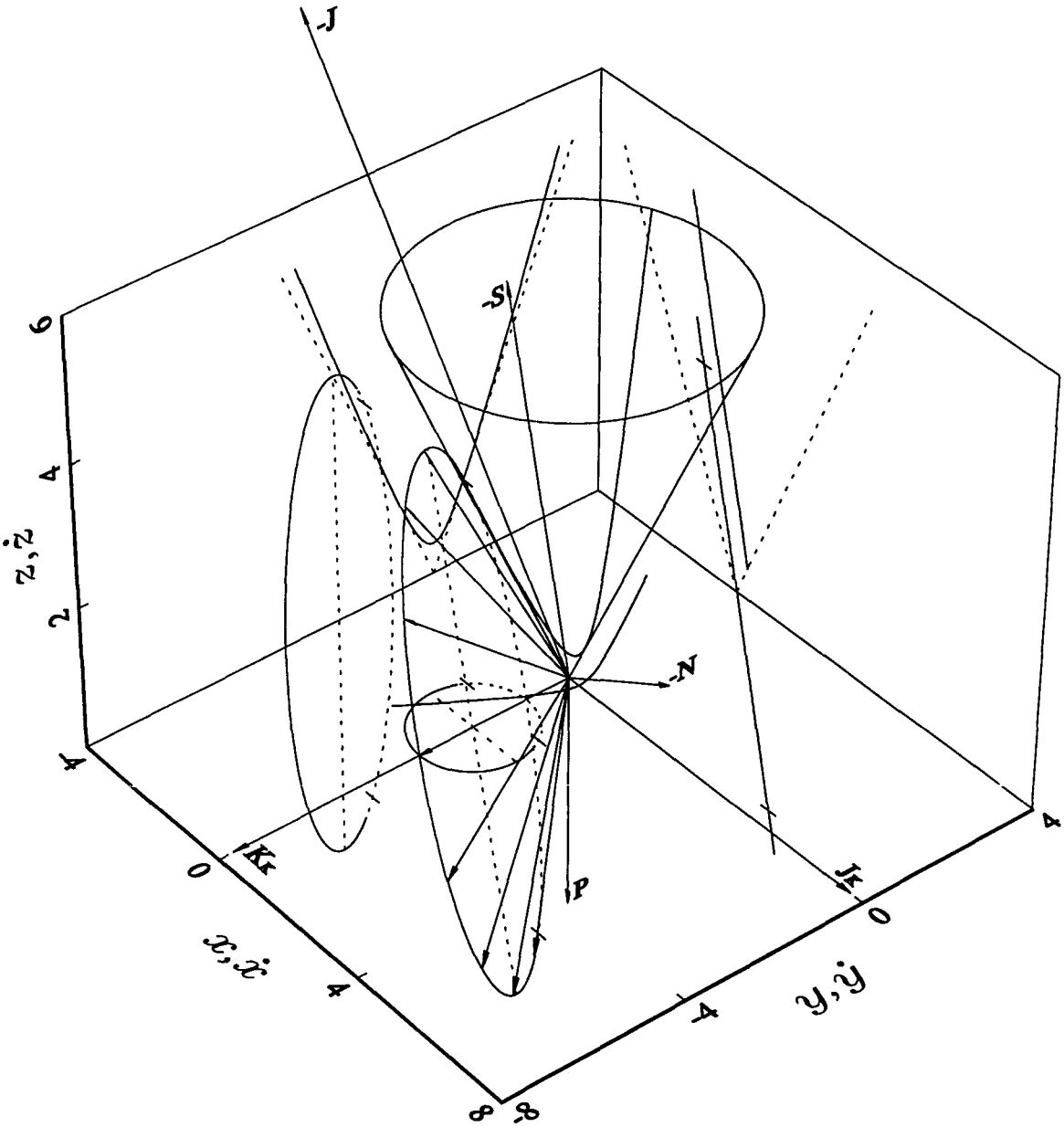

Figure 3.10.3. The elliptical MICZ velocity hodograph and hyperbolic orbit for $\mu < J$ with a selection of velocity vectors drawn from the origin. The velocity vectors move on a plane which is parallel to the orbital plane and, as t ranges from negative through positive infinity, the heads of the velocity vectors trace out a section of an ellipse. The projections of the velocity hodograph and orbit onto planes parallel to the $\dot{x}\dot{y}$, $\dot{x}\dot{z}$, $\dot{y}\dot{z}$, xy, xz and yz planes are also shown. The constants are chosen as for Figure 3.10.2. The origin lies on the hodographic plane outside the circumference of the hodographic ellipse.

of the projection of the velocity hodograph as t ranges from negative through positive infinity.

The $\dot{x}\dot{z}$ projection shows the images of the orbital cone with dotted lines, together with the respective projections of the orbit and velocity hodograph. Note that the $\dot{x}\dot{z}$ projection of the velocity hodograph is obtained by manipulating the first and third equations of (3.9.35) into the form

$$\dot{z} = -\cot\gamma\dot{x}, \quad |\dot{x}| \leq \frac{\mu L}{P^2}, \tag{3.10.16}$$

which is the equation of a straight line with slope $-\cot\gamma$ which passes through the origin and which is bisected by the $\dot{x}-$axis. The projection of the velocity hodograph is seen to be parallel to the projection of the orbit as was shown in (3.6.6) and (3.6.7). As t ranges from negative through positive infinity, the projection ranges from the point $\left((2H)^{\frac{1}{2}}L\mu/(Pq), -(2H)^{\frac{1}{2}}\lambda/P\right)$ when $\phi = \pi - \arccos(1/e^*)$ to $(\mu L/P^2, -\lambda q/P^2)$ when $\phi = \pi/2$ then to $(0,0)$ when $\phi = 0$ to $(-\mu L/P^2, \lambda q/P^2)$ when $\phi = -\pi/2$ to $\left(-(2H)^{\frac{1}{2}}L\mu/(Pq), (2H)^{\frac{1}{2}}\lambda/P\right)$ when $\phi = -\pi + \arccos(1/e^*)$, *i.e.* the length of the projection of the velocity hodograph tends to $2(2H\lambda^2 + \mu^2)^{\frac{1}{2}}/P$. The two short line segments intersecting the $\dot{x}\dot{z}$ projection of the velocity hodograph indicate the limits of extent of the projection of the velocity hodograph as t ranges from negative through positive infinity.

The $\dot{y}\dot{z}$ projection shows the images of the orbital cone with dotted lines, together with the respective projections of the orbit and velocity hodograph. Note that the $\dot{y}\dot{z}$ projection of the velocity hodograph is obtained by manipulating the second and third equations of (3.9.35) into the form

$$\left(\frac{\dot{y} + \frac{L}{P^2}(2HP^2 + \mu^2)^{\frac{1}{2}}}{\frac{\mu L}{P^2}}\right)^2 + \left(\frac{\dot{z}}{\frac{\lambda}{P^2}(2HP^2 + \mu^2)^{\frac{1}{2}}}\right)^2 = 1,$$
$$\dot{y} \leq -\frac{2HL}{(2HP^2 + \mu^2)^{\frac{1}{2}}}, \tag{3.10.17}$$

which is the equation for an ellipse symmetrically placed about the $\dot{z} = 0$ axis, with semi–major axis length $\lambda(2HP^2 + \mu^2)^{\frac{1}{2}}/P^2$ which is just the projection of the semi–major axis of (3.9.37) onto the $\dot{y}\dot{z}-$plane, *i.e.* $a\cos\gamma$, semi–minor axis length $\mu L/P^2$ which is consistent with that of (3.9.37) since it is parallel to the $\dot{y}\dot{z}-$plane, eccentricity of $\left(1-\mu^2L^2/(\lambda^2(2HP^2+\mu^2))\right)^{\frac{1}{2}}$ and centred at $\left(-L(2HP^2+\mu^2)^{\frac{1}{2}}/P^2, 0\right)$ which also agrees with the centre of (3.9.37) which lies along the $\dot{y}-$axis. It is worth noting that the focus of the ellipse on the cone does not project onto the focus of the ellipse projected into the $\dot{y}\dot{z}-$plane in general. As t ranges from negative through

positive infinity, the projection ranges from the point $\left(-2LH/q, -(2H)^{\frac{1}{2}}\lambda/P\right)$ when $\phi = \pi - \arccos(1/e^*)$ to $(-Lq/P^2, -\lambda q/P^2)$ when $\phi = \pi/2$ to $\left(-L(\mu+q)/P^2, 0\right)$ when $\phi = 0$ to $(-Lq/P^2, \lambda q/P^2)$ when $\phi = -\pi/2$ to $\left(-2LH/q, (2H)^{\frac{1}{2}}\lambda/P\right)$ when $\phi = -\pi + \arccos(1/e^*)$, *i.e.* the ellipse is not completed even as t ranges from negative through positive infinity. The dotted line completes the velocity hodograph. However, it should be remembered that the projection of the velocity vectors never closes as t ranges from negative through positive infinity. The two short line segments intersecting the $\dot{y}\dot{z}$ projection of the velocity hodograph indicate the limits of extent of the projection of the velocity hodograph as t ranges from negative through positive infinity.

The conserved vectors $\boldsymbol{K}_K$, $\boldsymbol{J}_K$, $\boldsymbol{J}$, $\boldsymbol{P}$, $\boldsymbol{N}$ and $\boldsymbol{S}$ are drawn as in Figure 3.10.2.

3.11 Discussion

Using the first integrals of the MICZ system it has been possible to describe, using very elementary methods, the complete geometry of the orbits. Despite the comments of McIntosh and Cisneros [94] referred to earlier, the orbital quantities can be expressed fairly simply in terms of the conserved quantities and orbit parameters. In particular the distance from the origin to the geometric centre of the orbit, OC, is proportional to J in both the elliptical and hyperbolic cases. The distance from the origin to the intersection of the axis of symmetry of the cone and the plane of the orbit, OB, is proportional to P. It is also of physical interest that OC becomes shorter with increasing magnitude of the energy and that OB becomes shorter with increasing Coulomb constant and longer with increasing monopole strength. The orbit of the MICZ problem is described by the intersection of a plane and a right circular cone, and the projection of the orbit into the ϕ–plane is a focus–centred conic section which corresponds naturally with the orbit of the standard Kepler problem. Analogues of Kepler's three laws of motion have been obtained and shown to be natural extensions of the laws in the plane.

The rôles of the two vectors $\boldsymbol{P}$ and $\boldsymbol{J}$ are very similar to their analogues in the classical Kepler–Coulomb problem in that $\boldsymbol{P}$, like the angular momentum, determines the orientation in space and $\boldsymbol{J}$, like the Laplace–Runge–Lenz vector, determines the orientation of the orbit within the orientation induced by $\boldsymbol{P}$ by pointing along the direction of the location of the geometric centre of the orbit and the direction of the major axis. A linear combination of $\boldsymbol{P}$ and $\boldsymbol{J}$ naturally gives rise to two vectors

one of which is parallel to the normal to the orbital and hodographic planes and the other which is parallel to the orbital and hodographic planes. The latter vector $\boldsymbol{S}$ also behaves like the Laplace–Runge–Lenz vector in that it provides the orbit equation for the orbit on the tilted plane in a natural way.

3.12 The Lie Algebras of the Classical Monopole–Oscillator and Related Problems

The Lie point symmetries of the equation of motion for an electric charge interacting with a magnetic monopole (taken as fixed at the origin) have been studied by Moreira *et al.* [101]. They concluded that the equation of motion describing the above system

$$\ddot{\boldsymbol{r}} + \frac{\lambda}{r^3}\boldsymbol{L} = \boldsymbol{0} \tag{3.12.1}$$

possessed six symmetries (see §4.1) and the corresponding Lie algebra $so(2,1)\oplus so(3)$. In addition to the well-known Poincaré vector [107]

$$\boldsymbol{P} = \boldsymbol{L} - \lambda\hat{\boldsymbol{r}} \tag{3.12.2}$$

with which the algebra $so(3)$ is usually associated they further obtained another three scalar first integrals

$$I_1 = \frac{1}{2}\,\dot{\boldsymbol{r}}\cdot\dot{\boldsymbol{r}} \tag{3.12.3}$$

$$I_2 = (t\dot{\boldsymbol{r}} - \boldsymbol{r})\cdot\boldsymbol{r} \tag{3.12.4}$$

$$I_3 = (t\dot{\boldsymbol{r}} - \boldsymbol{r})\cdot(t\dot{\boldsymbol{r}} - \boldsymbol{r}) \tag{3.12.5}$$

the first by inspection and I_2 and I_3 using Lutzky's method [87].

Jackiw [56] applied Noether's theorem to the Lagrangian corresponding to (3.12.1) (with an additional potential term proportional to r^{-2}). He obtained the integrals (3.12.3)–(3.12.5) which also included the contribution from the extra potential term and observed that the commutators of the integrals possessed the algebra $o(2,1)$. He emphasized the close connection between the monopole problem and the Kepler–Coulomb problem by observing that the algebras of the commutation relations of the first integrals are in both cases six–dimensional although there are some differences in detail. As far as the Lie algebras of the symmetries of the differential equations are concerned, the monopole has the six–dimensional algebra $so(2,1)\oplus so(3)$ whereas the Kepler–Coulomb problem has the five–dimensional algebra $A_2\oplus so(3)$ (see Leach and

Gorringe [79]). The A_2 contribution to the algebra is as a result of invariance under time translation and rescaling. It was also demonstrated in Gorringe and Leach [40] that the Lie algebra corresponding to the Kepler–Coulomb problem is also found for all central force problem where the force obeys a power law.

In their study of the Lie point symmetries of the differential equation

$$\ddot{\boldsymbol{r}} + f(r)\boldsymbol{L} + g(r)\boldsymbol{r} = \boldsymbol{0} \tag{3.12.6}$$

Leach and Gorringe [79] discovered that the equation

$$\ddot{\boldsymbol{r}} + \frac{\lambda}{r^3}\boldsymbol{L} + \left(\frac{\mu}{r^4} - \varepsilon\right)\boldsymbol{r} = \boldsymbol{0} \tag{3.12.7}$$

possessed the algebra $sl(2,R) \oplus so(3)$, regardless of the values of the parameters λ, μ and ε provided that both λ and μ are not simultaneously zero. In the case where λ and μ are both zero, (3.12.7) would have the twenty–four element algebra, $sl(5,R)$, of the three–dimensional linear system.

It was also observed that, for $\varepsilon = 0$, the $sl(2,R)$ algebra associated with (3.12.7) consisted of invariance under time translation, a self–similar transformation and a conformal transformation. The introduction of ε replaces the latter two symmetries, (see §4.4), but the algebra remains $sl(2,R)$. We note that in Leach and Gorringe [79] the algebra $sl(2,R)$, which is isomorphic to $so(2,1)$, is preferred to the $so(2,1)$ which is often used in the literature. The elements of this algebra generate infinitesimal transformations in (r,t) space and we believe it is better to use $sl(2,R)$ to avoid the suggestion of rotation in the physical space.

When $\varepsilon = -\omega^2$, (3.12.7) is referred to as the monopole–oscillator, although strictly speaking it is not due to the presence of the $\mu r^{-4}\boldsymbol{r}$ term. For the special case $\mu = -\lambda^2$ McIntosh and Cisneros [94] observed an increase in the number of first integrals. The reason for the increase will become clear in the subsequent discussion. Curiously the presence of the r^{-2} potential relates the problem more closely to currently studied physical models of monopole motion (see for example Mladenov and Tsanov [97], Cordani [23], Atiyah and Hitchin [1, 2] and Manton [89]).

We now study the properties of the first integrals of (3.12.7) for general values of μ and for $\varepsilon = -\omega^2$ (monopole–oscillator), $\varepsilon = 0$ (monopole–free particle) and $\varepsilon = \omega^2$ (monopole–repulsor). When $\mu \neq -\lambda^2$, we find that the Lie algebra of the six first integrals under the operation of taking the Poisson Bracket is $sl(2, R) \oplus so(3)$ which is the same algebra as for the point symmetries of the differential equation under the operation of taking the Lie Bracket. The orbit equations are then constructed using the energy–like first integral and the rôles played by the parameters λ and μ are investigated especially in the case $\mu = -\lambda^2$.

3.13 The Lie Algebras of the First Integrals of the Monopole–Oscillator, Monopole–Free Particle and Monopole–Repulsor

We consider the three related problems.

1) The monopole–oscillator

$$\ddot{\boldsymbol{r}} + \frac{\lambda}{r^3}\boldsymbol{L} + \left(\frac{\mu}{r^4} + \omega^2\right)\boldsymbol{r} = \boldsymbol{0}. \tag{3.13.1}$$

2) The monopole–free particle

$$\ddot{\boldsymbol{r}} + \frac{\lambda}{r^3}\boldsymbol{L} + \frac{\mu}{r^4}\boldsymbol{r} = \boldsymbol{0}. \tag{3.13.2}$$

3) The monopole–repulsor

$$\ddot{\boldsymbol{r}} + \frac{\lambda}{r^3}\boldsymbol{L} + \left(\frac{\mu}{r^4} - \omega^2\right)\boldsymbol{r} = \boldsymbol{0}. \tag{3.13.3}$$

Taking the vector product of $\boldsymbol{r}$ with (3.13.1), (3.13.2) and (3.13.3) separately yields in all cases Poincaré's vector

$$\boldsymbol{P} = \boldsymbol{L} - \lambda\hat{\boldsymbol{r}}. \tag{3.13.4}$$

In component form, (3.13.4) can be written as

$$\begin{aligned} P_1 &= x_2p_3 - x_3p_2 - \frac{\lambda x_1}{r} \\ P_2 &= x_3p_1 - x_1p_3 - \frac{\lambda x_2}{r} \\ P_3 &= x_1p_2 - x_2p_1 - \frac{\lambda x_3}{r}, \end{aligned} \tag{3.13.5}$$

where the mechanical momentum $\boldsymbol{p} = (p_1, p_2, p_3) = \dot{\boldsymbol{r}}$. Using the mechanical momentum the basic Poisson Bracket relations are

$$[x_i, x_j]_{PB} = 0, \qquad [x_i, p_j]_{PB} = \delta_{ij}, \qquad [p_i, p_j]_{PB} = \lambda \varepsilon_{ijk} \frac{x_k}{r^3} \tag{3.13.6}$$

and we immediately obtain the well–known result (see Mladenov [96])

$$[P_i, P_j]_{PB} = \varepsilon_{ijk} P_k \tag{3.13.7}$$

and the usual $so(3)$ symmetry.

Taking the scalar product of (3.13.1) with $\dot{\boldsymbol{r}}$, $\dot{\boldsymbol{r}} \sin 2\omega t$ and $\dot{\boldsymbol{r}} \cos 2\omega t$ in turn and integrating by parts we obtain

$$I_1 = \frac{1}{2}\left(\boldsymbol{p}\cdot\boldsymbol{p} - \frac{\mu}{r^2} + \omega^2 r^2\right) \tag{3.13.8}$$

$$I_2 = \frac{1}{2}\sin 2\omega t \left(\boldsymbol{p}\cdot\boldsymbol{p} - \frac{\mu}{r^2} - \omega^2 r^2\right) - \omega \boldsymbol{p}\cdot\boldsymbol{r} \cos 2\omega t \tag{3.13.9}$$

$$I_3 = \frac{1}{2}\cos 2\omega t \left(\boldsymbol{p}\cdot\boldsymbol{p} - \frac{\mu}{r^2} - \omega^2 r^2\right) + \omega \boldsymbol{p}\cdot\boldsymbol{r} \sin 2\omega t. \tag{3.13.10}$$

I_1 is, of course, the Hamiltonian of the system. The Poisson Bracket relations amongst the Is are

$$[I_1, I_2]_{PB} = 2\omega I_3, \qquad [I_2, I_3]_{PB} = -2\omega I_1, \qquad [I_3, I_1] = 2\omega I_2 \tag{3.13.11}$$

and so the algebra of the Is is $sl(2, R)$. It can be shown that

$$[P_i, I_j]_{PB} = 0 \quad \forall i, j, \tag{3.13.12}$$

which confirms that the algebra of the first integrals of (3.13.1) is given by $sl(2, R) \oplus so(3)$. The integrals are not independent since

$$\lambda^2 + \mu = P^2 + \omega^{-2}(I_2^2 + I_3^2 - I_1^2) \tag{3.13.13}$$

which is a hyperboloid of one sheet in the six–dimensional space of first integrals.

We now turn our attention to the second equation of motion (3.13.2). Taking the scalar product of (3.13.2) with $\dot{\boldsymbol{r}}$, $t\dot{\boldsymbol{r}}$ and $t^2\dot{\boldsymbol{r}}$ in turn and integrating by parts we find that

$$J_1 = \frac{1}{2}\left(\boldsymbol{p}\cdot\boldsymbol{p} - \frac{\mu}{r^2}\right) \tag{3.13.14}$$

$$J_2 = \frac{1}{2}\, t \left(\boldsymbol{p}\cdot\boldsymbol{p} - \frac{\mu}{r^2}\right) - \frac{1}{2}\, \boldsymbol{p}\cdot\boldsymbol{r} \tag{3.13.15}$$

$$J_3 = \frac{1}{2}\, t^2 \left(\boldsymbol{p}\cdot\boldsymbol{p} - \frac{\mu}{r^2}\right) - t\boldsymbol{p}\cdot\boldsymbol{r} + \frac{1}{2}\, r^2. \tag{3.13.16}$$

J_1 represents the Hamiltonian. The Poisson Bracket relations amongst the Js are

$$[J_1, J_2]_{PB} = J_1, \qquad [J_2, J_3]_{PB} = J_3, \qquad [J_3, J_1]_{PB} = -2J_2 \tag{3.13.17}$$

which is an alternate representation of $sl(2, R)$. Replacing I by J in (3.13.12) leaves the result unchanged and so the algebra is $sl(2, R) \oplus so(3)$. The integrals are related by

$$\lambda^2 + \mu = P^2 + 4J_2^2 - 4J_1 J_3 \tag{3.13.18}$$

which is the same surface as given by (3.13.13).

The above procedure is again repeated for the third equation (3.13.3). The scalar product of $\dot{\boldsymbol{r}}, \dot{\boldsymbol{r}} \sinh 2\omega t$ and $\dot{\boldsymbol{r}} \cosh 2\omega t$ with (3.13.3) gives

$$K_1 = \frac{1}{2}\left(\boldsymbol{p}\cdot\boldsymbol{p} - \frac{\mu}{r^2} - \omega^2 r^2\right) \tag{3.13.19}$$

$$K_2 = \frac{1}{2}\sinh 2\omega t\left(\boldsymbol{p}\cdot\boldsymbol{p} - \frac{\mu}{r^2} + \omega^2 r^2\right) - \omega \boldsymbol{p}\cdot\boldsymbol{r}\cosh 2\omega t \tag{3.13.20}$$

$$K_3 = \frac{1}{2}\cosh 2\omega t\left(\boldsymbol{p}\cdot\boldsymbol{p} - \frac{\mu}{r^2} + \omega^2 r^2\right) + \omega \boldsymbol{p}\cdot\boldsymbol{r}\sinh 2\omega t. \tag{3.13.21}$$

K_1 is the Hamiltonian of the systen and the Poisson Bracket relations amongst the Ks are

$$[K_1, K_2]_{PB} = 2\omega K_3, \quad [K_2, K_3]_{PB} = -2\omega K_1, \quad [K_3, K_1]_{PB} = -2\omega K_2 \tag{3.13.22}$$

which is again $sl(2, R)$. All the Poisson Brackets between Ps and Ks are zero as in the previous cases and so the algebra of the first integrals is again $sl(2, R) \oplus so(3)$. The integrals are related to each other through

$$\lambda^2 + \mu = P^2 + \omega^{-2}(K_1^2 + K_2^2 - K_3^2) \tag{3.13.23}$$

which is again an hyperboloid of one sheet.

The structure of (3.13.18) can be manipulated more into the form of (3.13.13) and (3.13.23) by defining

$$2J_1 = J_2' + J_3' \qquad 2J_2 = J_1' \qquad 2J_3 = J_2' - J_3' \tag{3.13.24}$$

so that (3.13.18) becomes

$$\lambda^2 + \mu = P^2 + J_3'^2 + J_1'^2 - J_2'^2. \tag{3.13.25}$$

On close inspection of (3.13.13), (3.13.23) and (3.13.25) the structure is similar, but in each case the ordering of the indices different. This could be rectified by relabelling, but the above exercise shows that K_1, K_2, K_3 for instance are not obtained from I_1, I_2, I_3 respectively under a canonical transformation. In fact the associations are $K_1 \leftrightarrow I_3$, $K_2 \leftrightarrow I_2$, $K_3 \leftrightarrow I_1$. This phenomenon was observed some time ago in connection with the quadratic first integrals of systems possessing quadratic Hamiltonians (see Leach [71]).

The monopole–oscillator problem can be treated in much the same way as the monopole–Kepler problem. By taking the vector product of $\boldsymbol{P}$ with the equation of motion (3.13.1) the equation on the cone can be projected into the plane, further rotated through $\pi/2$ about the projection axis, and scaled by P. The differential equation becomes

$$(\boldsymbol{r} \times \boldsymbol{P})^{\cdot\cdot} + \left(\frac{L^4(\lambda^2 + \mu)}{|\boldsymbol{r} \times \boldsymbol{P}|^4} + \omega^2 \right) \boldsymbol{r} \times \boldsymbol{P} = \boldsymbol{0}. \tag{3.13.26}$$

Note that the angular momentum component of the equation of motion contributes to the centripetal force term of the equivalent central force problem. Similarly the equation of motion for the monopole–free particle (3.13.2) can be written as

$$(\boldsymbol{r} \times \boldsymbol{P})^{\cdot\cdot} + \left(\frac{L^4(\lambda^2 + \mu)}{|\boldsymbol{r} \times \boldsymbol{P}|^4} \right) \boldsymbol{r} \times \boldsymbol{P} = \boldsymbol{0} \tag{3.13.27}$$

and for the monopole–repulsor (3.13.3) as

$$(\boldsymbol{r} \times \boldsymbol{P})^{\cdot\cdot} + \left(\frac{L^4(\lambda^2 + \mu)}{|\boldsymbol{r} \times \boldsymbol{P}|^4} - \omega^2 \right) \boldsymbol{r} \times \boldsymbol{P} = \boldsymbol{0}. \tag{3.13.28}$$

Note that in the case $\mu = -\lambda^2$, (3.13.26) becomes a three–dimensional isotropic harmonic oscillator in terms of the vector $\boldsymbol{r} \times \boldsymbol{P}$. The three–dimensional isotropic harmonic oscillator has twenty one first integrals quadratic in the velocities (L_{ij} gives three, A_{ij} six, B_{ij} six and C_{ij} six, see §3.20) and the orbit of $\boldsymbol{r} \times \boldsymbol{P}$ can be obtained from the nine autonomous integrals.

3.14 The Geometry of the Monopole–Oscillator

Let the angle between Poincaré's vector, $\boldsymbol{P}$, and $\hat{\boldsymbol{r}}$ be $\pi - \alpha$. Using (3.13.4) the scalar product of $\boldsymbol{P}$ with $\hat{\boldsymbol{r}}$ gives

$$\cos\alpha = \frac{\lambda}{P} \tag{3.14.1}$$

which confirms that the motion is on the surface of a right circular cone of semi–vertex angle α and axis of symmetry along the line of $\boldsymbol{P}$. Although the angular momentum, $\boldsymbol{L}$, is not conserved, its magnitude, L, is. Since $[\boldsymbol{P}, \boldsymbol{L}, \boldsymbol{r}]$ is zero, $\boldsymbol{L}$ describes a right circular cone of semi–vertex angle $(\pi/2 - \alpha)$. The salient features of the geometry are depicted in Figure 3.14.1 which shows the orientation of the larger orbital and smaller angular momentum cones which meet at the origin and a typical orbit for the case $\mu = -\lambda^2$. Note from the diagram how the vector $\boldsymbol{P}$ is constructed from the vectors $\boldsymbol{L}$ and $-\lambda\hat{\boldsymbol{r}}$, where $-\lambda\hat{\boldsymbol{r}}$ is in the opposite direction to $\boldsymbol{r}$ and scaled by λ. From (3.13.4) and (3.14.1) it follows that

$$\sin\alpha = \frac{L}{P}. \tag{3.14.2}$$

Since the plane polar angle α is constant,

$$L = r^2 \sin\alpha \dot{\phi}, \tag{3.14.3}$$

where ϕ is the azimuthal angle in the plane through O, perpendicular to $\boldsymbol{P}$. The orbit equation is easily obtained by rewriting (3.13.8) in terms of $\dot{r}$

$$\dot{r} = \left(2I_1 - \frac{(L^2 - \mu)}{r^2} - \omega^2 r^2\right)^{\frac{1}{2}}. \tag{3.14.4}$$

Using (3.14.2) and (3.14.3), $\dot{r}$ can be expressed in terms of ϕ as follows

$$\dot{r} = \frac{P}{r^2}\frac{\mathrm{d}r}{\mathrm{d}\phi} \tag{3.14.5}$$

and $\dot{r}$ in (3.14.4) can be replaced using (3.14.5) and solved to give the orbit equation

$$r^2 = \frac{L^2 - \mu}{I_1 - \left(I_1^2 - \omega^2(L^2 - \mu)\right)^{\frac{1}{2}} \cos\left(2\left(\frac{L^2-\mu}{L^2+\lambda^2}\right)^{\frac{1}{2}}(\phi - \phi_0)\right)} \tag{3.14.6}$$

provided $I_1^2 > \omega^2(L^2 - \mu) > 0$. It is now a simple matter to plot the orbit remembering that the plane polar angle α remains constant. In cartesian coordinates

$$\begin{aligned} x &= r\sin\alpha\cos\phi \\ y &= r\sin\alpha\sin\phi \\ z &= r\cos\alpha, \end{aligned} \tag{3.14.7}$$

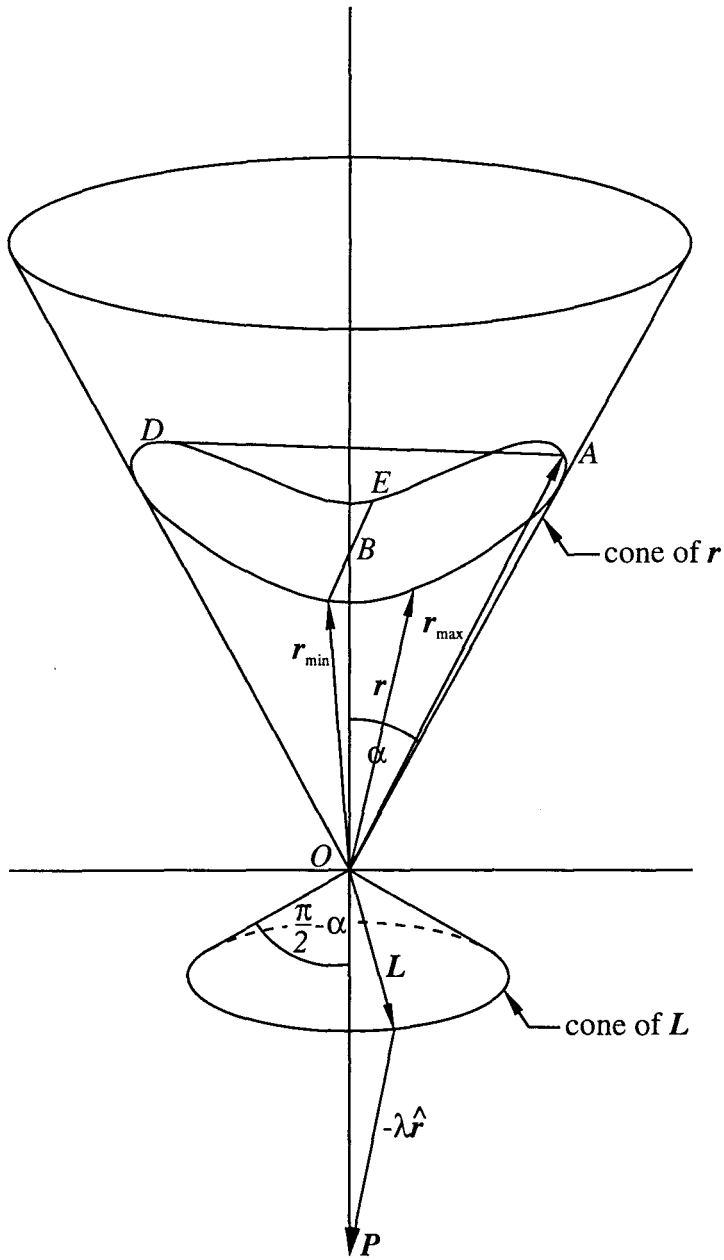

Figure 3.14.1. The typical geometry of the monopole–oscillator orbit when $\mu = -\lambda^2$. The larger orbital and smaller angular momentum cones are shown together with a typical orbit and the orientation of $\boldsymbol{P}$. The origin O is at the point of contact between the two cones, A marks one of the two points of furthest approach from O and E one of the two points of closest approach. The orbit is not a conic section although certain projections are conic sections. α and $\pi/2 - \alpha$ are the the semi–vertex angles of the orbital and angular momentum cones respectively.

where r is calculated from (3.14.6), and α is determined from (3.14.1) or (3.14.2). Equation (3.14.6) is very reminiscent of the orbit equation for the three–dimensional isotropic harmonic oscillator (see (1.7.16)). This comes as no surprise since, for $\mu = -\lambda^2$, (3.13.1) can be rewritten as a three–dimensional isotropic harmonic oscillator as shown earlier in (3.13.26). In this case (3.14.6) is equivalent to equation (1.7.16) where the rôle of L^2 has now been replaced by P^2 and λ^2 by ω^2. The rôles of μ and λ can be seen in (3.14.6). The orbit is not closed unless $\left(L^2 - \mu\right)^{\frac{1}{2}}$ and $\left(L^2 + \lambda^2\right)^{\frac{1}{2}}$ are commensurate. The orbit precesses counter–clockwise if $L^2 - \mu < L^2 + \lambda^2$ and clockwise if $L^2 - \mu > L^2 + \lambda^2$. For $\mu = -\lambda^2$ the orbit closes after one revolution and the projection of the orbit onto the ϕ–plane is an ellipse. The orbit on the cone is not elliptical, but rather is as if the ellipse were lifted from the plane and bent to fit onto the surface of the cone.

The angular momentum for the planar three–dimensional isotropic harmonic oscillator (3.13.26) with $\mu = -\lambda^2$ is given by

$$\boldsymbol{L}_O = (\boldsymbol{r} \times \boldsymbol{P}) \times (\dot{\boldsymbol{r}} \times \boldsymbol{P}) = L^2 \boldsymbol{P} \tag{3.14.8}$$

and the energy integral by

$$E_O = \frac{1}{2}(\dot{\boldsymbol{r}} \times \boldsymbol{P}) \cdot (\dot{\boldsymbol{r}} \times \boldsymbol{P}) + \frac{1}{2}\omega^2 (\boldsymbol{r} \times \boldsymbol{P}) \cdot (\boldsymbol{r} \times \boldsymbol{P}) = L^2 I_1. \tag{3.14.9}$$

In addition to these integrals a unit Laplace–Runge–Lenz vector can be constructed for the equation of motion of the three–dimensional isotropic harmonic oscillator in the variable $\boldsymbol{r} \times \boldsymbol{P}$ using a variation of Fradkin's method described in §§1.6 and 1.7 which gives

$$\begin{aligned} \hat{\boldsymbol{J}}_O &= \left(F - U\frac{\partial F}{\partial U}\right) \boldsymbol{r} \,\widehat{\times}\, \boldsymbol{P} + \frac{1}{L_O^2}\frac{\partial F}{\partial U}(\dot{\boldsymbol{r}} \times \boldsymbol{P}) \times \boldsymbol{L}_O \\ &= \left(F - u\frac{\partial F}{\partial u}\right) \boldsymbol{r} \,\widehat{\times}\, \boldsymbol{P} + \frac{1}{LP^2}\frac{\partial F}{\partial u}(\dot{\boldsymbol{r}} \times \boldsymbol{P}) \times \boldsymbol{P}, \end{aligned} \tag{3.14.10}$$

where $U = 1/|\boldsymbol{r} \times \boldsymbol{P}| = u/L$ and $F = \left(E_O + (E_O^2 - \omega^2 L_O^2)^{1/2} - L_O^2 U^2\right)^{1/2} / (4E_O^2 - 4\omega^2 L_O^2)^{1/4}$. Making the necessary substitutions, (3.14.10) can be simplified and scaled by J_O to give

$$\begin{aligned} \boldsymbol{J}_O = \pm\left(\frac{J_O}{2\omega}\right)^{\frac{1}{2}} &\left[E_O + \omega J_O - L_O^2 U^2\right]^{-\frac{1}{2}} \Big((E_O + \omega J_O)\boldsymbol{r} \,\widehat{\times}\, \boldsymbol{P} - \\ &U(\dot{\boldsymbol{r}} \times \boldsymbol{P}) \times \boldsymbol{L}_O\Big), \end{aligned} \tag{3.14.11}$$

where

$$J_O = \left(\frac{E_O^2}{\omega^2} - L_O^2\right)^{\frac{1}{2}}. \tag{3.14.12}$$

The choice of the arbitrary function $Q(E_O)$ is again motivated by the structure of the Jauch–Hill–Fradkin analogue and is found to be

$$Q(E_O) = \frac{E_O}{\omega} \tag{3.14.13}$$

which is consistent with (1.7.4). Equation (3.14.11) can be simplified following the procedure described in §1.7 to give

$$\boldsymbol{J}_O = \pm J_O \frac{1}{e\left(|\boldsymbol{r}\times\boldsymbol{P}|^2 - b^2\right)^{\frac{1}{2}}}\left(\boldsymbol{r}\times\boldsymbol{P} - \frac{b^2}{P^2L^2}(\dot{\boldsymbol{r}}\times\boldsymbol{P})\times\boldsymbol{P}\right), \tag{3.14.14}$$

and similarly the corresponding Hamilton vector can be constructed using

$$\begin{aligned}\boldsymbol{K}_O &= \hat{\boldsymbol{P}}\times\boldsymbol{J}_O \\ &= \pm J_O \frac{(1-e^2)^{\frac{1}{2}}}{e\left(a^2 - |\boldsymbol{r}\times\boldsymbol{P}|^2\right)^{\frac{1}{2}}}\left(\frac{a^2}{P^2L^2}(\dot{\boldsymbol{r}}\times\boldsymbol{P})\times\boldsymbol{P} - \boldsymbol{r}\times\boldsymbol{P}\right).\end{aligned} \tag{3.14.15}$$

The same restrictions apply as for the three–dimensional isotropic harmonic oscillator regarding the discontinuities and the choice of sign of the Laplace–Runge–Lenz and Hamilton vector analogues. In fact (3.14.14) and (3.14.15) are identical in form to (1.7.7) and (1.7.8) using the variable substitutions $\lambda \to \omega$, $\boldsymbol{r} \to \boldsymbol{r}\times\boldsymbol{P}$, $\dot{\boldsymbol{r}} \to \dot{\boldsymbol{r}}\times\boldsymbol{P}$, $\boldsymbol{L} \to \boldsymbol{L}_O$ remembering that the semi–major and semi–minor axis lengths are scaled by P as a result of the projection and so a^2/P^2 and b^2/P^2 in (3.14.15) and (3.14.14) respectively have the same length as a^2 and b^2 respectively in (1.7.8) and (1.7.7). It should also be noted that $\hat{\boldsymbol{J}}_O$ and $\hat{\boldsymbol{K}}_O$ as given by (3.14.14) and (3.14.15) are rotated counter–clockwise through $\pi/2$ radians from the expected positions $\boldsymbol{i}$ and $-\boldsymbol{j}$ respectively. This is in agreement with the projection of the orbit into the ϕ–plane which is also rotated counter–clockwise through $\pi/2$ radians and scaled by P. In the diagrams that follow $\boldsymbol{J}_O$ and $\boldsymbol{K}_O$ will be rotated clockwise through $\pi/2$ radians to lie along the cartesian unit vectors $\boldsymbol{i}$ and $-\boldsymbol{j}$ respectively in such a way that when the cone is rotated about the x–axis so that $\boldsymbol{P}$ lies along $\boldsymbol{k}$, $\boldsymbol{J}_O$ and $\boldsymbol{K}_O$ lie along the cartesian vectors $\boldsymbol{i}$ and $\boldsymbol{j}$ respectively and hence mimic the behaviour of $\boldsymbol{L}$, $\boldsymbol{J}$ and $\boldsymbol{K}$ respectively of the three–dimensional isotropic harmonic oscillator.

The choice of the arbitrary function $Q(E_O)$ (3.14.13) gives rise to the Jauch–Hill–Fradkin tensor analogue

$$
\begin{aligned}
A_{ij} &= \left[Q(E_O) \pm \left[Q^2(E_O) - L_O^2\right]^{\frac{1}{2}}\right] \hat{\boldsymbol{J}}_{Oi} \hat{\boldsymbol{J}}_{Oj} + \\
&\quad \left[Q(E_O) \mp \left[Q^2(E_O) - L_O^2\right]^{\frac{1}{2}}\right] \left(\hat{\boldsymbol{P}} \times \hat{\boldsymbol{J}}_O\right)_i \left(\hat{\boldsymbol{P}} \times \hat{\boldsymbol{J}}_O\right)_j \\
&= \frac{1}{w}\left((\dot{\boldsymbol{r}} \times \boldsymbol{P})_i (\dot{\boldsymbol{r}} \times \boldsymbol{P})_j + \omega^2 (\boldsymbol{r} \times \boldsymbol{P})_i (\boldsymbol{r} \times \boldsymbol{P})_j\right). \qquad (3.14.16)
\end{aligned}
$$

Making the substitution $\boldsymbol{r} \times \boldsymbol{P} = \boldsymbol{u}$ and scaling (3.14.16) by ω gives the equation of the velocity hodograph

$$\dot{\boldsymbol{u}}^T (2E_O I - A)\, \dot{\boldsymbol{u}} = \omega^2 L_O^2. \qquad (3.14.17)$$

Since $\hat{\boldsymbol{P}}$ is constant, the motion is planar and for convenience we assign u_3 to be the variable in the direction of $\hat{\boldsymbol{P}}$. The eigenvalues of the 2x2 matrix in (3.14.17) which determine the velocity hodograph in the plane, are

$$\lambda = E_O \pm \left(E_O^2 - w^2 L_O^2\right)^{\frac{1}{2}}, \qquad (3.14.18)$$

and, if we rotate the velocity hodograph (3.14.17) so that the cartesian unit vectors $\boldsymbol{i}$ and $\boldsymbol{j}$ become principal axes we obtain

$$\left(\frac{\dot{u}_1}{\left(E_O - (E_O^2 - \omega^2 L_O^2)^{\frac{1}{2}}\right)^{\frac{1}{2}}}\right)^2 + \left(\frac{\dot{u}_2}{\left(E_O + (E_O^2 - \omega^2 L_O^2)^{\frac{1}{2}}\right)^{\frac{1}{2}}}\right)^2 = 1. \qquad (3.14.19)$$

Equation (3.14.19) can be simplified to obtain

$$\left(\frac{\dot{x}}{\frac{L\left(I_1 + (I_1^2 - \omega^2 P^2)^{\frac{1}{2}}\right)^{\frac{1}{2}}}{P}}\right)^2 + \left(\frac{\dot{y}}{\frac{L\left(I_1 - (I_1^2 - \omega^2 P^2)^{\frac{1}{2}}\right)^{\frac{1}{2}}}{P}}\right)^2 = 1 \qquad (3.14.20)$$

which is the equation of an ellipse symmetrically placed about the $\dot{x}-$axis, with semi-major axis of length $L\left(I_1 + ({I_1}^2 - \omega^2 P^2)^{\frac{1}{2}}\right)^{\frac{1}{2}}/P$, semi-minor axis of length $L\left(I_1 - ({I_1}^2 - \omega^2 P^2)^{\frac{1}{2}}\right)^{\frac{1}{2}}/P$ and eccentricity $\left(4({I_1}^2 - \omega^2 P^2)\right)^{\frac{1}{4}} \left(I_1 - ({I_1}^2 - \omega^2 P^2)^{\frac{1}{2}}\right)^{\frac{1}{2}}/(\omega P)$.

The equation of the orbit is then given by

$$\boldsymbol{u}^T (2E_O I - A)\, \boldsymbol{u} = L_O^2. \qquad (3.14.21)$$

If we rotate the orbit (3.14.21) so that the cartesian unit vectors $\boldsymbol{i}$ and $\boldsymbol{j}$ become the principal axes we obtain

$$\left(\frac{u_1}{\frac{\left(E_O - (E_O^2 - \omega^2 L_O^2)^{\frac{1}{2}}\right)^{\frac{1}{2}}}{\omega}}\right)^2 + \left(\frac{u_2}{\frac{\left(E_O + (E_O^2 - \omega^2 L_O^2)^{\frac{1}{2}}\right)^{\frac{1}{2}}}{\omega}}\right)^2 = 1. \qquad (3.14.22)$$

Equation (3.14.22) can be simplified to obtain

$$\left(\frac{x}{\frac{L\left(I_1+(I_1^2-\omega^2P^2)^{\frac{1}{2}}\right)^{\frac{1}{2}}}{\omega P}}\right)^2+\left(\frac{y}{\frac{L\left(I_1-(I_1^2-\omega^2P^2)^{\frac{1}{2}}\right)^{\frac{1}{2}}}{\omega P}}\right)^2=1 \tag{3.14.23}$$

which is the equation of an ellipse symmetrically placed about the $x-$axis, concentric to (3.14.20), with semi–major axis of length $L\left(I_1+(I_1{}^2-\omega^2P^2)^{\frac{1}{2}}\right)^{\frac{1}{2}}/(\omega P)$, semi–minor axis of length $L\left(I_1-(I_1{}^2-\omega^2P^2)^{\frac{1}{2}}\right)^{\frac{1}{2}}/(\omega P)$ and eccentricity $\left(4(I_1{}^2-\omega^2P^2)\right)^{\frac{1}{4}}\left(I_1-(I_1{}^2-\omega^2P^2)^{\frac{1}{2}}\right)^{\frac{1}{2}}/(\omega P)$. Note that both (3.14.20) and (3.14.23) describe the projection of the velocity hodograph and the orbit in the $\phi-$plane without the scaling by P since the equations are now written in terms of the components of $\dot{\boldsymbol{r}}$ and $\boldsymbol{r}$ rather than those of $\dot{\boldsymbol{r}}\times\boldsymbol{P}$ and $\boldsymbol{r}\times\boldsymbol{P}$ respectively.

The presence of two orthogonal vectors in the $xy-$plane would seem to suggest the existence of additional vectors lying out of the plane which would project onto the line of $\boldsymbol{J}_O$ and $\boldsymbol{K}_O$ in the $xy-$plane. Two such vectors are given by

$$\boldsymbol{U}=\pm\boldsymbol{J}_O-\frac{\lambda J_O}{L}\hat{\boldsymbol{P}} \tag{3.14.24}$$

which lie on the surface of the cone collinear with the two vectors directed from the origin to the two points of closest approach. Two other such vectors are given by

$$\boldsymbol{V}=\pm\boldsymbol{K}_O-\frac{\lambda K_O}{L}\hat{\boldsymbol{P}} \tag{3.14.25}$$

which lie on the surface of the cone collinear with the two vectors directed from the origin to the two points of furthest approach. Note that $\hat{\boldsymbol{P}}\times\boldsymbol{U}=\pm\boldsymbol{K}_O$ and $\hat{\boldsymbol{P}}\times\boldsymbol{V}=\mp\boldsymbol{J}_O$. Different linear combinations of the vectors shown above can also be constructed. However, they are not nearly as important as those described above because they do not appear to provide any useful additional geometric information on the monopole–oscillator problem.

In the case $\mu=-\lambda^2$ the parametric equations for the orbit can be obtained by substituting for r from (3.14.6) in (3.14.7) to give

$$
\begin{aligned}
x &= \frac{L\cos\phi}{\left(I_1 - (I_1^2 - \omega^2 P^2)^{\frac{1}{2}}\cos 2\phi\right)^{\frac{1}{2}}} \\
y &= \frac{L\sin\phi}{\left(I_1 - (I_1^2 - \omega^2 P^2)^{\frac{1}{2}}\cos 2\phi\right)^{\frac{1}{2}}} \\
z &= \frac{\lambda}{\left(I_1 - (I_1^2 - \omega^2 P^2)^{\frac{1}{2}}\cos 2\phi\right)^{\frac{1}{2}}}.
\end{aligned}
\tag{3.14.26}
$$

For this case the equation of motion (3.13.26) becomes that of the three–dimensional isotropic harmonic oscillator in the variable $\boldsymbol{r} \times \boldsymbol{P}$. The orbit equation is then given by

$$
|\boldsymbol{r} \times \boldsymbol{P}|^2 = L^2 r^2 = \frac{L^2 P^2}{I_1 - \left({I_1}^2 - \omega^2 P^2\right)^{\frac{1}{2}}\cos 2\phi},
\tag{3.14.27}
$$

i.e. the projection of the orbit into the $\phi-$plane describes a geometric–centred ellipse symmetrically placed about the $x-$axis with the centre at the intersection of $\boldsymbol{P}$ and the $\phi-$plane. It is well–known that the intersection of a plane and a right circular cone describes a conic section on the cone. However, in this case, although the projection of the orbit on the cone into the $\phi-$plane describes a geometric–centred ellipse, the orbit on the cone does not lie on a plane. The xz and yz projections of the orbit on the cone will be studied later in the section where it will be shown that this peculiar geometry is the result of the intersection between the cone and a surface which is closely related to two different conic sections. This association gives an interesting geometric interpretation as to why the three–dimensional isotropic harmonic oscillator ellipse differs from that of the Kepler problem. The eccentricity of the ellipse is given by

$$
\frac{1}{\omega P}\left(4(I_1^2 - \omega^2 P^2)\right)^{\frac{1}{4}}\left(I_1 - (I_1^2 - \omega^2 P^2)^{\frac{1}{2}}\right)^{\frac{1}{2}}
\tag{3.14.28}
$$

which no longer appears to be related in a transparent way to the slope of the cone $(\cot\alpha)$ as was the case in the MICZ problem. Note also that $\boldsymbol{P}$ behaves like $\boldsymbol{L}$ in the three–dimensional isotropic harmonic oscillator.

It is easy to show using the orbit equation (3.14.6) that the maximum length of the vector $\boldsymbol{r}$, $r_{\max}$ on the surface of the cone is reduced in length by the factor $\sin\alpha$ when projected into the ϕ–plane due to its inclination with respect to $\boldsymbol{P}$ and so the projection

$$r_{\max}\sin\alpha = \frac{L}{\omega P}\Big(I_1 + (I_1^2 - \omega^2 P^2)^{\frac{1}{2}}\Big)^{\frac{1}{2}} = \frac{1}{P}|\boldsymbol{r}\times\boldsymbol{P}|_{\max}, \tag{3.14.29}$$

is consistent with the result for the semi–major axis length of the projected ellipse from (3.14.27) up to a scaling factor of P and ignoring the rotation brought about by the transformation. Similarly the minimum length of the vector $\boldsymbol{r}$, $r_{\min}$ on the surface of the cone is reduced in length by the same factor $\sin\alpha$ when projected into the ϕ–plane due to its inclination with respect to $\boldsymbol{P}$ and so the projection

$$r_{\min}\sin\alpha = \frac{L}{\omega P}\Big(I_1 - (I_1^2 - \omega^2 P^2)^{\frac{1}{2}}\Big)^{\frac{1}{2}} = \frac{1}{P}|\boldsymbol{r}\times\boldsymbol{P}|_{\min} \tag{3.14.30}$$

is consistent with the result for the semi–minor axis length of the projected ellipse from (3.14.27) up to a scaling factor of P and ignoring the rotation brought about by the transformation. Note also that the orbit on the cone does not lie in a plane as was the case for the monopole–Kepler problem. The orbit resembles the outline of a saddle which is draped over the cone in such a way that its projection describes a geometric–centred ellipse.

The parametric equations for the velocity hodograph can be obtained by differentiating the cartesian components x, y and z (3.14.26), substituting for $\phi = -L/(r^2\sin\alpha)$ to give

$$\begin{aligned}
\dot{x} &= \frac{\Big(I_1 + (I_1^2 - \omega^2 P^2)^{\frac{1}{2}}\Big)\sin\alpha\sin\phi}{\Big(I_1 - (I_1^2 - \omega^2 P^2)^{\frac{1}{2}}\cos 2\phi\Big)^{\frac{1}{2}}} \\
\dot{y} &= -\frac{\Big(I_1 - (I_1^2 - \omega^2 P^2)^{\frac{1}{2}}\Big)\sin\alpha\cos\phi}{\Big(I_1 - (I_1^2 - \omega^2 P^2)^{\frac{1}{2}}\cos 2\phi\Big)^{\frac{1}{2}}} \\
\dot{z} &= \frac{(I_1^2 - \omega^2 P^2)^{\frac{1}{2}}\cos\alpha\sin 2\phi}{\Big(I_1 - (I_1^2 - \omega^2 P^2)^{\frac{1}{2}}\cos 2\phi\Big)^{\frac{1}{2}}}.
\end{aligned} \tag{3.14.31}$$

The analogues of Kepler's three laws of motion for this system then become :-

(i) For positive energies the orbit resembles the outline of a saddle which is draped over the cone in such a way that its projection describes a geometric–centred ellipse. The origin is not coplanar with the orbit.

(ii) Equal areas are swept out on the cone in equal times. As in the monopole–Kepler problem, the area swept out on the cone is given by (denoting the quantities on the cone with the subscript MO and those in the plane with $\perp MO$)

$$\mathrm{d}\mathbf{A}_{MO} = \frac{1}{2}\boldsymbol{r} \times \dot{\boldsymbol{r}}\ \mathrm{d}t \tag{3.14.32}$$

and so

$$\frac{\mathrm{d}A_{MO}}{\mathrm{d}t} = \frac{1}{2}L = \text{const.} \tag{3.14.33}$$

Similarly for the ellipse in the $\phi-$plane

$$\frac{\mathrm{d}A_{\perp MO}}{\mathrm{d}t} = \frac{1}{2}\left|(\boldsymbol{r} \times \boldsymbol{P}) \times (\dot{\boldsymbol{r}} \times \boldsymbol{P})\right| = \frac{1}{2}L^2P. \tag{3.14.34}$$

After rescaling $\mathrm{d}A_{\perp MO}/\mathrm{d}t$ by P^2, since we are dealing with an area, it is clear that the rate of increse in area on the cone is larger than on the projected ellipse by the factor $P/L = 1/\sin\alpha$ as was the case for the MICZ elliptical orbit.

The surface area extending from the base of the orbital cone to the line of the orbit is found by integrating (3.14.33) over the period of the motion which gives

$$A_{MO} = \frac{1}{2}\int_0^{2\pi} r^2 \sin\alpha\dot{\phi}\ \mathrm{d}t. \tag{3.14.35}$$

Substituting for r^2 from (3.14.6) we can express the integrand in terms of ϕ and obtain

$$A_{MO} = \frac{1}{2}\sin\alpha\int_0^{2\pi} \frac{P^2\mathrm{d}\phi}{I_1 - (I_1^2 - \omega^2P^2)^{\frac{1}{2}}\cos 2\phi}. \tag{3.14.36}$$

Making the substitution $\eta = 2\phi$ gives

$$A_{MO} = \frac{P^2\sin\alpha}{I_1}\int_0^{\pi} \frac{\mathrm{d}\eta}{1 - (1 - \omega^2P^2/I_1^2)^{\frac{1}{2}}\cos\eta}, \tag{3.14.37}$$

which can be integrated using G&R[43, 3.613.1 with n=0] to give

$$A_{MO} = \frac{\pi L}{\omega}. \tag{3.14.38}$$

The area of the ellipse projected in the plane is given by

$$A_{\perp MO} = \pi ab = \frac{\pi PL^2}{\omega}, \tag{3.14.39}$$

which upon rescaling by P^2 gives

$$A_{\perp MO} = \frac{\pi L^2}{P\omega} = A_{MO} \sin\alpha, \tag{3.14.40}$$

and so we observe that the surface area of the section of cone between the origin and the line of the orbit is inversely proportional to ω.

As expected the ratio of $A_{MK}/A_{\perp MK}$ is again P/L which is the same ratio as we obtained for the areal velocities. Alternatively we can consider an infinitesimal area on the cone stretching from the origin to two closely spaced points on the orbit. If we project this area into the plane, it is clear that the projection is just $\Delta A_{\perp MO} = \Delta A_{MO} \sin\alpha$ which, extended over the complete area in both cases, is the result we obtained previously.

(iii) Equation (3.14.33) can be integrated over one revolution to give an alternate expression for the area,

$$A_{MO} = \frac{1}{2} LT. \tag{3.14.41}$$

Equating (3.14.38) with (4.14.41) gives the analogue of Kepler's third law, *i.e.*,

$$T = \frac{2\pi}{\omega} \tag{3.14.42}$$

for both the orbit on the cone and the orbit in the plane, *i.e.* the period is inversely proportional to ω.

The initial conditions were chosen so that the projection of the orbit on the cone into the $\phi-$plane is identical to the corresponding three–dimensional isotropic harmonic oscillator orbit and also that the projection of the velocity hodograph into the $\phi-$plane is coincident with that of the oscillator as shown in Figure 1.7.2 of Chapter 1. This was done in much the same way as that described for the MICZ problem by equating certain quantities on the cone on projection into the $\phi-$plane with the equivalent quantities for the three–dimensional isotropic harmonic oscillator. In the subsequent discussion, the starred quantities will be used to denote the constants used in Chapter 1 for the oscillator. The constants have the values, as before, $\mu_k^* = 1.25$, $\theta_0^* = 0$, $a_k^* = 1.89\dot{3}\dot{9}$, $\lambda^* = (\mu_k^*/a_k^{*3})^{\frac{1}{2}}$, $E^* = 0.4694$ and $L^* = 1$. Combinations of the semi–major and semi–minor axis lengths for both the projections of the velocity hodograph and the orbit of the monopole–oscillator were equated with the corresponding expressions for the three–dimensional isotropic harmonic oscillator to force both the the velocity hodographs and the orbits to coincide so that a comparison between the two problems can be made. Multiplying the squares of the lengths of the semi–major and semi–minor axes for both the projection of the monopole–oscillator

velocity hodograph (3.14.20) and making a comparison with the same quantity in the case of the three–dimensional isotropic harmonic oscillator gives

$$\omega = \frac{\lambda^* P L^*}{L^2}. \tag{3.14.43}$$

Summing the squares of the lengths of the semi–major and semi–minor axes for both the projection of the monopole–oscillator velocity hodograph (3.14.20) and making a comparison with the same quantity in the case of the three–dimensional isotropic harmonic oscillator gives, using (3.14.43),

$$I_1 = \frac{P^2 E^*}{L^2}. \tag{3.14.44}$$

Repeating the above procedures for the projection of the monopole–oscillator orbit (3.14.23) and making the same comparisons with the three–dimensional isotropic harmonic oscillator gives

$$\omega = \frac{\lambda^* L^2}{P L^*}, \tag{3.14.45}$$

and eliminating ω from (3.14.43) and (3.14.45) gives

$$P = \frac{L^2}{L^*}, \tag{3.14.46}$$

which is the same result obtained previously for the MICZ problem, and substituting this result in either (3.14.43) or (3.14.45) gives

$$\omega = \lambda^*, \tag{3.14.47}$$

and similarly substituting (3.14.46) in (3.14.44) gives

$$I_1 = \frac{L^2}{L^{*2}} E^*. \tag{3.14.48}$$

Using the definition of P it can be shown that

$$\lambda = \frac{L}{L^*}\left(L^2 - L^{*2}\right)^{\frac{1}{2}}, \tag{3.14.49}$$

and using (3.14.1) and (3.14.2)

$$\alpha = \arccos\left(\frac{(L^2 - L^{*2})^{\frac{1}{2}}}{L}\right) = \arcsin\left(\frac{L^*}{L}\right), \tag{3.14.50}$$

as was found for the MICZ problem. Note that the angle α only depends on the projection of the monopole–oscillator angular momentum $\boldsymbol{L}$ onto the three–dimensional isotropic harmonic oscillator angular momentum $\boldsymbol{L}^*$ which is directed along the line of $\boldsymbol{P}$. The magnitude of $\boldsymbol{J}_O$ can also be expressed in terms of L and L^* using the above expressions (3.14.46)–(3.14.48) to obtain

$$J_O = \frac{L^4}{\lambda^* L^{*2}}\left(E^{*2} - \lambda^{*2} L^{*2}\right)^{\frac{1}{2}}. \tag{3.14.51}$$

For convenience, L was chosen to be 1.85 and using the values for the starred quantities given above, P, ω, I_1, λ, α and J_O were calculated using (3.14.46)–(3.14.51).

Figure 3.14.2 shows the orbit for the monopole–oscillator where $\mu = -\lambda^2$. The diagram shows the two right circular orbital and angular momentum cones which extend in opposite directions along the line of $\boldsymbol{P}$ with origin and point of contact at the apices of the two cones. A selection of displacement and corresponding angular momentum vectors has been drawn from the origin to their respective positions on the orbital and angular momentum cones. The orbit resembles the outline of a saddle which is draped over the cone in such a way that its xy projection describes a geometric–centred ellipse. The origin is not enclosed by the orbit. In order to illustrate the behaviour more clearly, projections of the orbit onto planes parallel to the xy, xz and yz planes are shown, together with projections of the angular momentum curve and the projected images of the cones onto the respective planes. The constant magnitude of the angular momentum is reflected by the angular momentum vectors moving on the surface of a cone which is truncated perpendicular to the axis of symmetry to a height of L^2/P below the origin. The components of the angular momentum are given by $L = (\lambda L \cos\phi/P, \lambda L \sin\phi/P, -L^2/P)$ using (3.14.26) and (3.14.31).

The xy projection of the orbit is elliptical as described by the first two equations of (3.14.26) which can be manipulated into the form

$$\left(\frac{x}{\frac{L\left(I_1+(I_1^2-\omega^2P^2)^{\frac{1}{2}}\right)^{\frac{1}{2}}}{\omega P}}\right)^2 + \left(\frac{y}{\frac{L\left(I_1-(I_1^2-\omega^2P^2)^{\frac{1}{2}}\right)^{\frac{1}{2}}}{\omega P}}\right)^2 = 1 \tag{3.14.52}$$

which is the cartesian representation of an ellipse symmetrically placed about the $x = 0$ and $y = 0$ axes, with semi–major axis length $a = L\left(I_1 + (I_1{}^2 - \omega^2P^2)^{\frac{1}{2}}\right)^{\frac{1}{2}}/(\omega P)$ which is the projection of $r_{\max}$ onto the $xy-$plane, *i.e.* $r_{\max}\sin\alpha$, semi–minor axis of length $b = L\left(I_1 - (I_1{}^2 - \omega^2P^2)^{\frac{1}{2}}\right)^{\frac{1}{2}}/(\omega P)$, which is the projection of $r_{\min}$ onto the $xy-$plane, *i.e.* $r_{\min}\sin\alpha$, eccentricity of $\left(4(I_1{}^2 - \omega^2P^2)\right)^{\frac{1}{4}}\left(I_1 - (I_1{}^2 - \omega^2P^2)^{\frac{1}{2}}\right)^{\frac{1}{2}}/(\omega P)$

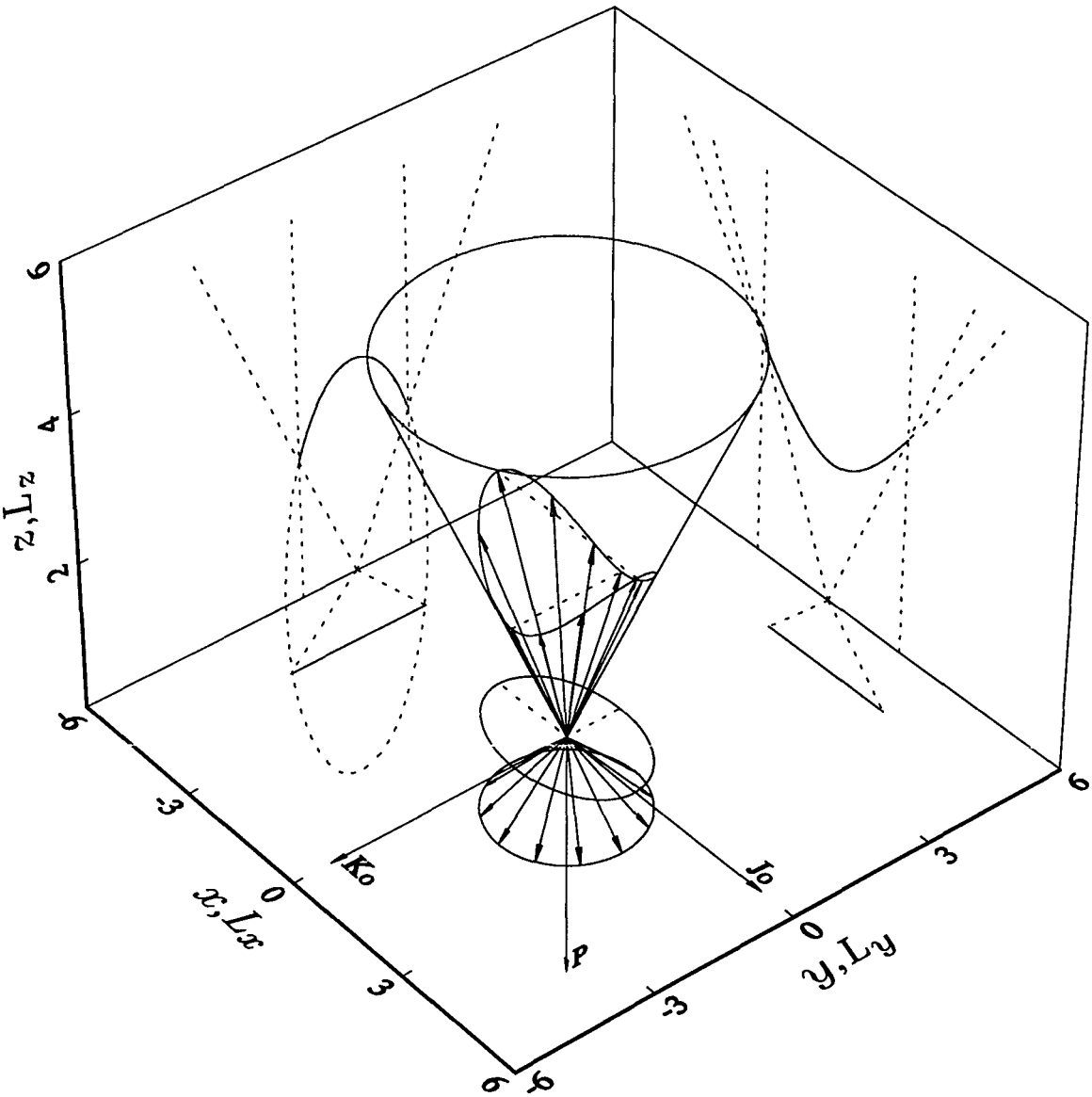

Figure 3.14.2. The monopole–oscillator orbit and angular momentum curve for $\mu = -\lambda^2$ with a selection of displacement and angular momentum vectors drawn from the origin. The radial and angular momentum vectors move on the surfaces of two right circular cones extending in opposite directions along the line of $\boldsymbol{P}$ with origin and point of contact at the apices of the two cones. The projections of the orbit and angular momentum curve onto planes parallel to the xy, xz, yz, L_xL_y, L_xL_z and L_yL_z planes are also shown. The constants have the values $\omega = 0.4289$, $P = 3.4225$, $\lambda = 2.8794$, $\alpha = 0.5711$, $L = 1.85$ and $I_1 = 1.6065$. The origin is not enclosed by the orbit.

and centred at the origin. The projected orbit is consistent with the planar elliptical three–dimensional isotropic harmonic oscillator orbit with $\mu_k^* = 1.25$, $\theta_0^* = 0$, $a_k^* = 1.893\dot{9}$, $\lambda^* = (\mu_k/a_k^3)^{\frac{1}{2}}$, $E^* = 0.4694$ and $L^* = 1$. As t ranges over one period and choosing the azimuthal angle ϕ to range between π and $-\pi$, the projection ranges from $(-a, 0)$ when $\phi = \pi$ where $a = r_{\max} \sin\alpha$ and $b = r_{\min} \sin\alpha$ to $(0, b)$ when $\phi = \pi/2$ to $(a, 0)$ when $\phi = 0$ to $(0, -b)$ when $\phi = -\pi/2$ to $(-a, 0)$ when $\phi = -\pi$. The projection of the angular momentum curve onto its corresponding plane describes a circle with radius $\lambda L/P$ symmetrically placed about the L_x-axis, *i.e.* ${L_x}^2 + {L_y}^2 = (\lambda L/P)^2$. As t ranges over one period, the projection ranges from $(-\lambda L/P, 0)$ when $\phi = \pi$ to $(0, \lambda L/P)$ when $\phi = \pi/2$ to $(\lambda L/P, 0)$ when $\phi = 0$ to $(0, -\lambda L/P)$ when $\phi = -\pi/2$ to $(-\lambda L/P, 0)$ when $\phi = -\pi$, *i.e.* the circle is completed. The projection of the angular momentum vectors describes a circle after one revolution of the orbit.

The xz projection shows the images of the orbital and angular momentum cones with dotted lines, together with the projections of the orbit and angular momentum curves. Note that the xz projection of the orbit is obtained by manipulating the first and third equations of (3.14.26) into the form

$$\left(\frac{z}{\frac{\lambda\left(I_1 - (I_1^2 - \omega^2 P^2)^{\frac{1}{2}}\right)^{\frac{1}{2}}}{\omega P}} \right)^2 - \left(\frac{x}{\frac{L}{\left(4(I_1^2 - \omega^2 P^2)\right)^{\frac{1}{4}}}} \right)^2 = 1 \qquad (3.14.53)$$

subject to the condition that

$$|x| \leq \frac{L}{\omega P} \left(I_1 + (I_1^2 - \omega^2 P^2)^{\frac{1}{2}}\right)^{\frac{1}{2}} \qquad (3.14.54)$$

which is the cartesian representation of a section of a hyperbola symmetrically placed about the $x = 0$ and $z = 0$ axes, with vertices at $(0, \pm a)$ where $a = \lambda\Big(I_1 - (I_1^2 - \omega^2 P^2)^{\frac{1}{2}}\Big)^{\frac{1}{2}}/(\omega P)$ and $b = L/\Big(4(I_1^2 - \omega^2 P^2)\Big)^{\frac{1}{4}}$ foci at $(0, \pm(a^2 + b^2)^{\frac{1}{2}})$, eccentricity of $(a^2 + b^2)^{\frac{1}{2}}/a$ and centred at the origin. The distance from the centre to a vertex a agrees with the length of the projection of $r_{\min}$ onto the $xz-$plane, *i.e.* $r_{\min} \cos\alpha$. The transverse axis is the same length as the distance between the two vertices $2a$. The conjugate axis has the length $2b$. The asymptotes are given by $z = ax/b$, *i.e.* a combination of the first and third equations of (3.14.26). The relationship between the eccentricity e of the hyperbolic projection in the $xz-$plane and that of the elliptical projection in the $xy-$plane, e^*, is found to be $e^2 = 1/m^2 b^2/\Big(a^{*2}(1 - e^{*2})\Big) + 1$, where m is the slope of the cone $(\cot\alpha)$ and the superscript $*$ refers to the equivalent quantities in (3.14.52). Note that the semi–transverse axis length of (3.14.53)

and the semi–minor axis length of (3.14.52) are not involved in the relationship between the two eccentricities. The magnitude of the limits of extent of the variable x which are indicated with two dotted lines parallel to the $z-$axis agree with the length of the projection of $r_{\max}$ onto the $xy-$plane, *i.e.* $r_{\max}\sin\alpha$. The magnitude of z at these two points agrees with the height of the projection of $r_{\max}$ onto the $xz-$plane, *i.e.* $r_{\max}\cos\alpha$. As t ranges over one period, the projection ranges from $(-c,d)$ when $\phi=\pi$ where $a=r_{\min}\cos\alpha$, $c=r_{\max}\sin\alpha$ and $d=r_{\max}\cos\alpha$ to $(0,a)$ when $\phi=\pi/2$ to (c,d) when $\phi=0$ to $(0,a)$ when $\phi=-\pi/2$ to $(-c,d)$ when $\phi=-\pi$. The L_xL_z projection of the angular momentum curve extends along the base of the triangle describing the L_xL_z projection of the image of the angular momentum cone, perpendicular to the L_z-axis. As t ranges over one period, the projection ranges from $(-\lambda L/P,-L^2/P)$ when $\phi=\pi$ to $(0,-L^2/P)$ when $\phi=\pi/2$ to $(\lambda L/P,-L^2/P)$ when $\phi=0$ to $(0,-L^2/P)$ when $\phi=-\pi/2$ to $(-\lambda L/P,-L^2/P)$ when $\phi=-\pi$, *i.e.* the full length of the base of the angular momentum triangle. In other words the angular momentum vectors will have swept over the entire surface area of the angular momentum cone.

The yz projection shows the images of the orbital and angular momentum cones with dotted lines, together with the projections of the orbit and angular momentum curves. Note that the yz projection of the orbit is obtained by manipulating the second and third equations of (3.14.26) into the form

$$\left(\frac{y}{\frac{L}{\left(4(I_1^2-\omega^2P^2)\right)^{\frac{1}{4}}}}\right)^2+\left(\frac{z}{\frac{\lambda\left(I_1+(I_1^2-\omega^2P^2)^{\frac{1}{2}}\right)^{\frac{1}{2}}}{\omega P}}\right)^2=1 \qquad (3.14.55)$$

subject to the condition that

$$|y|\leq\frac{L}{\omega P}\left(I_1-(I_1^2-\omega^2P^2)^{\frac{1}{2}}\right)^{\frac{1}{2}} \qquad (3.14.56)$$

which is the equation of a section of an ellipse symmetrically placed about the $y=0$ and $z=0$ axes, with semi–major axis length $a=\lambda\left(I_1+(I_1^2-\omega^2P^2)^{\frac{1}{2}}\right)^{\frac{1}{2}}/(\omega P)$, which is equivalent to the projection of $r_{\max}$ onto the $yz-$plane, *i.e.* $r_{\max}\cos\alpha$, semi–minor axis length $b=L/\left(4(I_1^2-\omega^2P^2)\right)^{\frac{1}{4}}$, eccentricity of $(a^2-b^2)^{\frac{1}{2}}/a$ and centred at the origin. The relationship between the eccentricity e of the elliptical projection in the $xz-$plane and that of the elliptical projection in the $xy-$plane, e^*, is found to be $e^2=1/m^2b^2(e^{*2}-1)/b^{*2}+1$, where m is the slope of the cone, $(\cot\alpha)$, and the superscript $*$ refers to the equivalent quantities in (3.14.52). Note that the semi–major axis lengths of both projections are not involved in the relationship between

the two eccentricities. The magnitude of the limits of extent of the variable y which are indicated with two dotted lines parallel to the $z-$axis agree with the length of the projection of $r_{\min}$ onto the $xy-$plane, *i.e.* $r_{\min}\sin\alpha$. The magnitude of z at these two points agrees with the height of the projection of $r_{\min}$ onto the $xz-$plane, *i.e.* $r_{\min}\cos\alpha$. As t ranges over one period, the projection ranges from $(0,a)$ when $\phi=\pi$ where $a=r_{\max}\cos\alpha$, $c=r_{\min}\sin\alpha$ and $d=r_{\min}\cos\alpha$ to (c,d) when $\phi=\pi/2$ to $(0,a)$ when $\phi=0$ to $(-c,d)$ when $\phi=-\pi/2$ to $(0,a)$ when $\phi=-\pi$. The L_yL_z projection of the angular momentum curve lies along the base of the triangle describing the L_yL_z projection of the image of the angular momentum cone, perpendicular to the L_z-axis. As t ranges over one period, the line segment extends along the full length of the base of the angular momentum triangle from the point $(0,-L^2/P)$ when $\phi=\pi$ to $(\lambda L/P,-L^2/P)$ when $\phi=\pi/2$ to $(0,-L^2/P)$ when $\phi=0$ to $(-\lambda L/P,-L^2/P)$ when $\phi=-\pi/2$ to $(0,-L^2/P)$ when $\phi=-\pi$. In other words the angular momentum vectors will have swept over the entire surface area of the angular momentum cone.

The conserved vector $\boldsymbol{K}_O$ which has been rotated clockwise through $\pi/2$ radians to lie along the cartesian unit vector $-\boldsymbol{j}$ is given by (3.14.15) and has length $(E_O^2/\omega^2-L_O^2)^{\frac{1}{2}}$ and is scaled by L for convenience in Figure 3.14.2. The vector $\boldsymbol{J}_O$, which is perpendicular to $\boldsymbol{K}_O$, is also rotated clockwise through $\pi/2$ radians to lie along the cartesian unit vector $\boldsymbol{i}$. $\boldsymbol{J}_O$ also has the length $(E_O^2/\omega^2-L_O^2)^{\frac{1}{2}}$ and is similarly scaled by L in Figure 3.14.2. The Poincaré vector, $\boldsymbol{P}$, lies along the cartesian unit vector $-\boldsymbol{k}$. Note that, when the cone is rotated about the $x-$axis so that $\boldsymbol{P}$ lies along $\boldsymbol{k}$, the vectors $\boldsymbol{K}_O$ and $\boldsymbol{J}_O$ lie along the cartesian unit vectors $\boldsymbol{j}$ and $\boldsymbol{i}$ respectively and hence mimic the behaviour of $\boldsymbol{L}$, $\boldsymbol{K}$ and $\boldsymbol{J}$ respectively of the standard three–dimensional isotropic harmonic oscillator. The Poincaré vector is given by (3.13.4) and has components $\left(0,0,-(L^2+\lambda^2)^{\frac{1}{2}}\right)$.

Figure 3.14.3 shows the velocity hodograph for the monopole–oscillator where $\mu=-\lambda^2$. A selection of velocity vectors corresponding to the displacement vectors shown in Figure 3.14.2 has been drawn from the origin to their respective positions on the velocity hodograph. In order to illustrate the $\dot{\boldsymbol{r}}$ behaviour more clearly, projections of the velocity hodograph onto planes parallel to the $\dot{x}\dot{y}$, $\dot{x}\dot{z}$ and $\dot{y}\dot{z}$ planes are also shown, together with the projected images of the orbital cone onto the respective planes.

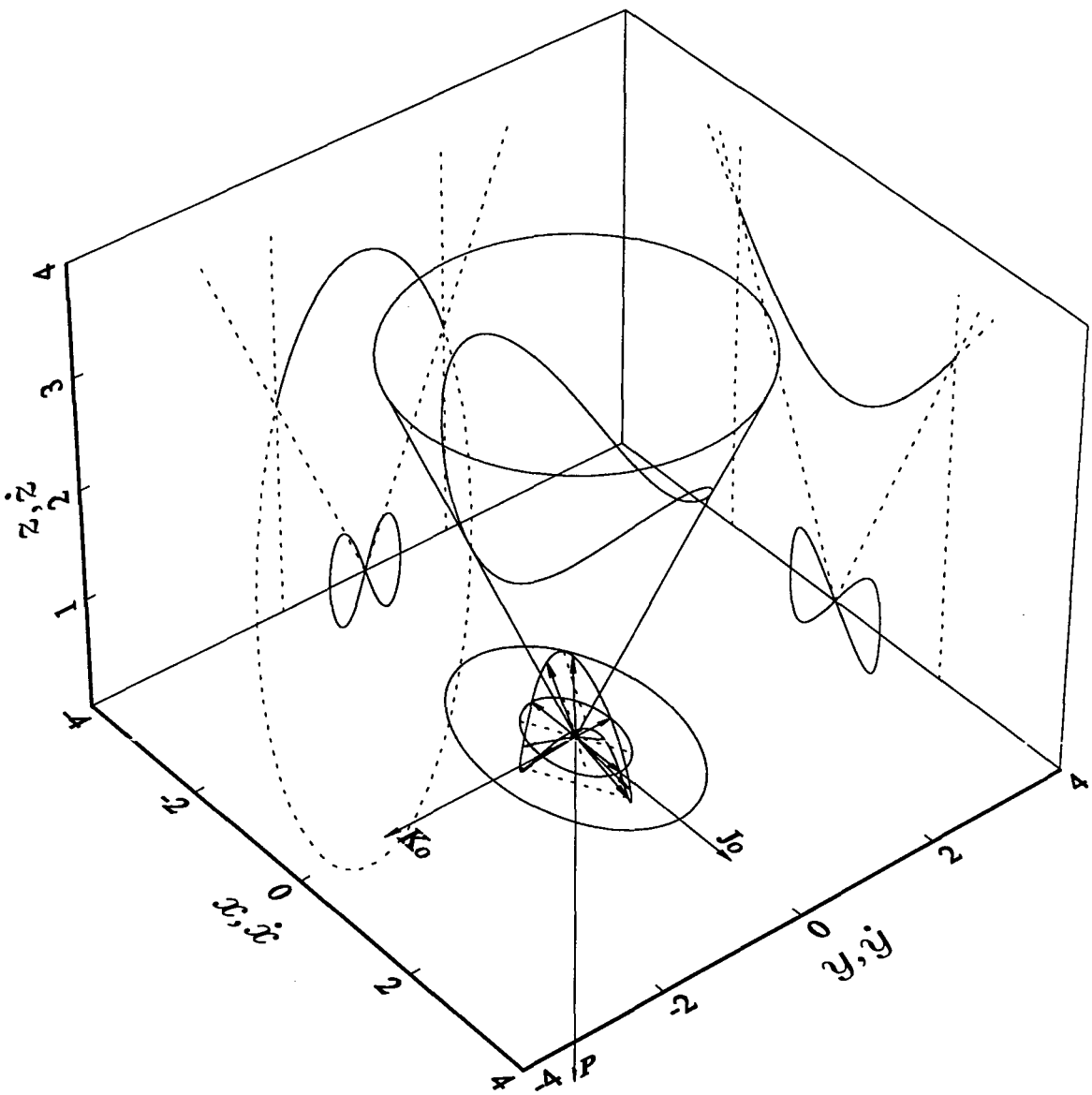

Figure 3.14.3. The monopole–oscillator velocity hodograph and orbit for $\mu = -\lambda^2$ with a selection of velocity vectors drawn from the origin. The velocity vectors are not confined to a plane although, as t ranges over one period, the heads of the velocity vectors projected into the $\dot{x}\dot{y}$–plane trace out a complete ellipse. The projections of the velocity hodograph and orbit onto planes parallel to the $\dot{x}\dot{y}$, $\dot{x}\dot{z}$, $\dot{y}\dot{z}$, xy, xz and yz planes are also shown. The constants are chosen as for Figure 3.14.2. The origin is enclosed by the velocity hodograph.

The $\dot{x}\dot{y}$ projection of the velocity hodograph is obtained by manipulating the first two equations of (3.14.31) into the form

$$\left(\frac{\dot{x}}{\frac{L\left(I_1+(I_1^2-\omega^2P^2)^{\frac{1}{2}}\right)^{\frac{1}{2}}}{P}}\right)^2+\left(\frac{\dot{y}}{\frac{L\left(I_1-(I_1^2-\omega^2P^2)^{\frac{1}{2}}\right)^{\frac{1}{2}}}{P}}\right)^2=1 \tag{3.14.57}$$

which is the cartesian equation of an ellipse concentric to (3.14.52) symmetrically placed about the $\dot{x}=0$ and $\dot{y}=0$ axes, with semi-major axis of length $a=L\Big(I_1+(I_1{}^2-\omega^2P^2)^{\frac{1}{2}}\Big)^{\frac{1}{2}}/P$, semi-minor axis of length $b=L\Big(I_1-(I_1{}^2-\omega^2P^2)^{\frac{1}{2}}\Big)^{\frac{1}{2}}/P$ and eccentricity $\Big(4(I_1{}^2-\omega^2P^2)\Big)^{\frac{1}{4}}\Big(I_1-(I_1{}^2-\omega^2P^2)^{\frac{1}{2}}\Big)^{\frac{1}{2}}/(\omega P)$ and centred at the origin. The projected velocity hodograph is consistent with the planar velocity hodograph for the elliptical three-dimensional isotropic harmonic oscillator with $\mu_k^*=1.25$, $\theta_0^*=0$, $a_k^*=1.893\dot{9}$, $\lambda^*=(\mu_k^*/a_k^{*3})^{\frac{1}{2}}$, $E^*=0.4694$ and $L^*=1$. As t ranges over one period, the projection ranges from the point $(0,b)$ when $\phi=\pi$ where $a=\omega r_{\max}\sin\alpha$ and $b=\omega r_{\min}\sin\alpha$ to $(a,0)$ when $\phi=\pi/2$ to $(0,-b)$ when $\phi=0$ to $(-a,0)$ when $\phi=-\pi/2$ to $(0,b)$ when $\phi=-\pi$, *i.e.* the ellipse is completed. The projection of the velocity vectors describes an ellipse after one revolution of the orbit.

The $\dot{x}\dot{z}$ projection shows the images of the orbital cone with dotted lines, together with the respective projections of the orbit and velocity hodograph. Note that the $\dot{x}\dot{z}$ projection of the velocity hodograph is obtained by manipulating the first and third equations of (3.14.31) into the form

$$\dot{z}^2=\frac{4B^2\cot^2\alpha\dot{x}^2}{(A+B)}\left(\frac{(A+B)\sin^2\alpha-\dot{x}^2}{(A+B)^2\sin^2\alpha-2B\dot{x}^2}\right), \tag{3.14.58}$$

where $A=I_1$ and $B=(I_1^2-\omega^2P^2)^{\frac{1}{2}}$, which describes a butterfly-shaped curve symmetrically placed about the $\dot{x}=0$ axis and is reminiscent of quartic curves such as the *lemniscates* of Bernoulli and Gerono. As t ranges over one period, the projection ranges from the point $(0,0)$ when $\phi=\pi$ where $a=\omega r_{\max}\sin\alpha$ and $b=\omega r_{\min}\sin\alpha$ to $(a,0)$ when $\phi=\pi/2$ to $(0,0)$ when $\phi=0$ to $(-a,0)$ when $\phi=-\pi/2$ to $(0,0)$ when $\phi=-\pi$.

The $\dot{y}\dot{z}$ projection shows the images of the orbital cone with dotted lines, together with the respective projections of the orbit and velocity hodograph. Note that the $\dot{y}\dot{z}$ projection of the velocity hodograph is obtained by manipulating the second and third equations of (3.14.31) into the form

$$\dot{z}^2=\frac{4B^2\cot^2\alpha\dot{y}^2}{(B-A)}\left(\frac{\dot{y}^2+(B-A)\sin^2\alpha}{(B-A)^2\sin^2\alpha+2B\dot{y}^2}\right), \tag{3.14.59}$$

where $A = I_1$ and $B = (I_1^2 - \omega^2 P^2)^{\frac{1}{2}}$, which describes a butterfly–shaped curve symmetrically placed about the $\dot{y} = 0$ axis and is reminiscent of quartic curves such as the *lemniscates* of Bernoulli and Gerono. As t ranges over one period, the projection ranges from the point $(b, 0)$ when $\phi = \pi$ where $a = \omega r_{\max} \sin\alpha$ and $b = \omega r_{\min} \sin\alpha$ to $(0, 0)$ when $\phi = \pi/2$ to $(-b, 0)$ when $\phi = 0$ to $(0, 0)$ when $\phi = -\pi/2$ to $(b, 0)$ when $\phi = -\pi$.

The conserved vectors $\boldsymbol{K}_O$ and $\boldsymbol{J}_O$ are scaled by L for convenience while $\boldsymbol{P}$ is drawn as in Figure 3.14.2

Figure 3.14.4 shows the same orbit and velocity hodograph as those shown in Figure 3.14.3 but rotated about the $z, \dot{z}$–axis in such a way that the $\dot{z}$–maxima are vertically aligned above the $x, \dot{x}$ axis. This was done to investigate whether the $\dot{x}\dot{z}$ and $\dot{y}\dot{z}$ projections of the velocity hodograph could be rotated onto principal axes in both orthogonal planes in such a way that their structure became more transparent. The angle of rotation about the $\dot{z}$–axis was calculated as follows. Replacing occurrences of ϕ with ρ to avoid confusion, the $\dot{z}$ component of (3.14.31) becomes

$$\dot{z}(\phi = \rho) = \frac{B \cos\alpha \sin 2\rho}{(A - B\cos 2\rho)^{\frac{1}{2}}}, \tag{3.14.60}$$

where $A = I_1$ and $B = (I_1^2 - \omega^2 P^2)^{\frac{1}{2}}$, which can be differentiated with respect to ρ to give

$$\frac{\mathrm{d}\dot{z}}{\mathrm{d}\rho} = -\frac{B^2 \cos\alpha \left(\cos^2 2\rho - \frac{2A}{B}\cos 2\rho + 1\right)}{(A - B\cos 2\rho)^{\frac{3}{2}}}. \tag{3.14.61}$$

To calculate ρ at a maximum or a minimum we set (3.14.61) equal to zero and solve the resulting quadratic equation in $\cos 2\rho$ to obtain

$$\cos 2\rho = \frac{A \pm (A^2 - B^2)^{\frac{1}{2}}}{B}. \tag{3.14.62}$$

Only the smaller of the two solutions shown in (3.14.62) is of physical interest. The azimuthal angle at the maximum or minimum $\dot{z}$ value is given by

$$\gamma = \arctan\left(\frac{\dot{y}(\phi = \rho)}{\dot{x}(\phi = \rho)}\right) = \arctan\left(\pm\frac{(B - A)}{(B + A)}\frac{(1 + \cos 2\rho)^{\frac{1}{2}}}{(1 - \cos 2\phi)^{\frac{1}{2}}}\right), \tag{3.14.63}$$

using the first two equations of (3.14.31), which can be solved using the smaller of the two solutions in (3.14.62) to obtain

$$\gamma = \mp \arctan\left(\frac{(A - B)^{\frac{3}{4}}}{(A + B)^{\frac{3}{4}}}\right), \tag{3.14.64}$$

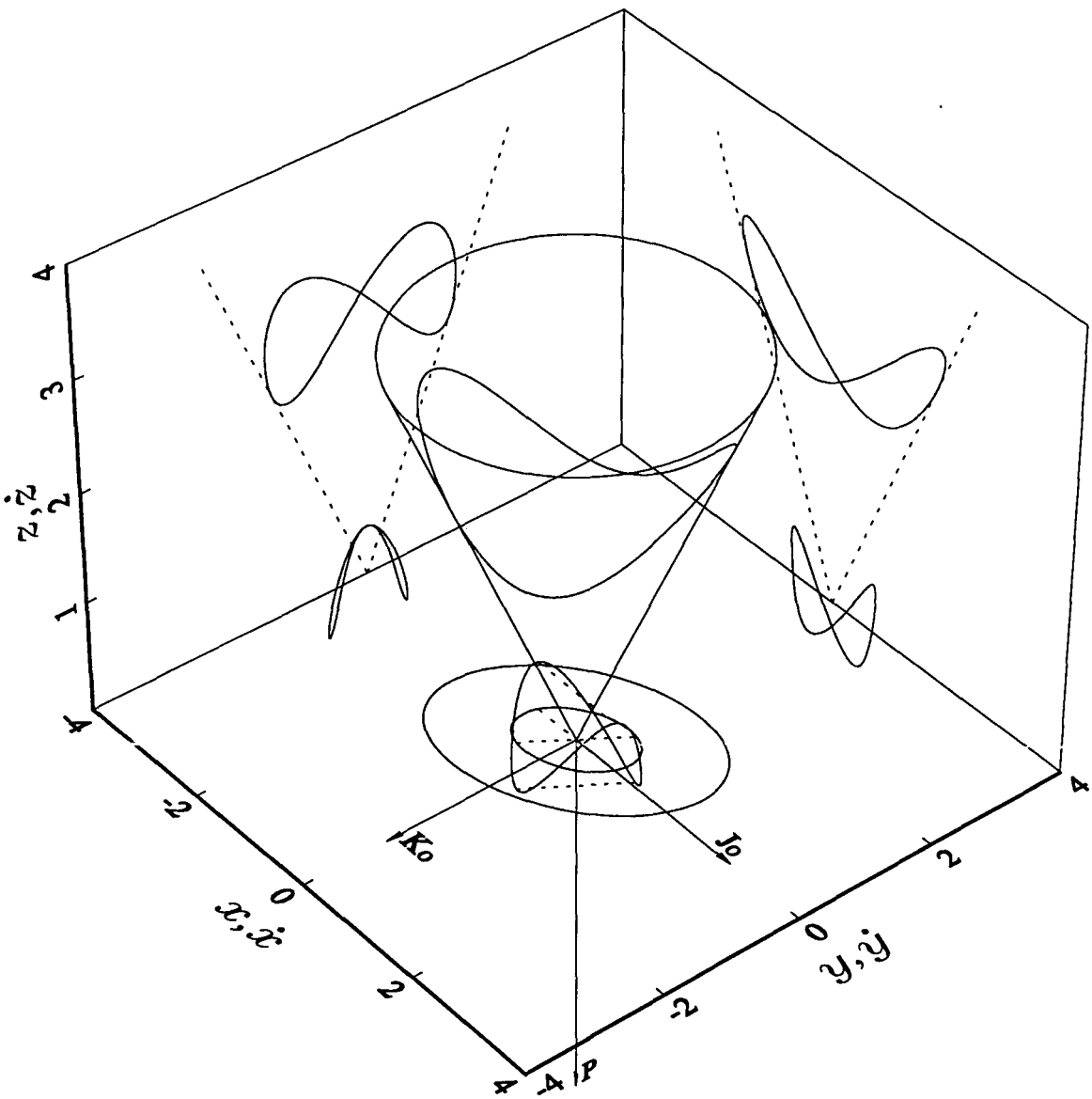

Figure 3.14.4. A counter–clockwise rotation of the monopole–oscillator velocity hodograph and orbit for $\mu = -\lambda^2$ as shown in Figure 3.14.3 through 0.4826 radians about the $z, \dot{z}-$axis so that the $\dot{z}$ maxima are vertically aligned above the $x, \dot{x}-$axis. The projections of the velocity hodograph and orbit onto planes parallel to the $\dot{x}\dot{y}$, $\dot{x}\dot{z}$, $\dot{y}\dot{z}$, xy, xz and yz planes are also shown. Note that the conic section properties of the xz and yz projections of the orbit are no longer apparent and also the lack of any recognisable structure for the $\dot{x}\dot{z}$ and $\dot{y}\dot{z}$ projections of the velocity hodograph. The constants are chosen as for Figure 3.14.2.

where the top sign gives the azimuthal angle for the $\dot{z}-$maximum and the lower sign the angle for the $\dot{z}-$minimum. The second $\dot{z}-$maximum is separated from the first $\dot{z}-$maximum by π radians which is also the case for the two $\dot{z}-$minima. Substituting the values for the constants as used in Figures 3.14.2 and 3.14.3, the azimuthal angle γ corresponding to the $\dot{z}-$maximum value closest to the origin was found to be $\gamma = -0.4826$ radians. The conserved vectors $\boldsymbol{K}_O$ and $\boldsymbol{J}_O$ are scaled by L for convenience while $\boldsymbol{P}$ is drawn as in Figure 3.14.2.

Figure 3.14.4 shows the results of performing a counter–clockwise rotation of both the orbit and the velocity hodograph by 0.4826 radians about the $z, \dot{z}-$axis. The rotated coordinates $(X, Y, Z)^T$ are obtained from the equation

$$\begin{pmatrix} X \\ Y \\ Z \end{pmatrix} = \begin{pmatrix} \cos\gamma & -\sin\gamma & 0 \\ \sin\gamma & \cos\gamma & 0 \\ 0 & 0 & 1 \end{pmatrix} \begin{pmatrix} x \\ y \\ z \end{pmatrix}. \tag{3.14.65}$$

Referring to Figure 3.14.4 it can be seen that the projection of the orbit into the $xy-$plane describes an ellipse rotated about the $z-$axis whilst the xz and yz projections now resemble figure–of–eight shaped curves which would not be obviously associated with conic sections (*cf.* Figure 3.14.3). This shows the importance of using principal axes in order to study the xz, $\dot{x}\dot{z}$, yz and $\dot{y}\dot{z}$ projections of the orbit and velocity hodograph in particular.

The projection of the velocity hodograph into the $\dot{x}\dot{y}$ plane also describes an ellipse rotated about the $\dot{z}-$axis whilst in the case of the $\dot{y}\dot{z}$ projection of the velocity hodograph, the $\dot{z}-$maxima now coincide at a point along the $\dot{z}-$axis unlike the $\dot{y}\dot{z}$ projection shown in Figure 3.14.3. The fact that this projection is not described by a single line shows that the velocity hodograph cannot be obtained from two intersecting sheets as was the case with the orbit (see (3.14.53) and (3.14.55)). The $\dot{x}\dot{z}$ projection is seen to retain a figure–of–eight shape which is again not a single line. In conclusion it appears that the velocity hodograph cannot be simplified through rotation onto suitable principal axes and only the $\dot{x}\dot{y}$ projection appears to be associated with a conic section. The short dotted line segments joining the $\dot{z}-$maxima and minima on the velocity hodograph have also been projected into the $\dot{x}\dot{y}-$plane where they confirm that the $\dot{z}-$maxima lie along the $x, \dot{x}-$axis while the $\dot{z}-$minima lie in a line which on projection into the $\dot{x}\dot{y}-$plane is not orthogonal to the $x, \dot{x}-$axis. Alternatively, referring to equation (3.14.63), a $\dot{z}-$maximum and its closest $\dot{z}-$minimum are separated by an azimuthal angle of $2|\gamma| \neq \pi/2$ radians. This further indicates that the $\dot{x}\dot{z}$ and $\dot{y}\dot{z}$ projections are not described by single lines.

The conserved vectors $\boldsymbol{K}_O$ and $\boldsymbol{J}_O$ are scaled by L for convenience while $\boldsymbol{P}$ is drawn as in Figure 3.14.3

Figure 3.14.5 geometrically demonstrates the construction of $\boldsymbol{L}$ corresponding with Figures 3.14.2 and 3.14.3. The parallelograms which represent the magnitude of $\boldsymbol{L} = \boldsymbol{r} \times \dot{\boldsymbol{r}}$ have equal areas as a consequence of L being conserved. In this case the parallelograms are no longer confined to the same plane as was the case with the three–dimensional isotropic harmonic oscillator (see Figure 1.7.3). The orbital cone is shown together with the orbit, velocity hodograph and the xz and yz projections of the orbit, velocity hodograph and images of the cone. The dotted line linking opposite vertices divides the parallelogram in two which gives a geometric representation of the constant magnitude of the areal velocity.

Figure 3.14.6 shows both the projected displacements and corresponding projected velocities in the xy and $\dot{x}\dot{y}$ planes at regular time intervals for the monopole–oscillator problem. The projections of the displacements and the corresponding velocities both in this diagram and in the following three figures are coincident with those of the three–dimensional isotropic harmonic oscillator problem as shown in Figures 1.7.2, 1.7.3 and 1.7.4 when the cone is rotated about the $x-$axis so that $\boldsymbol{P}$ lies along $\boldsymbol{k}$ and the vectors $\boldsymbol{K}_K$ and $\boldsymbol{J}_K$ lie along the cartesian unit vectors $\boldsymbol{j}$ and $\boldsymbol{i}$ respectively and hence mimic the behaviour of $\boldsymbol{L}$, $\boldsymbol{K}$ and $\boldsymbol{J}$ respectively of the three–dimensional isotropic harmonic oscillator problem, on account of the choice of constants as described earlier in §3.14. The shaded regions confirm Kepler's second law in the plane that equal areas are swept out in equal times. This result also extends to the cone where equal areas are swept out on the surface of the cone in equal times. However, the area swept out on the cone is larger than that swept out in the plane by the factor P/L. It should be obvious that the initial phase difference between the projected displacement and projected velocity vectors in the xy and $\dot{x}\dot{y}$ planes is $\pi/2$ radians as the projected displacement lies along the $+x-$axis at $t = 0$ while the projected velocity is purely along the $+\dot{y}-$axis. The phase difference in general between the projected displacement and projected velocity vectors is not constant as with the three–dimensional isotropic harmonic oscillator problem since $(\boldsymbol{r} \times \boldsymbol{P}) \cdot (\dot{\boldsymbol{r}} \times \boldsymbol{P}) = L^2 r\dot{r}$ which is nonzero except when $\dot{r} = 0$, *i.e.* at the extremities of the motion. This is also evident by comparing the angle between the corresponding projected displacement and projected velocity vectors for a range of time intervals using the solid round time markers on the projected orbit and the corresponding solid square time markers on the projected velocity hodograph and counting the number of round markers from the rightmost vertex of the ellipse in a counter–clockwise direction to the projected

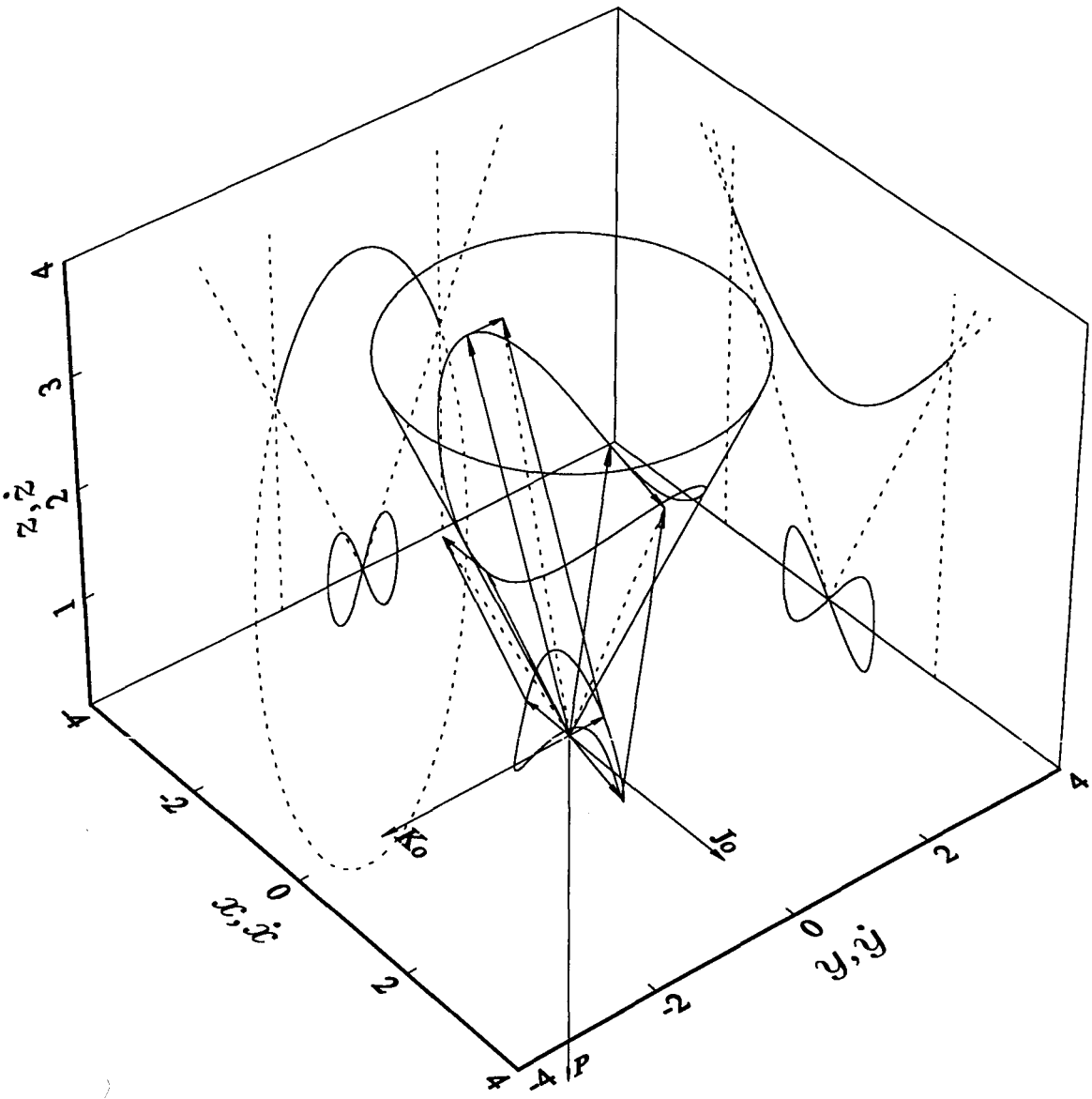

Figure 3.14.5. The monopole–oscillator orbit with its corresponding velocity hodograph associated with Figures 3.14.2 and 3.14.3 demonstrating the construction of $\boldsymbol{L}$. The area of the parallelograms which are now no longer confined to a plane is equal to the constant magnitude of $\boldsymbol{L}$. The orbital cone is shown together with the orbit, velocity hodograph and the projection of the orbit, velocity hodograph and images of the cone onto planes parallel to the xy, xz, yz, $\dot{x}\dot{y}$, $\dot{x}\dot{z}$ and $\dot{y}\dot{z}$ planes. The dotted lines linking opposite vertices divide the parallelograms in two and give a geometric representation of the constant areal velocity. The constants are chosen as for Figure 3.14.2.

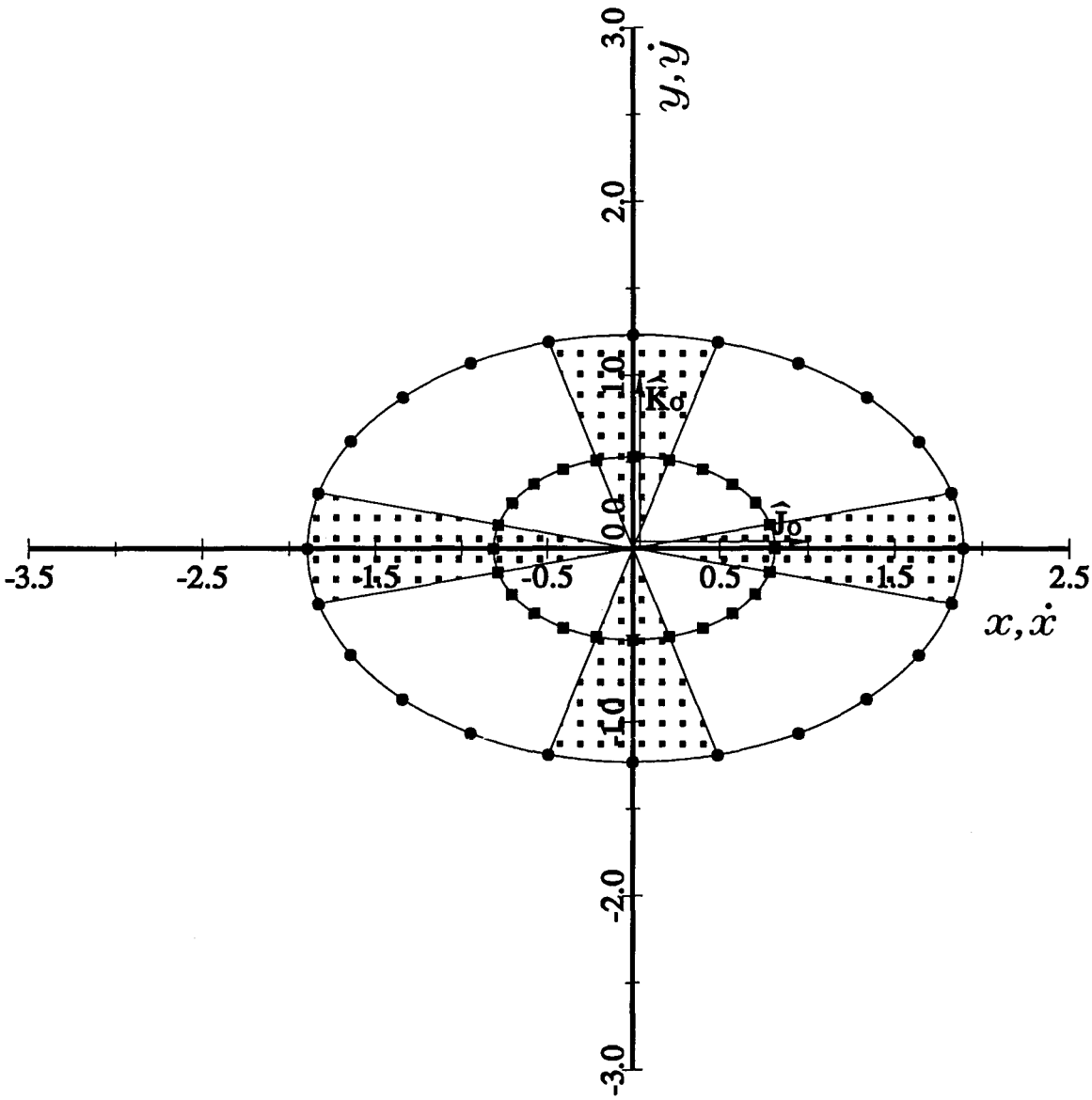

Figure 3.14.6. The projection of the monopole–oscillator orbit and corresponding velocity hodograph into the xy and $\dot{x}\dot{y}$ planes. The circles (-•-•-•-) show the projected displacements of the particle at the time intervals $iT/24$, $i = 0, \ldots, 24$ and the squares (-■-■-■-) give the corresponding projected velocities. The phase difference between the projected velocity and displacement vectors is not constant although the projected displacement vector shifted in time by $\pi/2$ radians moves in phase with the corresponding projected velocity vector. The constants are chosen as for Figure 3.14.2.

displacement of interest and then counting off the same number of square markers on the projected velocity hodograph starting from the square marker at the top of the projected velocity hodograph (since at t=0 the projected velocity is purely along the $+\dot{y}-$axis) in a counter–clockwise direction to obtain the corresponding projected velocity or *vice versa*. Alternatively, if the projected velocity hodograph plot is rotated clockwise through $\pi/2$ radians about the geometric centre of the ellipse, it is apparent that the corresponding projected displacements, projected velocities and the origin are not collinear except at the vertices of the ellipses. Note, however, that the projected radial vector $(\boldsymbol{r} \times \boldsymbol{P})(t)$ with the addition of $\pi/2$ radians to its argument, *i.e.* $(\boldsymbol{r} \times \boldsymbol{P})(\pi/2+t)$ moves in phase with the vector $(\dot{\boldsymbol{r}} \times \boldsymbol{P})(t)$ since projected radii drawn from the origin to the solid round time markers on the projected orbit also pass through the solid square time markers on the projected velocity hodograph. This behaviour is also apparent from the parametric representation of the plane polar angle between the projected displacement and the $x-$axis which can be expressed in terms of the tangent of a function of t which can be converted into an equation of the same form as that for the parametric representation of the plane polar angle between the projected velocity and the $\dot{x}-$axis which involves a cotangent of the same function of t through the addition of $\pi/2$ radians to the argument of the tangent function and *vice versa* (see (1.7.21)–(1.7.22)). Further, as in the case of the three–dimensional isotropic harmonic oscillator (see Figure 1.7.3), the sum of the plane polar angle between the projected displacement and the $x-$axis at the time $(\pi/2-t)$ and the plane polar angle between the projected velocity and the $\dot{x}-$axis at the time t is equal to π radians realising that the solid round and solid square time markers on the projected orbit and projected velocity hodograph respectively represent the projected displacement and projected velocity of the particle at the regular time intervals $iT/24 = i\pi/(12\lambda^*), i = 0, \ldots, 24$ and so an addition of $\pi/2$ radians to the argument of time represents a shift of 6 consecutive time markers along either the projected orbit or the projected velocity hodograph which does not necessarily correspond with a plane polar angular shift of $\pi/2$ radians. In other words the regular time intervals do not correspond with regular increments of the plane polar angles and as a result the collinearity between the origin, the projected displacements shifted in time by $\pi/2$ radians and the projected velocities is no longer present when the markers are drawn at regular increments in terms of the plane polar angles. In summary, the phase difference between $\boldsymbol{r}$ and $\dot{\boldsymbol{r}}$ is not constant in the monopole–oscillator problem which is also the case between $\boldsymbol{r} \times \boldsymbol{P}$ and $\dot{\boldsymbol{r}} \times \boldsymbol{P}$ for the projected quantities of the monopole–oscillator problem although in the projected problem the origin, the displacements shifted in time by $\pi/2$ radians and the velocities are collinear.

The relationship between the periodic time of the orbit and the length of the generalised semi–major axis $r_{\max}$ is identical to that shown in Figure 1.7.11 for the family of orbits which have the same generalised semi–major axis lengths as those shown in Figure 1.7.10. It must be appreciated, however, that R, the generalised semi–major axis, is a factor $1/\sin\alpha$ times larger than the semi–major axis length of the orbit projected into the $xy-$plane whilst μ is equal in magnitude to λ^* for the equivalent problem in the plane and as a result the ratio $T = 2\pi/\omega = 2\pi/\lambda^*$ is form invariant for the choice of initial conditions described earlier in §3.14.

From (3.14.55) we obtain a rather important result. The intersection of a suitable elliptical cylinder with axis of symmetry lying in the $\phi-$plane and a right circular cone with apex on the $\phi-$plane and axis of symmetry perpendicular to the plane has a projection in the $\phi-$plane which describes a geometric–centred ellipse. Alternatively from (3.14.53) the intersection of a suitable hyperbolic sheet with axis of symmetry lying in the $\phi-$plane and the right circular cone described above also has a geometric–centred elliptical projection in the $\phi-$plane. In contrast, the MICZ problem showed that the intersection of a plane and a right circular cone with apex on the $\phi-$plane and axis of symmetry perpendicular to the plane has a projection in the $\phi-$plane which describes a focus–centred conic. These two results give a geometric interpretation of the reasons for the difference in location of the origin in both the Kepler and three–dimensional isotropic harmonic oscillator problems. In most textbooks dealing with the subject, the connection between the orbit of the Kepler problem and the plane section of the cone is usually mentioned. However, no explanation as to why this is the case has been proposed. In fact the geometric–centred elliptical orbit of the three–dimensional isotropic harmonic oscillator is also an elliptical conic section, although from what we have seen above its connection with the cone is more involved. The results above demonstrate that the plane section of the cone is naturally associated with the plane polar focus–centred representation of the conic section and the intersection of the elliptical cylinder with the cone with the geometric–centred cartesian representation of an ellipse.

Figure 3.14.7 shows the orbit for the monopole–oscillator where $\mu = 8L^2/9 - \lambda^2/9$. The diagram shows the right circular orbital cone extending along the line of $\boldsymbol{P}$ with origin at the apex of the cone. The equation of motion in this case is given by (3.13.1) with the corresponding orbit equation (3.14.6) whilst for the projection of the motion into the $\phi-$plane, the equation of motion is given by (3.13.26) with corresponding orbit equation $|\boldsymbol{r} \times \boldsymbol{P}|^2$ equal to L^2 times equation (3.14.6). The energy of this orbit, I_1, is chosen to be 1.1824 whilst the argument of the cosine term in (3.14.6) is

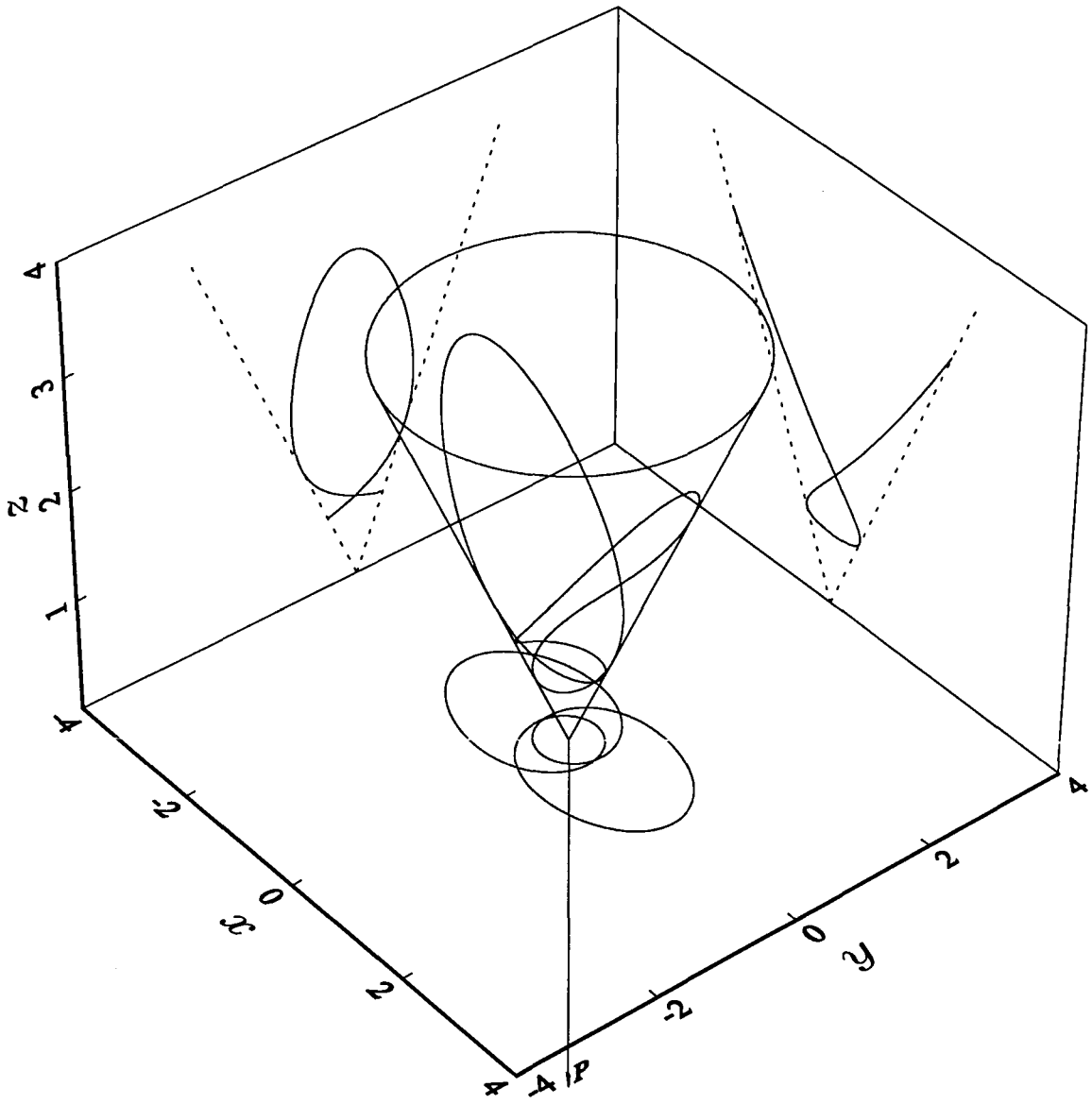

Figure 3.14.7. The monopole–oscillator orbit for $\mu = 8L^2/9 - \lambda^2/9$. The radial vectors move on the surface of a right circular cone extending along the line of $\boldsymbol{P}$ with origin at the apex of the cone. The heads of the radial vectors move on the surface of a frustrum of the orbital cone. The orbit has two-fold rotational symmetry about $\boldsymbol{P}$ and circles the origin three times before closing. The projections of the orbit onto planes parallel to the xy, xz and yz planes are also shown. The constants have the values $\omega = 0.4289$, $P = 3.4225$, $\lambda = 2.8794$, $\alpha = 0.5711$, $L = 1.85$ and $I_1 = 1.1824$. The origin is not enclosed by the orbit.

$2(\phi - \phi_0)/3$. The orbit is closed since $(L^2 - \mu)^{\frac{1}{2}}$ and $(L^2 + \lambda^2)^{\frac{1}{2}}$ are commensurate and circles the origin three times before closing. The tips of the radial vectors move on the surface of a frustrum of the orbital cone whilst the orbit in the ϕ–plane has two interlocking lobes which are a reflection of the periodicity of the cosine term of (3.14.6). The orbit on the cone has two–fold rotational symmetry about $\boldsymbol{P}$. The origin is not enclosed by the orbit. In order to illustrate the behaviour more clearly, projections of the orbit onto planes parallel to the xy, xz and yz planes are shown, together with the projected images of the cones onto the respective planes. The magnitude of the angular momentum is constant throughout the motion.

Figure 3.14.8 shows the velocity hodograph for the monopole–oscillator where $\mu = 8L^2/9 - \lambda^2/9$. In order to illustrate the $\dot{\boldsymbol{r}}$ behaviour more clearly, projections of the velocity hodograph onto planes parallel to the $\dot{x}\dot{z}$ and $\dot{y}\dot{z}$ planes are also shown and seen to display a certain symmetry. The velocity hodograph is also closed.

Figure 3.14.9 shows the orbit for the monopole–oscillator where $\mu = -8L^2 - 9\lambda^2$. The diagram shows the right circular orbital cone extending along the line of $\boldsymbol{P}$ with origin at the apex of the cone. The equation of motion in this case is given by (3.13.1) with the corresponding orbit equation (3.14.6) whilst for the projection of the motion into the ϕ–plane, the equation of motion is given by (3.13.26) with corresponding orbit equation $|\boldsymbol{r} \times \boldsymbol{P}|^2$ equal to L^2 times equation (3.14.6). The energy of this orbit, I_1, is chosen to be 5.4230 whilst the argument of the cosine term in (3.14.6) is $6(\phi - \phi_0)$. The orbit is closed since $(L^2 - \mu)^{\frac{1}{2}}$ and $(L^2 + \lambda^2)^{\frac{1}{2}}$ are commensurate and circles the origin only once before closing. The tips of the radial vectors move on the surface of a frustrum of the orbital cone whilst the orbit in the ϕ–plane has six distinct bulges which are a reflection of the periodicity of the cosine term of (3.14.6). The orbit on the cone has six–fold rotational symmetry about $\boldsymbol{P}$. The origin is not enclosed by the orbit. In order to illustrate the behaviour more clearly, projections of the orbit onto planes parallel to the xy, xz and yz planes are shown, together with the projected images of the cones onto the respective planes. The magnitude of the angular momentum is constant throughout the motion.

Figure 3.14.10 shows the velocity hodograph for the monopole–oscillator where $\mu = -8L^2 - 9\lambda^2$. In order to illustrate the $\dot{\boldsymbol{r}}$ behaviour more clearly, projections of the velocity hodograph onto planes parallel to the $\dot{x}\dot{z}$ and $\dot{y}\dot{z}$ planes are also shown and seen to display a certain symmetry. The velocity hodograph is also closed.

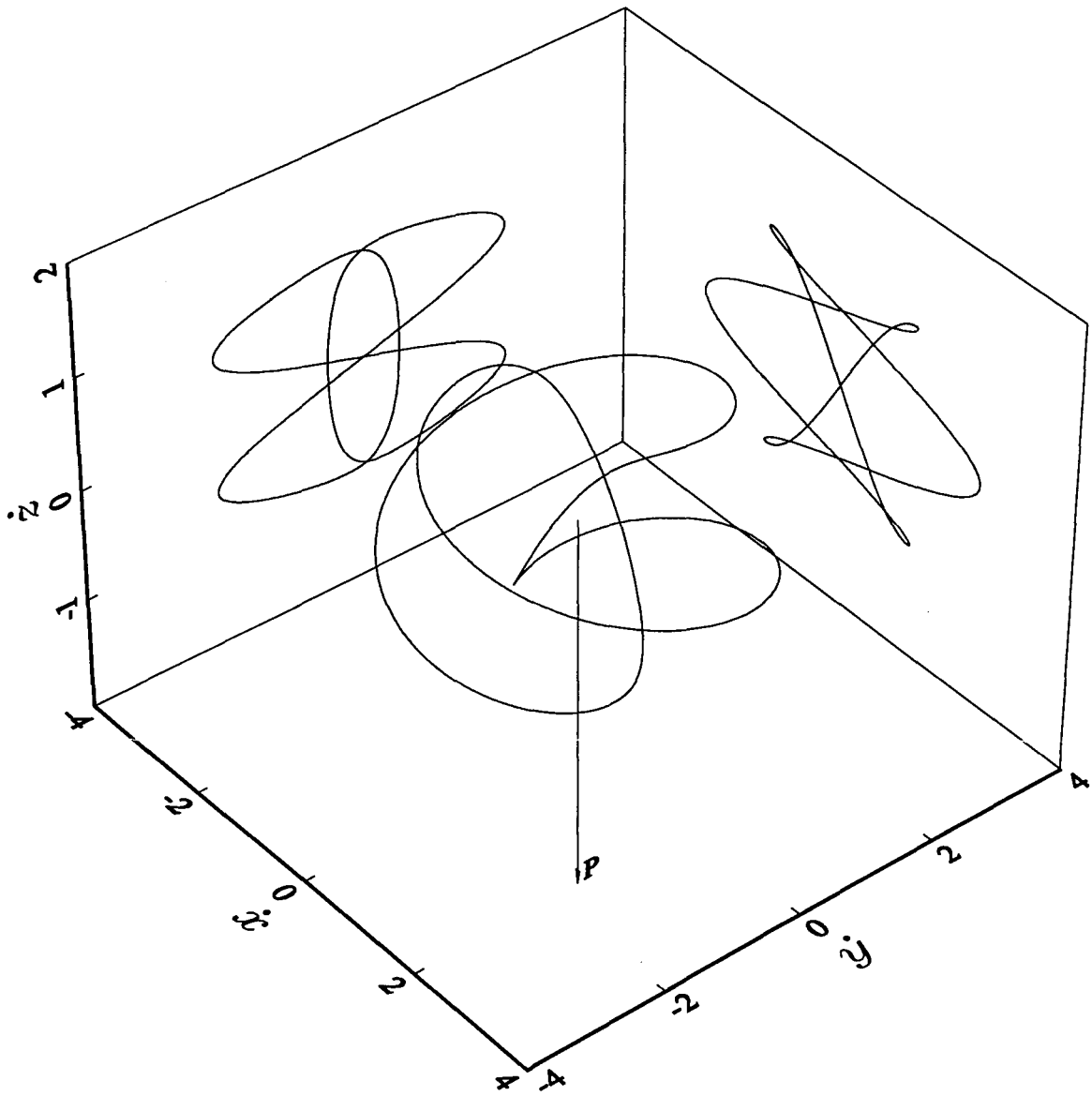

Figure 3.14.8. The monopole–oscillator velocity hodograph for $\mu = 8L^2/9 - \lambda^2/9$. The projections of the velocity hodograph onto planes parallel to the $\dot{x}\dot{z}$ and $\dot{y}\dot{z}$ planes are also shown. The constants are chosen as for Figure 3.14.7. The origin is enclosed by the velocity hodograph.

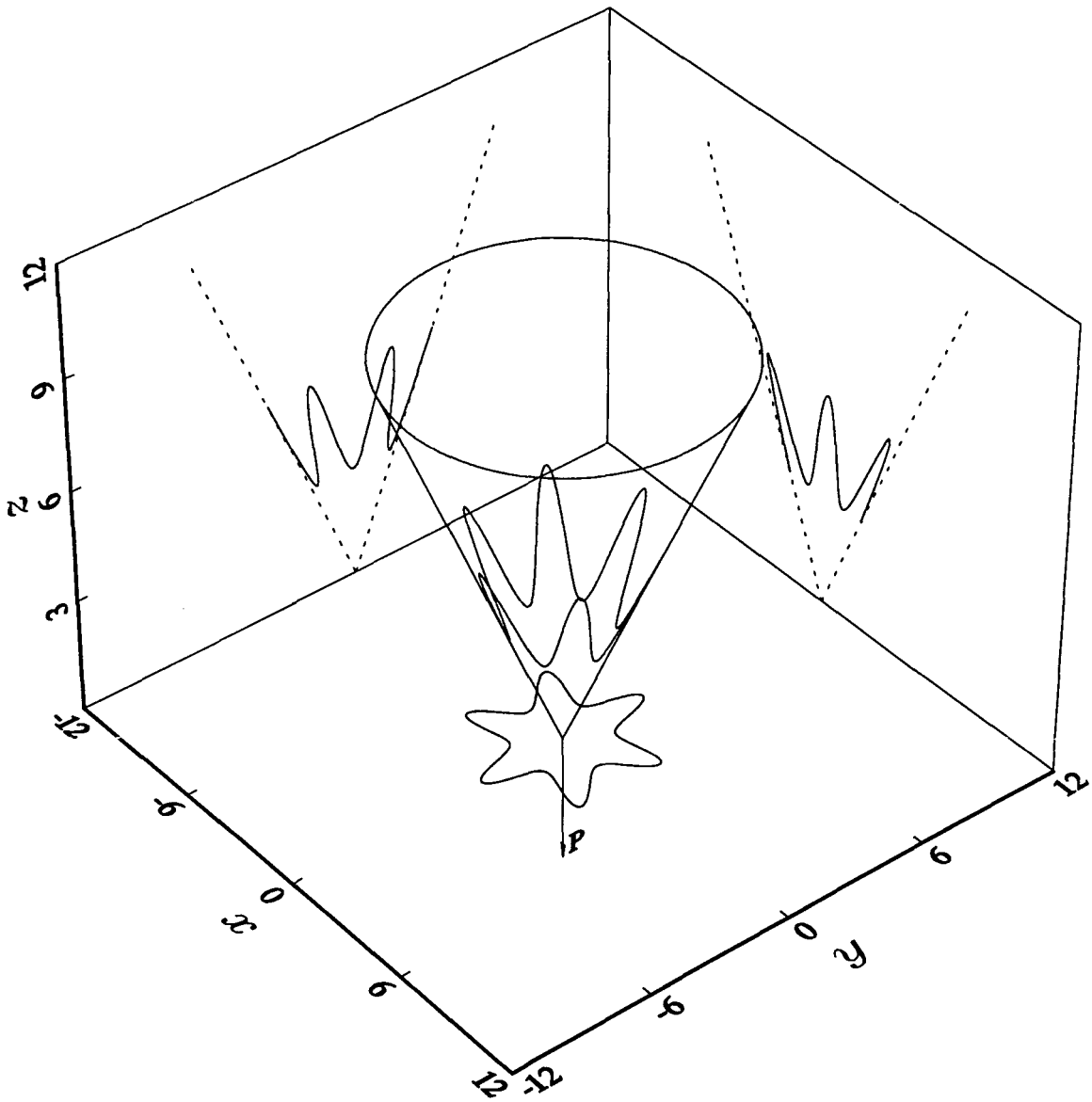

Figure 3.14.9. The monopole–oscillator orbit for $\mu = -8L^2 - 9\lambda^2$. The radial vectors move on the surface of a right circular cone extending along the line of $\boldsymbol{P}$ with origin at the apex of the cone. The heads of the radial vectors move on the surface of a frustrum of the orbital cone. The orbit has six–fold rotational symmetry about $\boldsymbol{P}$ and circles the origin only once before closing. The projections of the orbit onto planes parallel to the xy, xz and yz planes are also shown. The constants have the values $\omega = 0.4289$, $P = 3.4225$, $\lambda = 2.8794$, $\alpha = 0.5711$, $L = 1.85$ and $I_1 = 5.4230$. The origin is not enclosed by the orbit.

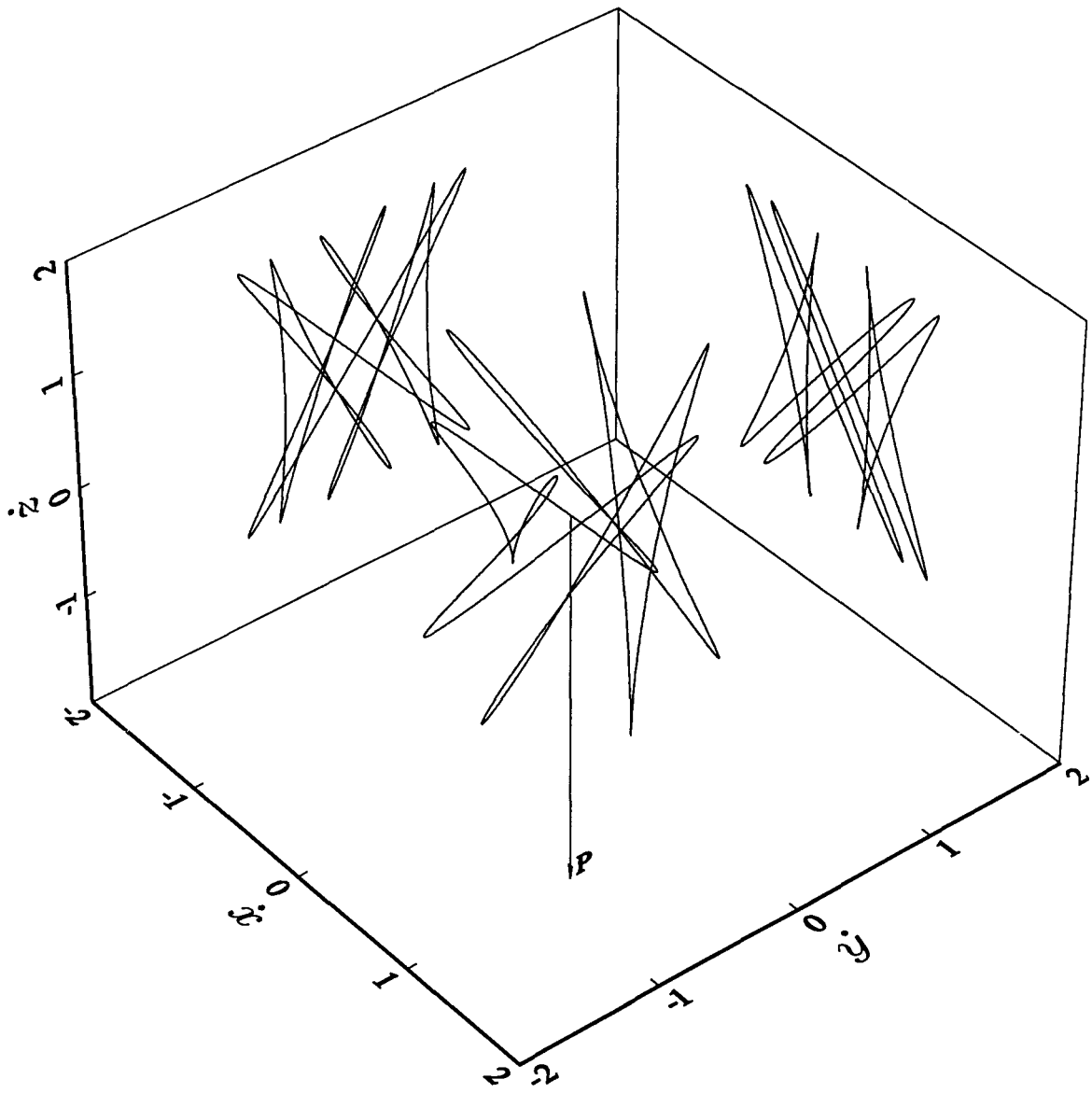

Figure 3.14.10. The monopole–oscillator velocity hodograph for $\mu = -8L^2 - 9\lambda^2$. The projections of the velocity hodograph onto planes parallel to the $\dot{x}\dot{z}$ and $\dot{y}\dot{z}$ planes are also shown. The constants are chosen as for Figure 3.14.9. The origin is enclosed by the velocity hodograph.

3.15 The Geometry of the Monopole–Free Particle

The treatment of the monopole–free particle closely follows that for the monopole–oscillator problem. Again the motion takes place on a right circular cone of semi–vertex angle α and axis of symmetry along the line of $\boldsymbol{P}$. Although the angular momentum, $\boldsymbol{L}$, is not conserved, its magnitude, L, is. Since $[\boldsymbol{P}, \boldsymbol{L}, \boldsymbol{r}]$ is zero, $\boldsymbol{L}$ describes a right circular cone of semi–vertex angle $(\pi/2 - \alpha)$. The salient features of the geometry are depicted in Figure 3.15.1 which shows the orientation of the larger orbital and smaller angular momentum cones which meet at the origin and a typical orbit for the case $\mu = -\lambda^2$. Note from the diagram how the vector $\boldsymbol{P}$ is constructed from the vectors $\boldsymbol{L}$ and $-\lambda\hat{\boldsymbol{r}}$, where $-\lambda\hat{\boldsymbol{r}}$ is in the opposite direction to $\boldsymbol{r}$ and scaled by λ.

Applying the same method as used to determine the orbit equation of the monopole–oscillator gives using (3.13.14) and (3.14.5)

$$r\cos\left[\left(\frac{L^2-\mu}{L^2+\lambda^2}\right)^{\frac{1}{2}}(\phi-\phi_0)\right] = \left(\frac{L^2-\mu}{2J_1}\right)^{\frac{1}{2}}, \tag{3.15.1}$$

where we have chosen the positive root of (3.15.1), *i.e.* the argument of the cosine is restricted to the interval $(-\pi/2, \pi/2)$. When $\mu = -\lambda^2$, the projection of the orbit on the ϕ–plane is a straight line and so the orbit on the cone is a hyperbola. When $\mu \neq -\lambda^2$, the projection of the orbit on the ϕ–plane is reminiscent of a Newton–Cotes spiral and the orbit on the cone is a twisted hyperbola. Some representative orbits and their projections are depicted in Figures 3.15.2–3.15.7.

The monopole–free particle with $\mu = -\lambda^2$ belongs to the class of problems studied previously in §§3.1–3.11 which possess a Laplace–Runge–Lenz analogue. Using the notation of equation (3.1.15) with $h(r) = -\lambda/r$ and $k = 0$, the Laplace–Runge–Lenz analogue (3.1.14) is found to be

$$\boldsymbol{J} = \dot{\boldsymbol{r}}\times\boldsymbol{L} + \frac{\lambda}{r}\boldsymbol{L} = \dot{\boldsymbol{r}}\times\boldsymbol{P}. \tag{3.15.2}$$

The scalar product of (3.15.2) with $\boldsymbol{P}$ is zero and hence $\boldsymbol{J}$ is perpendicular to $\boldsymbol{P}$ and lies on the plane. The scalar product of (3.15.2) with $\boldsymbol{r}$ reveals that the projection of $\boldsymbol{r}$ onto $\boldsymbol{J}$ is a constant $L^2/J = L/(2H)^{\frac{1}{2}}$ and so the motion is on a plane perpendicular to $\boldsymbol{J}$ and hence parallel to $\boldsymbol{P}$. This is consistent with the orbit on the cone describing a hyperbola.

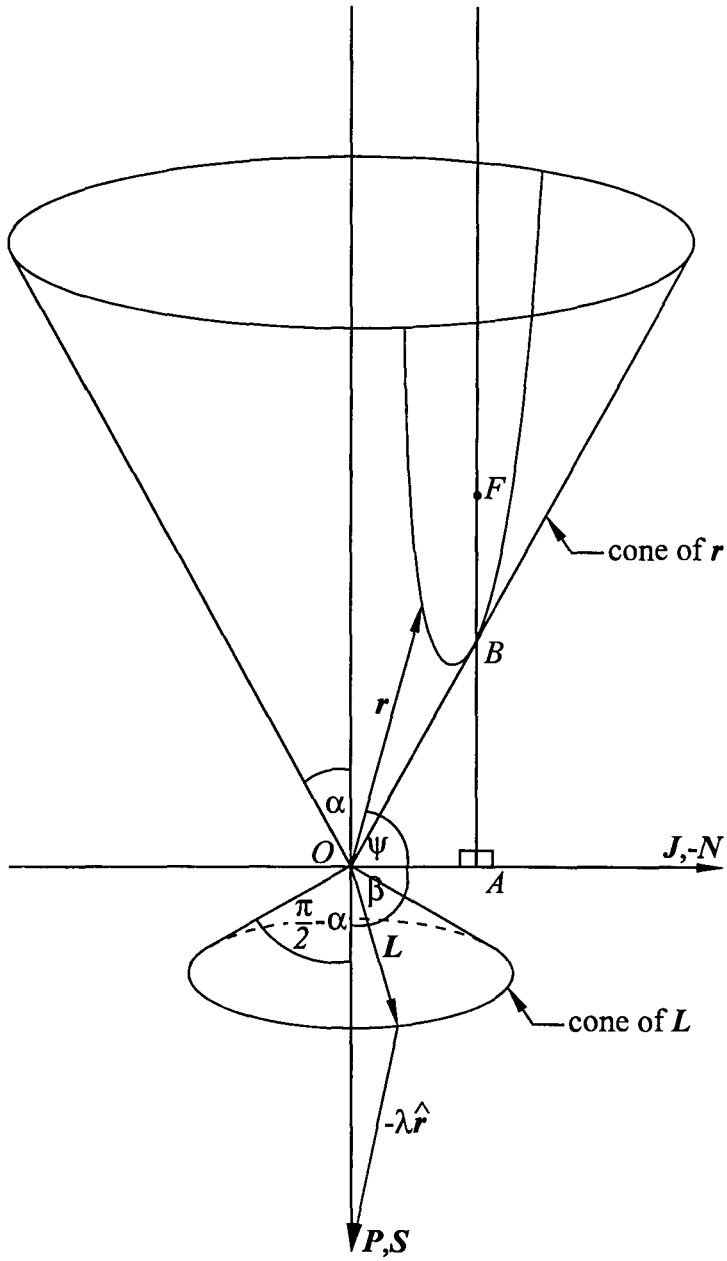

Figure 3.15.1. The typical geometry of the monopole–free particle orbit when $\mu = -\lambda^2$. The larger orbital and smaller angular momentum cones are shown together with a typical hyperbolic orbit and the orientation of $\boldsymbol{P}$, $\boldsymbol{J}$, $-\boldsymbol{N}$ and $\boldsymbol{S}$. The origin O is at the point of contact between the two cones, F is the focus of the hyperbola and A marks the geometric centre of the hyperbola. B marks the point of closest approach from O. The orbit is a conic section as are certain projections. α and $\pi/2-\alpha$ are the semi–vertex angles of the orbital and angular momentum cones respectively, ψ is the angle between $\boldsymbol{J}$ and $\boldsymbol{r}$ and β is between $\boldsymbol{P}$ and $\boldsymbol{J}$.

The geometry of the monopole–free particle in the case $\mu = -\lambda^2$ is identical to that described in Figures 3.7.3 and 3.7.4. Figure 3.15.2 shows the hyperbolic orbit for the monopole–free particle where $\mu = -\lambda^2$ for a different set of initial conditions from those used in Figure 3.7.3. The diagram shows the right circular orbital cone extending along the line of $\boldsymbol{P}$ with origin at the apex of the cone. The equation of motion in this case is given by (3.13.2) with the corresponding orbit equation (3.15.1) whilst for the projection of the motion into the $\phi-$plane, the equation of motion is given by (3.13.27) with corresponding orbit equation $|\boldsymbol{r} \times \boldsymbol{P}|$ equal to L times equation (3.15.1). The energy of this orbit, J_1, is chosen to be 0.4771 whilst the argument of the cosine term in (3.15.1) is $(\phi - \phi_0)$. The orbit is not closed and approaches asymptotically before leaving asymptotically, a process which is repeated for the projection of the orbit in the $\phi-$plane. The orbit on the cone is hyperbolic as is the yz projection of the orbit and correspondingly the xy and xz projections of the orbit are straight lines. The orbit on the cone has no rotational symmetry about $\boldsymbol{P}$. The origin is not enclosed by the orbit. In order to illustrate the behaviour more clearly, projections of the orbit onto planes parallel to the xy, xz and yz planes are shown, together with projections of the angular momentum curve and the projected images of the cones onto the respective planes. The magnitude of the angular momentum is constant throughout the motion.

Figure 3.15.3 shows the straight–line velocity hodograph for the monopole–free particle where $\mu = -\lambda^2$ for a different set of initial conditions from those used in Figure 3.7.4. In order to illustrate the $\dot{\boldsymbol{r}}$ behaviour more clearly, projections of the velocity hodograph onto planes parallel to the $\dot{x}\dot{y}$, $\dot{x}\dot{z}$ and $\dot{y}\dot{z}$ planes are also shown, together with the projected images of the orbital cone onto the respective planes. The velocity hodograph is bounded at both ends by the tangents to the asymptotes of the orbit on the cone.

From (3.7.10) we obtain a rather important result. The intersection of a suitable hyperbolic sheet with axis of symmetry lying perpendicular to the $\phi-$plane and a right circular cone with apex on the $\phi-$plane and axis of symmetry perpendicular to the plane has a projection in the $\phi-$plane which describes a straight line. Alternatively from (3.7.9.1) and (3.7.9.2) the intersection of a plane perpendicular to $\phi-$plane and the right circular cone described above also has a straight–line projection in the $\phi-$plane. Since the monopole–free particle problem with $\mu = -\lambda^2$ is also an MICZ monopole, the degenerate conic section in the $\phi-$plane describing the three-dimensional free particle orbit (3.7.11) is consistent with either the projection of a

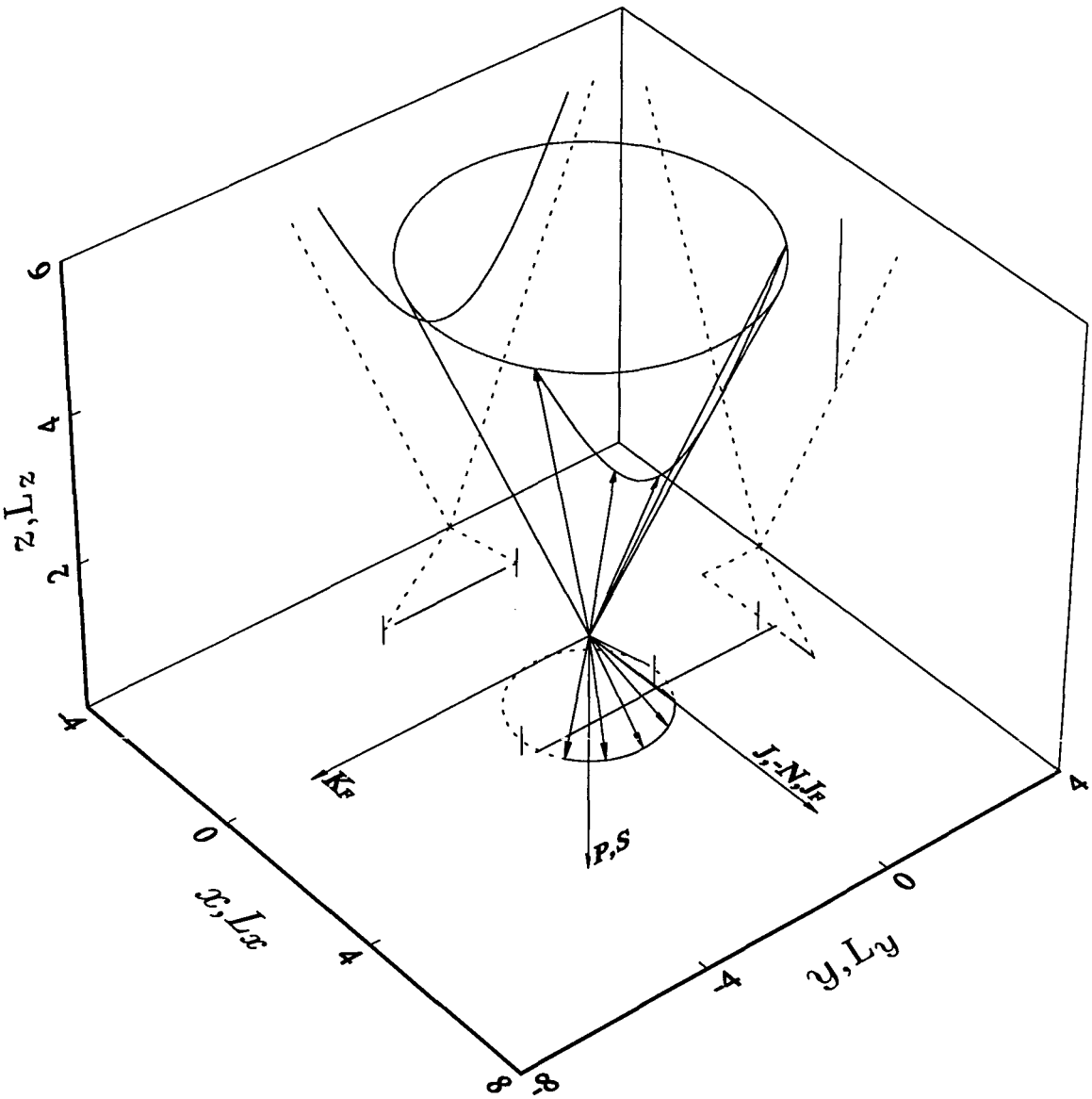

Figure 3.15.2. The monopole–free particle hyperbolic orbit and angular momentum curve for $\mu = -\lambda^2$ with a selection of displacement and angular momentum vectors drawn from the origin. The radial and angular momentum vectors move on the surfaces of two right circular cones extending in opposite directions along the line of $\boldsymbol{P}$ with origin and point of contact at the apices of the two cones. The projections of the orbit and angular momentum curve onto planes parallel to the xy, xz, yz, L_xL_y, L_xL_z and L_yL_z planes are also shown. The constants have the values $\omega = 0$, $P = 3.4225$, $\lambda = 2.8794$, $\alpha = 0.5711$, $L = 1.85$ and $J_1 = 0.4771$. The origin lies out of the orbital plane.

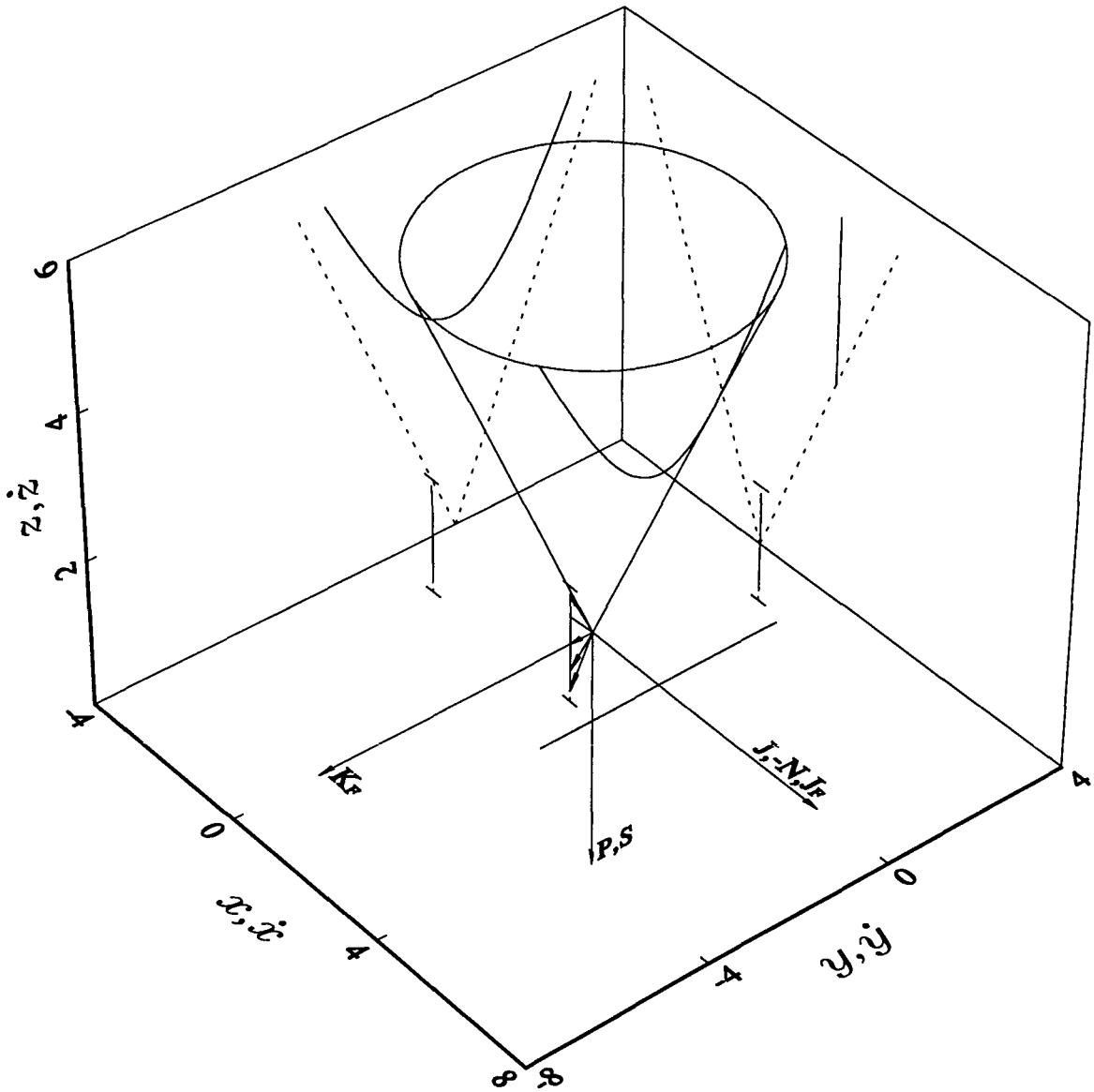

Figure 3.15.3. The monopole–free particle straight-line velocity hodograph and hyperbolic orbit for $\mu = -\lambda^2$ with a selection of velocity vectors drawn from the origin. The velocity vectors move on a plane which is parallel to the orbital plane and, as t ranges from negative through positive infinity, the velocity vectors sweep out a plane isoceles triangle lying in the $\dot{y}\dot{z}-$plane with base of length $2\lambda J/LP$ and height J/P. The projections of the velocity hodograph and orbit onto planes parallel to the $\dot{x}\dot{y}$, $\dot{x}\dot{z}$, $\dot{y}\dot{z}$, xy, xz and yz planes are also shown. The constants are chosen as for Figure 3.15.2. The origin lies in the hodographic plane touching one vertex of the triangle.

plane conic section or the projection of the intersection of a hyperbolic sheet with a right circular cone.

Figure 3.15.4 shows the orbit for the monopole–free particle where $\mu = 35L^2/36 - \lambda^2/36$. The diagram shows the right circular orbital cone extending along the line of $\boldsymbol{P}$ with origin at the apex of the cone. The equation of motion in this case is given by (3.13.2) with the corresponding orbit equation (3.15.1) whilst for the projection of the motion into the ϕ–plane, the equation of motion is given by (3.13.27) with corresponding orbit equation $|\boldsymbol{r} \times \boldsymbol{P}|$ equal to L times equation (3.15.1). The energy of this orbit, J_1, is chosen to be 0.0133 whilst the argument of the cosine term in (3.15.1) is $(\phi - \phi_0)/6$. The orbit is not closed and spirals inwards asymptotically, circles the origin twice before spiralling outwards asymptotically, a process which is repeated for the projection of the orbit in the ϕ–plane. The orbit on the cone has no rotational symmetry about $\boldsymbol{P}$. The origin is not enclosed by the orbit. In order to illustrate the behaviour more clearly, projections of the orbit onto planes parallel to the xy, xz and yz planes are shown, together with the projected images of the cones onto the respective planes. The magnitude of the angular momentum is constant throughout the motion.

Figure 3.15.5 shows the velocity hodograph for the monopole–free particle where $\mu = 35L^2/36 - \lambda^2/36$. In order to illustrate the $\dot{\boldsymbol{r}}$ behaviour more clearly, projections of the velocity hodograph onto planes parallel to the $\dot{x}\dot{z}$ and $\dot{y}\dot{z}$ planes are also shown and seen to display a certain symmetry. The velocity hodograph is bounded at both ends by the tangents to the asymptotes of the orbit on the cone.

Figure 3.15.6 shows the orbit for the monopole–free particle where $\mu = -3L^2 - 4\lambda^2$. The diagram shows the right circular orbital cone extending along the line of $\boldsymbol{P}$ with origin at the apex of the cone. The equation of motion in this case is given by (3.13.2) with the corresponding orbit equation (3.15.1) whilst for the projection of the motion into the ϕ–plane, the equation of motion is given by (3.13.27) with corresponding orbit equation $|\boldsymbol{r} \times \boldsymbol{P}|$ equal to L times equation (3.15.1). The energy of this orbit, J_1, is chosen to be 1.9083 whilst the argument of the cosine term in (3.15.1) is $2(\phi - \phi_0)$. The orbit is not closed and approaches asymptotically before leaving asymptotically, a process which is repeated for the projection of the orbit in the ϕ–plane. The orbit on the cone is hyperbolic as are the xy and xz projections of the orbit and correspondingly the xz projection of the orbit is a straight line. The orbit on the cone has no rotational symmetry about $\boldsymbol{P}$. The origin is not enclosed by the orbit. In order to illustrate the behaviour more clearly, projections of the orbit onto planes

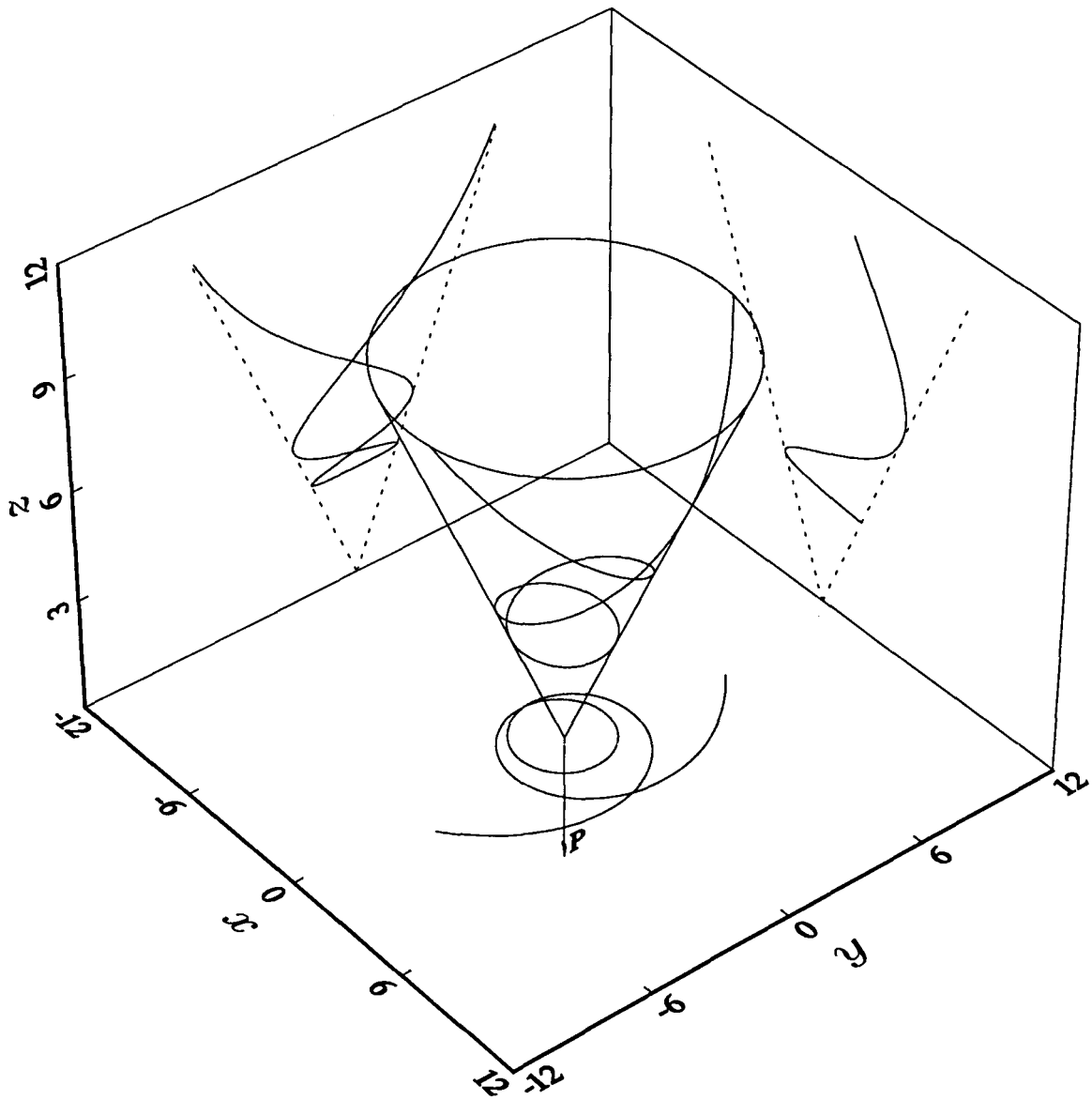

Figure 3.15.4. The monopole–free particle orbit for $\mu = 35L^2/36 - \lambda^2/36$. The radial vectors move on the surface of a right circular cone extending along the line of $\boldsymbol{P}$ with origin at the apex of the cone. The orbit on the cone resembles a twisted hyperbola which approaches asymptotically, circles the origin twice before leaving asymptotically. The projections of the orbit onto planes parallel to the xy, xz and yz planes are also shown. The constants have the values $\omega = 0$, $P = 3.4225$, $\lambda = 2.8794$, $\alpha = 0.5711$, $L = 1.85$ and $J_1 = 0.0133$. The origin is not enclosed by the orbit.

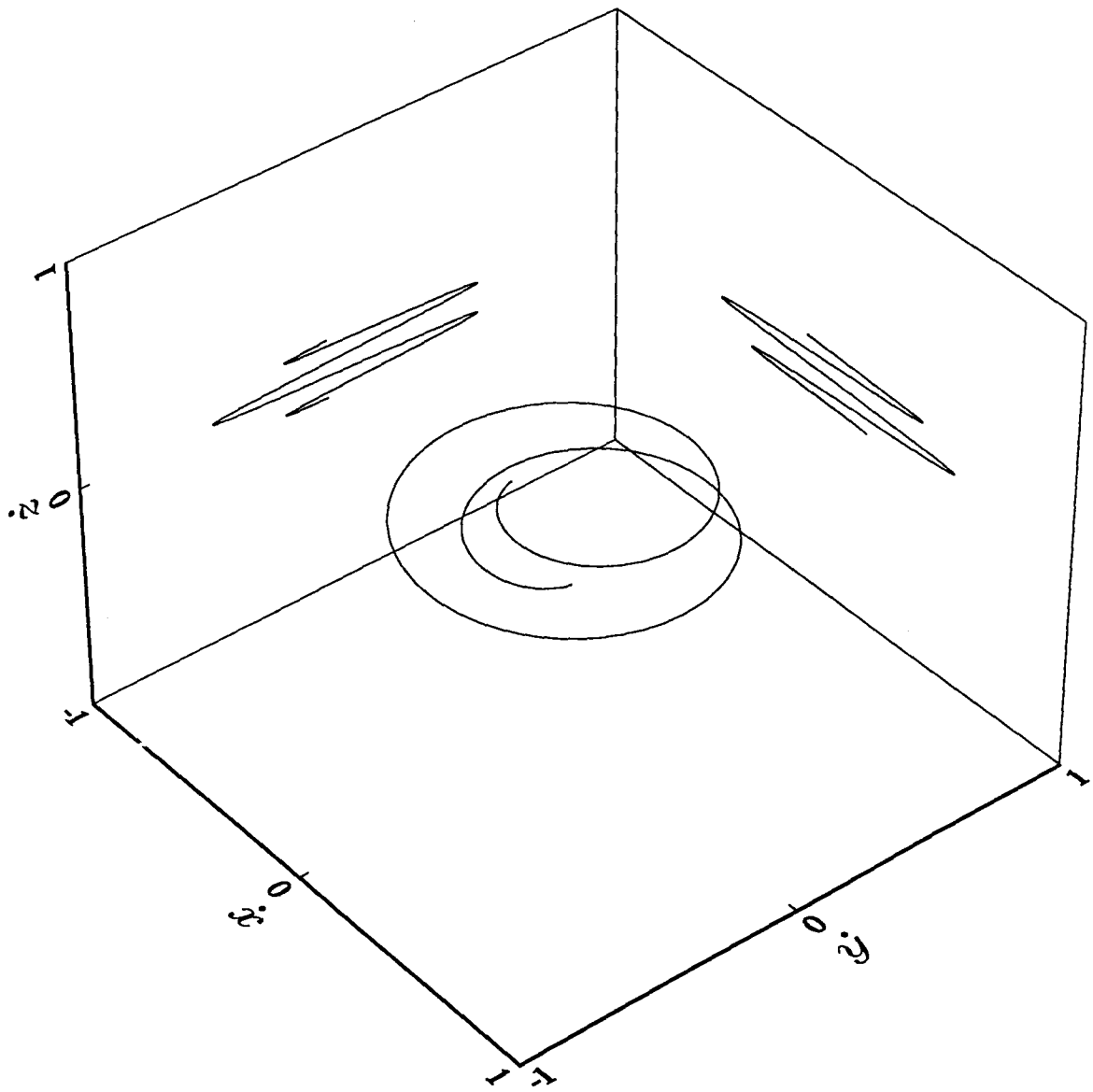

Figure 3.15.5. The monopole–free particle velocity hodograph for $\mu = 35L^2/36 - \lambda^2/36$. The projections of the velocity hodograph onto planes parallel to the $\dot{x}\dot{z}$ and $\dot{y}\dot{z}$ planes are also shown. The constants are chosen as for Figure 3.15.4. The origin is enclosed by the velocity hodograph.

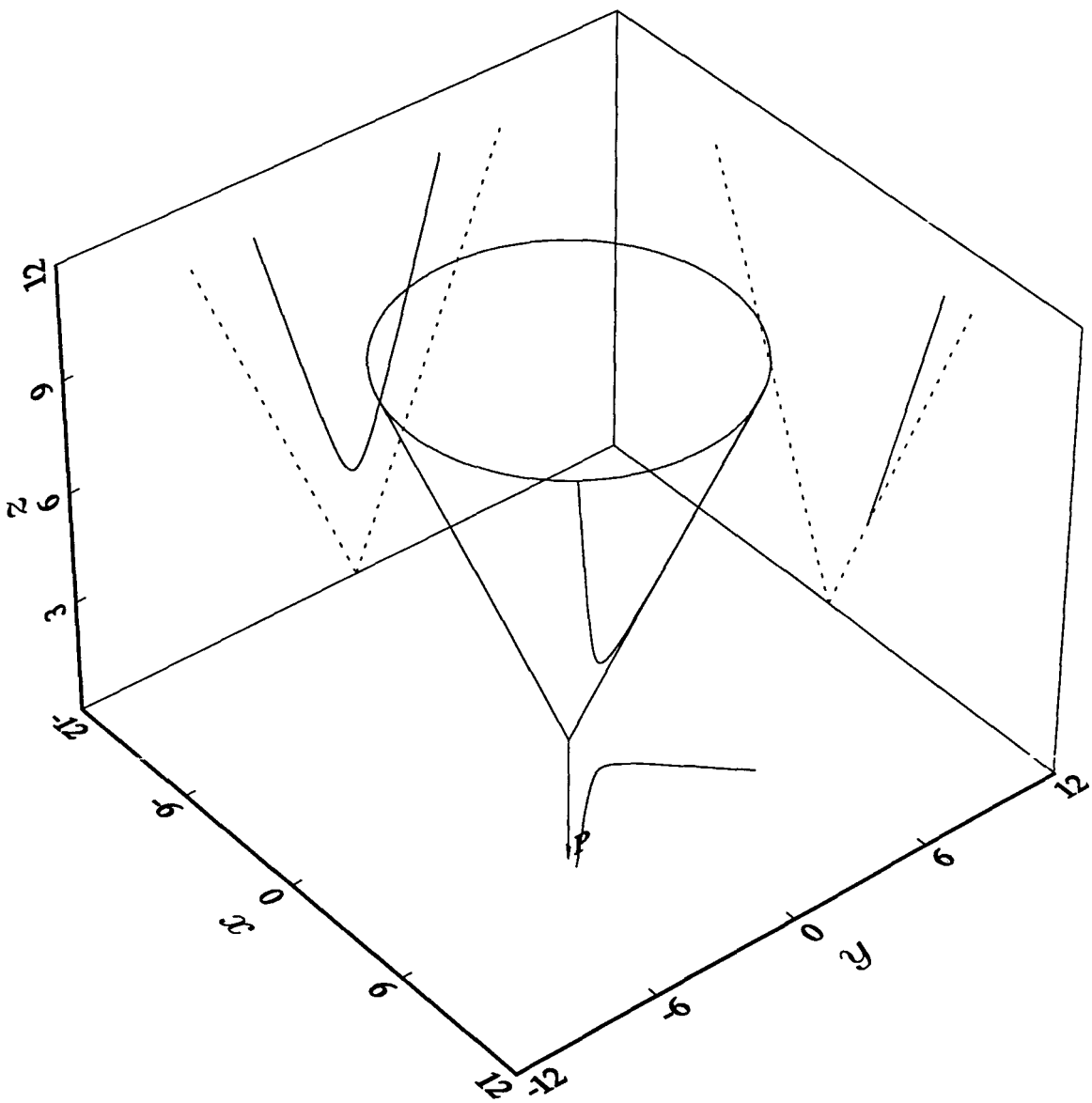

Figure 3.15.6. The monopole–free particle orbit for $\mu = -3L^2 - 4\lambda^2$. The radial vectors move on the surface of a right circular cone extending along the line of $\boldsymbol{P}$ with origin at the apex of the cone. The orbit on the cone is hyperbolic. The projections of the orbit onto planes parallel to the xy, xz and yz planes are also shown. The constants have the values $\omega = 0$, $P = 3.4225$, $\lambda = 2.8794$, $\alpha = 0.5711$, $L = 1.85$ and $J_1 = 1.9083$. The xy and yz projections of the orbit are also hyperbolic while the xz projection is a straight–line. The origin is not enclosed by the orbit.

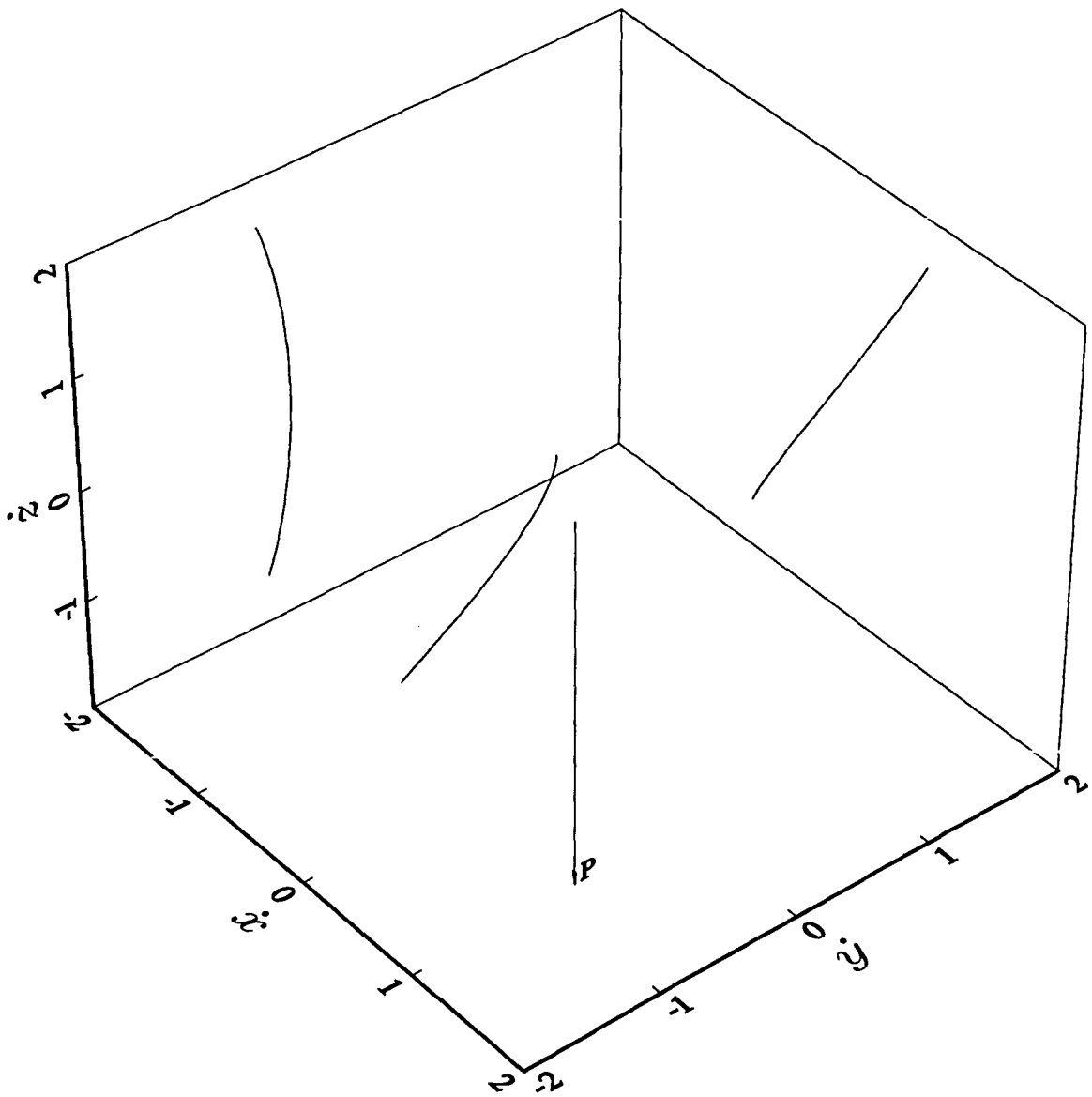

Figure 3.15.7. The monopole–free particle velocity hodograph for $\mu = -3L^2 - 4\lambda^2$. The projections of the velocity hodograph onto planes parallel to the $\dot{x}\dot{z}$ and $\dot{y}\dot{z}$ planes are also shown. The constants are chosen as for Figure 3.15.6.

parallel to the xy, xz and yz planes are shown, together with the projected images of the cones onto the respective planes. The magnitude of the angular momentum is constant throughout the motion.

Figure 3.15.7 shows the velocity hodograph for the monopole–free particle where $\mu = -3L^2 - 4\lambda^2$. In order to illustrate the $\dot{\boldsymbol{r}}$ behaviour more clearly, projections of the velocity hodograph onto planes parallel to the $\dot{x}\dot{z}$ and $\dot{y}\dot{z}$ planes are also shown. The velocity hodograph is bounded at both ends by the tangents to the asymptotes of the orbit on the cone.

3.16 The Geometry of the Monopole–Repulsor

The treatment of the monopole–repulsor closely follows that for the monopole–oscillator problem. Again the motion takes place on a right circular cone of semi–vertex angle α and axis of symmetry along the line of $\boldsymbol{P}$. Although the angular momentum, $\boldsymbol{L}$, is not conserved, its magnitude, L, is. Since $[\boldsymbol{P}, \boldsymbol{L}, \boldsymbol{r}]$ is zero, $\boldsymbol{L}$ describes a right circular cone of semi–vertex angle $(\pi/2 - \alpha)$. The salient features of the geometry are depicted in Figure 3.16.1 which shows the orientation of the larger orbital and smaller angular momentum cones which meet at the origin and a typical orbit for the case $\mu = -\lambda^2$. Note from the diagram how the vector $\boldsymbol{P}$ is constructed from the vectors $\boldsymbol{L}$ and $-\lambda\hat{\boldsymbol{r}}$, where $-\lambda\hat{\boldsymbol{r}}$ is in the opposite direction to $\boldsymbol{r}$ and scaled by λ.

Using the methods described earlier, (3.13.19) and (3.14.5) can be solved to obtain the orbit equation

$$r^2 = \frac{L^2 - \mu}{K_1 + \left({K_1}^2 + \omega^2(L^2 - \mu)\right)^{\frac{1}{2}} \cos\left(2\left(\frac{L^2-\mu}{L^2+\lambda^2}\right)^{\frac{1}{2}}(\phi - \phi_0)\right)} \tag{3.16.1}$$

provided $L^2 - \mu > 0$. The value of r becomes infinite when the denominator of (3.16.1) becomes zero. This happens for

$$\cos 2\psi = -\frac{K_1}{\left(K_1^2 + \omega^2(L^2 - \mu)\right)^{\frac{1}{2}}}, \tag{3.16.2}$$

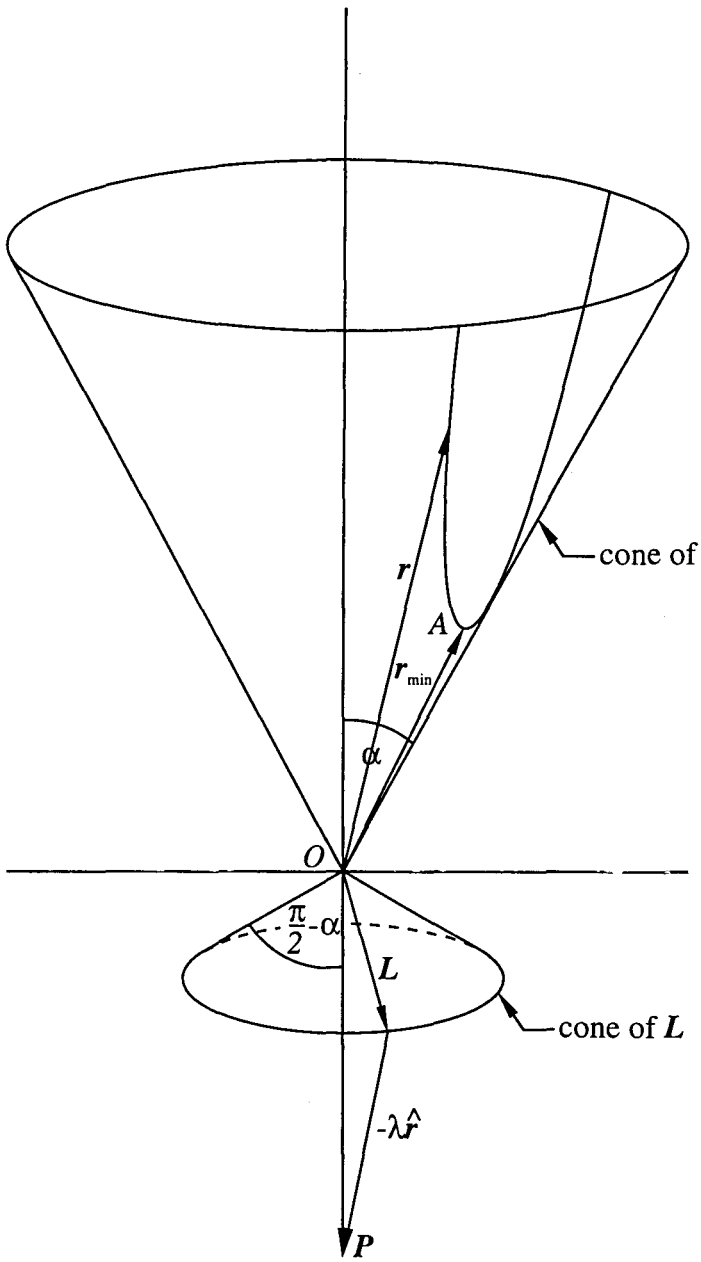

Figure 3.16.1. The typical geometry of the monopole–repulsor orbit when $\mu = -\lambda^2$. The larger orbital and smaller angular momentum cones are shown together with a typical orbit and the orientation of $\boldsymbol{P}$. The origin O is at the point of contact between the two cones and A marks the point of closest approach from O. The orbit is not a conic section although certain projections are conic sections. α and $\pi/2 - \alpha$ are the semi–vertex angles of the orbital and angular momentum cones respectively. The angular momentum is constant in magnitude but not in direction.

where ψ denotes the argument of the cosine function in (3.16.1). In the case $\mu = -\lambda^2$ the projection of the orbit in the ϕ–plane is an hyperbola centred on O. On the cone, however, the orbit is no longer hyperbolic, but fits the cone in such a way that the projection remains hyperbolic. It is now a simple matter to plot the orbit remembering that the polar angle α remains constant. In cartesian coordinates

$$\begin{aligned} x &= r\sin\alpha\cos\phi \\ y &= r\sin\alpha\sin\phi \\ z &= r\cos\alpha, \end{aligned} \tag{3.16.3}$$

where r is calculated from (3.16.1), and α is determined either from (3.14.1) or (3.14.2). Equation (3.16.1) is very reminiscent of the orbit equation for the three–dimensional isotropic repulsor which is not surprising since for $\mu = -\lambda^2$, (3.13.3) can be rewritten as an isotropic repulsor as shown earlier in (3.13.28). The rôles of μ and λ can be seen in (3.16.1). When $(L^2-\mu)^{\frac{1}{2}} > (L^2+\lambda^2)^{\frac{1}{2}}$, the range of ϕ is reduced. However, when $(L^2-\mu)^{\frac{1}{2}} < (L^2+\lambda^2)^{\frac{1}{2}}$, the range of ϕ is increased and the projection of the orbit in the azimuthal plane may spiral around the origin if $(L^2-\mu)^{\frac{1}{2}}/(L^2+\lambda^2)^{\frac{1}{2}}$ is sufficiently small. For $\mu = -\lambda^2$ the orbit is unbounded as t ranges from negative through positive infinity and the projection of the orbit onto the azimuthal plane is hyperbolic. The orbit on the cone is not hyperbolic, but rather is as if the hyperbola were lifted from the plane and bent to fit onto the surface of the cone.

The treatment for the monopole–repulsor closely follows that for the monopole–oscillator. The angular momentum for the planar three–dimensional isotropic repulsor (3.13.28) with $\mu = -\lambda^2$ is given by

$$\boldsymbol{L}_R = (\boldsymbol{r}\times\boldsymbol{P})\times(\dot{\boldsymbol{r}}\times\boldsymbol{P}) = L^2\boldsymbol{P} \tag{3.16.4}$$

and the energy integral by

$$E_R = \frac{1}{2}(\dot{\boldsymbol{r}}\times\boldsymbol{P})\cdot(\dot{\boldsymbol{r}}\times\boldsymbol{P}) - \frac{1}{2}\omega^2(\boldsymbol{r}\times\boldsymbol{P})\cdot(\boldsymbol{r}\times\boldsymbol{P}) = L^2K_1. \tag{3.16.5}$$

In addition to these integrals a unit Laplace–Runge–Lenz vector can be constructed for the equation of motion of the three–dimensional isotropic repulsor in the variable $\boldsymbol{r}\times\boldsymbol{P}$ using a variation of Fradkin's method described in §§1.6 and 1.7 which gives

$$\begin{aligned} \hat{\boldsymbol{J}}_R &= \left(F - U\frac{\partial F}{\partial U}\right)\boldsymbol{r}\,\widehat{\times}\,\boldsymbol{P} + \frac{1}{L_R^2}\frac{\partial F}{\partial U}(\dot{\boldsymbol{r}}\times\boldsymbol{P})\times\boldsymbol{L}_R \\ &= \left(F - u\frac{\partial F}{\partial u}\right)\boldsymbol{r}\,\widehat{\times}\,\boldsymbol{P} + \frac{1}{LP^2}\frac{\partial F}{\partial u}(\dot{\boldsymbol{r}}\times\boldsymbol{P})\times\boldsymbol{P}, \end{aligned} \tag{3.16.6}$$

where $U = 1/|\boldsymbol{r} \times \boldsymbol{P}| = u/L$ and $F = \left(L_R^2U^2 + (E_R^2 + \omega^2 L_R^2)^{1/2} - E_R\right)^{1/2}/(4E_R^2 + 4\omega^2 L_R^2)^{1/4}$. Making the necessary substitutions, (3.16.6) can be simplified and scaled by J_R to give

$$\boldsymbol{J}_R = \pm\left(\frac{J_R}{2\omega}\right)^{\frac{1}{2}}\left[\omega J_R - E_R + L_R^2U^2\right]^{-\frac{1}{2}}\Big((\omega J_R - E_R)\boldsymbol{r}\,\widehat{\times}\,\boldsymbol{P} + U(\dot{\boldsymbol{r}} \times \boldsymbol{P}) \times \boldsymbol{L}_R\Big), \tag{3.16.7}$$

where

$$J_R = \left(\frac{E_R^2}{\omega^2} + L_R^2\right)^{\frac{1}{2}}. \tag{3.16.8}$$

The choice of the arbitrary function $Q(E_R)$ is again motivated by the structure of the Jauch–Hill–Fradkin analogue and is also found to be

$$Q(E_R) = \frac{E_R}{\omega} \tag{3.16.9}$$

which is consistent with (1.7.4). Equation (3.16.7) can be simplified following the procedure described in §1.7 to give

$$\boldsymbol{J}_R = \pm J_R \frac{1}{e\left(|\boldsymbol{r} \times \boldsymbol{P}|^2 + b^2\right)^{\frac{1}{2}}}\left(\boldsymbol{r} \times \boldsymbol{P} + \frac{b^2}{P^2L^2}(\dot{\boldsymbol{r}} \times \boldsymbol{P}) \times \boldsymbol{P}\right), \tag{3.16.10}$$

and similarly the corresponding Hamilton vector can be constructed using

$$\begin{aligned}\boldsymbol{K}_R &= \hat{\boldsymbol{P}} \times \boldsymbol{J}_R \\ &= \pm J_R \frac{(e^2-1)^{\frac{1}{2}}}{e\left(|\boldsymbol{r} \times \boldsymbol{P}|^2 - a^2\right)^{\frac{1}{2}}}\left(\boldsymbol{r} \times \boldsymbol{P} - \frac{a^2}{P^2L^2}(\dot{\boldsymbol{r}} \times \boldsymbol{P}) \times \boldsymbol{P}\right).\end{aligned} \tag{3.16.11}$$

The same restrictions apply as for the three–dimensional isotropic harmonic oscillator regarding the discontinuities and the choice of sign of the Laplace–Runge–Lenz and Hamilton vector analogues. In fact (3.16.10) and (3.16.11) are identical in form to the Laplace–Runge–Lenz and Hamilton vector analogues for the three–dimensional isotropic repulsor using the variable substitutions $\lambda \to \omega$, $\boldsymbol{r} \to \boldsymbol{r} \times \boldsymbol{P}$, $\dot{\boldsymbol{r}} \to \dot{\boldsymbol{r}} \times \boldsymbol{P}$, $\boldsymbol{L} \to \boldsymbol{L}_O$ remembering that the semi–transverse and semi–conjugate axis lengths are scaled by P as a result of the projection and so a^2/P^2 and b^2/P^2 in (3.16.11) and (3.16.10) respectively have the same length as a^2 and b^2 in the case of the three–dimensional isotropic repulsor. It should also be noted that $\hat{\boldsymbol{J}}_R$ and $\hat{\boldsymbol{K}}_R$ as given by (3.16.10) and (3.16.11) are rotated counter–clockwise through $\pi/2$ radians from the expected positions $\boldsymbol{i}$ and $-\boldsymbol{j}$ respectively. This is in agreement with the projection of the orbit into the $\phi-$plane which is also rotated counter–clockwise through $\pi/2$ radians and scaled by P. In the diagrams that follow $\boldsymbol{J}_R$ and $\boldsymbol{K}_R$ will be rotated

clockwise through $\pi/2$ radians to lie along the cartesian unit vectors $\boldsymbol{i}$ and $-\boldsymbol{j}$ respectively in such a way that when the cone is rotated about the $x-$axis so that $\boldsymbol{P}$ lies along $\boldsymbol{k}$, $\boldsymbol{J}_O$ and $\boldsymbol{K}_O$ lie along the cartesian vectors $\boldsymbol{i}$ and $\boldsymbol{j}$ respectively and hence mimic the behaviour of $\boldsymbol{L}$, $\boldsymbol{J}$ and $\boldsymbol{K}$ respectively of the standard three-dimensional isotropic repulsor.

The choice of the arbitrary function $Q(E_R)$ (3.16.9) gives rise to the Jauch–Hill–Fradkin tensor analogue

$$\begin{aligned} A_{ij} &= \left[Q(E_R) \mp \left[Q^2(E_R) + L_R^2\right]^{\frac{1}{2}}\right] \hat{\boldsymbol{J}}_{Ri}\hat{\boldsymbol{J}}_{Rj} + \\ &\quad \left[Q(E_R) \pm \left[Q^2(E_R) + L_R^2\right]^{\frac{1}{2}}\right] \left(\hat{\boldsymbol{P}} \times \hat{\boldsymbol{J}}_R\right)_i \left(\hat{\boldsymbol{P}} \times \hat{\boldsymbol{J}}_R\right)_j \\ &= \frac{1}{w}\left((\dot{\boldsymbol{r}} \times \boldsymbol{P})_i(\dot{\boldsymbol{r}} \times \boldsymbol{P})_j - \omega^2 (\boldsymbol{r} \times \boldsymbol{P})_i (\boldsymbol{r} \times \boldsymbol{P})_j\right). \end{aligned} \tag{3.16.12}$$

Making the substitution $\boldsymbol{r} \times \boldsymbol{P} = \boldsymbol{u}$ and scaling (3.16.12) by ω gives the equation of the velocity hodograph

$$\dot{\boldsymbol{u}}^T (2E_R I - A)\, \dot{\boldsymbol{u}} = -\omega^2 L_R^2. \tag{3.16.13}$$

Since $\hat{\boldsymbol{P}}$ is constant, the motion is planar and for convenience we assign u_3 to be the variable in the direction of $\hat{\boldsymbol{P}}$. The eigenvalues of the 2x2 matrix in (3.16.13) which determine the velocity hodograph in the plane are

$$\lambda = E_R \mp \left(E_R^2 + w^2 L_R^2\right)^{\frac{1}{2}}, \tag{3.16.14}$$

and, if we rotate the velocity hodograph (3.16.13) so that the cartesian unit vectors $\boldsymbol{i}$ and $\boldsymbol{j}$ become principal axes we obtain

$$\left(\frac{\dot{u}_1}{\left(E_R + (E_R^2 + \omega^2 L_R^2)^{\frac{1}{2}}\right)^{\frac{1}{2}}}\right)^2 - \left(\frac{\dot{u}_2}{\left((E_R^2 + \omega^2 L_R^2)^{\frac{1}{2}} - E_R\right)^{\frac{1}{2}}}\right)^2 = 1. \tag{3.16.15}$$

Equation (3.16.15) can be simplified to obtain

$$\left(\frac{\dot{x}}{\frac{L\left((K_1^2+\omega^2 P^2)^{\frac{1}{2}} - K_1\right)^{\frac{1}{2}}}{P}}\right)^2 - \left(\frac{\dot{y}}{\frac{L\left(K_1+(K_1^2+\omega^2 P^2)^{\frac{1}{2}}\right)^{\frac{1}{2}}}{P}}\right)^2 = -1, \tag{3.16.16}$$

which is the equation of a hyperbola symmetrically placed about the $\dot{y}-$axis, with vertices at $\left(0, \pm L\left(K_1 + (K_1^2 + \omega^2 P^2)^{\frac{1}{2}}\right)^{\frac{1}{2}}/P\right)$, foci at $\left(0, \pm L\left(4(K_1^2 + \omega^2 P^2)\right)^{\frac{1}{4}}/P\right)$, eccentricity of $\left(4({K_1}^2 + \omega^2 P^2)\right)^{\frac{1}{4}}\left(({K_1}^2 + \omega^2 P^2)^{\frac{1}{2}} - K_1\right)^{\frac{1}{2}}/(\omega P)$ and centre at $(0,0)$.

The equation of the orbit is then given by

$$\boldsymbol{u}^T (2E_R I - A)\,\boldsymbol{u} = L_R^2. \tag{3.16.17}$$

If we rotate the orbit (3.16.17) so that the cartesian unit vectors $\boldsymbol{i}$ and $\boldsymbol{j}$ become the principal axes we obtain

$$-\left(\frac{u_1}{\frac{\left(E_R+(E_R^2+\omega^2 L_R^2)^{\frac{1}{2}}\right)^{\frac{1}{2}}}{\omega}}\right)^2 + \left(\frac{u_2}{\frac{\left((E_R^2+\omega^2 L_R^2)^{\frac{1}{2}}-E_R\right)^{\frac{1}{2}}}{\omega}}\right)^2 = 1. \tag{3.16.18}$$

Equation (3.16.18) can be simplified to obtain

$$\left(\frac{x}{\frac{L\left((K_1^2+\omega^2P^2)^{\frac{1}{2}}-K_1\right)^{\frac{1}{2}}}{\omega P}}\right)^2 - \left(\frac{y}{\frac{L\left(K_1+(K_1^2+\omega^2P^2)^{\frac{1}{2}}\right)^{\frac{1}{2}}}{\omega P}}\right)^2 = 1 \tag{3.16.19}$$

which is the equation of a hyperbola symmetrically placed about the $x-$axis, vertices at $\left(\pm L\left((K_1^2 + \omega^2 P^2)^{\frac{1}{2}} - K_1\right)^{\frac{1}{2}}/(\omega P), 0\right)$, foci at $\left(\pm L\left(4(K_1^2 + \omega^2 P^2)\right)^{\frac{1}{4}}/(\omega P), 0\right)$, eccentricity of $\left(4({K_1}^2 + \omega^2 P^2)\right)^{\frac{1}{4}}\left(({K_1}^2 + \omega^2 P^2)^{\frac{1}{2}} + K_1\right)^{\frac{1}{2}}/(\omega P)$ and centre at $(0,0)$. Note also that ω^2 times equation (3.16.16) is conjugate to (3.16.19) and also that the sum of the inverse squares of the eccentricities of (3.16.19) and (3.16.16) add to unity as for a conjugate pair of hyperbolae. The asymptotes for both sets of hyperbolae are given by $y = \pm\left(K_1 + (K_1^2 + \omega^2 P^2)^{\frac{1}{2}}\right)^{\frac{1}{2}} x/\left((K_1^2 + \omega^2 P^2)^{\frac{1}{2}} - K_1\right)^{\frac{1}{2}}$. Note that both (3.16.16) and (3.16.19) describe the projection of the velocity hodograph and the orbit in the $\phi-$plane without the scaling by P since the equations are now written in terms of the components of $\dot{\boldsymbol{r}}$ and $\boldsymbol{r}$ rather than those of $\dot{\boldsymbol{r}} \times \boldsymbol{P}$ and $\boldsymbol{r} \times \boldsymbol{P}$ respectively.

The presence of two orthogonal vectors in the $xy-$plane would seem to suggest the existence of additional vectors lying out of the plane but which would project onto the line of $\boldsymbol{J}_R$ and $\boldsymbol{K}_R$ in the xy plane. Two such vectors are given by

$$\boldsymbol{U} = \pm\boldsymbol{J}_R - \frac{\lambda J_R}{L}\hat{\boldsymbol{P}}, \tag{3.16.20}$$

which lie on the surface of the cone collinear with the two vectors directed from the origin to the points of closest and furthest approach (infinity), respectively. Two other such vectors are given by

$$\boldsymbol{V} = \pm\boldsymbol{K}_R - \frac{\lambda K_R}{L}\hat{\boldsymbol{P}}. \tag{3.16.21}$$

Note that $\hat{\boldsymbol{P}} \times \boldsymbol{U} = \pm\boldsymbol{K}_R$ and $\hat{\boldsymbol{P}} \times \boldsymbol{V} = \mp\boldsymbol{J}_R$. Different linear combinations of the vectors shown above can also be constructed. However, they are not nearly as important as those described above because they do not appear to provide any useful additional geometric information on the monopole–oscillator problem.

In the case $\mu = -\lambda^2$ the parametric equations for the orbit can be obtained by substituting for r from (3.16.1) in (3.16.3) to give

$$\begin{aligned} x &= \frac{L\cos\phi}{\left(K_1 + (K_1^2 + \omega^2 P^2)^{\frac{1}{2}}\cos 2\phi\right)^{\frac{1}{2}}} \\ y &= \frac{L\sin\phi}{\left(K_1 + (K_1^2 + \omega^2 P^2)^{\frac{1}{2}}\cos 2\phi\right)^{\frac{1}{2}}} \\ z &= \frac{\lambda}{\left(K_1 + (K_1^2 + \omega^2 P^2)^{\frac{1}{2}}\cos 2\phi\right)^{\frac{1}{2}}}. \end{aligned} \tag{3.16.22}$$

For this case the equation of motion (3.13.28) becomes that of the three–dimensional isotropic repulsor in the variable $\boldsymbol{r} \times \boldsymbol{P}$. The orbit equation is then given by

$$|\boldsymbol{r} \times \boldsymbol{P}|^2 = L^2 r^2 = \frac{L^2 P^2}{K_1 + \left({K_1}^2 + \omega^2 P^2\right)^{\frac{1}{2}}\cos 2\phi}, \tag{3.16.23}$$

i.e. the projection of the orbit into the $\phi-$plane describes a geometric–centred hyperbola symmetrically placed about the $x-$axis with the centre at the intersection of $\boldsymbol{P}$ and the $\phi-$plane. It is well known that the intersection of a plane and a right circular cone describes a conic section on the cone. However, in this case, although the projection of the orbit on the cone into the $\phi-$plane describes a geometric–centred hyperbola, the orbit on the cone does not lie on a plane. The xz and yz projections of the orbit will be studied later in the section where it will be shown that this peculiar geometry is the result of the intersection between the cone and a surface which is closely related to two different conic sections. This association gives an interesting geometric interpretation as to why the repulsor hyperbola differs from that of the

Kepler problem. The eccentricity of the orbital hyperbola is given by

$$\frac{1}{\omega P}\Big(4(K_1^2+\omega^2P^2)\Big)^{\frac{1}{4}}\Big(K_1+(K_1^2+\omega^2P^2)^{\frac{1}{2}}\Big)^{\frac{1}{2}} \tag{3.16.24}$$

which no longer appears to be related in a transparent way to the slope of the cone ($\cot\alpha$) as was the case in the MICZ problem. Note also that $\boldsymbol{P}$ behaves like $\boldsymbol{L}$ in the standard three–dimensional isotropic repulsor.

It is easy to show using the orbit equation (3.16.1) that the minimum length of the vector $\boldsymbol{r}$, $r_{\min}$ on the surface of the cone is reduced in length by the factor $\sin\alpha$ when projected into the ϕ–plane due to its inclination with respect to $\boldsymbol{P}$ and so the projection

$$r_{\min}\sin\alpha=\frac{L}{\omega P}\Big((K_1^2+\omega^2P^2)^{\frac{1}{2}}-K_1\Big)^{\frac{1}{2}}=\frac{1}{P}|\boldsymbol{r}\times\boldsymbol{P}|_{\min}, \tag{3.16.25}$$

is consistent with the result for the semi–transverse axis length of the projected hyperbola from (3.16.19) up to a scaling factor of P and ignoring the rotation brought about by the transformation. Note also that the orbit on the cone does not lie in a plane as was the case for the monopole–Kepler problem. The orbit resembles a bent hyperbola which is draped over the cone in such a way that its projection describes a geometric–centred hyperbola.

The parametric equations for the velocity hodograph can be obtained by differentiating the cartesian components x, y and z (3.16.22) and substituting for $\phi=-L/(r^2\sin\alpha)$ to give

$$\begin{aligned}
\dot{x} &= -\frac{\Big((K_1^2+\omega^2P^2)^{\frac{1}{2}}-K_1\Big)\sin\alpha\sin\phi}{\Big(K_1+(K_1^2+\omega^2P^2)^{\frac{1}{2}}\cos 2\phi\Big)^{\frac{1}{2}}}\\
\dot{y} &= -\frac{\Big(K_1+(K_1^2+\omega^2P^2)^{\frac{1}{2}}\Big)\sin\alpha\cos\phi}{\Big(K_1+(K_1^2+\omega^2P^2)^{\frac{1}{2}}\cos 2\phi\Big)^{\frac{1}{2}}}\\
\dot{z} &= -\frac{(K_1^2+\omega^2P^2)^{\frac{1}{2}}\cos\alpha\sin 2\phi}{\Big(K_1+(K_1^2+\omega^2P^2)^{\frac{1}{2}}\cos 2\phi\Big)^{\frac{1}{2}}}.
\end{aligned} \tag{3.16.26}$$

The values of the constants used to draw Figures 3.16.2 and 3.16.3 were calculated in the same way as was done for the monopole–oscillator case, except that the calculations were done using the semi–transverse and semi–conjugate axes in place of the semi–major and semi–minor axes respectively, in the equivalent calculations to those determining equations (3.14.43)–(3.14.50). In the subsequent discussion, the starred quantites will be used to denote the constants used in the three–dimensional isotropic repulsor. The resulting equations for P, ω, K_1, λ and α were found to be identical in structure to those of (3.14.46)–(3.14.50) replacing occurences of I_1 by the energy of the monopole–repulsor, K_1, and E^* by the energy of the three–dimensional isotropic repulsor. The constants have the values $\mu_k^* = 1.25$, $\theta_0^* = 0$, $a_k^* = 1.89\dot{3}\dot{9}$, $\lambda^* = (\mu_k^*/a_k^{*3})^{\frac{1}{2}}$, $E^* = -0.1906$ and $L^* = 1$. For convenience, L was chosen to be 1.85 and using the values for the starred quantities given above, P, ω, K_1, λ and α were calculated using (3.14.46)–(3.14.50). The magnitude of $\boldsymbol{J}_R$ was found to be

$$J_R = \frac{L^4}{\lambda^* L^{*2}}\left(E^{*2} + \lambda^{*2} L^{*2}\right)^{\frac{1}{2}}. \tag{3.16.27}$$

Figure 3.16.2 shows the orbit for the monopole–repulsor where $\mu = -\lambda^2$. The diagram shows the two right circular orbital and angular momentum cones which extend in opposite directions along the line of $\boldsymbol{P}$ with origin and point of contact at the apices of the two cones. A selection of displacement and corresponding angular momentum vectors has been drawn from the origin to their respective positions on the orbital and angular momentum cones. The orbit resembles a bent hyperbola which is draped over the cone in such a way that its xy projection describes a geometric–centred hyperbola. The origin is not enclosed by the orbit. In order to illustrate the behaviour more clearly, projections of the orbit onto planes parallel to the xy, xz and yz planes are shown, together with projections of the angular momentum curve and the projected images of the cones onto the respective planes. The constant magnitude of the angular momentum is reflected by the angular momentum vectors moving on the surface of a cone which is truncated perpendicular to the axis of symmetry to a height of L^2/P below the origin. The components of the angular momentum are given by $L = (\lambda L \cos\phi/P, \lambda L \sin\phi/P, -L^2/P)$ using (3.16.22) and (3.16.26). The two short line segments drawn perpendicular to the angular momentum curve indicate the limits of extent of the angular momentum as t ranges from negative through positive infinity.

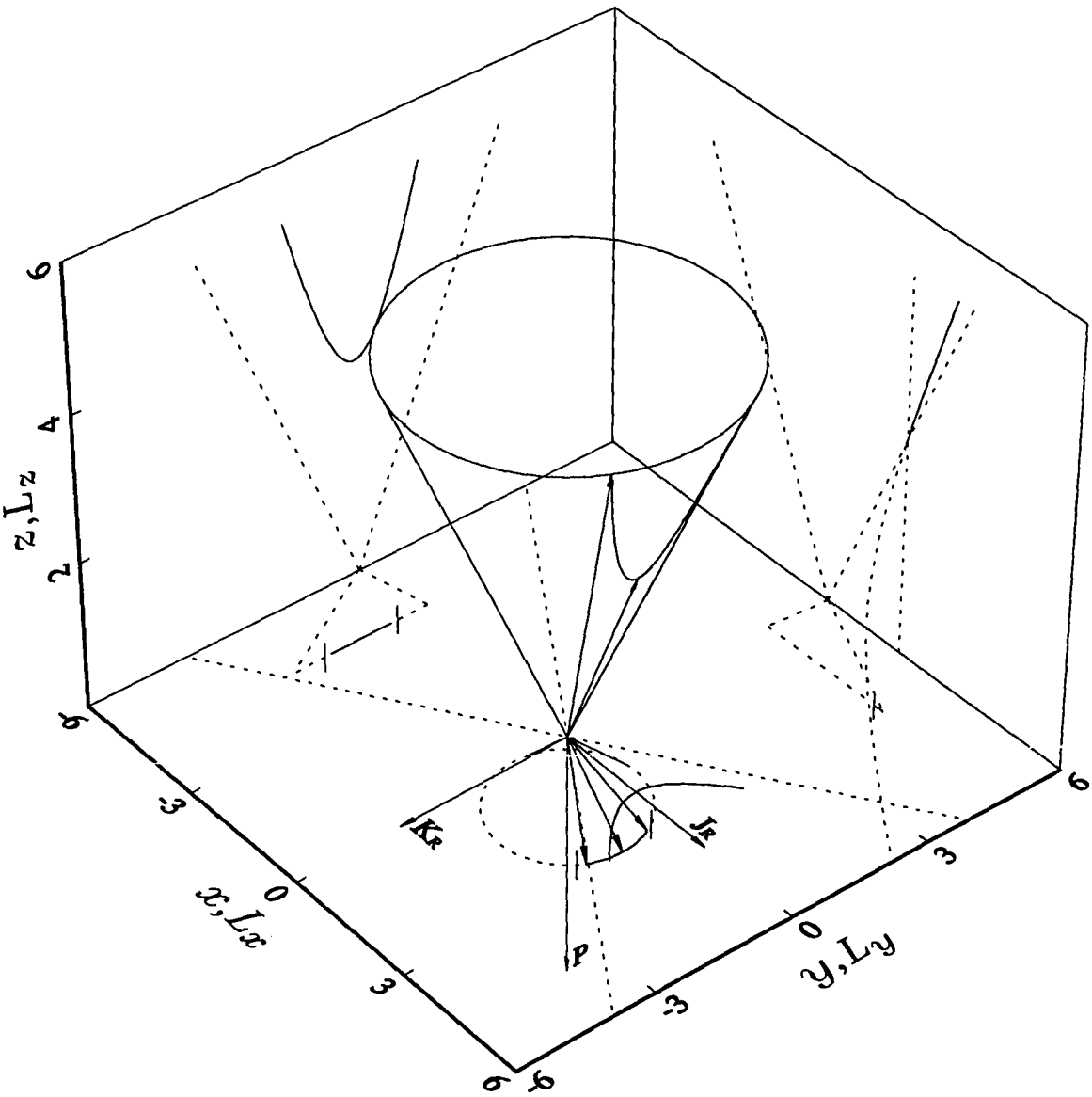

Figure 3.16.2. The monopole–repulsor orbit and angular momentum curve for $\mu = -\lambda^2$ with a selection of displacement and angular momentum vectors drawn from the origin. The radial and angular momentum vectors move on the surfaces of two right circular cone extending in opposite directions along the line of $\boldsymbol{P}$ with origin and point of contact at the apices of the two cones. The projections of the orbit and angular momentum curve onto planes parallel to the xy, xz, yz, L_xL_y, L_xL_z and L_yL_z planes are also shown. The constants have the values $\omega = 0.4289$, $P = 3.4225$, $\lambda = 2.8794$, $\alpha = 0.5711$, $L = 1.85$ and $K_1 = -0.6524$. The origin is not enclosed by the orbit.

The xy projection of the orbit is hyperbolic as described by the first two equations of (3.16.22) which can be manipulated into the form

$$\left(\frac{x}{\frac{L\left((K_1^2+\omega^2P^2)^{\frac{1}{2}}-K_1\right)^{\frac{1}{2}}}{\omega P}}\right)^2-\left(\frac{y}{\frac{L\left(K_1+(K_1^2+\omega^2P^2)^{\frac{1}{2}}\right)^{\frac{1}{2}}}{\omega P}}\right)^2=1 \qquad (3.16.28)$$

which is the cartesian representation of a hyperbola symmetrically placed about the $x=0$ and $y=0$ axes, with vertices at $(\pm a,0)$ where $a=L\left((K_1^2+\omega^2P^2)^{\frac{1}{2}}-K_1\right)^{\frac{1}{2}}/(\omega P)$ and $b=L\left(K_1+(K_1^2+\omega^2P^2)^{\frac{1}{2}}\right)^{\frac{1}{2}}/(\omega P)$, foci at $\left(\pm(a^2+b^2)^{\frac{1}{2}},0\right)$, eccentricity of $(a^2+b^2)^{\frac{1}{2}}/a$ and centred at the origin. The distance from the centre to a vertex a agrees with the length of the projection of $r_{\min}$ onto the $\phi-$plane, *i.e.* $r_{\min}\sin\alpha$. The transverse axis is the same length as the distance between the two vertices $2a$. The conjugate axis has the length $2b$. The asymptotes are given by $y=bx/a$, *i.e.* a combination of the first and second equations of (3.16.22). The projected orbit is consistent with the planar hyperbolic three–dimensional isotropic repulsor orbit with $\mu_k^*=1.25$, $\theta_0^*=0$, $a_k^*=1.893\dot{9}$, $\lambda^*=(\mu_k^*/a_k^{*3})^{\frac{1}{2}}$, $E^*=-0.1906$ and $L^*=1$. As t ranges from negative through positive infinity, the azimuthal angle ϕ ranges between $\pi/2-\delta$ where $\delta=\arccos\left(K_1/(K_1^2+\omega^2P^2)^{\frac{1}{2}}\right)/2$ and $-\pi/2+\delta$ and the projection ranges from $(+\infty,+\infty)$ when $\phi=\pi/2-\delta$ to (c,d) when $\phi=\pi/6$ where $c=3^{\frac{1}{2}}2^{\frac{1}{2}}L/\left(2\left(2K_1+(K_1^2+\omega^2P^2)^{\frac{1}{2}}\right)^{\frac{1}{2}}\right)$ and $d=2^{\frac{1}{2}}L/\left(2\left(2K_1+(K_1^2+\omega^2P^2)^{\frac{1}{2}}\right)^{\frac{1}{2}}\right)$, to $(a,0)$ when $\phi=0$ where $a=r_{\min}\sin\alpha$ to $(c,-d)$ when $\phi=-\pi/6$ to $(+\infty,-\infty)$ when $\phi=-\pi/2+\delta$. The projection of the angular momentum curve onto its corresponding plane describes a section of a circle with radius $\lambda L/P$ symmetrically placed about the L_x-axis, *i.e.* ${L_x}^2+{L_y}^2=(\lambda L/P)^2$. As t ranges from negative through positive infinity, the projection ranges from (f,g) when $\phi=\pi/2-\delta$ where $f=\lambda L\left((K_1^2+\omega^2P^2)^{\frac{1}{2}}-K_1\right)^{\frac{1}{2}}/\left(2P^2(K_1^2+\omega^2P^2)^{\frac{1}{2}}\right)^{\frac{1}{2}}$ and $g=\lambda L\left(K_1+(K_1^2+\omega^2P^2)^{\frac{1}{2}}\right)^{\frac{1}{2}}/\left(2P^2(K_1^2+\omega^2P^2)^{\frac{1}{2}}\right)^{\frac{1}{2}}$ and to $\left(3^{\frac{1}{2}}\lambda L/(2P),\lambda L/(2P)\right)$ when $\phi=\pi/6$ to $(\lambda L/P,0)$ when $\phi=0$ to $\left(3^{\frac{1}{2}}\lambda L/(2P),-\lambda L/(2P)\right)$ when $\phi=-\pi/6$ to $(f,-g)$ when $\phi=-\pi/2+\delta$, *i.e.* the circle is not completed even as t ranges from negative through positive infinity. The dotted line completes the angular momentum cone. However, it should be remembered that the projection of the angular momentum vectors never closes as t ranges from negative through positive infinity.

The xz projection shows the images of the orbital and angular momentum cones with dotted lines, together with the projections of the orbit and angular momentum curves. Note that the xz projection of the orbit is obtained by manipulating the first and third equations of (3.16.22) into the form

$$\left(\frac{x}{\frac{L}{\left(4(K_1^2+\omega^2P^2)\right)^{\frac{1}{4}}}}\right)^2-\left(\frac{z}{\frac{\lambda\left(K_1+(K_1^2+\omega^2P^2)^{\frac{1}{2}}\right)^{\frac{1}{2}}}{\omega P}}\right)^2=1 \qquad (3.16.29)$$

subject to the condition that

$$|x|\geq\frac{L}{\omega P}\left((K_1^2+\omega^2P^2)^{\frac{1}{2}}-K_1\right)^{\frac{1}{2}} \qquad (3.16.30)$$

which is the cartesian representation of a section of a hyperbola symmetrically placed about the $x=0$ and $z=0$ axes, with vertices at $(\pm a,0)$ where $a=L/\left(4(K_1^2+\omega^2P^2)\right)^{\frac{1}{4}}$ and $b=\lambda\left(K_1+(K_1^2+\omega^2P^2)^{\frac{1}{2}}\right)^{\frac{1}{2}}/(\omega P)$, foci at $(\pm(a^2+b^2)^{\frac{1}{2}},0)$, eccentricity of $(a^2+b^2)^{\frac{1}{2}}/a$ and centred at the origin. The transverse axis is the same length as the distance between the two vertices $2a$. The conjugate axis has the length $2b$. The asymptotes are given by $z=bx/a$, *i.e.* a combination of the first and third equations of (3.16.22). The relationship between the eccentricity e of the hyperbolic projection in the $xz-$plane and that of the hyperbolic projection in the $xy-$plane, e^*, is found to be $e^2=m^2a^{*2}(e^{*2}-1)/a^2+1$, where m is the slope of the cone, $(\cot\alpha)$, and the superscript $*$ refers to the equivalent quantities in (3.16.28). Note that the semi-conjugate axis lengths of both projections are not involved in the relationship between the two eccentricities. The magnitude of the lower limit of extent of the variable x which is indicated with a dotted line parallel to the $z-$axis agrees with the length of the projection of $r_{\min}$ onto the $xy-$plane, *i.e.* $r_{\min}\sin\alpha$. The magnitude of z at this point agrees with the height of the projection of $r_{\min}$ onto the $xz-$plane, *i.e.* $r_{\min}\cos\alpha$. As t ranges from negative through positive infinity, the projection ranges from $(+\infty,+\infty)$ when $\phi=\pi/2-\delta$ where $\delta=\arccos\left(K_1/(K_1^2+\omega^2P^2)^{\frac{1}{2}}\right)/2$ to (c,d) when $\phi=\pi/6$ where $c=3^{\frac{1}{2}}2^{\frac{1}{2}}L/\left(2\left(2K_1+(K_1^2+\omega^2P^2)^{\frac{1}{2}}\right)^{\frac{1}{2}}\right)$ and $d=2^{\frac{1}{2}}\lambda/\left(2K_1+(K_1^2+\omega^2P^2)^{\frac{1}{2}}\right)^{\frac{1}{2}}$, to $(r_{\min}\sin\alpha,r_{\min}\cos\alpha)$ when $\phi=0$ to (c,d) when $\phi=-\pi/6$ to $(+\infty,+\infty)$ when $\phi=-\pi/2+\delta$. The L_xL_z projection of the angular momentum curve extends along the base of the triangle describing the L_xL_z projection of the image of the angular momentum cone, perpendicular to the L_z-axis. As t ranges from negative through positive infinity, the projection ranges from $(f,-L^2/P)$ when $\phi=\pi/2-\delta$ where $f=\lambda L\left((K_1^2+\omega^2P^2)^{\frac{1}{2}}-K_1\right)^{\frac{1}{2}}/\left(2P^2(K_1^2+\omega^2P^2)^{\frac{1}{2}}\right)^{\frac{1}{2}}$ to $(3^{\frac{1}{2}}\lambda L/(2P),-L^2/P)$ when $\phi=\pi/6$ to $(\lambda L/P,-L^2/P)$ when $\phi=0$

to $(3^{\frac{1}{2}}\lambda L/(2P), -L^2/P)$ when $\phi = -\pi/6$ to $(f, -L^2/P)$ when $\phi = -\pi/2 + \delta$, *i.e.* only a section along the length of the base of the angular momentum triangle. In other words the angular momentum vectors will never sweep over the entire surface area of the angular momentum cone even as the time ranges from negative through positive infinity. The short line segment drawn perpendicular to the xz projection of the angular momentum curve indicates the limit of extent of the projection of the angular momentum as t ranges from negative through positive infinity.

The yz projection shows the images of the orbital and angular momentum cones with dotted lines, together with the projections of the orbit and angular momentum curves. Note that the yz projection of the orbit is obtained by manipulating the second and third equations of (3.16.22) into the form

$$\left(\frac{z}{\frac{\lambda\left((K_1^2+\omega^2P^2)^{\frac{1}{2}}-K_1\right)^{\frac{1}{2}}}{\omega P}}\right)^2 - \left(\frac{y}{\frac{L}{\left(4(K_1^2+\omega^2P^2)\right)^{\frac{1}{4}}}}\right)^2 = 1 \qquad (3.16.31)$$

which is the equation of a hyperbola symmetrically placed about the $y = 0$ and $z = 0$ axes, with vertices at $(0, \pm a)$ where $a = \lambda\left((K_1^2 + \omega^2P^2)^{\frac{1}{2}} - K_1\right)^{\frac{1}{2}}/(\omega P)$ and $b = L/\left(4(K_1^2 + \omega^2P^2)\right)^{\frac{1}{4}}$, foci at $\left(0, \pm(a^2 + b^2)^{\frac{1}{2}}\right)$, eccentricity of $(a^2 + b^2)^{\frac{1}{2}}/a$ and centred at the origin. The distance from the centre to a vertex a agrees with the length of the projection of $r_{\min}$ onto the $yz-$plane, *i.e.* $r_{\min}\cos\alpha$. The transverse axis is the same length as the distance between the two vertices $2a$. The conjugate axis has the length $2b$. The asymptotes are given by $z = ay/b$, *i.e.* a combination of the second and third equations of (3.16.22). The relationship between the eccentricity e of the hyperbolic projection in the $yz-$plane and that of the hyperbolic projection in the $xy-$plane, e^*, is found to be $e^2 = 1/m^2b^2(e^{*2} - 1)/b^{*2} + 1$, where m is the slope of the cone, $(\cot\alpha)$, and the superscript $*$ refers to the equivalent quantities in (3.16.28). Note that the semi–transverse axis lengths of both projections are not involved in the relationship between the two eccentricities. As t ranges from negative through positive infinity, the projection ranges from $(+\infty, +\infty)$ when $\phi = \pi/2 - \delta$ where $\delta = \arccos\left(K_1/(K_1^2 + \omega^2P^2)^{\frac{1}{2}}\right)/2$ to (c, d) when $\phi = \pi/6$ where $c = 2^{\frac{1}{2}}L/\left(2\left(2K_1 + (K_1^2 + \omega^2P^2)^{\frac{1}{2}}\right)^{\frac{1}{2}}\right)$ and $d = 2^{\frac{1}{2}}\lambda/\left(2K_1 + (K_1^2 + \omega^2P^2)^{\frac{1}{2}}\right)^{\frac{1}{2}}$, to $(0, r_{\min}\cos\alpha)$ when $\phi = 0$ to $(-c, d)$ when $\phi = -\pi/6$ to $(-\infty, +\infty)$ when $\phi = -\pi/2 + \delta$. The L_xL_z projection of the angular momentum curve extends along the base of the triangle describing the L_xL_z projection of the image of the angular momentum cone, perpendicular to the L_z-axis. As t ranges from negative through positive infinity, the projection ranges from $(g, -L^2/P)$ when $\phi = \pi/2 - \delta$ where

$g = \lambda L\Big(K_1 + (K_1^2 + \omega^2 P^2)^{\frac{1}{2}}\Big)^{\frac{1}{2}} / \Big(2P^2(K_1^2 + \omega^2 P^2)^{\frac{1}{2}}\Big)^{\frac{1}{2}}$ to $(\lambda L/(2P), -L^2/P)$ when $\phi = \pi/6$ to $(0, -L^2/P)$ when $\phi = 0$ to $(-\lambda L/(2P), -L^2/P)$ when $\phi = -\pi/6$ to $(-g, -L^2/P)$ when $\phi = -\pi/2 + \delta$, *i.e.* only a section along the length of the base of the angular momentum triangle. In other words the angular momentum vectors will never sweep over the entire surface area of the angular momentum cone even as the time ranges from negative through positive infinity. The two short line segments drawn perpendicular to the yz projection of the angular momentum curve indicate the limits of extent of the projection of the angular momentum as t ranges from negative through positive infinity.

The conserved vector $\boldsymbol{K}_R$ which has been rotated clockwise through $\pi/2$ radians to lie along the cartesian unit vector $-\boldsymbol{j}$ is given by (3.16.11) and has length $(E_R^2/\omega^2 + L_R^2)^{\frac{1}{2}}$ and is scaled by L^2 for convenience in Figure 3.16.2. The vector $\boldsymbol{J}_R$, which is perpendicular to $\boldsymbol{K}_R$, is also rotated clockwise through $\pi/2$ radians to lie along the cartesian unit vector $\boldsymbol{i}$. $\boldsymbol{K}_R$ also has the length $(E_R^2/\omega^2 + L_R^2)^{\frac{1}{2}}$ and is similarly scaled by L^2 in Figure 3.16.2. The Poincaré vector, $\boldsymbol{P}$, lies along the cartesian unit vector $-\boldsymbol{k}$. Note that, when the cone is rotated about the $x-$axis so that $\boldsymbol{P}$ lies along $\boldsymbol{k}$, the vectors $\boldsymbol{K}_R$ and $\boldsymbol{J}_R$ lie along the cartesian unit vectors $\boldsymbol{j}$ and $\boldsymbol{i}$ respectively and hence mimic the behaviour of $\boldsymbol{L}$, $\boldsymbol{K}$ and $\boldsymbol{J}$ respectively of the standard three–dimensional isotropic repulsor. The Poincaré vector is given by (3.13.4) and has components $\Big(0, 0, -(L^2 + \lambda^2)^{\frac{1}{2}}\Big)$.

Figure 3.16.3 shows the velocity hodograph for the monopole–repulsor where $\mu = -\lambda^2$. A selection of velocity vectors corresponding to the displacement vectors shown in Figure 3.16.2 has been drawn from the origin to their respective positions on the velocity hodograph. In order to illustrate the $\dot{\boldsymbol{r}}$ behaviour more clearly, projections of the velocity hodograph onto planes parallel to the $\dot{x}\dot{y}$, $\dot{x}\dot{z}$ and $\dot{y}\dot{z}$ planes are also shown, together with the projected images of the orbital cone onto the respective planes.

The $\dot{x}\dot{y}$ projection of the velocity hodograph is obtained by manipulating the first two equations of (3.16.26) into the form

$$\left(\frac{\dot{y}}{\frac{L\Big(K_1+(K_1^2+\omega^2P^2)^{\frac{1}{2}}\Big)^{\frac{1}{2}}}{P}}\right)^2 - \left(\frac{\dot{x}}{\frac{L\Big((K_1^2+\omega^2P^2)^{\frac{1}{2}}-K_1\Big)^{\frac{1}{2}}}{P}}\right)^2 = 1, \qquad (3.16.32)$$

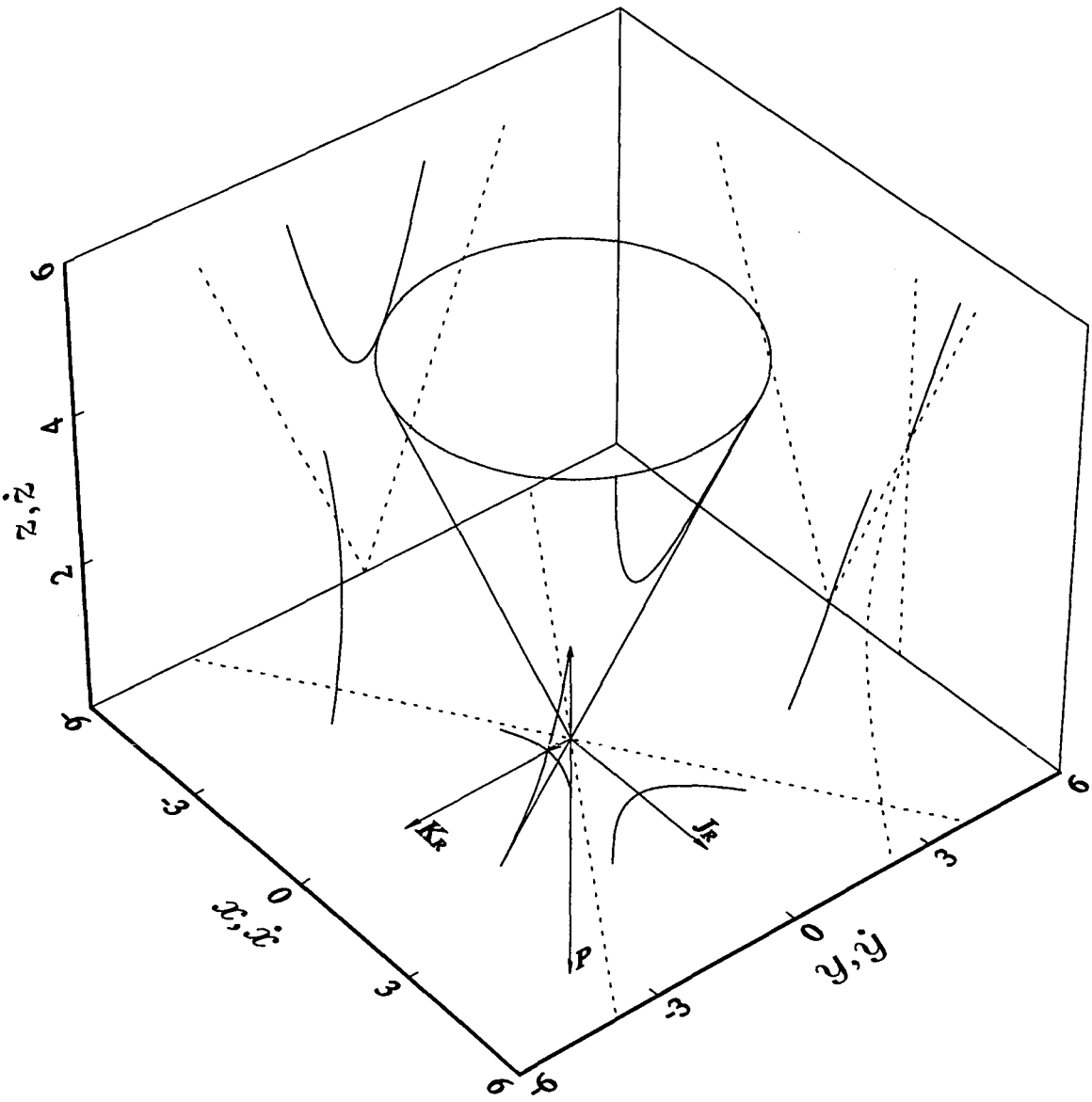

Figure 3.16.3. The monopole–repulsor velocity hodograph and orbit for $\mu = -\lambda^2$ with a selection of velocity vectors drawn from the origin. The velocity vectors are not confined to a plane although, as t ranges from negative through positive infinity, the heads of the velocity vectors projected into the $\dot{x}\dot{y}-$plane trace out a hyperbola. The projections of the velocity hodograph and orbit onto planes parallel to the $\dot{x}\dot{y}$, $\dot{x}\dot{z}$, $\dot{y}\dot{z}$, xy, xz and yz planes are also shown. The constants are chosen as for Figure 3.16.2.

which is the cartesian equation of a hyperbola symmetrically placed about the $\dot{x} = 0$ and $\dot{y} = 0$ axes, with vertices at $(0, \pm a)$ where $a = L\Big(K_1 + (K_1^2 + \omega^2 P^2)^{\frac{1}{2}}\Big)^{\frac{1}{2}}/P$ and $b = L\Big((K_1^2+\omega^2 P^2)^{\frac{1}{2}} - K_1\Big)^{\frac{1}{2}}/P$, foci at $\Big(0, \pm(a^2+b^2)^{\frac{1}{2}}\Big)$, eccentricity of $(a^2+b^2)^{\frac{1}{2}}/a$ and centred at the origin. The transverse axis is the same length as the distance between the two vertices $2a$. The conjugate axis has the length $2b$. The asymptotes are given by $\dot{y} = a\dot{x}/b$, *i.e.* a combination of the first and second equations of (3.16.26). Note that the asymptotes of (3.16.32) have the same gradient as the asymptotes of (3.16.28) which confirms that ω^2 times (3.16.32) is conjugate to (3.16.28). The projected velocity hodograph is consistent with the planar velocity hodograph for the hyperbolic three–dimensional isotropic repulsor with $\mu_k^* = 1.25$, $\theta_0^* = 0$, $a_k^* = 1.893\dot{9}$, $\lambda^* = (\mu_k^*/a_k^{*3})^{\frac{1}{2}}$, $E^* = -0.1906$ and $L^* = 1$. As t ranges from negative through positive infinity, the projection ranges from $(-\infty, -\infty)$ when $\phi = \pi/2 - \delta$ to $(-c, -d)$ when $\phi = \pi/6$ where $c = 2^{\frac{1}{2}} L\Big((K_1^2+\omega^2 P^2)^{\frac{1}{2}} - K_1\Big)/\Big(2P\Big(2K_1 + (K_1^2+\omega^2 P^2)^{\frac{1}{2}}\Big)^{\frac{1}{2}}\Big)$ and $d = 3^{\frac{1}{2}} 2^{\frac{1}{2}} L\Big(K_1 + (K_1^2 + \omega^2 P^2)^{\frac{1}{2}}\Big)/\Big(2P\Big(2K_1 + (K_1^2 + \omega^2 P^2)^{\frac{1}{2}}\Big)^{\frac{1}{2}}\Big)$ and to $(0, -a)$ when $\phi = 0$ where $a = L\Big(K_1 + (K_1^2+\omega^2 P^2)^{\frac{1}{2}}\Big)^{\frac{1}{2}}/P$ which is ω times the semi–conjugate axis length of (3.16.28), to $(c, -d)$ when $\phi = -\pi/6$ to $(+\infty, -\infty)$ when $\phi = -\pi/2 + \delta$, *i.e.* the projection of the velocity vectors describes a hyperbola as t ranges from negative through positive infinity.

The $\dot{x}\dot{z}$ projection shows the images of the orbital cone with dotted lines, together with the respective projections of the orbit and velocity hodograph. Note that the $\dot{x}\dot{z}$ projection of the velocity hodograph is obtained by manipulating the first and third equations of (3.16.26) into the form

$$\dot{z}^2 = \frac{4B^2 \cot^2 \alpha \dot{x}^2}{(B - A)} \left(\frac{(B - A)\sin^2 \alpha + \dot{x}^2}{(B - A)^2 \sin^2 \alpha + 2B\dot{x}^2} \right), \tag{3.16.33}$$

where $A = K_1$ and $B = (K_1^2 + \omega^2 P^2)^{\frac{1}{2}}$, which is closely related to (3.14.58). As t ranges from negative through positive infinity, the projection ranges from $(-\infty, -\infty)$ when $\phi = \pi/2 - \delta$ to $(-c, -d)$ when $\phi = \pi/6$ where $c = 2^{\frac{1}{2}} L\Big((K_1^2 + \omega^2 P^2)^{\frac{1}{2}} - K_1\Big)/\Big(2P\Big(2K_1 + (K_1^2 + \omega^2 P^2)^{\frac{1}{2}}\Big)^{\frac{1}{2}}\Big)$ and $d = 3^{\frac{1}{2}} 2^{\frac{1}{2}} \lambda (K_1^2 + \omega^2 P^2)^{\frac{1}{2}}/\Big(2P\Big(2K_1 + (K_1^2 + \omega^2 P^2)^{\frac{1}{2}}\Big)^{\frac{1}{2}}\Big)$ and to $(0, 0)$ when $\phi = 0$ to (c, d) when $\phi = -\pi/6$ to $(+\infty, +\infty)$ when $\phi = -\pi/2 + \delta$.

The $\dot{y}\dot{z}$ projection shows the images of the orbital cone with dotted lines, together with the respective projections of the orbit and velocity hodograph. Note that the $\dot{y}\dot{z}$ projection of the velocity hodograph is obtained by manipulating the second and third equations of (3.16.26) into the form

$$\dot{z}^2 = \frac{4B^2 \cot^2 \alpha \dot{y}^2}{(A+B)} \left(\frac{\dot{y}^2 - (A+B)\sin^2 \alpha}{2B\dot{y}^2 - (A+B)^2 \sin^2 \alpha} \right), \tag{3.16.34}$$

where $A = K_1$ and $B = (K_1^2 + \omega^2 P^2)^{\frac{1}{2}}$, which is symmetrically placed about the $\dot{z} = 0$ axis and closely related to (3.14.59). As t ranges from negative through positive infinity, the projection ranges from $(-\infty, -\infty)$ when $\phi = \pi/2 - \delta$ to $(-c, -d)$ when $\phi = \pi/6$ where $c = 3^{\frac{1}{2}} 2^{\frac{1}{2}} L\Big(K_1 + (K_1^2 + \omega^2 P^2)^{\frac{1}{2}}\Big) / \Big(2P\Big(2K_1 + (K_1^2 + \omega^2 P^2)^{\frac{1}{2}}\Big)^{\frac{1}{2}}\Big)$ and $d = 3^{\frac{1}{2}} 2^{\frac{1}{2}} \lambda (K_1^2 + \omega^2 P^2)^{\frac{1}{2}} / \Big(2P\Big(2K_1 + (K_1^2 + \omega^2 P^2)^{\frac{1}{2}}\Big)^{\frac{1}{2}}\Big)$ and to $(-a, 0)$ when $\phi = 0$ where $a = L\Big(K_1 + (K_1^2 + \omega^2 P^2)^{\frac{1}{2}}\Big)^{\frac{1}{2}} / P$ which is ω times the semi-conjugate axis length of (3.16.28), to $(-c, d)$ when $\phi = -\pi/6$ to $(-\infty, +\infty)$ when $\phi = -\pi/2 + \delta$.

The conserved vectors $\boldsymbol{K}_R$ and $\boldsymbol{J}_R$ are scaled by L^2 for convenience while $\boldsymbol{P}$ is drawn as in Figure 3.16.2

From (3.16.29) we obtain a rather important result. The intersection of a suitable hyperbolic sheet with axis of symmetry lying in the ϕ–plane and a right circular cone with apex on the ϕ–plane and axis of symmetry perpendicular to the plane has a projection in the ϕ–plane which describes a geometric–centred hyperbola. Alternatively from (3.16.31) the intersection of a different hyperbolic sheet with axis of symmetry perpendicular to the ϕ–plane and the right circular cone described above also has a geometric–centred hyperbolic projection in the ϕ–plane. In contrast, the MICZ problem showed that the intersection of a plane and a right circular cone with apex on the ϕ–plane and axis of symmetry perpendicular to the plane has a projection in the ϕ–plane which describes a focus–centred conic. These two results give a geometric interpretation of the reasons for the difference in location of the origin in both the hyperbolic Kepler and three–dimensional isotropic repulsor problems. In most textbooks dealing with the subject, the connection between the orbit of the Kepler problem and the plane section of the cone is usually mentioned. However, no explanation as to why this is the case has been proposed. In fact the geometric–centred hyperbolic orbit of the repulsor is also a hyperbolic conic section, although from what we have seen above its connection with the cone is more involved. The results above demonstrate that the plane section of the cone is naturally associated

with the plane polar focus–centred representation of the conic section and the intersection of the hyperbolic sheet with the cone with the geometric–centred cartesian representation of the hyperbola.

Figure 3.16.4 shows the orbit for the monopole–repulsor where $\mu = 63L^2/64 - \lambda^2/64$. The diagram shows the right circular orbital cone extending along the line of $\boldsymbol{P}$ with origin at the apex of the cone. The equation of motion in this case is given by (3.13.3) with the corresponding orbit equation (3.16.1) whilst for the projection of the motion into the $\phi-$plane, the equation of motion is given by (3.13.28) with corresponding orbit equation $|\boldsymbol{r} \times \boldsymbol{P}|^2$ equal to L^2 times equation (3.16.1). The energy of this orbit, K_1, is chosen to be zero whilst the argument of the cosine term in (3.16.1) is $(\phi - \phi_0)/4$. The orbit on the cone spirals inwards asymptotically, circles the origin twice before spiralling outwards asymptotically and ultimately closes as t ranges from negative through positive infinity, a process which is repeated for the projection of the orbit in the $\phi-$plane. The orbit on the cone has no rotational symmetry about $\boldsymbol{P}$. The origin is not enclosed by the orbit. In order to illustrate the behaviour more clearly, projections of the orbit onto planes parallel to the xy, xz and yz planes are shown, together with the projected images of the cones onto the respective planes. The magnitude of the angular momentum is constant throughout the motion.

Figure 3.16.5 shows the velocity hodograph for the monopole–repulsor where $\mu = 63L^2/64 - \lambda^2/64$. In order to illustrate the $\dot{\boldsymbol{r}}$ behaviour more clearly, projections of the velocity hodograph onto planes parallel to the $\dot{x}\dot{z}$ and $\dot{y}\dot{z}$ planes are also shown and seen to display a certain symmetry. The velocity hodograph is bounded at both ends by the tangents to the asymptotes of the orbit on the cone.

Figure 3.16.6 shows the orbit for the monopole–repulsor where $\mu = -3L^2 - 4\lambda^2$. The diagram shows the right circular orbital cone extending along the line of $\boldsymbol{P}$ with origin at the apex of the cone. The equation of motion in this case is given by (3.13.3) with the corresponding orbit equation (3.16.1) whilst for the projection of the motion into the $\phi-$plane, the equation of motion is given by (3.13.28) with corresponding orbit equation $|\boldsymbol{r} \times \boldsymbol{P}|^2$ equal to L^2 times equation (3.16.1). The energy of this orbit, K_1, is chosen to be 0.7789 whilst the argument of the cosine term in (3.16.1) is $4(\phi - \phi_0)$. The orbit is not closed and approaches asymptotically before leaving asymptotically, a process which is repeated for the projection of the orbit in the $\phi-$plane. The orbit on the cone is not hyperbolic and neither are the xy, xz and yz projections of the orbit. The orbit on the cone has no rotational symmetry about $\boldsymbol{P}$. The origin is not enclosed by the orbit. In order to illustrate the behaviour more clearly, projections

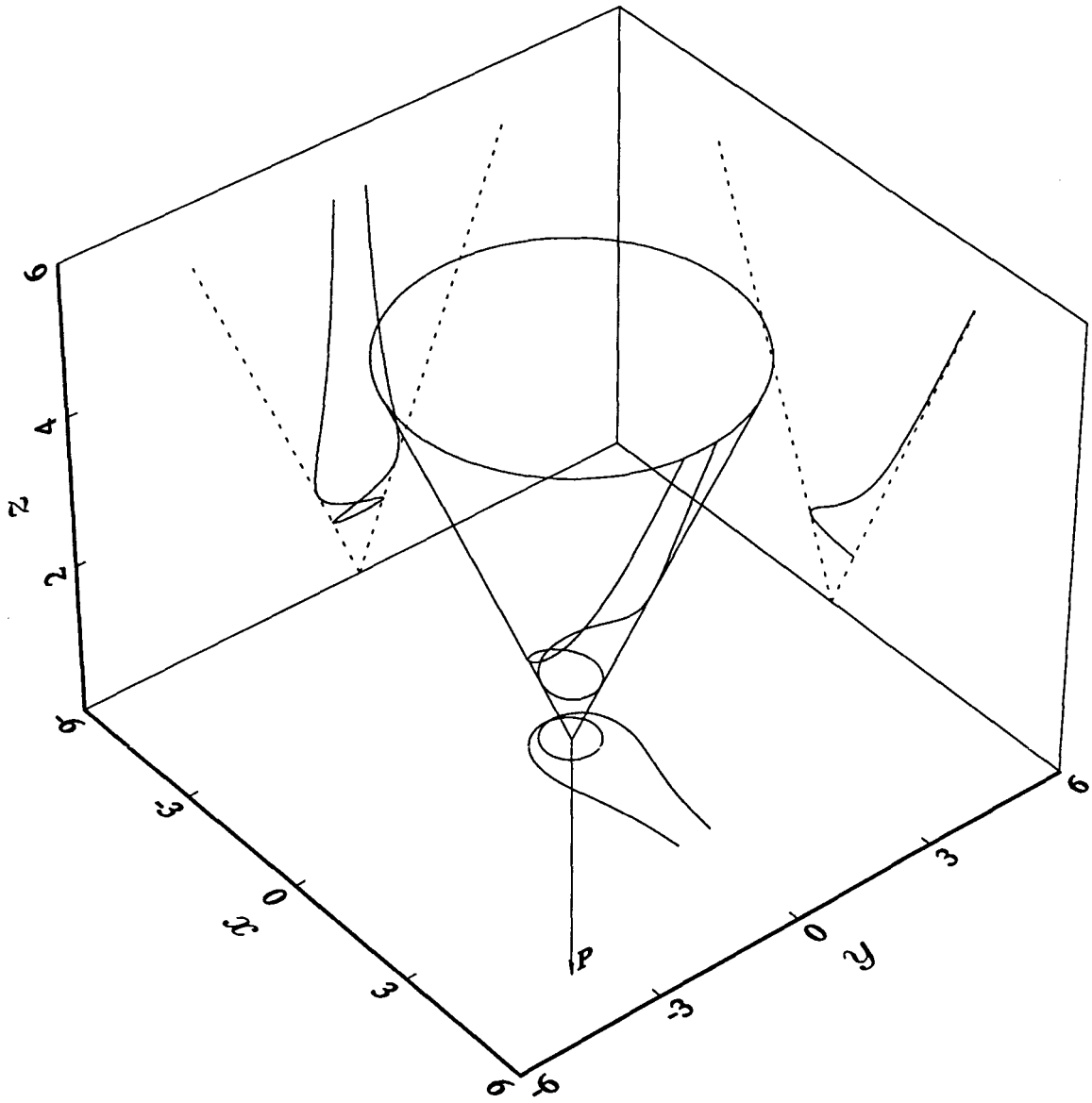

Figure 3.16.4. The monopole–repulsor orbit for $\mu = 63L^2/64 - \lambda^2/64$. The radial vectors move on the surface of a right circular cone extending along the line of $\boldsymbol{P}$ with origin at the apex of the cone. The orbit on the cone approaches asymptotically, circles the origin twice before leaving asymptotically. Both branches of the orbit meet at infinity. The projections of the orbit onto planes parallel to the xy, xz and yz planes are also shown. The constants have the values $\omega = 0.4289$, $P = 3.4225$, $\lambda = 2.8794$, $\alpha = 0.5711$, $L = 1.85$ and $K_1 = 0$. The origin is not enclosed by the orbit.

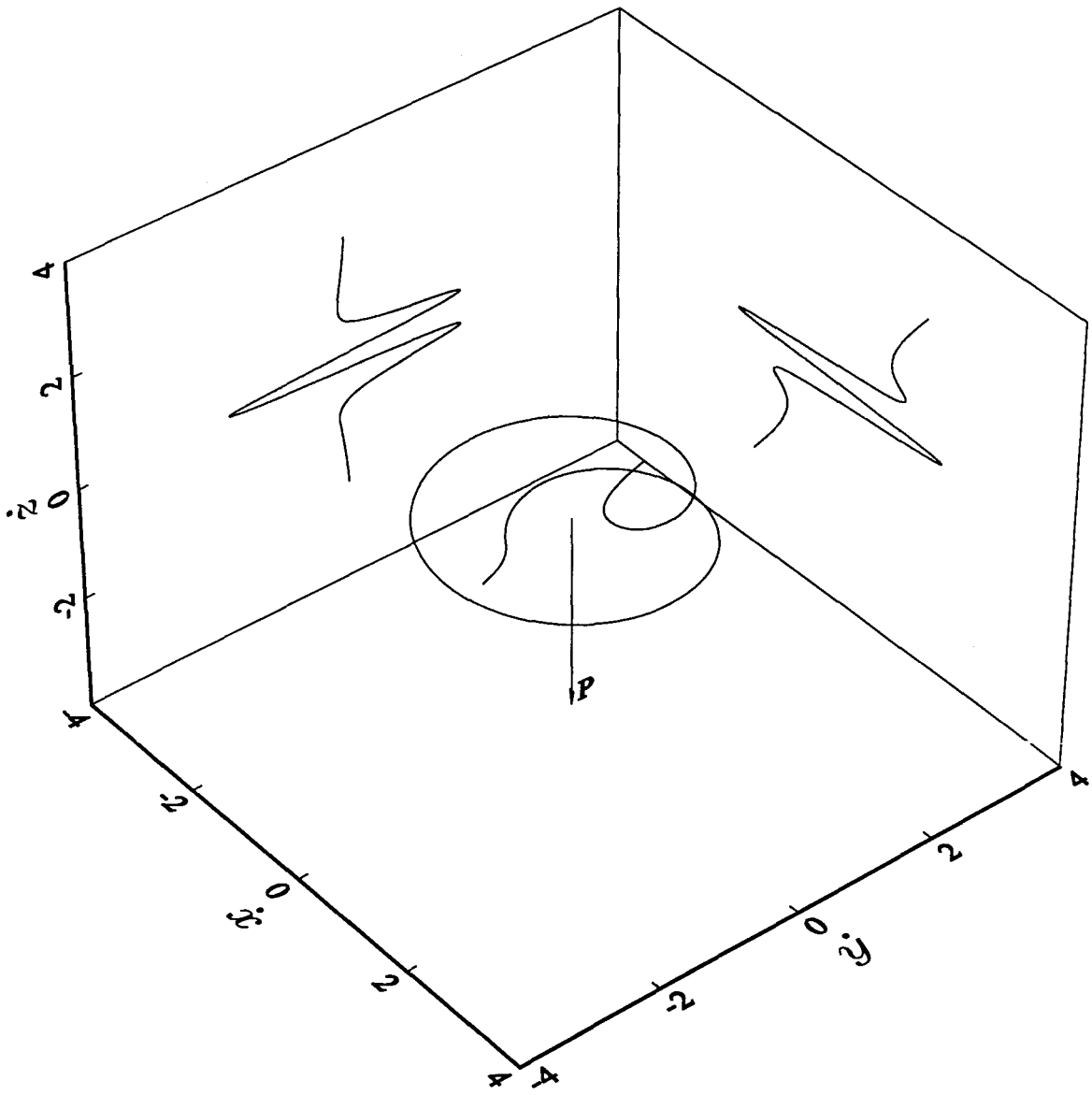

Figure 3.16.5. The monopole–repulsor velocity hodograph for $\mu = 63L^2/64 - \lambda^2/64$. The projections of the velocity hodograph onto planes parallel to the $\dot{x}\dot{z}$ and $\dot{y}\dot{z}$ planes are also shown. The constants are chosen as for Figure 3.16.4. The origin is enclosed by the velocity hodograph.

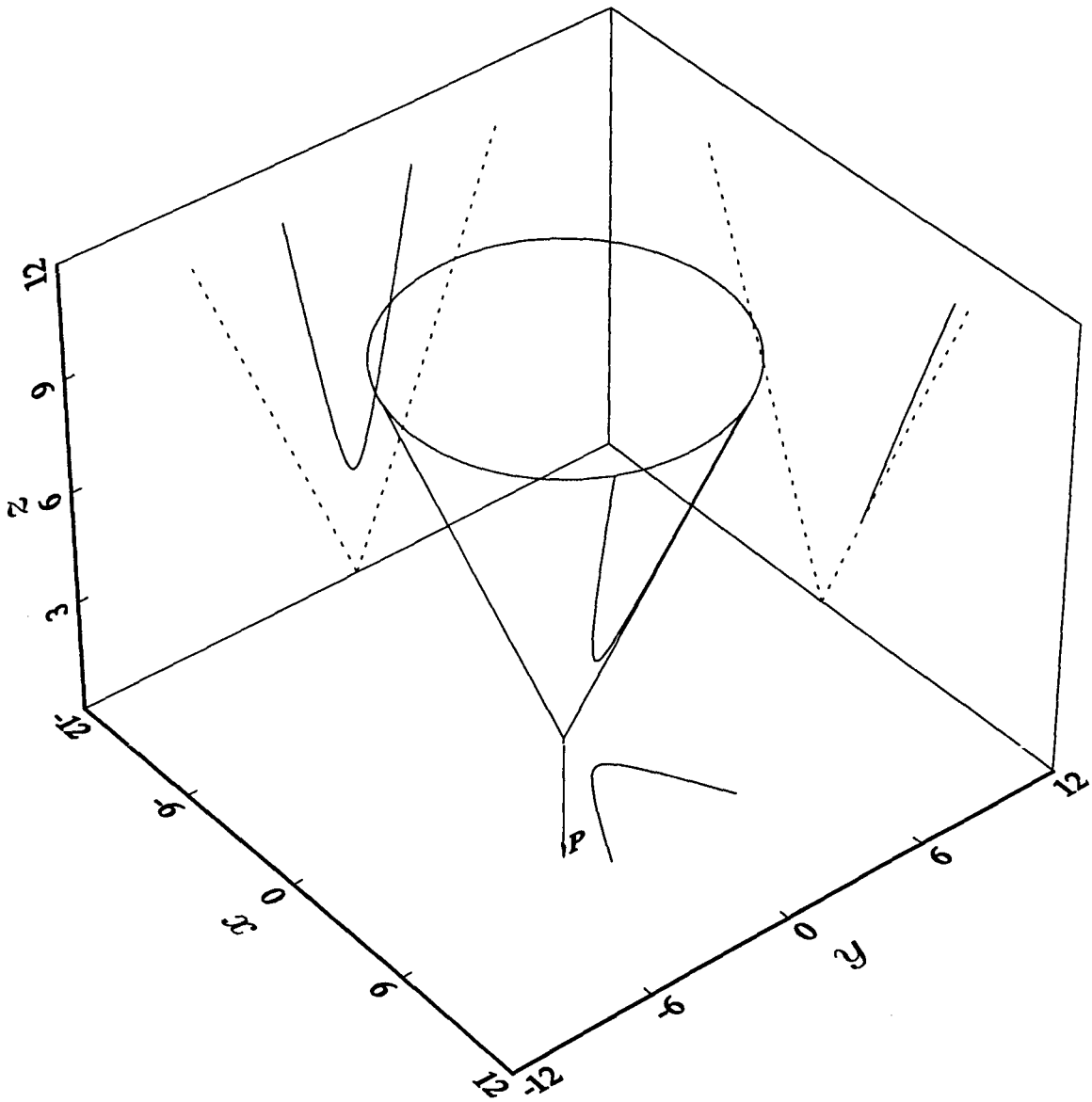

Figure 3.16.6. The monopole–repulsor orbit for $\mu = -3L^2 - 4\lambda^2$. The radial vectors move on the surface of a right circular cone extending along the line of $\boldsymbol{P}$ with origin at the apex of the cone. The orbit on the cone is not hyperbolic and nor are the projections of the orbit into the respective planes. The projections of the orbit onto planes parallel to the xy, xz and yz planes are also shown. The constants have the values $\omega = 0.4289$, $P = 3.4225$, $\lambda = 2.8794$, $\alpha = 0.5711$, $L = 1.85$ and $K_1 = 0.7789$. The origin is not enclosed by the orbit.

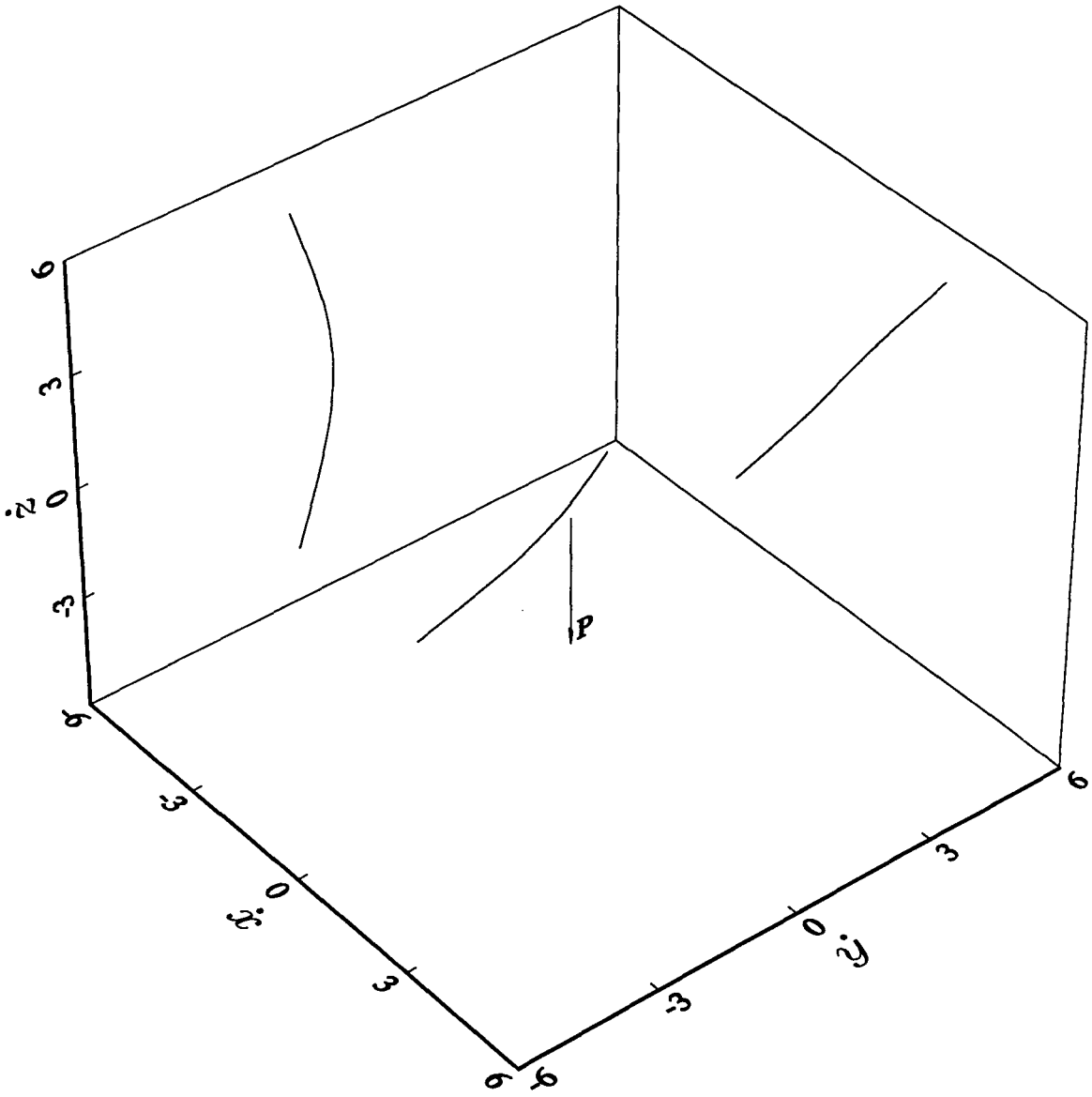

Figure 3.16.7. The monopole–repulsor velocity hodograph for $\mu = -3L^2 - 4\lambda^2$. The projections of the velocity hodograph onto planes parallel to the $\dot{x}\dot{z}$ and $\dot{y}\dot{z}$ planes are also shown. The constants are chosen as for Figure 3.16.6.

of the orbit onto planes parallel to the xy, xz and yz planes are shown, together with the projected images of the cones onto the respective planes. The magnitude of the angular momentum is constant throughout the motion.

Figure 3.16.7 shows the velocity hodograph for the monopole–repulsor where $\mu = -3L^2 - 4\lambda^2$. In order to illustrate the $\dot{\boldsymbol{r}}$ behaviour more clearly, projections of the velocity hodograph onto planes parallel to the $\dot{x}\dot{z}$ and $\dot{y}\dot{z}$ planes are also shown. The velocity hodograph is bounded at both ends by the tangents to the asymptotes of the orbit on the cone.

3.17 The Stationary Solutions

In the preceding discussion we have studied dynamical solutions to equations (3.13.1)–(3.13.3). There has been some interest in the existence of static solutions of the Bogomolny–Prasad–Sommerfield equations (*cf.* Manton [88]). For completeness we consider the existence of static solutions to the equations of motion mentioned above. The requirement for a static solution is that $\boldsymbol{r}$ remain constant, in which case both $\dot{r}$ and L are zero.

3.17.1 The Monopole–Oscillator

From the equation of motion (3.13.1), a static solution is obtained when

$$r^4 = -\frac{\mu}{\omega^2}, \tag{3.17.1}$$

i.e. μ must be negative. The first integrals (3.13.8)–(3.13.10) take the values

$$I_1 = \omega(-\mu)^{\frac{1}{2}} \qquad I_2 = 0 \qquad I_3 = 0. \tag{3.17.2}$$

3.17.2 The Monopole–Free Particle

From the equation of motion (3.13.2) a static solution is only possible if $\mu = 0$. The values of the first integrals (3.13.14)–(3.13.16) are then

$$J_1 = 0 \qquad J_2 = 0 \qquad J_3 = \frac{1}{2}r^2 \tag{3.17.3}$$

where the value of r is arbitrary.

3.17.3 The Monopole–Repulsor

From the equation of motion (3.13.3) a static solution is possible when

$$r^4 = \frac{\mu}{\omega^2}, \tag{3.17.4}$$

i.e. μ must be positive. The values of the integrals (3.13.19)–(3.13.21) are then

$$K_1 = -\omega\mu^{\frac{1}{2}} \qquad K_2 = 0 \qquad K_3 = 0. \tag{3.17.5}$$

In each case a stationary solution is possible. In the case of the monopole–oscillator and the monopole–repulsor the radial distance is determined by the relative strengths of the centrifugal potential and the oscillator or repulsor respectively. For the free particle no forces are acting and so there is no restriction on the value which $\boldsymbol{r}$ can take.

3.18 Discussion

The equations of motion (3.13.1)–(3.13.3) for the monopole–oscillator, monopole–free particle and monopole–repulsor admit a rich structure. For general λ and μ they are unusual in that the Lie algebra of the commutators of the point symmetries of the equations of motion is the same as that of the Poisson Brackets of the six first integrals namely $sl(2,R) \oplus so(3)$. The orbit equations are very characteristic of the two–dimensional analogues except that now the two–dimensional curves are lifted onto the surface of a cone which is a characteristic of the monopole. The possibility of a 'hyperbolic' orbit wrapping itself round on an invisible cone a number of times is in itself interesting.

It is interesting to note that the orbits on the cone are in general not conic sections. However, the projections when $\mu = -\lambda^2$ are either conic sections or lie along conic sections except in the case of the monopole–free particle where the orbit, an hyperbola, is a conic section. This may indeed be related to the existence of a conserved Laplace–Runge–Lenz vector for the latter problem, which is perpendicular to $\boldsymbol{P}$. In the case $\mu = -\lambda^2$, the orbit of the monopole–oscillator is described by the intersection of an elliptical cylinder and a right circular cone and the projection of the orbit into the ϕ–plane is a geometric–centred ellipse which corresponds naturally with the orbit of the three–dimensional isotropic harmonic oscillator. Analogues of Kepler's three laws of motion have been obtained and shown to be natural extensions of the results for the three–dimensional isotropic harmonic oscillator in the plane.

The vector $\boldsymbol{P}$ determines the orientation of the orbit in space. Similarly, in the case $\mu = -\lambda^2$, the orbit of the monopole–repulsor is described by the intersection of a hyperbolic sheet and a right circular cone and the projection of the orbit into the ϕ–plane is a geomteric–centred hyperbola which corresponds naturally with the orbit of the three–dimensional isotropic repulsor.

3.19 The First Integrals Associated with the Lie Symmetries of the Monopole–Oscillator

The monopole–oscillator, with equation of motion

$$\ddot{\boldsymbol{r}} + \frac{\lambda}{r^3}\boldsymbol{L} + \left(\frac{\mu}{r^4} + \omega^2\right)\boldsymbol{r} = 0 \tag{3.19.1}$$

has the following Lie symmetry generators

$$\begin{aligned}
G_1 &= \frac{\partial}{\partial t} \\
G_2 &= \sin 2\omega t \, \frac{\partial}{\partial t} + \omega \cos 2\omega t \left(x \, \frac{\partial}{\partial x} + y \, \frac{\partial}{\partial y} + z \, \frac{\partial}{\partial z} \right) \\
&= \sin 2\omega t \, \frac{\partial}{\partial t} + \omega r \cos 2\omega t \, \frac{\partial}{\partial r} \\
G_3 &= \cos 2\omega t \, \frac{\partial}{\partial t} - \omega \sin 2\omega t \left(x \, \frac{\partial}{\partial x} + y \, \frac{\partial}{\partial y} + z \, \frac{\partial}{\partial z} \right) \\
&= \cos 2\omega t \, \frac{\partial}{\partial t} - \omega r \sin 2\omega t \, \frac{\partial}{\partial r} \\
G_4 &= z\frac{\partial}{\partial y} - y\frac{\partial}{\partial z} \\
G_5 &= x\frac{\partial}{\partial z} - z\frac{\partial}{\partial x} \\
G_6 &= y\frac{\partial}{\partial x} - x\frac{\partial}{\partial y}.
\end{aligned} \tag{3.19.2}$$

For complete details of the derivation of the generators see Chapter 4.

In §P3.2 we noted that for a three–dimensional problem we would find five independent first integrals per generator provided the equations for the characteristics can be solved. An example of this has been given by Leach in his treatment of the Kepler problem [72] in which all of the autonomous first integrals, energy, angular momentum and Laplace–Runge–Lenz vector were found from the generator of time translations $\partial/\partial t$. Certain first integrals are naturally associated with certain generators: $\partial/\partial t$ is associated with energy, and the generators $z\partial/\partial y - y\partial/\partial z$, $x\partial/\partial z - z\partial/\partial x$ and $y\partial/\partial x - x\partial/\partial y$ with rotational invariance (in this problem not angular momentum which is not conserved). The integrals which naturally relate to G_2 and G_3 are not *a priori* obvious and will be investigated below. It must, however, be stressed that each generator is capable of providing the full set of integrals, although the manipulations involved may be rather contrived.

According to the Lie method as described in §P3.2, a function $I(t, q_i, \ldots, \dot{q}_i)$ which is associated with a symmetry G is a first integral if

$$G^{[1]}I = 0 \tag{3.19.3}$$

and

$$\left.\frac{\mathrm{d}I}{\mathrm{d}t}\right|_{\boldsymbol{E}=\boldsymbol{0}} = 0, \tag{3.19.4}$$

where $\boldsymbol{E}\ (t, q_i, \ldots, \dot{q}_i) = \boldsymbol{0}$ is the equation of motion (3.19.1). Substituting the first extension of the time invariance symmetry G_1 in (3.19.3) gives the characteristics as solutions to the associated Lagrange's system

$$\frac{\mathrm{d}t}{1} = \frac{\mathrm{d}x}{0} = \frac{\mathrm{d}y}{0} = \frac{\mathrm{d}z}{0} = \frac{\mathrm{d}\dot{x}}{0} = \frac{\mathrm{d}\dot{y}}{0} = \frac{\mathrm{d}\dot{z}}{0}. \tag{3.19.5}$$

They are

$$\begin{aligned} u_1 &= x & v_1 &= \dot{x} \\ u_2 &= y & v_2 &= \dot{y} \\ u_3 &= z & v_3 &= \dot{z}, \end{aligned} \tag{3.19.6}$$

which are individually invariant under the infinitesimal transformation generated by $G_1^{[1]}$. Substituting for the equation of motion reveals

$$\begin{aligned} \dot{u}_1 &= v_1 & \dot{v}_1 &= -\lambda r^{-3}(u_2v_3 - u_3v_2) - (\mu r^{-4} + \omega^2)u_1 \\ \dot{u}_2 &= v_2 & \dot{v}_2 &= -\lambda r^{-3}(u_3v_1 - u_1v_3) - (\mu r^{-4} + \omega^2)u_2 \\ \dot{u}_3 &= v_3 & \dot{v}_3 &= -\lambda r^{-3}(u_1v_2 - u_2v_1) - (\mu r^{-4} + \omega^2)u_3, \end{aligned} \tag{3.19.7}$$

and the corresponding Lagrange's system for (3.19.4) is

$$\begin{aligned}\frac{\mathrm{d}u_1}{v_1} &= \frac{\mathrm{d}u_2}{v_2} = \frac{\mathrm{d}u_3}{v_3} = \frac{\mathrm{d}v_1}{-\lambda r^{-3}(u_2v_3 - u_3v_2) - (\mu r^{-4} + \omega^2)u_1} \\ &= \frac{\mathrm{d}v_2}{-\lambda r^{-3}(u_3v_1 - u_1v_3) - (\mu r^{-4} + \omega^2)u_2} \\ &= \frac{\mathrm{d}v_3}{-\lambda r^{-3}(u_1v_2 - u_2v_1) - (\mu r^{-4} + \omega^2)u_3}. \end{aligned} \tag{3.19.8}$$

Our interest is in finding a first integral which is invariant under time translation and thus we do not need to introduce an auxiliary time variable [55]. For convenience we shall denote the ith member of (3.19.8) as (3.19.8.i, $i = 1, 6$) and then form the combination

$$\begin{aligned}(\mu r^{-4} + \omega^2)\Big[u_1(3.19.8.1) + u_2(3.19.8.2) + u_3(3.19.8.3)\Big] + \\ v_1(3.19.8.4) + v_2(3.19.8.5) + v_3(3.19.8.6)\end{aligned} \tag{3.19.9}$$

which gives

$$\frac{\mathrm{d}\left[\frac{1}{2}\,v_1^2 + \frac{1}{2}\,v_2^2 + \frac{1}{2}\,v_3^2 - \frac{1}{2}\,\mu r^{-2} + \frac{1}{2}\,\omega^2(u_1^2 + u_2^2 + u_3^2)\right]}{0} \tag{3.19.10}$$

which is just the differential of the required characteristic and, reverting to the original coordinates, becomes

$$I_1 = \frac{1}{2}\left(\dot{\boldsymbol{r}} \cdot \dot{\boldsymbol{r}} - \frac{\mu}{r^2} + \omega^2 r^2\right). \tag{3.19.11}$$

The result for $\omega = 0$ is obvious.

If I_6 is a first integral associated with G_6, then the characteristics of (3.19.3) are found from

$$\frac{\mathrm{d}t}{0} = \frac{\mathrm{d}x}{y} = \frac{\mathrm{d}y}{-x} = \frac{\mathrm{d}z}{0} = \frac{\mathrm{d}\dot{x}}{\dot{y}} = \frac{\mathrm{d}\dot{y}}{-\dot{x}} = \frac{\mathrm{d}\dot{z}}{0} \tag{3.19.12}$$

and are

$$\begin{aligned} u_1 &= t & v_1 &= \dot{x}^2 + \dot{y}^2 \\ u_2 &= x^2 + y^2 & v_2 &= (x\dot{y} - y\dot{x})(u_2v_1)^{-\frac{1}{2}} \\ u_3 &= z & v_3 &= \dot{z}. \end{aligned} \tag{3.19.13}$$

Since

$$\begin{aligned}
\dot{u}_1 &= 1 & v_1 &= 2(u_2v_1)^{\frac{1}{2}}\left[\lambda r^{-3}v_2v_3 - (\mu r^{-4}+\omega^2)(1-v_2^2)^{\frac{1}{2}}\right] \\
\dot{u}_2 &= 2(u_2v_1)^{\frac{1}{2}}(1-v_2^2)^{\frac{1}{2}} & \dot{v}_2 &= (1-v_2^2)^{\frac{1}{2}}(u_2v_1)^{-\frac{1}{2}}\left\{\lambda r^{-3}\left[(1-v_2^2)^{\frac{1}{2}}u_2v_3 - u_3(u_2v_1)^{\frac{1}{2}}\right]\right. \\
& & & \left. - v_1v_2 + u_2v_2(\mu r^{-4}+\omega^2)\right\} \\
\dot{u}_3 &= v_3 & \dot{v}_3 &= -\lambda r^{-3}(u_2v_1)^{\frac{1}{2}}v_2 - (\mu r^{-4}+\omega^2)u_3, \qquad (3.19.14)
\end{aligned}$$

where $r^2 = u_2 + {u_3}^2$, the characteristics of (3.19.4) are found from

$$\begin{aligned}
\frac{\mathrm{d}u_1}{1} &= \frac{\mathrm{d}u_2}{2(u_2v_1)^{\frac{1}{2}}(1-v_2^2)^{\frac{1}{2}}} = \frac{\mathrm{d}u_3}{v_3} \\
&= \frac{\mathrm{d}v_1}{2(u_2v_1)^{\frac{1}{2}}\left[\lambda r^{-3}v_2v_3 - (\mu r^{-4}+\omega^2)(1-v_2^2)^{\frac{1}{2}}\right]} \\
&= \frac{\mathrm{d}v_2}{(1-v_2^2)^{\frac{1}{2}}(u_2v_1)^{-\frac{1}{2}}\left\{\lambda r^{-3}\left[(1-v_2^2)^{\frac{1}{2}}u_2v_3 - u_3(u_2v_1)^{\frac{1}{2}}\right] - v_1v_2 + u_2v_2(\mu r^{-4}+\omega^2)\right\}} \\
&= \frac{\mathrm{d}v_3}{-\lambda r^{-3}(u_2v_1)^{\frac{1}{2}}v_2 - (\mu r^{-4}+\omega^2)u_3}. \qquad (3.19.15)
\end{aligned}$$

Making the combination

$$\begin{aligned}
& \frac{1}{2}\left[v_1v_2(u_2v_1)^{-\frac{1}{2}} + \lambda u_3 r^{-3}\right](3.19.15.2) - \lambda u_2 r^{-3}(3.19.15.3) \\
+\ & \frac{1}{2}u_2v_2(u_2v_1)^{-\frac{1}{2}}(3.19.15.4) + (u_2v_1)^{\frac{1}{2}}(3.19.15.5) \qquad (3.19.16)
\end{aligned}$$

gives

$$\frac{\mathrm{d}\left[v_2(u_2v_1)^{\frac{1}{2}} - \lambda u_3 r^{-1}\right]}{0} \qquad (3.19.17)$$

which gives the first integral

$$I_6 = x\dot{y} - y\dot{x} - \frac{\lambda z}{r}. \qquad (3.19.18)$$

Similarly I_4 and I_5 corresponding to G_4 and G_5 can be determined by cyclic permutations

$$\begin{aligned}
I_4 &= y\dot{z} - z\dot{y} - \frac{\lambda x}{r} \\
I_5 &= z\dot{x} - x\dot{z} - \frac{\lambda y}{r}. \qquad (3.19.19)
\end{aligned}$$

We immediately recognize that I_4, I_5 and I_6 are the components of the conserved vector

$$\boldsymbol{P} = \boldsymbol{L} - \lambda \hat{\boldsymbol{r}} \tag{3.19.20}$$

which is just the Poincaré's vector for the simple charge monopole problem [107, 101]. It is interesting to note that the additional term $(\mu r^{-4} + \omega^2)\boldsymbol{r}$ does not destroy the structure of this vector. In light of the algebra of the two problems being identical this should not really be surprising. The result is unchanged for $\omega^2 = 0$.

If I_2 is the first integral associated with G_2, the characteristics of (3.19.3) are

$$\begin{aligned}
u_1 &= \frac{x^2}{\sin 2\omega t} & v_1 &= \sin 2\omega t(\dot{x} - \omega x \cot 2\omega t)^2 \\
u_2 &= \frac{y^2}{\sin 2\omega t} & v_2 &= \sin 2\omega t(\dot{y} - \omega y \cot 2\omega t)^2 \\
u_3 &= \frac{z^2}{\sin 2\omega t} & v_3 &= \sin 2\omega t(\dot{z} - \omega z \cot 2\omega t)^2.
\end{aligned} \tag{3.19.21}$$

Since

$$\begin{aligned}
\dot{u}_1 &= \frac{2}{\sin 2\omega t}(u_1 v_1)^{\frac{1}{2}} \\
\dot{u}_2 &= \frac{2}{\sin 2\omega t}(u_2 v_2)^{\frac{1}{2}} \\
\dot{u}_3 &= \frac{2}{\sin 2\omega t}(u_3 v_3)^{\frac{1}{2}} \\
\dot{v}_1 &= \frac{2v_1^{\frac{1}{2}}}{\sin 2\omega t}\left\{-\frac{\lambda}{\rho^{\frac{3}{2}}}\left[(u_2 v_3)^{\frac{1}{2}} - (u_3 v_2)^{\frac{1}{2}}\right] + \left(\omega^2 - \frac{\mu}{\rho^2}\right) u_1^{\frac{1}{2}}\right\} \\
\dot{v}_2 &= \frac{2v_2^{\frac{1}{2}}}{\sin 2\omega t}\left\{-\frac{\lambda}{\rho^{\frac{3}{2}}}\left[(u_3 v_1)^{\frac{1}{2}} - (u_1 v_3)^{\frac{1}{2}}\right] + \left(\omega^2 - \frac{\mu}{\rho^2}\right) u_2^{\frac{1}{2}}\right\} \\
\dot{v}_3 &= \frac{2v_3^{\frac{1}{2}}}{\sin 2\omega t}\left\{-\frac{\lambda}{\rho^{\frac{3}{2}}}\left[(u_1 v_2)^{\frac{1}{2}} - (u_2 v_1)^{\frac{1}{2}}\right] + \left(\omega^2 - \frac{\mu}{\rho^2}\right) u_3^{\frac{1}{2}}\right\},
\end{aligned} \tag{3.19.22}$$

where $\rho = u_1 + u_2 + u_3$, the characteristics of (3.19.4) are found from the associated Lagrange's system

$$\begin{aligned}
\frac{\mathrm{d}u_1}{(u_1v_1)^{\frac{1}{2}}} &= \frac{\mathrm{d}u_2}{(u_2v_2)^{\frac{1}{2}}} = \frac{\mathrm{d}u_3}{(u_3v_3)^{\frac{1}{2}}} \\
&= \frac{\mathrm{d}v_1}{v_1^{\frac{1}{2}}\left\{\left(\omega^2 - \frac{\mu}{\rho^2}\right)u_1^{\frac{1}{2}} - \frac{\lambda}{\rho^{\frac{3}{2}}}\left[(u_2v_3)^{\frac{1}{2}} - (u_3v_2)^{\frac{1}{2}}\right]\right\}} \\
&= \frac{\mathrm{d}v_2}{v_2^{\frac{1}{2}}\left\{\left(\omega^2 - \frac{\mu}{\rho^2}\right)u_2^{\frac{1}{2}} - \frac{\lambda}{\rho^{\frac{3}{2}}}\left[(u_3v_1)^{\frac{1}{2}} - (u_1v_3)^{\frac{1}{2}}\right]\right\}} \\
&= \frac{\mathrm{d}v_3}{v_3^{\frac{1}{2}}\left\{\left(\omega^2 - \frac{\mu}{\rho^2}\right)u_3^{\frac{1}{2}} - \frac{\lambda}{\rho^{\frac{3}{2}}}\left[(u_1v_2)^{\frac{1}{2}} - (u_2v_1)^{\frac{1}{2}}\right]\right\}}. \qquad (3.19.23)
\end{aligned}$$

(If it were necessary to introduce time as an auxiliary variable in (3.19.23), it would be in the form $2\mathrm{d}t/\sin 2\omega t$ as can be seen from (3.19.22)). Making the combination

$$\left(\frac{\mu}{\rho^2} - \omega^2\right)\Big[(3.19.23.1) + (3.19.23.2) + (3.19.23.3)\Big] + \mathrm{d}v_1 + \mathrm{d}v_2 + \mathrm{d}v_3 \qquad (3.19.24)$$

gives

$$\frac{\mathrm{d}\left[v_1 + v_2 + v_3 - \frac{\mu}{\rho} - \omega^2\rho\right]}{0} \qquad (3.19.25)$$

and again the term in parentheses is the characteristic. Rewriting in terms of physical coordinates and scaling by a factor of $\frac{1}{2}$ we obtain

$$I_2 = \frac{1}{2}\sin 2\omega t\left(\dot{\boldsymbol{r}}\cdot\dot{\boldsymbol{r}} - \frac{\mu}{r^2} - \omega^2 r^2\right) - \omega\boldsymbol{r}\cdot\dot{\boldsymbol{r}}\cos 2\omega t. \qquad (3.19.26)$$

Adopting a similar technique for G_3 yields

$$I_3 = \frac{1}{2}\cos 2\omega t\left(\dot{\boldsymbol{r}}\cdot\dot{\boldsymbol{r}} - \frac{\mu}{r^2} - \omega^2 r^2\right) + \omega\boldsymbol{r}\cdot\dot{\boldsymbol{r}}\sin 2\omega t. \qquad (3.19.27)$$

As can be expected, I_1, I_2 and I_3 are not independent. Taking the product $\boldsymbol{P}\cdot\boldsymbol{P}$ where $\boldsymbol{P}$ is given in (3.19.20), gives

$$P^2 = L^2 + \lambda^2 \qquad (3.19.28)$$

and so L^2 is a constant. It can then be shown that

$$I_2^2 + I_3^2 = I_1^2 - \omega^2\,(L^2 - \mu). \qquad (3.19.29)$$

For $\omega = 0$ the integrals reduce to

$$I_2 = \frac{1}{2}\, t \left(\dot{\boldsymbol{r}} \cdot \dot{\boldsymbol{r}} - \frac{\mu}{r^2} \right) - \frac{1}{2}\, \boldsymbol{r} \cdot \dot{\boldsymbol{r}} \tag{3.19.30}$$

which is just $\lim_{\omega \to 0}(I_2/2\omega)$, and

$$I_3 = \frac{1}{2}\, t^2 \left(\dot{\boldsymbol{r}} \cdot \dot{\boldsymbol{r}} - \frac{\mu}{r^2} \right) - t\boldsymbol{r} \cdot \dot{\boldsymbol{r}} + \frac{1}{2}\, \boldsymbol{r} \cdot \boldsymbol{r} \tag{3.19.31}$$

which is is $\lim_{\omega \to 0}(I_1 - I_3)/2\omega^2$.

3.20 Discussion

The monopole–oscillator with or without the extra force described by the equation of motion

$$\dot{\boldsymbol{r}} + \frac{\lambda}{r^3}\boldsymbol{L} + \left(\frac{\mu}{r^4} + \omega^2 \right) \boldsymbol{r} = \boldsymbol{0} \tag{3.20.1}$$

is rather interesting in terms of its algebra. From a geometric point of view its possession of the six–dimensional symmetry algebra $sl(2, R) \oplus so(3)$ is unusual. It should be remembered that the Kepler problem has only a five–dimensional algebra. For the monopole–oscillator, the algebra is insensitive to the values of the parameters λ, μ, and ω^2. The algebra only degenerates to the twenty–four element $sl(5, R)$ when both λ and μ are zero. The parameters λ and μ can be separately zero without affecting the algebra which implies that the two terms are equivalent in their symmetry breaking effect.

The structure of the integrals I_1, I_2 and I_3 illustrates a feature previously observed with the first integrals of quadratic Hamiltonians [56]. The three–dimensional isotropic harmonic oscillator with equation of motion

$$\ddot{\boldsymbol{r}} + \omega^2 \boldsymbol{r} = \boldsymbol{0} \tag{3.20.2}$$

has the following first integrals which are quadratic in the velocities:

$$\begin{aligned} A_{ij} &= \dot{x}_i \dot{x}_j + x_i x_j \\ B_{ij} &= (\dot{x}_i \dot{x}_j - x_i x_j) \sin 2\omega t - \omega (x_i \dot{x}_j + \dot{x}_i x_j) \cos 2\omega t \\ C_{ij} &= (\dot{x}_i \dot{x}_j - x_i x_j) \cos 2\omega t + \omega (x_i \dot{x}_j + \dot{x}_i x_j) \sin 2\omega t, \end{aligned} \tag{3.20.3}$$

where the indices range over the values 1, 2, 3. These integrals correspond to our G_1, G_2 and G_3 of the monopole–oscillator problem which are in fact symmetries of (3.20.2) as well. The μ and λ terms of (3.20.1) seem to dispose of the non–diagonal terms ($i \neq j$ terms). Something else worth noting is that the $x_i x_j$ term in the A_{ij} tensor changes sign in both the B_{ij} and C_{ij} terms. For (3.20.1), however, it is only the sign of the harmonic component and not the inverse square part of the potential which changes sign in both I_2 and I_3, which would imply that the inverse square potential adds to the angular momentum contribution to the kinetic energy of the motion.

It can be seen that the generators obtained via Lie's method do give rise to the first integrals, although a certain amount of mental dexterity may in fact be required. Our emphasis has so far been on the natural first integral associated with a particular generator. It turns out that a more transparent derivation of I_6 (3.19.18) would be through (3.19.23) which has a simpler and more symmetric structure. The combination is

$$\left[(v_2/u_1)^{\frac{1}{2}} + \lambda(u_3/\rho^3)^{\frac{1}{2}}\right](3.19.23.1) - \left[(v_1/u_2)^{\frac{1}{2}} - \lambda(u_3/\rho^3)^{\frac{1}{2}}\right](3.19.23.2) -$$

$$\lambda(u_3/\rho^3)^{-\frac{1}{2}}(u_1+u_2)(3.19.23.3) - (u_2/v_1)^{\frac{1}{2}}(3.19.23.4) +$$

$$(u_1/v_2)^{\frac{1}{2}}(3.19.23.5). \qquad (3.20.4)$$

Although it can be argued that either the direct method or Noether's theorem are far more mechanical to apply, one must remember that the latter requires the existence of a Lagrangian as well as a guess at the velocity dependence of the integral and, in the former, the velocity dependence condition. If, however, there exist integrals which are not linear or quadratic in the velocities, the correct choice of velocity dependence can be very difficult, if not impossible.

CHAPTER 4

SYMMETRIES AND THE EXISTENCE OF CONSERVED VECTORS

4.1 Preliminaries

A second order differential equation is invariant under a Lie point transformation generated by a symmetry generator, G, if the twice extended symmetry generator, $G^{[2]}$, acting on the differential equation is zero whenever the differential equation holds, *i.e.*,

$$G^{[2]}\boldsymbol{E}\ (q_i, \dot{q}_i, \ddot{q}_i)\Big|_{E=\mathbf{0}} = \mathbf{0}. \tag{4.1.1}$$

In a three–dimensional cartesian basis G is given by (see (P3.17))

$$G = \tau\,\frac{\partial}{\partial t} + \xi\,\frac{\partial}{\partial x} + \eta\,\frac{\partial}{\partial y} + \zeta\,\frac{\partial}{\partial z}, \tag{4.1.2}$$

where τ, ξ, η and ζ are functions of t, x, y and z. The twice extended generator in this basis is then

$$\begin{aligned} G^{[2]} &= G + (\dot{\xi} - \dot{x}\dot{\tau})\,\frac{\partial}{\partial \dot{x}} + (\dot{\eta} - \dot{y}\dot{\tau})\,\frac{\partial}{\partial \dot{y}} + (\dot{\zeta} - \dot{z}\dot{\tau})\,\frac{\partial}{\partial \dot{z}} \\ &+ (\ddot{\xi} - 2\ddot{x}\dot{\tau} - \dot{x}\ddot{\tau})\,\frac{\partial}{\partial \ddot{x}} + (\ddot{\eta} - 2\ddot{y}\dot{\tau} - \dot{y}\ddot{\tau})\,\frac{\partial}{\partial \ddot{y}} + (\ddot{\zeta} - 2\ddot{z}\dot{\tau} - \dot{z}\ddot{\tau})\,\frac{\partial}{\partial \ddot{z}}. \end{aligned} \tag{4.1.3}$$

The total derivatives of τ can be expressed in terms of partial derivatives as

$$\dot{\tau} = \frac{\partial \tau}{\partial t} + \dot{x}\,\frac{\partial \tau}{\partial x} + \dot{y}\,\frac{\partial \tau}{\partial y} + \dot{z}\,\frac{\partial \tau}{\partial z}, \tag{4.1.4}$$

$$\begin{aligned} \ddot{\tau} &= \frac{\partial^2 \tau}{\partial t^2} + 2\dot{x}\,\frac{\partial^2 \tau}{\partial x \partial t} + 2\dot{y}\,\frac{\partial^2 \tau}{\partial y \partial t} + 2\dot{z}\,\frac{\partial^2 \tau}{\partial z \partial t} \\ &+ \dot{x}^2\,\frac{\partial^2 \tau}{\partial x^2} + \dot{y}^2\,\frac{\partial^2 \tau}{\partial y^2} + \dot{z}^2\,\frac{\partial^2 \tau}{\partial z^2} + 2\dot{x}\dot{y}\,\frac{\partial^2 \tau}{\partial x \partial y} \\ &+ 2\dot{y}\dot{z}\,\frac{\partial^2 \tau}{\partial y \partial z} + 2\dot{z}\dot{x}\,\frac{\partial^2 \tau}{\partial z \partial x} + \ddot{x}\,\frac{\partial \tau}{\partial x} + \ddot{y}\,\frac{\partial \tau}{\partial y} + \ddot{z}\,\frac{\partial \tau}{\partial z} \end{aligned} \tag{4.1.5}$$

and similarly for the total derivatives of ξ, η and ζ.

Application of (4.1.3) to the standard Kepler problem gives rise to the following symmetry generators [110]

$$\begin{aligned} G_1 &= \frac{\partial}{\partial t} \\ G_2 &= t\frac{\partial}{\partial t} + \frac{2}{3}\left(x\frac{\partial}{\partial x} + y\frac{\partial}{\partial y} + z\frac{\partial}{\partial z}\right) \\ G_3 &= z\frac{\partial}{\partial y} - y\frac{\partial}{\partial z} \\ G_4 &= x\frac{\partial}{\partial z} - z\frac{\partial}{\partial x} \\ G_5 &= y\frac{\partial}{\partial x} - x\frac{\partial}{\partial y} \end{aligned} \tag{4.1.6}$$

which have the following non–zero commutation relations

$$\begin{aligned} [G_1, G_2] &= G_1 \\ [G_3, G_4] &= G_5, \quad [G_4, G_5] = G_3, \quad [G_5, G_3] = G_4 \end{aligned} \tag{4.1.7}$$

from which it is evident that the Lie algebra is the direct sum $A_2 \oplus so(3)$. G_3, G_4 and G_5 are a result of the invariance of (1.5.1) under rotation, G_1 represents invariance under time translation and G_2, the generator often associated with the Laplace–Runge–Lenz vector, indicates invariance under the similarity transformation $(t, \boldsymbol{r}) \rightarrow (\bar{t}, \bar{\boldsymbol{r}} : t = \gamma\bar{t},\ \boldsymbol{r} = \gamma^{\frac{2}{3}}\bar{\boldsymbol{r}})$. It should of course be realised that any of the first integrals can in fact be constructed from any of the generators (4.1.6) and so the association is not strictly accurate in a mathematical sense although it is in a geometric sense. The two–dimensional algebra A_2 connected with G_1 and G_2 has recently found application in the analysis of one–dimensional nonlinear second order differential equations [76, 11].

Since the Kepler problem and the time–dependent Kepler problem are related by a point transformation, they both possess the same algebraic structure [73].

The symmetries of the charge–monopole described by the equation

$$\ddot{\boldsymbol{r}} = -\frac{\mu}{r^3}\boldsymbol{L} \tag{4.1.8}$$

have been studied in some detail by Moreira *et al.* [101]. They found the following set of generators

$$\begin{aligned}
G_1 &= \frac{\partial}{\partial t} \\
G_2 &= t\,\frac{\partial}{\partial t} + \frac{1}{2}\left(x\,\frac{\partial}{\partial x} + y\,\frac{\partial}{\partial y} + z\,\frac{\partial}{\partial z}\right) \\
G_3 &= t\left(t\,\frac{\partial}{\partial t} + x\,\frac{\partial}{\partial x} + y\,\frac{\partial}{\partial y} + z\,\frac{\partial}{\partial z}\right) \\
G_4 &= z\,\frac{\partial}{\partial y} - y\,\frac{\partial}{\partial z} \\
G_5 &= x\,\frac{\partial}{\partial z} - z\,\frac{\partial}{\partial x} \\
G_6 &= y\,\frac{\partial}{\partial x} - x\,\frac{\partial}{\partial y}
\end{aligned} \tag{4.1.9}$$

which possess the non–zero commutation relations

$$\begin{aligned}
[G_1, G_2] &= G_1, \quad [G_2, G_3] = G_3, \quad [G_3, G_1] = -2G_2 \\
[G_4, G_5] &= G_6, \quad [G_5, G_6] = G_4, \quad [G_6, G_4] = G_5.
\end{aligned} \tag{4.1.10}$$

In this case the algebra is the direct sum of the subalgebras $\{G_1, G_2, G_3\}$ and $\{G_4, G_5, G_6\}$ and is $sl(2, R) \oplus so(3)$. (Moreira *et al.* [101] use $so(2,1)$ rather than $sl(2, R)$). Since the algebraic structure of (4.1.8) is more complex than that of the Kepler problem (1.5.1), as Thompson [126] has already noted, the charge monopole problem cannot be related to the Kepler problem by a point transformation.

4.2 The Lie Symmetries of the Equation of Motion $\ddot{\boldsymbol{r}} + f(r)\boldsymbol{L} + g(r)\boldsymbol{r} = \boldsymbol{0}$

It would seem sensible to consider the symmetries of the more general equation

$$\ddot{\boldsymbol{r}} + f(r)\boldsymbol{L} + g(r)\boldsymbol{r} = \boldsymbol{0} \tag{4.2.1}$$

since for $f = 0$ and $g(r) = \mu/r^3$ we regain the Kepler problem, and for $f(r) = \mu/r^3$ and $g(r) = 0$ we obtain the charge monopole problem. One further class of problems which are also described by (4.2.1) has the equation of motion

$$\ddot{\boldsymbol{r}} + \frac{h'(r)}{r}\boldsymbol{L} + \left(h(r)h'(r) + \frac{k}{r^2}\right)\hat{\boldsymbol{r}} = \boldsymbol{0} \tag{4.2.2}$$

which has already been shown in §3.1 to possess Laplace–Runge–Lenz–like vectors.

Since the angular momentum has a regular structure in a cartesian basis, it makes sense to do the calculation in this basis to provide a further computational check through certain regularities in the determining equations. Thus we may write (4.2.1) as

$$\begin{aligned} \ddot{x} &+ f(y\dot{z} - z\dot{y}) + gx = 0 \\ \ddot{y} &+ f(z\dot{x} - x\dot{z}) + gy = 0 \\ \ddot{z} &+ f(x\dot{y} - y\dot{x}) + gz = 0. \end{aligned} \tag{4.2.3}$$

The second extension (4.1.3) is now applied to (4.2.3) individually with all the derivatives expanded using (4.1.4) and (4.1.5). Upon each subsequent application of (4.1.3) $\ddot{x}$, $\ddot{y}$, $\ddot{z}$ are replaced in (4.1.3) using (4.2.3). Since we have assumed a point transformation, the terms can be collected as coefficients of various combinations of powers of the total time derivatives $\dot{x}$, $\dot{y}$ and $\dot{z}$ and coefficients of linearly independent combinations then set to zero. This operation is extremely tedious to do by hand and the symbolic manipulation code REDUCE [112] was used to obtain the determining equations which were subsequently solved by hand. Forty eight partial differential equations were obtained, twelve of which were repeats of the six second–order equations for τ (4.2.4) below. The equations are listed in groups according to the order in which they were analysed.

$$\frac{\partial^2\tau}{\partial x^2} = 0 \qquad \frac{\partial^2\tau}{\partial x\partial y} = 0$$

$$\frac{\partial^2\tau}{\partial y^2} = 0 \qquad \frac{\partial^2\tau}{\partial y\partial z} = 0$$

$$\frac{\partial^2\tau}{\partial z^2} = 0 \qquad \frac{\partial^2\tau}{\partial z\partial x} = 0 \tag{4.2.4}$$

$$\begin{aligned}
\frac{\partial^2\xi}{\partial x^2} &= 2\,\frac{\partial^2\tau}{\partial x\partial t} + f\left(y\,\frac{\partial\tau}{\partial z} - z\,\frac{\partial\tau}{\partial y}\right)\\
\frac{\partial^2\xi}{\partial y^2} &= fz\,\frac{\partial\tau}{\partial y}\\
\frac{\partial^2\xi}{\partial z^2} &= -fy\,\frac{\partial\tau}{\partial z}\\
2\,\frac{\partial^2\xi}{\partial x\partial y} &= 2\,\frac{\partial^2\tau}{\partial y\partial t} + f\left(2z\,\frac{\partial\tau}{\partial x} - x\,\frac{\partial\tau}{\partial z}\right)\\
2\,\frac{\partial^2\xi}{\partial y\partial z} &= f\left(z\,\frac{\partial\tau}{\partial z} - y\,\frac{\partial\tau}{\partial y}\right)\\
2\,\frac{\partial^2\xi}{\partial z\partial x} &= 2\,\frac{\partial^2\tau}{\partial z\partial t} + f\left(x\,\frac{\partial\tau}{\partial y} - 2y\,\frac{\partial\tau}{\partial x}\right)
\end{aligned} \tag{4.2.5}$$

$$\begin{aligned}
\frac{\partial^2\eta}{\partial x^2} &= -fz\,\frac{\partial\tau}{\partial x}\\
\frac{\partial^2\eta}{\partial y^2} &= 2\,\frac{\partial^2\tau}{\partial y\partial t} + f\left(z\,\frac{\partial\tau}{\partial x} - x\,\frac{\partial\tau}{\partial z}\right)\\
\frac{\partial^2\eta}{\partial z^2} &= fx\,\frac{\partial\tau}{\partial z}
\end{aligned}$$

$$
\begin{aligned}
2\,\frac{\partial^2\eta}{\partial x\partial y} &= 2\,\frac{\partial^2\tau}{\partial x\partial t} + f\left(y\,\frac{\partial\tau}{\partial z} - 2z\,\frac{\partial\tau}{\partial y}\right)\\
2\,\frac{\partial^2\eta}{\partial y\partial z} &= 2\,\frac{\partial^2\tau}{\partial z\partial t} + f\left(2x\,\frac{\partial\tau}{\partial y} - y\,\frac{\partial\tau}{\partial x}\right)\\
2\,\frac{\partial^2\eta}{\partial z\partial x} &= f\left(x\,\frac{\partial\tau}{\partial x} - z\,\frac{\partial\tau}{\partial z}\right)
\end{aligned}
\tag{4.2.6}
$$

$$
\begin{aligned}
\frac{\partial^2\zeta}{\partial x^2} &= fy\,\frac{\partial\tau}{\partial x}\\
\frac{\partial^2\zeta}{\partial y^2} &= -fx\,\frac{\partial\tau}{\partial y}\\
\frac{\partial^2\zeta}{\partial z^2} &= 2\,\frac{\partial^2\tau}{\partial z\partial t} + f\left(x\,\frac{\partial\tau}{\partial y} - y\,\frac{\partial\tau}{\partial x}\right)\\
2\,\frac{\partial^2\zeta}{\partial x\partial y} &= f\left(y\,\frac{\partial\tau}{\partial y} - x\,\frac{\partial\tau}{\partial x}\right)\\
2\,\frac{\partial^2\zeta}{\partial y\partial z} &= 2\,\frac{\partial^2\tau}{\partial y\partial t} + f\left(z\,\frac{\partial\tau}{\partial x} - 2x\,\frac{\partial\tau}{\partial z}\right)\\
2\,\frac{\partial^2\zeta}{\partial z\partial x} &= 2\,\frac{\partial^2\tau}{\partial x\partial t} + f\left(2y\,\frac{\partial\tau}{\partial z} - z\,\frac{\partial\tau}{\partial y}\right)
\end{aligned}
\tag{4.2.7}
$$

$$
\begin{aligned}
2\,\frac{\partial^2\xi}{\partial x\partial t} - \frac{\partial^2\tau}{\partial t^2} + f\left(y\,\frac{\partial\zeta}{\partial x} + y\,\frac{\partial\xi}{\partial z} - z\,\frac{\partial\xi}{\partial y} - z\,\frac{\partial\eta}{\partial x}\right) + g\left(3x\,\frac{\partial\tau}{\partial x} + y\,\frac{\partial\tau}{\partial y} + z\,\frac{\partial\tau}{\partial z}\right) = 0\\
2\,\frac{\partial^2\eta}{\partial y\partial t} - \frac{\partial^2\tau}{\partial t^2} + f\left(z\,\frac{\partial\xi}{\partial y} + z\,\frac{\partial\eta}{\partial x} - x\,\frac{\partial\eta}{\partial z} - x\,\frac{\partial\zeta}{\partial y}\right) + g\left(x\,\frac{\partial\tau}{\partial x} + 3y\,\frac{\partial\tau}{\partial y} + z\,\frac{\partial\tau}{\partial z}\right) = 0\\
2\,\frac{\partial^2\zeta}{\partial z\partial t} - \frac{\partial^2\tau}{\partial t^2} + f\left(x\,\frac{\partial\eta}{\partial z} + x\,\frac{\partial\zeta}{\partial y} - y\,\frac{\partial\zeta}{\partial x} - y\,\frac{\partial\xi}{\partial z}\right) + g\left(x\,\frac{\partial\tau}{\partial x} + y\,\frac{\partial\tau}{\partial y} + 3z\,\frac{\partial\tau}{\partial z}\right) = 0
\end{aligned}
\tag{4.2.8}
$$

$$
\begin{aligned}
2\frac{\partial^2\xi}{\partial y\partial t}+f\left(y\frac{\partial\zeta}{\partial y}+z\frac{\partial\xi}{\partial x}-x\frac{\partial\xi}{\partial z}-z\frac{\partial\eta}{\partial y}-\zeta-z\frac{\partial\tau}{\partial t}\right) &- \frac{zf'}{r}(x\xi+y\eta+z\zeta)\\
&+ 2xg\frac{\partial\tau}{\partial y}=0\\
2\frac{\partial^2\xi}{\partial z\partial t}+f\left(y\frac{\partial\zeta}{\partial z}+x\frac{\partial\xi}{\partial y}-y\frac{\partial\xi}{\partial x}-z\frac{\partial\eta}{\partial z}+\eta+y\frac{\partial\tau}{\partial t}\right) &+ \frac{yf'}{r}(x\xi+y\eta+z\zeta)\\
&+ 2xg\frac{\partial\tau}{\partial z}=0\\
2\frac{\partial^2\eta}{\partial x\partial t}+f\left(z\frac{\partial\xi}{\partial x}+y\frac{\partial\eta}{\partial z}-z\frac{\partial\eta}{\partial y}-x\frac{\partial\zeta}{\partial x}+\zeta+z\frac{\partial\tau}{\partial t}\right) &+ \frac{zf'}{r}(x\xi+y\eta+z\zeta)\\
&+ 2yg\frac{\partial\tau}{\partial x}=0\\
2\frac{\partial^2\eta}{\partial z\partial t}+f\left(z\frac{\partial\xi}{\partial z}+x\frac{\partial\eta}{\partial y}-y\frac{\partial\eta}{\partial x}-x\frac{\partial\zeta}{\partial z}-\xi-x\frac{\partial\tau}{\partial t}\right) &- \frac{xf'}{r}(x\xi+y\eta+z\zeta)\\
&+ 2yg\frac{\partial\tau}{\partial z}=0\\
2\frac{\partial^2\zeta}{\partial x\partial t}+f\left(x\frac{\partial\eta}{\partial x}+y\frac{\partial\zeta}{\partial z}-z\frac{\partial\zeta}{\partial y}-y\frac{\partial\xi}{\partial x}-\eta-y\frac{\partial\tau}{\partial t}\right) &- \frac{yf'}{r}(x\xi+y\eta+z\zeta)\\
&+ 2zg\frac{\partial\tau}{\partial x}=0\\
2\frac{\partial^2\zeta}{\partial y\partial t}+f\left(x\frac{\partial\eta}{\partial y}+z\frac{\partial\zeta}{\partial x}-x\frac{\partial\zeta}{\partial z}-y\frac{\partial\xi}{\partial y}+\xi+x\frac{\partial\tau}{\partial t}\right) &+ \frac{xf'}{r}(x\xi+y\eta+z\zeta)\\
&+ 2zg\frac{\partial\tau}{\partial y}=0
\end{aligned}
\tag{4.2.9}
$$

$$
\begin{aligned}
\frac{\partial^2\xi}{\partial t^2}+f\left(y\frac{\partial\zeta}{\partial t}-z\frac{\partial\eta}{\partial t}\right)+g\left(\xi+2x\frac{\partial\tau}{\partial t}\right. &- \left. x\frac{\partial\xi}{\partial x}-y\frac{\partial\xi}{\partial y}-z\frac{\partial\xi}{\partial z}\right)\\
&+ \frac{xg'}{r}(x\xi+y\eta+z\zeta)=0\\
\frac{\partial^2\eta}{\partial t^2}+f\left(z\frac{\partial\xi}{\partial t}-x\frac{\partial\zeta}{\partial t}\right)+g\left(\eta+2y\frac{\partial\tau}{\partial t}\right. &- \left. x\frac{\partial\eta}{\partial x}-y\frac{\partial\eta}{\partial y}-z\frac{\partial\eta}{\partial z}\right)\\
&+ \frac{yg'}{r}(x\xi+y\eta+z\zeta)=0
\end{aligned}
$$

$$\frac{\partial^2\zeta}{\partial t^2} + f\left(x\frac{\partial\eta}{\partial t} - y\frac{\partial\xi}{\partial t}\right) + g\left(\zeta + 2z\frac{\partial\tau}{\partial t} - x\frac{\partial\zeta}{\partial x} - y\frac{\partial\zeta}{\partial y} - z\frac{\partial\zeta}{\partial z}\right) + \frac{zg'}{r}(x\xi + y\eta + z\zeta) = 0 \tag{4.2.10}$$

where $'$ denotes differentiation with respect to r.

The solution of (4.2.4) is

$$\tau = a(t) + b(t)x + c(t)y + d(t)z. \tag{4.2.11}$$

Substituting τ (4.2.11) into (4.2.5) gives rise to consistency requirements between third order mixed derivatives. Two distinct cases emerge. If $f = 0$, b, c and d remain unspecified. If $f \neq 0$, b, c and d are simultaneously zero. We analyse these cases in more detail.

4.3 The Case $f = 0$

The solutions of (4.2.5), (4.2.6) and (4.2.7) are

$$\begin{aligned} \xi &= \left(\dot{b}x + \dot{c}y + \dot{d}z\right)x + kx + ly + mz + n \\ \eta &= \left(\dot{b}x + \dot{c}y + \dot{d}z\right)y + px + qy + rz + s \\ \zeta &= \left(\dot{b}x + \dot{c}y + \dot{d}z\right)z + tx + uy + vz + w, \end{aligned} \tag{4.3.1}$$

where the functions k through w depend only on time. (In circumstances where confusion may arise between the functions $r(t)$ and $t(t)$, and the variables r and t, clarification will be given).

Substituting (4.2.11) and (4.3.1) into (4.2.9) forces l, m, p, r, t and u to be constant and, if g is not constant, b, c and d to be zero as well. For the sake of completeness we consider the case $g = \alpha$, a constant. Then b, c and d satisfy the equations

$$\ddot{b} + \alpha b = 0, \qquad \ddot{c} + \alpha c = 0, \qquad \ddot{d} + \alpha d = 0. \tag{4.3.2}$$

Solving (4.2.8) we obtain

$$2\dot{k} = 2\dot{q} = 2\dot{v} = \ddot{a}, \tag{4.3.3}$$

and from (4.2.10)

$$\ddot{k} + 2\alpha\dot{a} = 0 \qquad \ddot{n} + \alpha n = 0$$

$$\ddot{q} + 2\alpha\dot{a} = 0 \qquad \ddot{s} + \alpha s = 0$$

$$\ddot{v} + 2\alpha\dot{a} = 0 \qquad \ddot{w} + \alpha w = 0. \tag{4.3.4}$$

Solving (4.3.2) gives rise to six free constants, two for each of the b, c and d, three for a from (4.3.3) and (4.3.4), k, q and v each add one more and n, s and w give six more. In addition to these eighteen, l, m, p, r, t and u are constant, making twenty–four in total. Hence the Lie algebra is the twenty–four–dimensional $sl(5, R)$. This is not surprising as for $\alpha > 0$ we have the three–dimensional isotropic harmonic oscillator, for $\alpha = 0$ the three–dimensional free particle and for $\alpha < 0$ the three–dimensional isotropic repulsor.

When g is a nontrivial function, l, m, p, r, t and u are constants from (4.2.11), (4.3.1) and (4.2.9) and b, c and d are zero. Using (4.2.8) we again obtain (4.3.3) which can be integrated to give

$$\begin{aligned} k &= \frac{1}{2}(\dot{a} + K), \quad q = \frac{1}{2}(\dot{a} + Q), \quad v = \frac{1}{2}(\dot{a} + V), \quad l = \frac{1}{2}L, \\ m &= \frac{1}{2}M, \quad p = \frac{1}{2}P, \quad r = \frac{1}{2}R, \quad t = \frac{1}{2}T, \quad u = \frac{1}{2}U, \end{aligned} \tag{4.3.5}$$

where the constants are denoted by upper case symbols. Equations (4.2.10) now become

$$\begin{aligned} a^{(3)}x &+ 2\ddot{n} + 2g(n + 2x\dot{a}) + \frac{xg'}{r}\Big[\dot{a}r^2 + x(Kx + Ly + Mz + 2n) \\ &+ y(Px + Qy + Rz + 2s) + z(Tx + Uy + Vz + 2w)\Big] = 0 \end{aligned} \tag{4.3.6}$$

$$\begin{aligned} a^{(3)}y &+ 2\ddot{s} + 2g(s + 2y\dot{a}) + \frac{yg'}{r}\Big[\dot{a}r^2 + x(Kx + Ly + Mz + 2n) \\ &+ y(Px + Qy + Rz + 2s) + z(Tx + Uy + Vz + 2w)\Big] = 0 \end{aligned} \tag{4.3.7}$$

$$\begin{aligned} a^{(3)}z &+ 2\ddot{w} + 2g(w + 2z\dot{a}) + \frac{zg'}{r}\Big[\dot{a}r^2 + x(Kx + Ly + Mz + 2n) \\ &+ y(Px + Qy + Rz + 2s) + z(Tx + Uy + Vz + 2w)\Big] = 0, \end{aligned} \tag{4.3.8}$$

where $a^{(3)}$ represents $\mathrm{d}^3a/\mathrm{d}t^3$. This convention is also used below.

Combining $y\times(4.3.6)-x\times(4.3.7)$ and $z\times(4.3.6)-x\times(4.3.8)$ and suitably rearranging we obtain

$$\begin{aligned}(yn-xs)g &= -(y\ddot{n}-x\ddot{s})\\ (zn-xw)g &= -(z\ddot{n}-x\ddot{w})\end{aligned}\tag{4.3.9}$$

and, since g is a nontrivial function of r, it follows that n, s and w are zero. Equations (4.3.6), (4.3.7) and (4.3.8) reduce to the single equation

$$(Kx+Ly+Mz)x+(Px+Qy+Rz)y+(Tx+Uy+Vz)z=-\frac{r}{g'}\left[a^{(3)}+4g\dot{a}+g'r\dot{a}\right].\tag{4.3.10}$$

The partial derivative of (4.3.10) with respect to time gives

$$a^{(4)}+(4g+g'r)\ddot{a}=0.\tag{4.3.11}$$

If g is to be unspecified,

$$\begin{aligned}\ddot{a} &= 0\\ a &= A_0+A_1t.\end{aligned}\tag{4.3.12}$$

Equation (4.3.10) now becomes

$$(Kx+Ly+Mz)\,x+(Px+Qy+Rz)\,y+(Tx+Uy+Vz)\,z=-\frac{r}{g'}\,(4g+g'r)\,A_1.\tag{4.3.13}$$

It is evident that $P=-L$, $T=-M$ and $U=-R$ which gives rise to the $so(3)$ subalgebra. For general g, $K=Q=V=A_1=0$ and the algebra is $A_1\oplus so(3)$, where the subalgebras A_1 and A_2 used throughout are not to be confused with constants having the same symbol. However, if g is to be specified through (4.3.13), we can have $K=Q=V$ and (4.3.13) becomes

$$Kr^2=-\frac{r}{g'}\,(4g+g'r)\,A_1\tag{4.3.14}$$

from which we find that for A_1 nonzero

$$g=\frac{\mu}{r^{4A_1/(A_1+K)}},\tag{4.3.15}$$

which can equivalently be written as

$$g=\mu r^{\alpha},\tag{4.3.16}$$

where $\alpha = -4A_1/(A_1 + K)$. The generators are then

$$\begin{aligned} G_1 &= \frac{\partial}{\partial t} \\ G_2 &= A_1 t \frac{\partial}{\partial t} + \frac{1}{2}(A_1 + K)\left(x \frac{\partial}{\partial x} + y \frac{\partial}{\partial y} + z \frac{\partial}{\partial z}\right) \\ G_3 &= z \frac{\partial}{\partial y} - y \frac{\partial}{\partial z} \\ G_4 &= x \frac{\partial}{\partial z} - z \frac{\partial}{\partial x} \\ G_5 &= y \frac{\partial}{\partial x} - x \frac{\partial}{\partial y} \end{aligned} \tag{4.3.17}$$

which have the algebra $A_2 \oplus so(3)$ as was found for the Kepler problem (1.5.1) by Prince and Eliezer [110] and Leach [72]. The Kepler problem is recovered when $A_1 + K = \frac{4}{3} A_1$. G_2 can be more concisely written as $G_2 = t\partial/\partial t - 2/\alpha r \partial/\partial r$ in the notation of (4.3.16). See §1.8.

Equation (4.3.11) may alternatively be written as

$$\begin{aligned} rg' + 4g &= -4\epsilon \\ a^{(4)} - 4\epsilon \ddot{a} &= 0 \end{aligned} \tag{4.3.18}$$

which gives

$$g = \frac{\mu}{r^4} - \epsilon \tag{4.3.19}$$

and

$$a = A_0 + A_1 t + A_2 t^2 + A_3 t^3, \qquad \epsilon = 0 \tag{4.3.20}$$

$$a = A_0 + A_1 t + A_2 e^{2t\epsilon^{1/2}} + A_3 e^{-2t\epsilon^{1/2}}, \qquad \epsilon \neq 0. \tag{4.3.21}$$

Substituting (4.3.19)–(4.3.21) into (4.3.10) we see that, for $\epsilon = 0, K = Q = V = A_3 = 0$ and $P = -L$, $T = -M$ and $U = -R$. Thus the equation of motion

$$\ddot{\boldsymbol{r}} + \frac{\mu}{r^4} \boldsymbol{r} = \boldsymbol{0}, \tag{4.3.22}$$

has the symmetries

$$\begin{aligned} G_1 &= \frac{\partial}{\partial t} \\ G_2 &= 2t\frac{\partial}{\partial t} + x\frac{\partial}{\partial x} + y\frac{\partial}{\partial y} + z\frac{\partial}{\partial z} \\ G_3 &= t\left(t\frac{\partial}{\partial t} + x\frac{\partial}{\partial x} + y\frac{\partial}{\partial y} + z\frac{\partial}{\partial z}\right) \\ G_4 &= z\frac{\partial}{\partial y} - y\frac{\partial}{\partial z} \\ G_5 &= x\frac{\partial}{\partial z} - z\frac{\partial}{\partial x} \\ G_6 &= y\frac{\partial}{\partial x} - x\frac{\partial}{\partial y}. \end{aligned} \tag{4.3.23}$$

The Lie algebra of the generators is $sl(2,R) \oplus so(3)$ which we recognize as the same as that found for the charge monopole problem (4.1.8) by Moreira *et al.* [101].

When $\epsilon \neq 0$, $K = Q = V = A_1 = 0$ and $P = -L$, $T = -M$ and $U = -R$. The equation of motion

$$\ddot{\boldsymbol{r}} + \left(\frac{\mu}{r^4} - \epsilon\right)\boldsymbol{r} = \boldsymbol{0} \tag{4.3.24}$$

has the symmetries

$$\begin{aligned} G_1 &= \frac{\partial}{\partial t} \\ G_2 &= e^{2t\epsilon^{1/2}}\left(\epsilon^{-1/2}\frac{\partial}{\partial t} + x\frac{\partial}{\partial x} + y\frac{\partial}{\partial y} + z\frac{\partial}{\partial z}\right) \\ G_3 &= e^{-2t\epsilon^{1/2}}\left(\epsilon^{-1/2}\frac{\partial}{\partial t} - x\frac{\partial}{\partial x} - y\frac{\partial}{\partial y} - z\frac{\partial}{\partial z}\right) \\ G_4 &= z\frac{\partial}{\partial y} - y\frac{\partial}{\partial z} \\ G_5 &= x\frac{\partial}{\partial z} - z\frac{\partial}{\partial x} \\ G_6 &= y\frac{\partial}{\partial x} - x\frac{\partial}{\partial y}. \end{aligned} \tag{4.3.25}$$

The algebra is again $sl(2,R) \oplus so(3)$.

To summarize the case $f = 0$, we have three distinct results with increasing richness as g is more tightly specified. For the central force problem

$$\ddot{\boldsymbol{r}} + g(r)\boldsymbol{r} = \boldsymbol{0} \tag{4.3.26}$$

we have the usual four symmetries associated with invariance under a time translation as well as under rotation. When g is a power law so that the equation of motion is

$$\ddot{\boldsymbol{r}} + \mu r^{\alpha}\boldsymbol{r} = \boldsymbol{0}, \tag{4.3.27}$$

the above four symmetries are replicated plus a further one added indicating invariance under a similarity transformation. For the equation

$$\ddot{\boldsymbol{r}} + \frac{\mu}{r^4}\boldsymbol{r} = \boldsymbol{0}, \tag{4.3.28}$$

there is the further addition of an inversion transformation between t and r the third equation of (4.3.23), as is found in the case of the symmetry of the one–dimensional free particle (this generator can in fact be written more concisely as $t(t\,\partial/\partial t + r\,\partial/\partial r)$).

When the equation of motion takes the form

$$\ddot{\boldsymbol{r}} + \left(\frac{\mu}{r^4} - \epsilon\right)\boldsymbol{r} = \boldsymbol{0}, \tag{4.3.29}$$

the generator corresponding to self–similar transformations disappears, yet the algebra remains the six–dimensional $sl(2,R) \oplus so(3)$. Finally, when the equation of motion takes the form

$$\ddot{\boldsymbol{r}} + \epsilon\boldsymbol{r} = \boldsymbol{0}, \tag{4.3.30}$$

which describes a three–dimensional isotropic harmonic oscillator for $\epsilon > 0$, the three–dimensional free particle for $\epsilon = 0$ and the three–dimensional isotropic repulsor for $\epsilon < 0$, the algebra becomes the twenty–four–dimensional $sl(5,R)$.

Despite the existence of a Laplace–Runge–Lenz vector in the classical Kepler problem, we have shown that this does little to influence the construction of the symmetry algebra. Apart from the three–dimensional isotropic harmonic oscillator, all power law central force problems possess the same number of symmetries, yet global (or even local) representations for a Laplace–Runge–Lenz–like vector are rarely possible. Although the Kepler problem is regarded as unusual because of the Laplace–Runge–Lenz vector, in terms of the symmetry algebra of its equation of motion it is just one of an infinite number of problems.

4.4 The Case $f \neq 0$

We now return to the general equation (4.2.1) and attempt to obtain the symmetries. We recall that b, c and d were zero and this simplifies (4.2.11) and (4.3.1) to give

$$\begin{aligned} \tau &= a \\ \xi &= kx + ly + mz + n \\ \eta &= px + qy + rz + s \\ \zeta &= tx + uy + vz + w, \end{aligned} \tag{4.4.1}$$

where all lower case latin letters excluding x, y and z are functions of time. The set of equations (4.2.8) now reduces to

$$\begin{aligned} 2\dot{k} &- \ddot{a} + f\left[y(m+t) - z(l+p)\right] = 0 \\ 2\dot{q} &- \ddot{a} + f\left[z(l+p) - x(r+u)\right] = 0 \\ 2\dot{v} &- \ddot{a} + f\left[x(r+u) - y(m+t)\right] = 0 \end{aligned} \tag{4.4.2}$$

which give

$$2\dot{k} = 2\dot{q} = 2\dot{v} = \ddot{a} \tag{4.4.3}$$

$$l + p = 0, \qquad m + t = 0, \quad r + u = 0. \tag{4.4.4}$$

Equations (4.2.9) now become

$$2\dot{l} - \frac{zf'}{r}\Phi + f\left[z(k - q - v - \dot{a}) - w\right] = 0 \tag{4.4.5}$$

$$2\dot{m} + \frac{yf'}{r}\Phi + f\left[-y(k - q - v - \dot{a}) + s\right] = 0 \tag{4.4.6}$$

$$2\dot{r} - \frac{xf'}{r}\Phi + f\left[-x(k - q + v + \dot{a}) - n\right] = 0 \tag{4.4.7}$$

$$2\dot{p} + \frac{zf'}{r}\Phi + f\left[z(k - q + v + \dot{a}) + w\right] = 0 \tag{4.4.8}$$

$$2\dot{t} - \frac{yf'}{r}\Phi + f\left[-y(k + q - v + \dot{a}) - s\right] = 0 \tag{4.4.9}$$

$$2\dot{u} + \frac{xf'}{r}\Phi + f\left[x(k + q - v + \dot{a}) + n\right] = 0, \tag{4.4.10}$$

where $\Phi = x(kx + n) + y(qy + s) + z(vz + w)$ and the r in the denominator is the variable r and not the function $r(t)$.

Adding (4.4.5) to (4.4.8), (4.4.6) to (4.4.9), (4.4.7) to (4.4.10) and using the results of (4.4.4) we find that

$$k = q = v \tag{4.4.11}$$

$$\Phi = kr^2 + xn + ys + zw. \tag{4.4.12}$$

This reduces the number of independent equations in (4.4.5) to (4.4.10) to three, say (4.4.5), (4.4.7) and (4.4.9). Multiplying these by z, x and y respectively and adding we obtain

$$\begin{aligned} x\left[2\dot{r} - (rf' + f)n\right] \; &+ \; y\left[2\dot{t} - (rf' + f)s\right] + z\left[2\dot{l} - (rf' + f)w\right] \\ &- \; r^2\left[krf' + (k + \dot{a})f\right] = 0 \end{aligned} \tag{4.4.13}$$

from which it is evident that

$$krf' + (k + \dot{a})f = 0 \tag{4.4.14}$$

$$2\dot{r} - (rf' + f)n = 0 \tag{4.4.15}$$

$$2\dot{t} - (rf' + f)s = 0 \tag{4.4.16}$$

$$2\dot{l} - (rf' + f)w = 0. \tag{4.4.17}$$

Equation (4.4.14) has a solution for f if

$$k + \dot{a} = \nu k \tag{4.4.18}$$

where ν is a constant and correspondingly

$$f = \lambda r^{-\nu}, \tag{4.4.19}$$

for λ also a constant. The possibility $k = \dot{a} = 0$ leads to just the four symmetry case with algebra $A_1 \oplus so(3)$. Otherwise f will be zero and this case has been treated in §4.3. Combining (4.4.3) and (4.4.18) gives

$$\ddot{a}(3 - \nu) = 0. \tag{4.4.20}$$

We treat the cases $\nu = 3$ and $\nu \neq 3$ separately. If $\nu = 3$, (4.4.15)–(4.4.17) immediately gives $n = s = w = 0$ and r t, l, p, m and u constant. Using (4.4.4) these constants give the $so(3)$ subalgebra. Equations (4.2.10) all reduce to

$$rg' + 4g = -\frac{\ddot{k}}{k} = -4\epsilon, \tag{4.4.21}$$

using $\dot{a} = 2k$ from (4.4.18), and ϵ is a constant. Solving equation (4.4.21) gives

$$g = \frac{\mu}{r^4} - \epsilon. \tag{4.4.22}$$

For $\epsilon = 0$,

$$\begin{aligned} f &= \frac{\lambda}{r^3} \\ g &= \frac{\mu}{r^4} \\ k &= A_1 + A_2 t \\ a &= A_0 + 2A_1 t + A_2 t^2 \end{aligned} \tag{4.4.23}$$

which give rise to three symmetries in addition to the usual $so(3)$ generators, viz.

$$\begin{aligned} G_1 &= \frac{\partial}{\partial t} \\ G_2 &= 2t\frac{\partial}{\partial t} + x\frac{\partial}{\partial x} + y\frac{\partial}{\partial y} + z\frac{\partial}{\partial z} \\ G_3 &= t^2\frac{\partial}{\partial t} + t\left(x\frac{\partial}{\partial x} + y\frac{\partial}{\partial y} + z\frac{\partial}{\partial z}\right) \end{aligned} \tag{4.4.24}$$

and the algebra is $sl(2,R) \oplus so(3)$.

As shown before, the vector product of $\boldsymbol{r}$ with the equation of motion corresponding to (4.4.23)

$$\ddot{\boldsymbol{r}} + \frac{\lambda}{r^3}\boldsymbol{L} + \frac{\mu}{r^4}\boldsymbol{r} = \boldsymbol{0} \tag{4.4.25}$$

gives rise to Poincaré's vector $\boldsymbol{P}$

$$\boldsymbol{P} = \boldsymbol{L} - \lambda\hat{\boldsymbol{r}} \tag{4.4.26}$$

after integrating with respect to time. This vector is incidentally also conserved for the equation of motion of the charge–monopole problem (4.1.8). Taking the vector product of the equation of motion (4.4.25) with (4.4.26) gives the projected and rotated equation of motion

$$\ddot{\boldsymbol{r}} \times \boldsymbol{P} + \left(\frac{L^4(\lambda^2 + \mu)}{|\boldsymbol{r} \times \boldsymbol{P}|^4}\right)\boldsymbol{r} \times \boldsymbol{P} = \boldsymbol{0} \tag{4.4.27}$$

which is equivalent to the central force case (4.3.22) in the variable $\boldsymbol{r} \times \boldsymbol{P}$ (see §3.5 for a geometric interpretation of taking the vector product with $\boldsymbol{P}$).

For $\epsilon \neq 0$,

$$\begin{aligned} f &= \frac{\lambda}{r^3} \\ g &= \frac{\mu}{r^4} - \epsilon \\ k &= A_1 e^{2t\epsilon^{1/2}} - A_2 e^{-2t\epsilon^{1/2}} \\ a &= A_0 + \epsilon^{-1/2}\left(A_1 e^{2t\epsilon^{1/2}} + A_2 e^{-2t\epsilon^{1/2}}\right). \end{aligned} \tag{4.4.28}$$

In addition to the $so(3)$ generators we obtain

$$\begin{aligned} G_1 &= \frac{\partial}{\partial t} \\ G_2 &= e^{2t\epsilon^{1/2}}\left(\epsilon^{-1/2}\frac{\partial}{\partial t} + x\,\frac{\partial}{\partial x} + y\,\frac{\partial}{\partial y} + z\,\frac{\partial}{\partial z}\right) \\ G_3 &= e^{-2t\epsilon^{1/2}}\left(\epsilon^{-1/2}\frac{\partial}{\partial t} - x\,\frac{\partial}{\partial x} - y\,\frac{\partial}{\partial y} - z\,\frac{\partial}{\partial z}\right) \end{aligned} \tag{4.4.29}$$

and again the algebra is $sl(2,R) \oplus so(3)$. Similarly, taking the vector product of the equation of motion corresponding to (4.4.28)

$$\ddot{\boldsymbol{r}} + \frac{\lambda}{r^3}\boldsymbol{L} + \left(\frac{\mu}{r^4} - \epsilon\right)\boldsymbol{r} = \boldsymbol{0} \tag{4.4.30}$$

with $\boldsymbol{P}$ gives the projected and rotated equation of motion

$$\ddot{\boldsymbol{r}} \times \boldsymbol{P} + \left(\frac{L^4(\lambda^2+\mu)}{|\boldsymbol{r}\times\boldsymbol{P}|^4} - \epsilon\right)\boldsymbol{r}\times\boldsymbol{P} = \boldsymbol{0} \tag{4.4.31}$$

which is equivalent to the central force case (4.3.24) in the variable $\boldsymbol{r}\times\boldsymbol{P}$.

When $\nu \neq 3$, from (4.4.20) and (4.4.3)

$$a = A_0 + A_1 t, \qquad k = K_0. \tag{4.4.32}$$

From (4.4.18)

$$A_1 = (\nu - 1)K_0 \tag{4.4.33}$$

and, if $\nu = 1$, A_1 is zero. Equations (4.2.10) yield K_0 zero, the usual $so(3)$ constants and $n = s = w = 0$ so that the algebra is $A_1 \oplus so(3)$. For $\nu \neq 1$, (4.2.10) again gives K_0 zero and so A_1 from (4.4.33). The algebra is again $A_1 \oplus so(3)$.

4.5 Discussion

The equation of motion

$$\ddot{\boldsymbol{r}} + f(r)\boldsymbol{L} + g(r)\boldsymbol{r} = \boldsymbol{0} \tag{4.5.1}$$

is seen to possess the algebra $A_1 \oplus so(3)$ for general f and g with A_1 representing invariance under time translation and $so(3)$ the usual rotational invariance. Special cases of (4.5.1) with additional symmetry are

$$\ddot{\boldsymbol{r}} + \mu r^{\alpha}\boldsymbol{r} = \boldsymbol{0} \tag{4.5.2}$$

$$\ddot{\boldsymbol{r}} + \frac{\mu}{r^4}\boldsymbol{r} = \boldsymbol{0} \tag{4.5.3}$$

$$\ddot{\boldsymbol{r}} + \left(\frac{\mu}{r^4} - \epsilon\right)\boldsymbol{r} = \boldsymbol{0} \tag{4.5.4}$$

$$\ddot{\boldsymbol{r}} + \epsilon\boldsymbol{r} = \boldsymbol{0} \tag{4.5.5}$$

$$\ddot{\boldsymbol{r}} + \frac{\lambda}{r^3}\boldsymbol{L} + \frac{\mu}{r^4}\boldsymbol{r} = \boldsymbol{0} \tag{4.5.6}$$

$$\ddot{\boldsymbol{r}} + \frac{\lambda}{r^3}\boldsymbol{L} + \left(\frac{\mu}{r^4} - \epsilon\right)\boldsymbol{r} = \boldsymbol{0}. \tag{4.5.7}$$

The five–dimensional algebra of (4.5.2) was found to be $A_2 \oplus so(3)$ where the A_2 algebra represents invariance under the self–similar transformation

$$t = \gamma\bar{t} \qquad \boldsymbol{r} = \gamma^{-\frac{2}{\alpha}}\bar{\boldsymbol{r}} \tag{4.5.8}$$

as well as invariance under time translation. The interesting point about (4.5.2) is that, as far as symmetries are concerned, there is no distinction made between the Kepler problem and any other power law central force apart from the three–dimensional isotropic harmonic oscillator.

The equations of motion (4.5.3) and (4.5.4) both possess the algebra $sl(2,R) \oplus so(3)$ regardless of the values of the parameters. They may be regarded as direct extensions of the results of Moreira *et al.* [101] for the algebra of the charge monopole problem. Equation (4.5.5) has the twenty–four–dimensional algebra $sl(5,R)$ of the three–dimensional isotropic harmonic oscillator, free particle or repulsor depending on whether $\epsilon >, =, < 0$ respectively. Equations (4.5.6) and (4.5.7) have the algebra $sl(2,R) \oplus so(3)$ and also possess Poincaré vectors which project and rotate them onto equations of motion equivalent to (4.5.3) and (4.5.4) respectively, in terms of the vector $\boldsymbol{r} \times \boldsymbol{P}$.

The term $\mu \boldsymbol{r} r^{-4}$ can be interpreted as a centripetal force (Newton–Cotes) and the term $\epsilon \boldsymbol{r}$ represents a three–dimensional isotropic harmonic oscillator, free particle or repulsor depending on whether $\epsilon >, =, < 0$ respectively. The latter term does not affect the algebra nor the integrability of the equation. It should also be observed that L is constant in both (4.5.6) and (4.5.7). We note that the motion continues to be on the surface of a cone. Another scalar integral

$$I = \frac{1}{2}\left(\dot{\boldsymbol{r}}^2 - \frac{\mu}{r^2} - \epsilon r^2\right) \tag{4.5.9}$$

also exists. Equation (4.5.7) does not belong to the class of problems (4.2.2) treated by Leach and Gorringe [78]. However, when $\mu = -\lambda^2$, (4.5.6) does and in addition to the three integrals above, there is also the conserved vector

$$\begin{aligned} \boldsymbol{J} &= \dot{\boldsymbol{r}} \times \boldsymbol{L} + \frac{\lambda}{r}\boldsymbol{L} \\ &= \dot{\boldsymbol{r}} \times \boldsymbol{P} \end{aligned} \tag{4.5.10}$$

from which the orbit equation is easily obtained by taking the scalar product with $\boldsymbol{r}$ (see §3.7).

It is at first glance surprising, however, that the four–dimensional algebra of the MICZ problem (3.5.1), $A_1 \oplus so(3)$, is different from that of the five–dimensional algebra of the Kepler problem (1.5.1), $A_2 \oplus so(3)$, since the MICZ problem has a conserved Poincaré vector which projects and rotates it onto the equation of motion for the Kepler problem in terms of the vector $\boldsymbol{r} \times \boldsymbol{P}$ (see (3.5.11)). It should also be pointed out that in the case of the Kepler problem, the self–similar symmetry is a harbinger of Kepler's third law (1.5.48), while in the MICZ problem, although an analogue of this conservation law is present (3.9.53), it goes undetected using the symmetry treatment. Similarly, the six–dimensional algebra of the monopole–oscillator (3.13.1) with $\mu = -\lambda^2$, $sl(2,R) \oplus so(3)$, is different from that of the twenty–four–dimensional algebra of the three–dimensional isotropic harmonic oscillator (1.7.1), $sl(5,R)$, although the monopole–oscillator has a conserved Poincaré vector which projects and rotates it onto the equation of motion for the three–dimensional isotropic harmonic oscillator in terms of the vector $\boldsymbol{r} \times \boldsymbol{P}$ (see (3.13.26) with $\mu = -\lambda^2$). In the case of the three–dimensional isotropic harmonic oscillator, the self–similar symmetry also signals a Kepler–type third law (1.7.48), whilst in the monopole–oscillator problem, despite having an analogue of this conservation law (3.14.42), it is again overlooked by the symmetry treatment. One obvious drawback of using the Lie method is that, although the relationship between the MICZ and monopole–oscillator problems with the Kepler and oscillator problems respectively is obvious from a geometric point of

view (*i.e.*, a simple projection and rotation), this relationship goes undetected using the Lie analysis. It is not surprising then that the conservation laws (3.9.53) and (3.14.42) are not obviously apparent by looking at the symmetries of the equations of motion of the MICZ and monopole–oscillator problems respectively, since the conservation laws are not obviously associated with a point transformation as with their central force counterparts.

From these results it can also be concluded that the existence of symmetry and the existence of conserved vectors of the Laplace–Runge–Lenz type appear to be unrelated. The reason would appear to stem from two inherently dissimilar structures which, in the case of the Kepler problem and the charge monopole problem, neatly overlap.

CONCLUSIONS

The technique of applying vector operations directly to the equation of motion for the type of problems discussed in the earlier chapters has been shown to be very effective in the determination of conserved vectors. It is also very economical in terms of the amount of algebra required to obtain a solution. Due to the vector nature of the first integrals obtained using this method, the results are much easier to interpret than those which provide the integrals as separate components. For these reasons, this approach should be tried initially before resorting to more involved techniques such as Fradkin's method [29], the Lie technique, Noether's theorem or Whittaker's direct method [129].

The rôle of the angular momentum for these types of vector equations of motion is seen to be rather important. In Chapter 1 problems arising from the requirement that both the magnitude and direction of the angular momentum be restricted were studied in some detail. A general technique for finding conserved vectors of the Laplace–Runge–Lenz type was outlined and applied to the Kepler problem amongst other radially and angularly dependent equations of motion. Two non–conserved orthogonal vectors which are closely related to the scalar Lagrangian and also the Hamilton and Laplace–Runge–Lenz vectors were investigated for the Kepler problem and a possible method of construction was also developed for more general problems. Fradkin's method of finding conserved vectors and tensors was also studied and applied to the three–dimensional isotropic harmonic oscillator. A non–conserved tensor which is closely related to the scalar Lagrangian and also the Jauch–Hill–Fradkin tensor was also investigated for the three–dimensional isotropic harmonic oscillator together with a possible method of construction for more general problems. A comparison between the Kepler problem and the three–dimensional isotropic harmonic oscillator was done in order to illustrate the inherent similarities and differences between the two most important central force problems. Analogues of Kepler's laws of motion were obtained for the oscillator and the third law was shown to have a connection to that of the Kepler problem. The self–similar symmetry of the general central force problem was used to construct first integrals for the general central force problem and the Kepler problem was shown to be anomalous in that it is the only central force problem (apart from the free particle) which has a Laplace–Runge–Lenz vector analogue which is quadratric in the velocity. It was also possible to find a more general class of non–autonomous, radially dependent equations of motion possessing a Laplace–Runge–Lenz analogue which had previously been obtained using more involved techniques, by applying simple vector operations directly to the equations of motion.

In Chapter 2 it was shown that only the conservation of the direction of the angular momentum is required to fix the orbit in a plane. Making use of this relaxed angular momentum requirement it was possible to construct general classes of radially and angularly dependent problems having conserved Laplace–Runge–Lenz analogues, one of which had appeared previously in the literature in connection with the most general quadratic invariants for a two–dimensional integrable time–independent Hamiltonian. The time invariance Lie symmetry was then used to determine the components of the Laplace–Runge–Lenz vector as well as another integral which was previously obtained by calculating the Poisson bracket between the two components of the Laplace–Runge–Lenz vector in order to show that all conserved quantities can be obtained from any of the Lie symmetries and not only from the geometrically associated symmetry. Another class of velocity dependent and radially dependent problems was found which had conserved Laplace–Runge–Lenz vectors, of which one particular case was well–known in the literature in connection with the low level motion of artificial satellites. Two classes of related problems having focus–centred and geometric–centred conic section orbits were studied in some detail because of their connection with the Kepler problem and the three–dimensional isotropic harmonic oscillator. The presence of a conserved tensor for the oscillator–like equation of motion led to the application of Fradkin's method in this non–conservative system. A connection between certain classes of these problems and the usual central force problems was also obtained. For two restricted classes of problems selected from those mentioned above, it was also possible to find analogues of Kepler's three laws of motion and relate the period of elliptical motion to a fractional power of the semi–major axis length and also to investigate the rôle that eccentricity plays in the analogue of Kepler's third law. The self–similar Lie symmetry was also used in both of these problems to verify the eccentricity dependence of Kepler's third law. Interestingly, the velocity hodographs were no longer found to resemble their central force counterparts.

In Chapter 3, the magnitude but not the direction of the angular momentum was now required to be conserved. This prompted the study of a number of angular momentum dependent and radially dependent problems which are well–known in the literature, but have not been studied in any great detail from a geometric point of view. These include the MICZ monopole, the monopole–free particle, the monopole–oscillator and monopole–repulsor which are closely related to the Kepler problem, the free particle, the three–dimensional isotropic harmonic oscillator and the three–dimensional isotropic repulsor respectively. This prompted a careful investigation of the similarity between the orbits and velocity hodographs of the Kepler problem, free–particle, three–dimensional isotropic harmonic oscillator and repulsor. Most textbooks men-

tion the fact that the orbit equation for the Kepler problem is connected with a plane section of a cone, implying that the connection is almost coincidental. The results of Chapter 3 demonstrate why the Keplerian focus–centred orbit is related to a plane conic section. There it was shown that the projection of any plane section through a right circular cone perpendicular to the axis of the cone gives rise to a focus–centred conic, with the apex of the cone situated at one focus. In most textbooks no connection between the elliptical orbits of the three–dimensional isotropic harmonic oscillator and the elliptical plane sections of a right circular cone is mentioned although, using the argument put forward by most authors regarding the Kepler problem, the oscillator ellipse should also be connected with the elliptical plane sections of a right circular cone. From the results of Chapter 3 this is not the case since the projection of a plane section of a right circular cone is naturally associated with a focus–centred conic. In the case of the three–dimensional isotropic harmonic oscillator ellipse, the geometrically centred orbit is naturally associated with the projection of the intersection of a geometrically centred elliptical cylinder (with symmetry axis perpendicular to the axis of symmetry of the cone and in the plane of the apex of the cone) and the cone. The circular velocity hodograph for the Kepler problem was also shown to be associated with the projection of an elliptical plane section of a right circular cone, whilst the elliptical velocity hodograph for the three–dimensional isotropic harmonic oscillator is associated with a more complicated structure on the cone. The straight–line free particle orbit was shown to be naturally associated with either the projection of a plane (parallel to the symmetry axis) section of a cone, or the projection of the intersection of a geometrically centred hyperbolic sheet (with symmetry axis parallel to the axis of the cone) and the cone. The single point velocity hodograph for the free particle was also shown to be associated with the projection of a straight line velocity hodograph perpendicular to the projection plane. The hyperbolic focus–centred Keplerian orbit was shown to be naturally associated with the projection of a hyperbolic plane section of a right circular cone, whilst the geometric–centred repulsor orbit was naturally associated with the projection of the intersection of a geometrically centred hyperbolic sheet (with symmetry axis perpendicular to the axis of symmetry of the cone and in the plane of the apex of the cone) and the cone. The open circular velocity hodograph for the hyperbolic Kepler problem was also shown to be associated with the projection of a piece of an elliptical plane section of a right circular cone, whilst the hyperbolic velocity hodograph for the repulsor is associated with a more complicated structure on the cone. By applying vector techniques directly to the equations of motion it was possible to completely describe the MICZ monopole, monopole–free particle, monopole–oscillator and monopole–repulsor problems and obtain several new results stemming from the rich geometry of the Laplace–Runge–Lenz analogues as well as explore new classes of problems possessing conserved

vectors. It was also possible to apply Fradkin's technique to the projected equation of motion for the monopole–oscillator and monopole–repulsor problems to find conserved vectors and tensors. The Lie symmetries were also used to determine the conserved vectors for the monopole–oscillator problem, although this time the geometric symmetry associated with the conserved quantity was employed.

It would appear at this stage that it is possible to generalise the results of Chapters 2 and 3 to include problems where neither the magnitude nor the direction of the angular momentum is conserved. Equations of motion of the form

$$\ddot{\boldsymbol{r}} + a\boldsymbol{L} + b\dot{\boldsymbol{r}} + c\boldsymbol{r} = \boldsymbol{0}$$

appear to possess a generalised Poincaré vector

$$\boldsymbol{P} = \hat{\boldsymbol{L}} - \lambda\hat{\boldsymbol{r}}$$

provided certain simplifying assumptions are made. These type of problems may well provide interesting comparisons with their two–dimensional analogues particularly regarding analogues of Kepler's third law. These are problems to be considered in the future.

The results of Chapter 4 demonstrate that the Lie symmetry technique which can often provide very useful information on the geometric properties of differential equations is not always helpful such as in situations where two differential equations can be transformed into one another using only simple vector operations applied to the equations of motion which are not described by point transformations (see §4.5). The advent of freely available computer software such as the program LIE [50] which can entirely automate the extremely tedious calculations involved in applying the Lie method now makes it possible to apply this technique to representative examples of a general equation where previously the work and the inevitable mistakes involved in doing the calculations by hand made it impractical.

Due to the vector nature of many of the problems arising in electrodynamics, it would appear that the vector techniques applied here could be implemented successfully on similar types of problems. One such example of a vector equation of motion describes the path of an electron in a magnetic field, which moves in a helix on the surface of a cylinder. Other problems worth considering would be the equation of motion of an electric point charge in the field of a magnetic dipole, for which several first integrals are already known [100]. It might also be worthwhile to consider extensions to multipole potentials.

REFERENCES

[1] Atiyah M.F. and Hitchin N.J. "Low Energy Scattering of Non–Abelian Magnetic Monopoles", *Phil. Trans. R. Soc. Lond. A*, **315**, 459–469 (1985).

[2] Atiyah M.F. and Hitchin N.J. "Low Energy Scattering of Non–Abelian Monopoles", *Phys. Lett.*, **107A**, 21–25 (1985).

[3] Bacry H. "Comment on 'The Relationship between the Symmetries of and the Existence of Conserved Vectors for the Equation $\ddot{\boldsymbol{r}} + f(r)\boldsymbol{L} + g(r)\boldsymbol{r} = \boldsymbol{0}$' ", *J. Phys. A: Math. Gen.*, **24**, 1157–1159 (1991).

[4] Bacry H., Ruegg H. and Souriau J.M. "Dynamical Groups and Spherical Potentials in Classical Mechanics", *Commun. Math. Phys.*, **3**, 323–333 (1966).

[5] Bargmann V. "Zur Theorie des Wasserstoffatoms. Bemerkungen zur gleichnamigen Arbeit von V. Fock.", *Z. Phys.*, **99**, 576–582 (1936).

[6] Bates L. "Symmetry Preserving Deformations of the Kepler Problem" (Preprint University of Calgary, Department of Mathematics and Statistics, 1990).

[7] Bertrand J. "Théorème Relatif au Mouvement d'un Point Attiré Vers un Centre Fixe", *Comp. Rend. Acad. Sci. Paris*, **77**, 849–853 (1873).

[8] Bleuler K. and Kustaanheimo P.E. "Vectorielle Methoden in der Quantenmechanik I", *Ann. Acad. Sci. Fenn. A. VI* (Astronomisches Observatorium der Universität Helsinki, Finnland, 1967), pp. 1–14.

[9] Bluman G.W. and Kumei S. "Symmetries and Differential Equations" (Springer–Verlag, New York, 1989).

[10] Boulware D.G., Brown L.S., Cahn R.N., Ellis S.D. and Lee C. "Scattering on Magnetic Charge", *Phys. Rev. D*, **14**, 2708–2727 (1976).

[11] Bouquet S.E., Feix M.R. and Leach P.G.L. "Properties of Second Order Ordinary Differential Equations Invariant under Time Translation and Self–Similar Transformation", *J. Math. Phys.*, **32**, 1480–1490 (1991).

[12] Broucke R. "On the Construction of a Dynamical System from a Preassigned Family of Solutions", *Int. J. Engng Sci.*, **17**, 1151–1162 (1979).

[13] Broucke R. "Notes on the Central Force r^n", *Astro. Sp. Sci.*, **72**, 33–53 (1980).

[14] Brouwer D. and Hori G. "Theoretical Evaluation of Atmospheric Drag Effects in the Motion of an Artificial Satellite", *Astronom. J.*, **66**, 193–225 (1961).

[15] Buch L.H. and Denman H.H. "Conserved and Piecewise–Conserved Runge Vectors for the Isotropic Harmonic Oscillator", *Am. J. Phys.*, **43**, 1046–1048 (1975).

[16] Buch L.H. and Denman H.H. "Dynamical Symmetries and the Nonconservative Classical System", *Phys. Rev. D*, **11**, 279–281 (1975).

[17] Chen A.C. "Coulomb–Kepler Problem and the Harmonic Oscillator", *Am. J. Phys.*, **55**, 250–252 (1987).

[18] Child J.M. "Hamilton's Hodograph", *The Monist*, **25**, 615–624 (1915).

[19] Cohen I.B. "The Birth of a New Physics", (Penguin Books, England, 1987) Chap. 7.

[20] Collas P. "Algebraic Solution of the Kepler Problem Using the Runge–Lenz Vector", *Am. J. Phys.*, **38**, 253–255 (1970).

[21] Collinson C.D. "Investigation of Planetary Orbits using the Lenz–Runge Vector", *Bull. Inst. Math. Appl.*, **9**, 377–378 (1973).

[22] Collinson C.D. "The Mathematical Simplicity of the Inverse Square Force", *Mathl. Gaz.*, **61**, 139–140 (1977).

[23] Cordani B. "On the Fock Quantization of the Hydrogen Atom" (Preprint 47/1988 Dipartimento di Matematica 'F Enriques' Via C Saldini 50, 20133, Milano, Italia).

[24] Cushing J.T. "Kepler's Laws and Universal Gravitation in Newton's *Principia*", *Am. J. Phys.*, **50**, 617–628 (1982).

[25] Danby J.M.A. "Fundamentals of Celestial Mechanics" (Macmillan, New York, 1962), p. 231.

[26] Fehér L. Gy "The O(3,1) Symmetry Problem of the Charge Monopole Interaction", *J. Math. Phys.*, **28**, 234–239 (1987).

[27] Fock V. "Zur Theorie des Wasserstoffatoms", *Z. Phys.*, **98**, 145–154 (1935).

[28] Fradkin D.M. "Three Dimensional Isotropic Harmonic Oscillator and SU_3", *Am. J. Phys.*, **33**, 207–211 (1965).

[29] Fradkin D.M. "Existence of the Dynamic Symmetries O_4 and SU_3 for all Classical Central Potential Problems", *Prog. Theor. Phys.*, **37**, 798–812 (1967).

[30] Gascón F.G., Ramos F.B. and Aguirre–Daban E. "On the Polynomial First Integrals of Certain Second–Order Differential Equations", *J. Math. Phys.*, **23**, 2281–2285 (1982).

[31] Goldstein H. "Prehistory of the 'Runge–Lenz' Vector"', *Am. J. Phys.*, **43**, 737–738 (1975).

[32] Goldstein H. "More on the Prehistory of the Laplace or Runge–Lenz Vector", *Am. J. Phys.*, **44**, 1123–1124 (1976).

[33] Goldstein H. "Classical Mechanics" (World Student Series Edition, Addison–Wesley Publishing Company, Massachusetts, 1980), Chap. 3.

[34] Gorringe V.M. and Leach P.G.L. "Dynamical Properties of the System $\ddot{\boldsymbol{r}} = \ddot{u}\boldsymbol{r}/u - \mu\boldsymbol{r}/(ur^3)$" (Preprint University of Witwatersrand, Department of Computational and Applied Mathematics, 1986).

[35] Gorringe V.M. and Leach P.G.L. "Conserved Vectors for the Autonomous System $\ddot{\boldsymbol{r}} + g(r,\theta)\hat{\boldsymbol{r}} + h(r,\theta)\hat{\boldsymbol{\theta}} = \boldsymbol{0}$", *Physica*, **27D**, 243–248 (1987).

[36] Gorringe V.M. and Leach P.G.L. "Conserved Vectors and Orbit Equations for Motions in Two and Three Dimensions", Proc. Workshop on Finite Dimensional Integrable Nonlinear Dynamical Systems, edd Leach P.G.L. and Steeb W–H. (World Scientific, Singapore, 1988), pp. 190–204.

[37] Gorringe V.M. and Leach P.G.L. "Hamilton–Like Vectors for a Class of Kepler Problems with a Force Proportional to the Velocity", *Celest. Mech.*, **41**, 125–130 (1988).

[38] Gorringe V.M. and Leach P.G.L. "Lie Point Symmetries for Systems of Second Order Linear Ordinary Differential Equations", *Quæst. Math.*, **11**, 95–117 (1988).

[39] Gorringe V.M. and Leach P.G.L. "Conserved Vectors and Orbit Equations for Autonomous Systems governed by the Equation of Motion $\ddot{\boldsymbol{r}} + f\dot{\boldsymbol{r}} + g\boldsymbol{r} = \boldsymbol{0}$", *Am. J. Phys.*, **57**, 432–435 (1989).

[40] Gorringe V.M. and Leach P.G.L. "First Integrals Associated with the Additional Symmetry of Central Force Problems with Power Law Potentials", *Quæst. Math.*, **14**, 277–289 (1991).

[41] Gorringe V.M. and Leach P.G.L. "Kepler's Third Law and the Oscillator's Isochronism", *Am. J. Phys.*, **61**, 991–995 (1993).

[42] Gorringe V.M. and Leach P.G.L. "The First Integrals and their Lie Algebra of the Most General Autonomous Hamiltonian of the form $H = T + V$ possessing a Laplace–Runge–Lenz Vector", *J. Austral. Math. Soc. Ser. B* **34**, 511–522 (1993).

[43] Gradshteyn I.S. and Rhyzhik I.M. "Table of Integrals, Series, and Products" (Academic Press, Orlando, 1980), Chap. 2.

[44] Grammaticos B., Dorizzi B. and Ramani A. "Hamiltonians with High–Order Integrals and the 'Weak–Painlevé' Concept", *J. Math. Phys.*, **25**, 3470–3473 (1984).

[45] Greenberg D.F. "Accidental Degeneracy", *Am. J. Phys.*, **34**, 1101–1109 (1966).

[46] Günther N.J. and Leach P.G.L. "Generalised Invariants for the Time–Dependent Harmonic Oscillator", *J. Math. Phys.*, **18**, 572–576 (1977).

[47] Hall L.S. "A Theory of Exact and Approximate Configurational Invariants", *Physica*, **8D**, 90–113 (1983).

[48] Hamilton W.R. "On the Application of the Method of Quaternions to some Dynamical Questions", *Proc. R. Irish Acad.*, **3**, 344–353, appendix no. III p. xxxvi ff, especially p. xxxix (1847).

[49] Hankins T.L. "Sir William Rowan Hamilton" (John Hopkins University Press, Maryland, 1980), Chap. 24.

[50] Head A.K. "LIE 3.4 – Program for Lie Analysis of Differential Equations on IBM PC's" (Public Domain, Available by anonymous FTP from wuarchive.wustl.edu 128.252.135.4).

[51] Heintz W.H., "Determination of the Runge–Lenz Vector", *Am. J. Phys.*, **42**, 1078–1082 (1974).

[52] Hietarinta J. "Classical versus Quantum Integrability", *J. Math. Phys.*, **25**, 1833–1840 (1984).

[53] Hietarinta J. "A Listing of Integrable Two–Degree–of–Freedom Hamiltonian Systems" (Preprint University of Turku, Finland, 1985).

[54] Holas A. and March N.H. "A Generalisation of the Runge–Lenz Constant of Classical Motion in a Central Potential", *J. Phys. A: Math. Gen.*, **23**, 735–749 (1990).

[55] Ince E.L. "Ordinary Differential Equations" (Dover, New York, 1956), §2.701 p. 46.

[56] Jackiw R. "Dynamical Symmetry of the Magnetic Monopole", *Ann. Phys.*, **129**, 183–200 (1980).

[57] Jauch J.M. and Hill E.L. "On the Problem of Degeneracy in Quantum Mechanics", *Phys. Rev.*, **57**, 641–645 (1940).

[58] Jezewski D.J. and Mittleman D. "Integrals of Motion for the Classical Two-Body Problem with Drag", *Int. J. Non-Linear Mech.*, **18**, 119–124 (1983).

[59] Kaplan H. "The Runge–Lenz Vector as an 'Extra' Constant of the Motion", *Am. J. Phys.*, **54**, 157–161 (1986).

[60] Katzin G.H. and Levine J. "Time–Dependent Quadratic Constants of Motion, Symmetries, and Orbit Equations for Classical Particle Dynamical Systems with Time–Dependent Kepler Potentials", *J. Math. Phys.*, **23**, 552–563 (1982).

[61] Katzin G.H. and Levine J. "Time Dependent Vector Constants of Motion, Symmetries, and Orbit Equations for the Dynamical System $\ddot{\boldsymbol{r}} = \hat{\boldsymbol{I}}_r\left\{\left[\ddot{U}(t)/U(t)\right] r - \left[\mu_0/U(t)\right] r^{-2}\right\}$", *J. Math. Phys.*, **24**, 1761–1771 (1983).

[62] Kelland P. and Tait P.G. "Introduction to Quaternions" (Macmillan and Company, London, 1904), Chap. IX.

[63] Kelvin Lord and Tait P.G. "Elements of Natural Philosophy" (At the University Press, Cambridge, 1894).

[64] Kelvin Lord and Tait P.G. "Treatise on Natural Philosophy" (At the University Press, Cambridge, 1923), Part I.

[65] Kepler J. "Astronomia Nova" (Opera Omnia, Edidit Frisch C.H., Heyder and Zimmer, Francofurti, MDCCCLX), Volumen III.

[66] Kepler J. "Harmonices Mundi Liber V" (Opera Omnia, Edidit Frisch C.H., Heyder and Zimmer, Francofurti, MDCCCLXIV), Volumen V.

[67] Kepler J. "The Harmonies of the World: V" (Translated by Wallis C.G., Encyclopædia Britannica, Chicago, 1952).

[68] Koestler A. "The Watershed – A Biography of Johannes Kepler" (Heinemann Educational Books, London, 1961).

[69] Laplace P.S. "Traité de Mécanique Céleste" (Paris, An. VII. (1798–1799)), Tome I, Premiere Partie, Livre II, p. 165 ff.

[70] Laplace P.S. "Oeuvres" (Gauthier–Villars, Paris, 1843), Tome I, p. 187 ff.

[71] Leach P.G.L. "Quadratic Hamiltonians: The Four Classes of Invariants, their Interrelations and Symmetries", *J. Math. Phys.*, **21**, 32–37 (1980).

[72] Leach P.G.L. "Applications of the Lie Theory of Extended Groups in Hamiltonian Mechanics: The Oscillator and the Kepler Problem", *J. Austral. Math. Soc*, **23B**, 173–186 (1981).

[73] Leach P.G.L. "Classes of Potentials of Time–Dependent Central Force Fields which Possess First Integrals Quadratic in the Momenta", *J. Math. Phys*, **26**, 1613–1620 (1985).

[74] Leach P.G.L. "Comment on an Aspect of a Paper by G. Thompson", *J. Math. Phys.*, **27**, 153–156 (1986) and Erratum **27**, 2445–2446 (1986).

[75] Leach P.G.L. "The First Integrals and Orbit Equation for the Kepler Problem with Drag", *J. Phys. A: Math. Gen.*, **20**, 1997–2002 (1987).

[76] Leach P.G.L., Feix M.R. and Bouquet S.E. "Analysis and Solution of a Nonlinear Second Order Differential Equation through Rescaling and through a Dynamical Point of View", *J. Math. Phys.*, **29**, 2563–2569 (1988).

[77] Leach P.G.L. and Gorringe V.M. "Variations on Newton's Keplerian Theme", *S. Afr. J. Sci.*, **83**, 550–555 (1987).

[78] Leach P.G.L. and Gorringe V.M. "A Conserved Laplace–Runge–Lenz–Like Vector for a Class of Three–Dimensional Motions", *Phys. Lett. A*, **133**, 289–294 (1988).

[79] Leach P.G.L. and Gorringe V.M. "The Relationship between the Symmetries of and the Existence of Conserved Vectors for the Equation $\ddot{\boldsymbol{r}}+f(r)\boldsymbol{L}+g(r)\boldsymbol{r}=\boldsymbol{0}$", *J. Phys. A: Math. Gen.*, **23**, 2765–2774 (1990).

[80] Leach P.G.L. and Mahomed F. "Symmetries of Differential Equations – An Introduction to the How, the Why and the Wherefore" (Workshop on Dynamical Systems, Willem Pretorius Game Reserve, OVS, 1992).

[81] Lenz W. "Über den Bewegungsverlauf und die Quantenzustände der gestörten Keplerbewegung", *Z. Phys.*, **24**, 197–207 (1924).

[82] Lévy–Leblond J.M. "Conservation Laws for Gauge–Variant Lagrangians in Classical Mechanics", *Am. J. Phys.*, **39**, 502–506 (1971).

[83] Lewis H.R. "Classical and Quantum Systems with Time–Dependent Harmonic–Oscillator–Type Hamiltonians", *Phys. Rev. Lett.*, **18**, 510–512 (1967) and Erratum **18**, 636 (1967).

[84] Lewis H.R. "Class of Exact Invariants for Classical and Quantum Time–Dependent Harmonic Oscillators", *J. Math. Phys*, **9**, 1976–1986 (1968).

[85] Lewis H.R. and Leach P.G.L. "A Direct Approach to Finding the Exact Invariants for One–Dimensional Time–Dependent Classical Hamiltonians", *J. Math. Phys.*, **23**, 2371–2374 (1982).

[86] Lewis H.R. and Riesenfeld W.B. "An Exact Quantum Theory of the Time–Dependent Harmonic Oscillator and of a Charged Particle in a Time–Dependent Electromagnetic Field", *J. Math. Phys.*, **10**, 1458–1473 (1969).

[87] Lutzky M. "Dynamical Symmetries and Conserved Quantities", *J. Phys. A: Math. Gen.*, **12**, 973–981 (1979).

[88] Manton N.S. "A Remark on the Scattering of BPS Monopoles", *Phys. Lett.*, **110B**, 54–56 (1982).

[89] Manton N.S. "Monopole Interactions at Long Range", *Phys. Lett.*, **154B**, 397–400 (1985) and Erratum **157B**, 475 (1985).

[90] Maple (Version V Release 2, Waterloo Maple Software, 160 Columbia Street West, Waterloo, Ontario, Canada N2L 3L3, e–mail wmsi@daisy.uwaterloo.ca, 1993).

[91] Martínez–y–Romero R.P., Núñez–Yépez H.N. and Salas–Brito A.L. "Closed Orbits and Constants of Motion in Classical Mechanics", *Eur. J. Phys.*, **13**, 26–31 (1992).

[92] Mavraganis A.G. "The Almost Constant–Speed Two–Body Problem with Resistance" (Preprint National Technical University of Athens, Department of Engineering Science, 1991).

[93] Maxwell J.C. "Matter and Motion" (Sheldon Press, London, 1925), Chap. VIII.

[94] McIntosh H.V. and Cisneros A. "Degeneracy in the Presence of a Magnetic Monopole", *J. Math. Phys.*, **11**, 896–916 (1970).

[95] Mittleman D. and Jezewski D.J. "An Analytic Solution to the Classical Two–Body Problem with Drag", *Celest. Mech.*, **28**, 401–413 (1982).

[96] Mladenov I.M. "Scattering of Charged Particles off Dyons", *J. Phys. A: Math. Gen*, **21**, L1–L4 (1988).

[97] Mladenov I.M. and Tsanov V.V. "Geometric Quantisation of the MIC–Kepler Problem", *J. Phys. A: Math. Gen.*, **20**, 5865–5871 (1987).

[98] Moreira I.C. "A Note on the Invariants for the Time–Dependent Oscillator", *J. Phys. A: Math. Gen.*, **18**, 899–907 (1985).

[99] Moreira I.C. "Comments on a 'Direct Approach to Finding Exact Invariants for One–Dimensional Time-Dependent Classical Hamiltonians' " (Preprint Universade Federal do Rio de Janeiro, Instituto de Fisica, 1983).

[100] Moreira I.C. and Ritter O.M. "Time–Dependent Generalisations of the Kepler Problem, Charge–Monopole Problem and Charge–Magnetic Dipole Problems, their Symmetries and Invariants" (Preprint Universade Federal do Rio de Janeiro, Instituto de Fisica, 1990).

[101] Moreira I.C., Ritter O.M. and Santos F.C. "Lie Symmetries for the Charge–Monopole Problem", *J. Phys. A: Math. Gen.*, **18**, L427–L430 (1985).

[102] Newton I. "Mathematical Principles of Natural Philosophy and his System of the World" (Translated by A. Motte in 1729 and revised by F. Cajori, University of Califonia Press, Berkeley, 1946).

[103] Patera J., Sharp R.T. and Winternitz P. "Invariants of Real Low Dimension Lie Algebras", *J. Math. Phys.*, **17**, 986–994 (1976).

[104] Patera J. and Winternitz P. "Subalgebras of Real Three– and Four–Dimensional Lie Algebras", *J. Math. Phys.*, **18**, 1449–1455 (1977).

[105] Pauli W. "Über das Wasserstoffspektrum vom Standpunkt der neuen Quantenmechanik", *Z. Phys.*, **36**, 336–363 (1926).

[106] Peres A. "A Classical Constant of the Motion with Discontinuities", *J. Phys. A: Math. Gen.*, **12**, 1711–1713 (1979).

[107] Poincaré H. "Remarques sur une Expérience de M. Birkeland", *Comp. Rend. Acad. Sci. Paris*, **123**, 530–533 (1896).

[108] Pollard H. "Celestial Mechanics" (The Carus Mathematical Monographs No. 18, The Mathematical Association of America, 1976), Chap. 1.

[109] Prince G.E. and Eliezer C.J. "Symmetries of the Time–Dependent $N-$Dimensional Oscillator", *J. Phys. A: Math. Gen.*, **13**, 815–823 (1980).

[110] Prince G.E. and Eliezer C.J. "On the Lie Symmetries of the Classical Kepler Problem", *J. Phys. A: Math. Gen.*, **14**, 587–596 (1981).

[111] Rainwater J.C. and Weinstock R. "Inverse–Square Orbits: A Geometric Approach", *Am. J. Phys.*. **47**, 223–227 (1979) and additional correspondence **47**, 1093 (1979).

[112] REDUCE (Version 3.2, The Rand Corporation, Santa Monica, CA 90406, 1985).

[113] Routh E.J. "A Treatise on Dynamics of a Particle" (At the University Press, Cambridge, 1898).

[114] Runge C. "Vector Analysis" (Translated by H. Levy, Methuen, London, 1923), Vol. 1.

[115] Sarlet W. and Bahar L.Y. "A Direct Construction of First Integrals for Certain Non–Linear Dynamical Systems", *Int. J. Non–Linear Mech.*, **15**, 133–146 (1980).

[116] Sarlet W., Leach P.G.L. and Cantrijn F. "First Integrals Versus Configurational Invariants and a Weak Form of Complete Integrability", *Physica*, **17D**, 87–98 (1985).

[117] Sattinger D.H. and Weaver O.L. "Lie Groups and Algebras with Applications to Physics, Geometry, and Mechanics" (Springer–Verlag, New York, 1986).

[118] Sen T. "A Class of Integrable Potentials", *J. Math. Phys.*, **28**, 2841–2850 (1987).

[119] Sivardière J. "Precession of Elliptic Orbits", *Am. J. Phys.*, **52**, 909–912 (1984).

[120] Sivardière J. "Laplace Vectors for the Harmonic Oscillator", *Am. J. Phys.*, **57**, 524–525 (1989).

[121] Stickforth J. "The Classical Kepler Problem in Momentum Space", *Am. J. Phys.*, **46**, 74–75 (1978).

[122] Symon K. "Mechanics" (World Student Series Edition, Addison–Wesley Publishing Company, Massachusetts, 1969), Chap. 3.

[123] Taff L.G. "Celestial Mechanics" (Wiley–Interscience, New York, 1985), p. 40.

[124] Tait P.G. "An Elementary Treatise on Quaternions" (At the University Press, Cambridge, 1890), Chap XI.

[125] Thompson G. "Polynomial Constants of Motion in Flat Space", *J. Math. Phys.*, **25**, 3474–3478 (1984).

[126] Thompson G. "Second Order Systems with Runge–Lenz–Type Vectors", *Lett. Math. Phys.*, **14**, 69–75 (1987).

[127] Weinstock R. "Dismantling a Centuries–Old Myth: Newton's *Principia* and Inverse–Square Orbits", *Am. J. Phys.*, **50**, 610–617 (1982).

[128] Weinstock R. "Long–Buried Dismantling of a Centuries–Old Myth: Newton's *Principia* and Inverse–Square Orbits", *Am. J. Phys.*, **57**, 846–849 (1989).

[129] Whittaker E.T. "A Treatise on the Analytical Dynamics of Particles and Rigid Bodies" (Cambridge Mathematical Library, Cambridge University Press, Cambridge, 1989), Chap. 4.

[130] Yan C.C. "Determination of Vector Constant of Motion for a Particle Moving in a Conservative Central Force Field", *J. Phys. A: Math. Gen.*, **24**, 4731–4738 (1991).

[131] Yoshida T. "Determination of the Generalised Laplace–Runge–Lenz Vector by an Inverse Matrix Method", *Am. J. Phys.*, **57**, 376–377 (1987).

[132] Yoshida T. "Two Methods of Generalisation of the Laplace–Runge–Lenz Vector", *Eur. J. Phys.*, **8**, 258–259 (1987).

[133] Yoshida T. "A Vectorial Derivation of Kepler's Equation", *Am. J. Phys.*, **56**, 561–563 (1988).

[134] Zwanziger D. "Exactly Solvable Nonrelativistic Model of a Particle with both Electric and Magnetic Charges", *Phys. Rev.*, **176**, 1480–1488 (1968).